PARTICLE IMAGE VELOCIMETRY NEAR THE LEADING EDGE OF A SIKORSKY SSC-A09 WING DURING DYNAMIC STALL

A Thesis

by

RACHEL RENEE VANNELLI

Submitted to the Office of Graduate Studies of
Texas A&M University
in partial fulfillment of the requirements for the degree of

MASTER OF SCIENCE

December 2011

Major Subject: Aerospace Engineering

Particle Image Velocimetry Near the Leading Edge of a Sikorsky SSC-A09 Wing

During Dynamic Stall

PARTICLE IMAGE VELOCIMETRY NEAR THE LEADING EDGE OF A SIKORSKY SSC-A09 WING DURING DYNAMIC STALL

A Thesis

by

RACHEL RENEE VANNELLI

Submitted to the Office of Graduate Studies of
Texas A&M University
in partial fulfillment of the requirements for the degree of

MASTER OF SCIENCE

Approved by:

Chair of Committee,	Rodney D. W. Bowersox
Committee Members,	Simon North
	Othon Rediniotis
Head of Department,	Dimitris Lagoudas

December 2011

Major Subject: Aerospace Engineering

ABSTRACT

Particle Image Velocimetry Near the Leading Edge of a Sikorsky SSC-A09 Wing During Dynamic Stall. (December 2011)

Rachel Renee Vannelli, B.S., Texas A&M University

Chair of Advisory Committee: Dr. Rodney D. W. Bowersox

Dynamic stall has proven to be a complex problem in helicopter aerodynamics because it limits the helicopter flight regime. Dynamic stall is characterized by drastic increases in lift and a delay of stall due to rapid pitching motions of aerodynamic surfaces. Prediction and control of dynamic stall requires an understanding of the leading edge flow structure.

An investigation was conducted of dynamic stall near the leading edge of a large-scale Sikorsky SSC-A09 airfoil, dynamically pitching about its quarter chord, under realistic helicopter flight conditions ($M_\infty = 0.1$, $k = 0.1$, $Re_c = 1.0\times10^6$). A testing model with a chord of 0.46 m and a span of 2.13 m was designed and constructed for experimentation in the Dynamic Stall Facility at Texas A&M University. Particle image velocimetry data were recorded for the first 15% of the airfoil chord. Mean velocities, Reynolds stresses, and vorticity were computed. Analyses revealed that during the upstroke, stall onset is delayed in the leading edge region and the first indications of separation are observed at 18° angle of attack. The edge of the boundary layer has been characterized for $\alpha = 18°$. The roles of the Reynolds stresses and vorticity are examined.

To my family, for everything you do.

ACKNOWLEDGEMENTS

I would like to thank Dr. Rodney Bowersox, my committee chair, for all of his invaluable guidance and support throughout the course of this process. I extend my thanks to Dr. Othon Rediniotis and Dr. Simon North for serving as members on my supervising committee. I thank Karen Knabe and Colleen Leatherman, Aerospace Department staff members, for all their help with paperwork and deadlines. I also thank the Army Research Office for supporting this research financially.

I would like to thank all of the employees at the Oran W. Nicks Low Speed Wind Tunnel for assistance in construction and installation of the testing facilities and apparatus. Thank you to Jorge Martinez, the facility director, for working with me to schedule time for testing. Thank you to Ross Flach and Chris Adcock for all their help in manufacturing the testing apparatus. Thank you to Dave Shelby for all the hours he spent with me assembling and finishing the testing apparatus and turning it into a work of art.

Thanks go to my colleagues at the National Aerothermochemistry Laboratory for all their help in conducting experiments and processing data. Specifically, Chi Mai, who was always available to help me run my testing facility, no matter what time of day or night it was. I am grateful for all the help given to me by Alex Craig, Timothy Guenthner, Dr. Ray Humble, Nicole Mendoza, Scott Peltier, Brandon Pruski, Michael Semper, David Taylor, and Dr. Nathan Tichenor. Thanks also go to Dr. Dipankar Sahoo for designing the Dynamic Stall Facility and instructing me in its use.

Thanks go to my family and friends for supporting me throughout this endeavor. Special thanks to the Leach family for helping me through one of the most difficult decisions I've ever made. Thank you to the Davis family for going great lengths to ensure I completed this. Thank you to my parents and sisters for listening to everything I had to say, even if you didn't understand a word I said, and keeping me focused. Finally, I'd like to thank Jason Davis for everything you've done to make sure I do this and get it right.

NOMENCLATURE

ARO	Army Research Office
c	Chord length
CCD	Charge-coupled device
CFD	Computational Fluid Dynamics
DSF	Dynamic Stall Facility
f	Frequency of pitching motion [Hz]
k	Reduced frequency ($= \pi fc/U_\infty$)
LDV	Laser Doppler Velocimetry
LSV	Laser Speckle Velocimetry
LSWT	Low Speed Wind Tunnel
M_∞	Freestream Mach number
OWN	Oran W. Nicks
PDI	Point Diffraction Interferometry
PID	Proportional-Integral-Derivative
PIV	Particle Image Velocimetry
PTV	Particle Tracking Velocimetry
Q	Quality factor (signal to noise ratio in DaVis software)
Re	Reynolds number
TAMU	Texas A&M University
u	Instantaneous velocity component in the x-direction

u'	Fluctuating velocity component in the x-direction
U	Normalized mean velocity component in the x-direction ($=\bar{u}/U_\infty$)
U_∞	Freestream velocity
UAC	United Aircraft Corporation
v	Instantaneous velocity component in the y-direction
v'	Fluctuating velocity component in the y-direction
V	Normalized mean velocity component in the y-direction ($=\bar{v}/U_\infty$)
x, y, z	Cartesian coordinates
α	Angle of attack
α^+	Non-dimensional pitch rate ($=\dot{\alpha}c/U_\infty$)
σ_u	Reynolds averaged stream-wise normal stress ($=\overline{u'u'}/U_\infty^2$)
σ_v	Reynolds averaged vertical normal stress ($=\overline{v'v'}/U_\infty^2$)
τ_{xy}	Reynolds averaged shear stress ($=-\overline{u'v'}/U_\infty^2$)
ω_z	z-component of vorticity ($=\partial v/\partial x-\partial u/\partial y$)

TABLE OF CONTENTS

Page

LIST OF FIGURES

FIGURE Page

FIGURE Page

FIGURE Page

FIGURE Page

FIGURE Page

FIGURE Page

LIST OF TABLES

1. INTRODUCTION

This section provides an overview of the research conducted and analyzed in this thesis. Section 1.1 summarizes the practical motivation for examining the dynamic stall phenomenon. Section 1.2 provides a description of the research objectives for this study. In Section 1.3 a brief description of the research approach is given. The importance this research will have to the scientific community is discussed in Section 1.4. The introduction concludes with an overview of the topics that will be discussed throughout the remainder of this thesis.

1.1 Motivation for Examining the Dynamic Stall Problem

Forward flight is a defining phase of helicopter flight because of the manner in which forward motion is achieved (Ref. 1-3). Unlike in airplanes, forward flight is not achieved through axial thrust in the forward direction. Axial thrust is primarily in the vertical direction for a helicopter; therefore, in order to achieve forward flight the direction of the primary thrust vector must be altered.

A simple force and moment balance is done for the helicopter; for forward flight a net force along the longitudinal axis is needed (Ref. 1-3). To achieve a net force in the longitudinal direction we alter the direction of the principal thrust vector so it has a longitudinal component not just a vertical one. The thrust vector is tilted forward allowing for forward motion. To tilt the thrust vector the entire rotor must be tilted. The

---

This thesis follows the style of *Journal of the American Helicopter Society.*

helicopter fuselage plays no part in the thrust of a helicopter, including determining the direction of travel. Because rotors are equipped with various sets of hinges and possess the ability to bend and deform what is considered when discussing the rotor disc is actually called the tip-path plane. The tip-path plane is simply a plane that contains all rotor blade tips and sits above the helicopter. The fuselage is essentially a free-swinging pendulum attached to a rotor disc that is fixed in space according to aerodynamics. Rotor thrust is always perpendicular to the tip-path plane. By changing the tilt of the tip-path plane in the air the thrust vector tilts accordingly creating a thrust component in the direction of the tilt. The tilt must be great enough that the horizontal component of thrust is larger than the rotor H-force and sum of the various drags acting on the helicopter. H-force is defined as the force in the rotor plane that is caused by a net drag imbalance on all the blade elements.

Forward flight is different from vertical phases of helicopter flight in one primary way; local velocity distributions are different at each rotor blade (Ref. 1-3). Velocities at the tips of the advancing and retreating blades are compared in a quantity referred to as the tip-speed ratio. The resulting velocity difference is the net forward velocity. This is only true if the velocity at the tip of the advancing blade is greater than that of the retreating blade tip. Otherwise, the net velocity would be in the rearward direction.

The reverse flow region is important to helicopters and critical for dynamic stall to occur. In the reverse flow region, the flow is going in the correct direction for the helicopter, but for the retreating blade the flow is reversed (Ref. 1-3). The air is actually impinging on the trailing edge of the blade and flowing toward the leading edge in this

region. This region is always circular in shape and tangential to the hub on the root end of the retreating blade. The greater the helicopter's forward speed is, the larger the reverse flow region is. Modern helicopters traveling forward at maximum speed have a reverse flow region that can extend outward up to 45% of the way to the blade tip. The size of the reverse flow region extends from the hub a fraction of the rotor blade equivalent to the tip-speed ratio. Dynamic stall occurs primarily in this reverse flow region.

Dynamic stall is defined as the unsteady flow separation occurring on aerodynamic bodies, such as airfoils and wings, which execute rapid changes in angle of attack (Ref. 4). Dynamic stall is a complex aerodynamic occurrence observed on helicopter rotors, wind turbines, compressor blades, fighter aircraft, and several other aerodynamic surfaces that undergo rapid pitching motions. During dynamic stall, an aerodynamic surface experiences an increase in lift and a delay of flow separation and stall. This phenomenon has been a consistent challenge in the design of many aircraft, especially helicopters. Dynamic stall limits helicopters in the high speed flight regime and airplanes in the low speed flight regime. It has been suggested that developing methods to control dynamic stall would increase the flight envelope and maneuverability of aircraft.

Dynamic stall in helicopters is often referred to as retreating blade stall, wherein during forward flight, retreating rotor blades experience flow reversal, air moving opposite the direction of blade motion (Refs. 1-3). As forward speed of a helicopter increases, the speed of the retreating blade decreases. To maintain level flight it is

necessary to equalize lift across the area of the rotor disc. During hover, a no lift region exists in the center of the rotor disc. During normal cruise this no lift region shifts to the side, positioning itself over the root of the retreating rotor blade. If the angle of attack of the rotor disc is constant the amount of lift generated by the advancing blade side of the rotor disc will be much greater than the lift generated by the smaller area, slower moving retreating blade side of the rotor disc. To achieve the necessary balance across the rotor disc rapid changes in angle of attack of the retreating rotor blade must occur. The larger angles of attack of the retreating blade, coupled with the forward motion eventually lead to stall conditions.

When critical airspeeds are reached, the angle of attack at the tip of the retreating rotor blade gets large enough to cause local dynamic stall (Refs. 1-3). Dynamic stall can be broken into two fundamental periodic oscillatory motions, pitching and plunging. Pitching is a periodic motion through a range of angles of attack. Plunging is a periodic translational motion in a direction perpendicular to the freestream flow field. During dynamic stall, strong vortices are shed from the leading edge. These result in a brief increase in lift. The vortices move rearward over the upper surface of the rotor blade. As the vortices pass over the trailing edge, a drastic decrease in lift occurs. As the tip angle increases stall begins to spread inboard and the rotor blade tip begins to experience vibrations and buffeting. As the stall region grows, the entire helicopter begins to pitch up and roll toward the retreating blade.

1.2 Research Objectives

The Army Research Office (ARO) has proposed a study to examine the leading edge boundary layer physics just upstream of separation during the dynamic stall process for the high-lift Sikorsky SSC-A09 rotor section at realistic helicopter flight conditions. This objective can be broken up into three main goals. First, construct a large-scale rotor blade. Experiment on this rotor blade by observing the flow field as the rotor blade rapidly pitches. Second, characterize the flow field at the leading edge and determine the angles of attack at which dynamic stall occurs. Finally, analyze the leading edge boundary layer structure during the upstroke phase of the pitching process at a single dynamic stall angle.

It was recommended by the Army Research Laboratory (Dr. Preston Martin) that we focus our effort at Mach 0.1, $k = 0.1$, and $Re_c = 1.0\times10^6$ as the boundary layer is thicker near the nose than at higher Mach numbers and thus easier to resolve. This Mach number is slightly lower than is typically observed in the helicopter flight regime of Mach 0.2 to Mach 0.4. Additionally, at Mach 0.1 for a reduced frequency of 0.1, the required pitching frequency is 2.5 Hz, while at Mach 0.2 for a reduced frequency of 0.1, the required pitching frequency is 5.0 Hz. The DSF experiences considerably less vibration when operating at 2.5 Hz than 5.0 Hz, allowing for higher quality acquired data. In a companion study, higher Mach numbers were examined for a NACA 0012 wing section.

1.3 Overview of the Research Approach

To meet the scientific objective, a Sikorsky SSC-A09 rotor blade, or wing, was modeled and then manufactured at the Oran W. Nicks (OWN) Low Speed Wind Tunnel

(LSWT) machine shop. The pieces of the seven-foot wingspan SSC-A09 wing were assembled and prepared for testing.

Two systems were necessary for proper data acquisition in the OWN Low Speed Wind Tunnel. The first system was a hydraulic power unit coupled with a linear actuator, used to pitch the wing through a specified angle of attack range. The pitching range, 5 to 25 degrees, and frequency, 2.5 hertz, were determined using a reduced frequency of 0.1, as requested by the ARO, and the velocity at which the testing occurred, Mach 0.1; these are typical values of reduced frequency and Mach number for helicopter flight. A Particle Image Velocimetry (PIV) system was the second system required for data acquisition. A PIV laser illuminated seeding particles in the flow, which follow the flow over the pitching wing. A camera captured two images per pitching cycle. The second image was taken after a slight, but specified time lapse. Approximately 1200 image pairs were obtained for each angle of attack of interest: 16, 18, 20, 22, and 24 degrees.

The image pairs were then processed and post-processed to characterize the flow field. Instantaneous velocity fields were generated for each image pair. The instantaneous velocity vector fields were then averaged and post-processed to determine mean velocities (u- and v-components), Reynolds stresses, and vorticities.

1.4 Contribution to the Scientific Community

Understanding of the leading edge flow structure is critical toward prediction and control of dynamic stall. Attaining this insight at realistic Reynolds numbers is beyond the resources of modern, high fidelity simulations. Recent advances in experimental

methods have enabled experimental exploration of dynamic stall. This thesis provides documentation of the flow field over the leading edge of a large-scale Sikorsky SSC-A09 airfoil rapidly pitching and undergoing dynamic stall. Specifically, experimental data was gathered at realistic helicopter flight conditions ($M_\infty = 0.1$, $k = 0.1$, $Re = 1\times10^6$) for an airfoil largely unstudied in the dynamic stall regime but widely used in helicopters. Mean flow analyses were performed to characterize the flow field. This study is part of a larger program that includes a NACA 0012 wing tested under similar flow conditions.

1.5 Thesis Overview

The research discussed throughout this thesis is broken up into five remaining sections. Section 2 provides a summary of literature with a focus on experimental dynamic stall research. This literature review is organized chronologically to show the progress that has been made in research methods and what has been learned about the dynamic stall phenomenon. Experimental facilities are discussed in Section 3. These facilities include: the wind tunnel environment; the hydraulic system that drives pitching motion; and the rotor blade model. Section 4 focuses on data collection and reduction. Particle image velocimetry is discussed in detail – governing theory, image resolution, experimental implementation, and challenges encountered. Section 5 discusses the results generated from the data acquired in this study. Flow field average velocities and Reynolds stresses are examined for the angles of attack of interest. This thesis concludes with Section 6, which discusses the key elements of discovery throughout this study and future analysis that can expand the scope of dynamic stall research.

2. A CHRONOLOGICAL REVIEW OF DYNAMIC STALL LITERATURE

Dynamic stall is a phenomenon commonly observed in helicopter rotors. It has been found to be a limiting factor of the helicopter flight envelope. Due to the unsteady nature of the phenomenon, as well as the potential to exploit it for added lift, dynamic stall has been a focus of research since the late 1960s. This section will focus on the progression of experimental dynamic stall research through the 2000s.

Among the first aspects of dynamic stall research was studying the angle of attack, α, at various positions on the rotor disc. Paul Madden (Ref. 5) researched prediction of aerodynamic loading, particularly lift, on the rotor disc for high speed applications, via a numerical model. Special attention was paid to the reverse flow region on the retreating blade side of the rotor disc. On the retreating blade portion of the rotor disc, the stall boundary was found to have expanded slightly ahead of the reverse flow region and to have contracted slightly behind the reverse flow region.

F. O. Carta (Ref. 6) analyzed unsteady aerodynamic data obtained by the United Aircraft Research Laboratories for the Sikorsky Aircraft Division of the United Aircraft Corporation (UAC) to determine the susceptibility of helicopter rotor blades to experience a stall flutter instability. Stall flutter was categorized by Norman D. Ham (Ref. 7) to be a special case of dynamic stall. The UAC sponsored an extensive experimental investigation of a NACA 0012 airfoil oscillated in pitch about its quarter chord. The data was reduced to two quantities for comparison, aerodynamic damping parameter in pitch and reduced frequency, k. Carta determined that for mean incidence

angles below 9° measured damping parameter agreed with potential flow theory, while for mean incidence angles above 12° measured damping parameter departed from potential flow theory. Additionally, for low mean incidence angles the damping parameter increases linearly with reduced frequency, while for high mean incidence angles, the damping parameter initially increases with reduced frequency, then decreases to a negative level, then increases again. At high mean incidence angles, the damping parameter becoming negative is indicative of instability. In reference 4, Ham expands on the results generated by Carta, discussing pressure variation along the airfoil profile as well as pitching moment coefficient with respect to angle of attack. Dynamic stall, which begins at $\alpha = 20°$, is related to a drop in the leading edge suction value. Loss of leading edge suction signals a delay in stall conditions. Ham concludes that stall of airfoil sections undergoing rapid high angle of attack changes is delayed well beyond the static stall angle and results in a large pressure disturbance that leads to high lift and large nose down pitching moment. The magnitude of the pitching moment is substantial enough to generate significant pitching displacement of the blade (in the nose down direction). Finally, dynamic stall of helicopter rotors can be separated into three major phases: a delay in the loss of leading edge suction; a subsequent loss of leading edge suction with the formation of a large negative pressure disturbance that moves aft over the upper surface of the blade; complete, classic, upper surface separation.

In 1968 Norman Ham and Melvin Garelick (Ref. 8) published the results of an experimental study of the effects of pitching rate and pitching axis location on an airfoil undergoing non-oscillatory pitching motion to a large angle of attack. Time varying

pressures were measured at specified blade span-wise locations on a 5 inch (0.13 m) chord, 42 inch (1.07 m) span model of a NACA 0012 airfoil section. The model pitched from 0° to 30° at rates varying from 2 to 20 radians per second. Testing was conducted at a chord Reynolds number, Re_c, of 3.44×10^5. From pressure variations, dynamic lift and moment coefficients were calculated. Results indicated that at moderate to high pitching rates, intense vorticity shed from the wing leading edge after dynamic stall dominates aerodynamic loading. Additionally, it was concluded that oscillatory pitching motion experiences pitching moments that sustain the pitching motion for certain values of reduced frequency and mean pitching angle, resulting in the previously discussed phenomenon of stall flutter. Ham and Garelick verified that the peak aerodynamic loading values are greater for an airfoil undergoing dynamic stall than for the same airfoil under static conditions. Rate of change of angle of attack is the dominant factor for determining peak vortex induced lift and moment during dynamic stall when compared to the effects of pitch axis location and heaving velocity.

Franklin Harris and Richard Pruyn (Ref. 9) gathered experimental data from full scale flight tests and model rotor tests to demonstrate the practical symptoms of blade stall. Harris and Pruyn undertook this study to address the contradictions present in blade stall at the time. Significant differences exist between full-scale test data and model rotor data. The complexity of the dynamic stall phenomenon is pointed out: although boundary layer separation is necessary for stall by definition, in the dynamic case the separation may be the result of some other mechanism. Futhermore, it is suggested that the complexities of dynamic stall may be alleviated by approaching the problem

piecemeal, as separate occurrence of stall in each of three components – lift, drag, and pitching moment. The authors analyzed both their own test data and available, previously published data to ensure that their results would be unbiased. The validity of rotor model test data is questionable because Reynolds number effects are dependent upon scale. As compared to full scale rotors, models often experience more severe drag stall and may not experience lift stall symptoms. It was determined that lift stall decreases maximum speed capability by 23.15 m/s (45 knots) for conventional single rotor helicopters. Blade lift stall can be eliminated if the angle of attack of the blade sections increases without interruption through the third quadrant of the rotor disc. It is blade elastic twisting response to moment stall that causes the angle of attack increase interruption, which results in lift stall.

Dynamic stall characteristics of four helicopter rotor blade airfoils were experimentally determined in a two-dimensional wind tunnel by Jaan Liiva and Franklyn Davenport in reference 10. Symmetrical and cambered airfoils of 11% and 6% thickness ratio – Vertol 23010-1.58 and 13006-.7 and NACA 0012 and 0006 – were oscillated in pitch about the quarter chord at a Mach number, Reynolds number, and reduced frequency that complement full scale values. Static and dynamic data were obtained and compared for each of the four airfoils in question. All four airfoils exhibited increases in the maximum normal force coefficient attained during pitch oscillation. The dynamic increase in maximum normal force coefficient is highly dependent on Mach number. Near stall angles of attack, there were found to be regions of negative damping. Symmetrical airfoils featured a wider range and earlier inception of instability than their

cambered counterparts. The dynamic stall delay also reduced the average drag per pitching cycle. Finally, Liiva and Davenport identified simple equations for describing the experimental dynamic normal force coefficient as a function of only angle of attack and pitch rate.

The largest aerodynamic loads experienced by helicopters occur during forward motion while the blades are undergoing stall. Dynamic stall differs from static stall considerably such that the aerodynamic loading is significantly greater than in the classical stall scenario. Wayne Johnson (Ref. 11) developed a computational model for determining the loads experienced by rotor blades undergoing dynamic stall and reverse flow conditions during forward flight. Dynamic stall was modeled by first calculating the blade motion, then computing aerodynamic quantities dependent upon the non-dimensional rate of change of angle of attack. Reverse stall was comparatively easy to model, as reverse flow is essentially the same as conventional flow only in the opposite direction. The validity of the computations was verified by comparing the calculated results to experimental data. Johnson discussed the various effects of stall on blade pitch motions at several advance ratio ranges as well as the importance of dynamic stall. Dynamic stall is important because it results in initial lifts and moments that are much greater than their static stall counterparts. Additionally, the stalled area of the rotor disc is smaller due to the larger angle of attack at which stall occurs. Finally, he concluded that dynamic stall provides a means to alleviate the effects of stall on helicopter flight.

By the early 1970s, dynamic stall had been the focal point of a great deal of research; however, the stall type and mechanism were still unknown. Lars Ericsson and

J. Peter Reding (Ref. 12) examined both turbulent trailing edge stall and leading edge laminar bubble bursting stall. The unsteady airfoil characteristics were derived for incompressible, quasi-steady flow theory. Time history was considered a single discrete event. Ericsson and Reding were able to conclude first that the dominant characteristic of both leading edge and trailing edge stall is accelerated flow due to the nonzero pitch rate. Second, a simple analytical theory made use of existing experimental static data to accurately predict dynamic stall characteristics at low frequencies. It is important to note that leading edge and trailing edge vortex interactions were not included in this study. Finally, the success of the application of the developed theory suggests that in the future it will be possible to fully model the dynamic stall phenomenon.

An investigation was conducted by W. J. McCroskey and Richard K. Fisher, Jr. (Ref. 13) to examine the details of blade element airloads on retreating blades during stall. They tested a fully articulated, three-blade rotor model – at static, hover, and forward flight configurations – for measurements of the absolute pressure distribution, the boundary layer skin friction, the surface streamline direction, and the blade element angle of attack. The events that lead up to the retreating blade stall process were broken down into ten distinct stall onset events that build up over the rotor azimuth. Stall onset does not occur due to a singular breakdown of the local flow field. During forward flight, the flow field around a helicopter rotor blade is generally considered to be complex, unsteady, and three-dimensional. During the onset of retreating blade stall the three-dimensionality of the advancing blade flow field does not significantly affect the blade element airloads; therefore, unsteady, two-dimensional airfoils oscillating in pitch

produce similar force and moment measurements. The rate of change of angle of attack is one of the primary factors that distinguishes dynamic stall from static stall. Distinctions between lift stall and moment stall are due to the dynamic nature of the event, particularly the shedding of a vortex from the leading edge, which then passes over the airfoil in a finite time. Dynamic stall events are of a time dependent nature such that the stall mechanisms are increasingly dominated by dynamic vortex shedding. Empirical theories that existed at the time were incapable of accurately predicting the three-dimensional unsteady effects necessary for force and moment determination after the blade stalled completely.

Reference 14 was the collaboration of Johnson and Ham to discuss the role of the leading edge laminar separation bubble and shed vortex in the dynamic stall process. The goal was to determine the origin of the delay in stall angle of attack during dynamic stall. The sequence of events leading up to dynamic stall was discussed from an experimental point of view, taking into account both three-dimensional, articulated rotor tests and two-dimensional fixed wing tests. A 12% thickness Joukowsky airfoil is used in this investigation. Understanding the leading edge laminar separation bubble and shed vortex would allow for increased capability to theoretically predict dynamic stall. It was determined that the angle of attack at which the separation bubble reattached and the angle at which the suction dropped indicating stall were nearly identical. The separation bubble has an effect on stall onset, but little effect on airfoil loads. The loads are due to the behavior of the intense vortex shed from the vicinity of the leading edge, which causes a suction peak that follows the motion of the vortex. Johnson and Ham proposed

that the possible origin of the dynamic stall delay is due to the leading edge bubble, specifically, the unsteady pressure gradient at the transition point of the bubble. More work would be needed to determine when in the dynamic stall process the leading edge laminar separation bubble and shed vortex are the dominating factors. Johnson and Ham pointed out the future importance of documenting, via flow visualization, the dynamically stalling process at the leading edge of an airfoil undergoing sinusoidal oscillations.

A NACA 0012 model was oscillated over a range of incidence angles by Carta, G. L. Commerford, and R. G. Carlson (Ref. 15) to measure the unsteady lift and pitching moment experienced both in and out of the blade stall regime. The purpose of this study was to integrate available unsteady, two-dimensional airfoil test data into an existing rotor aeroelastic-variable inflow analysis. The model had a chord length of 5 inches (0.13 m) and a span of 4 inches (0.10 m). Lift and pitching moment curves versus angle of attack were produced for various mean incidence angles via experimental testing. Carta, Commerford, and Carlson determined that the nonsinusoidal response of an oscillating airfoil could be generated from sinusoidal data for the NACA 0012. Test data were used to predict the torsional response of full-scale and model-scale rotor blades.

Reference 16 discusses another experimental study conducted on a NACA 0012 in an unsteady, two-dimensional flow. This was among the first models to be of a larger scale, with a chord length of 4 feet (1.22 m), which was mounted vertically in a 7 foot by 10 foot (2.13 m by 3.05 m) wind tunnel. An analysis was conducted of Reynolds number, oscillation amplitude, and reduced frequency effects on the dynamic stall

phenomenon. Pressure, hot-wire, and smoke flow visualization data were recorded during testing. The stall process was broken down into steps and the loading during each phase were discussed. Vortex shedding was present in all of the Reynolds numbers tested, however, the higher the Reynolds number, the more likely a leading edge pressure peak was to be maintained. Martin *et al*. determined that a low amplitude, high reduced frequency motion might not be an accurate representation of the dynamic stall phenomenon as it is experienced by helicopters. These first large-scale two-dimensional tests seemed to effectively simulate rotor blade stall. Based on hot-wire, pressure, and strain gage measurements, the angle of stall initiation decreased with increasing *Re* and the angle of maximum lift increased with increasing *Re*. The data indicated the presence of a short bubble during both the upstroke and the downstroke phase of oscillation. The peaking of the leading edge velocity was determined to be the surest indicator of stall onset. Increasing reduced frequency further delayed stall onset. Future tests would focus on the leading edge region of the airfoil.

McCroskey, Carr, and McAlister (Ref. 17,18) studied the effects of leading edge geometries on dynamic stall and unsteady boundary layer separation on modified NACA 0012 airfoils of 1.22 m chord and 2.0 m span. Leading edge modifications were completed by connecting attachments to a standard NACA 0012 that altered the nature of the separation bubble. The geometry alterations resulted in the production of three different types of stall. The vortex shedding event – the distinguishing feature of dynamic stall – was evident in all cases tested regardless of airfoil shape, boundary layer state, or Reynolds number. The first type of stall observed was trailing edge stall due to

gradual progression of flow reversal and separation of the boundary layer from the trailing edge forward to the leading edge. The second stall type, classified as leading edge stall, developed from the abrupt breakdown of the turbulent flow on the forward portion of the airfoil. The final stall type was a special form of leading edge stall caused by abrupt laminar separation bubble bursting at the leading edge. While vortex shedding is a feature of all oscillating airfoils, the effects of the vortex on dynamic loads is dependent upon freestream flow characteristics and airfoil geometry. This was the first study that pointed out that leading edge laminar separation bubble bursting was not the defining characteristic of dynamic stall, as had been previously assumed.

R. W. Prouty (Ref. 19) assembled a survey of existing two-dimensional airfoil data to provide a basis for future airfoil development. The maximum static lift an airfoil is capable of producing corresponds to the type of stall that airfoil typically experiences. Reynolds number affects both the maximum lift and stall type, therefore airfoils with different chord lengths and tip speeds produce different results. Airfoils that experience leading edge and trailing edge stall have a higher maximum lift coefficient than those that experience thin airfoil stall. An airfoil that possesses forward camber, or a droop snoot, spreads out the negative pressure peak at the airfoil leading edge to aid in the prevention of laminar separation bubble bursting. Blunting the nose of an airfoil can produce a slight, but noticeable, increase in the maximum lift coefficient. Most successful high-lift airfoils have gentle changes in curvature at the nose. The Mach number range at which stall is likely to occur on helicopters is 0.25 to 0.5, due to local flow at the airfoil leading edge being supercritical. This can lead to an additional type of

stall known as shock stall, so named because the flow passes through a shockwave that increases the tendency for trailing edge stall. Favorable combinations of Mach number, Reynolds number, chord length, and angle of attack exist for each airfoil to operate at its maximum capacity. Airfoils with large maximum lift coefficients under static conditions will have large maximum lift coefficients under dynamic conditions. The dynamic stall overshoot seemed to be a fixed percentage of the static maximum lift coefficient. Drag divergence Mach number trends were provided for several airfoil profiles. It was found that aft camber lowered the drag divergence Mach number, while forward camber had minimal effect. Manners of alleviating pitching moment for multiple airfoil geometries were also briefly discussed.

Ericsson and Reding (Ref. 20) discussed the inability to simulate full-scale reduced frequency without compromising the full-scale Reynolds and Mach number simulation. This fact drew into question an earlier analysis of dynamic stall. In order for any unsteady airfoil analysis to be successful two criteria must be met. First, in the dynamic case there is a large overshoot of lift coefficient and therefore pitching moment coefficient. The second criterion is that pitch oscillations of an already stalled airfoil can reattach flow during particular portions of the pitching cycle. It was hypothesized that these events are the result of dynamic improvements to the boundary layer. Rampwise and oscillatory angle of attack changes were both examined. The mathematical analysis was then compared to existing experimental and numerical data to determine how it needed to be further modified. It was concluded that available experimental and numerical data supported equivalence between improving boundary layer through pitch

rate induced effects and increasing Reynolds number. Additionally, oscillatory stall data for different oscillation centers and measured negative damping for plunging oscillations are indicative of the two mechanisms that exist for dynamic boundary layer improvement.

To determine how harmonic velocity perturbations in the freestream affect dynamic stall, Pierce, Kunz, and Malone of reference 21 performed an experimental study of dynamic stall on a pitching rotor blade. Experimentation was conducted in a low speed wind tunnel modified with horizontal vanes to generate harmonic perturbations in the freestream speed via generating gusts of various frequencies. The blade model had a NACA 0012 airfoil profile with a 9 inch (0.23 m) chord and a 42 inch (1.07 m) span. A motor-crank-drive arm apparatus was used to articulate the model in the wind tunnel through a specific range of angles of attack. Moment data was acquired through an accelerometer and a strain gage bridge and filtered such that remaining moments would be due to the airloads alone. The work performed on the airfoil by the moment was also analyzed. It was concluded that varying the freestream velocity affects the unsteady aerodynamic moment of pitching airfoil oscillations in the vicinity of static stall conditions. For sinusoidal oscillations in angle of attack the aerodynamic work done on the airfoil by the freestream was not significantly affected by harmonic freestream variations.

In 1981, McCroskey presented a lecture series (Ref. 22) about the dynamic stall problem, summarizing the primary physical features of dynamic stall and discussing some of the attempts that had been made over the years to predict it. The general feature

of dynamic stall is the delay of stall onset to angles of attack much greater than those observed in static stall. The flow structure was broken down for each event in the dynamic stall process. Initially, there is a thin, attached boundary layer. This is followed by flow reversal within the boundary layer. The leading edge vortex is shed and begins to convect along the airfoil surface. As the vortex continues to move toward the trailing edge the maximum lift and moment occur, but decay rapidly as the vortex passes over the trailing edge. Secondary vortices may be shed until the flow reattaches at the leading edge. Lift, moment, and drag coefficients were plotted versus angle of attack for a typical airfoil at a specified Mach number and reduced frequency. Each point in the flow structure was marked on these plots. Pressure distributions as they varied with time were discussed. Pitch damping was named as the cause for stall flutter, which tends to occur when an airfoil is oscillating in and out of stall. Mean angle of attack shifts the lift and moment coefficient curves to lower or higher values depending upon if the damping is positive or negative. Stall is broken up into four regimes: no stall, stall onset, light stall, and deep stall. In light stall, some of the features of classical static stall are evident, particularly loss of lift and increase in drag. Light stall is the regime where negative damping is most likely to occur. It is also especially sensitive to airfoil geometry, reduced frequency, maximum angle of attack, and Mach number. It is distinguished by the small scale of the interaction (on the order of airfoil thickness, less than for static stall). Deep stall is governed by vortex shedding and the passage of the vortex over the airfoil surface. This is where lift, moment, and drag coefficients far exceed the static values during an upstroke. Some airfoil and flow parameters are more influential on the

dynamic stall phenomenon than others. Airfoil shape, freestream Mach number (above 0.2), reduced frequency, mean incidence angle, and motion amplitude all significantly affect dynamic stall. Reynolds number and Mach number – at low Mach numbers – affect dynamic stall in less significant ways. At the time, it was largely unknown how motion type, three-dimensional effects, and wind tunnel effects might affect experiment dynamic stall data. Each of these parameters and their affects were discussed at length in the lecture series. McCroskey described the methods for calculating and predicting the quantities of interest during dynamic stall, including the discrete potential vortex approach, numerous zonal method approaches, calculations of the Navier-Stokes equations, and several empirical correlation approaches. Finally, McCroskey discussed that further knowledge is required in many aspects of the dynamic stall process to fully understand it.

McCroskey, *et al*. (Ref. 23-26) conducted an experimental investigation of the dynamic stall characteristics of eight airfoils that were oscillated sinusoidally in pitch over numerous unsteady, two-dimensional flow conditions. The following eight airfoils were commonly used on helicopters but were not designed with dynamic stall considerations taken into account: NACA 0012, Ames-01, Wortmann FX-098, Sikorsky SC-1095, Hughes HH-02, Vertol VR-7, NLR-1, and NLR-7301. The objective of this investigation was to observe the dynamic stall characteristics for various airfoils and use that data to fulfill the need for a standard dynamic stall database. For each airfoil, four static data sets and an average of 55 dynamic, unsteady data sets were acquired. Testing was performed in 2 m by 3 m atmospheric pressure wind tunnel. Freestream Mach

number ranged to 0.3. Airfoil models had 0.65 m chords, 2.0 m spans, and were sinusoidally pitched about the quarter chord. Variable parameters included mean angle of oscillation, amplitude of oscillation, and frequency of oscillation. Instantaneous pressure signals were processed then numerically integrated to determine the unsteady lift, moment, and pressure drag. Hot-wire and hot-film data were used to determine boundary layer characteristics. Vortex shedding and stall regimes were described as they were in reference 22, also authored by McCroskey. Abrupt changes in the moment coefficient were used as the criteria to define the stall regimes. It was determined that flow parameters play a much larger role in dynamic stall behavior than the airfoil geometry; however, noticeable differences in behavior due to geometry still occurred. It was determined that the more advanced helicopter airfoil geometries offered advantages when compared to the more classical NACA 0012 profile. For a given set of flow parameters, the airfoil that has the highest lift coefficient also has the lowest Mach drag divergence. Additionally, airfoils that exhibit favorable static stall characteristics also tend to exhibit favorable dynamic stall characteristics. Qualitative observational differences in dynamic stall from airfoil to airfoil diminish as the airfoil pitches deeper into the deep stall regime. As Mach number increased, all airfoils tested would stall from the leading edge regardless of each airfoil's static stall behavior. Transonic flow phenomena in the retreating blade environment were stressed due to the development of a small supersonic bubble near the leading edge. This bubble was not necessarily accompanied by a shockwave. The importance of future work to accurately determine

and predict the rotor blade environment was emphasized for the successful improvement of rotor blade design.

In reference 27, Ericsson and Reding determined the importance of various unsteady flow mechanisms that affect dynamic stall. Many aerodynamic quantities, specifically airloads and accelerated flow effects, differ significantly depending on whether a lifting surface is undergoing pitching motions or plunging motions. Ericsson and Reding were among the first to mathematically differentiate, within their theoretical model, between the pitching and plunging motions that helicopter rotor blades experience. It was concluded that recent experimental results sufficiently proved the existence of a leading edge jet effect, which delays separation for pitching airfoils but promotes it for plunging airfoils. Recent experimental results also reconfirmed the dependence of dynamic stall on the dimensionless time rate of change of the angle of attack.

An overview of the progress made in dynamic stall research over fifteen years, ending near 1985, was assembled by Lawrence Carr (Ref. 28, 29). A brief history of the discovery of dynamic stall was presented, as well as the problem it poses for not only rotorcraft, but also on fighter aircraft, wind turbines, jet engine compressor blades, and insect wings. An explanation of the dynamic stall process and the events that comprise it was given, focusing on the vortex shedding event. The various motions that result in a dynamic stall situation were discussed and described, including in-plane oscillation and the concept of pitch-plunge equivalence. The effects of amplitude, mean incidence angle, and frequency of motion, as well as the location of the pitching axis were

discussed. Mach number, Reynolds number, and three-dimensional effects are also significant on influencing the stall delay and airloading during dynamic stall. Carr pointed out that theoretical and computational modeling of dynamic stall was only beginning to become commonplace in the field due to its numerous complexities. Many modeling attempts had been made prior to 1985, but they lacked the detail necessary to accurately predict the resultant flow and/or airloads from dynamic stall. Carr completed his review of dynamic stall research by discussing the numerous studies that have been conducted on controlling the dynamic stall vortex.

Up to this point in time, the fluid mechanical processes that produce the dynamic stall overshoot of static data had not been studied independent of the dynamic stall process as a whole. Ericsson and Reding, in reference 30, set out to use existing experimental data to analyze the events of dynamic stall individually and to illustrate the problems that result from using subscale test data to predict full scale characteristics. Rampwise angle of attack change can be broken into two components, a lag effect and change in angle of separation. The lag effect produces no overshoot, but the change in separation angle of attack causes overshoot due to two effects, accelerated flow and the leading edge jet. Accelerated flow is related to the pressure gradient time history, while the leading edge jet is the result of the boundary layer being strengthened during the upstroke and weakened during the downstroke. The second fluid mechanical process is the spilling of the leading edge vortex. As the spilled vortex travels along the surface of the airfoil, the overshoot in load increases until a maximum overshoot is reached at approximately 0.7c. Oscillatory motion complicates the dynamic stall process such that

phase and frequency must be taken into account. Plunging effects can be related to pitching effects such that the leading edge jet effect is opposite from what is observed in pitching effects. This results in large differences in load values. Compressibility effects are largely important when it comes to airfoil stall characteristics and were also algebraically modeled. Each of these unsteady flow properties were modeled simply with relations to static data.

In reference 31, Walker and Chou conducted small-scale experiments in which a NACA 0015 was rapidly pitched to high angles of attack to examine the initiation, development, and evolution of the flow around the characteristic dynamic stall vortex. Models were pitched about their quarter chords from 0° to 60° at multiple pitch rates and chord Reynolds numbers. Three experimental methods were used: smoke-wire flow visualization; dynamic surface pressure measurements – to determine transient aerodynamic loads; and near-surface hot-film velocity magnitude measurements – to aid in understanding the relative strengths of passing vortices. The dynamic stall vortex forms near the leading edge and is the dominant flow field feature. The large aerodynamic loads that were measured are not generated by the vortex. They are instead the result of vorticity accumulating around the airfoil, including the vortex. Reynolds number and pitch rate were determined to have second order effects on the flow field for constant values of the non-dimensional pitch rate, α^+, which is the dominant factor of the flow field.

A stroboscopic schlieren system was used by Chandasekhara and Carr (Ref. 32, 33) to study the compressibility effects on a dynamically stalled NACA 0012.

Freestream Mach number and reduced frequency and their effects on the dynamic stall vortex were observed. The experiments were small-scale (0.08 m chord) and conducted in the Compressible Dynamic Stall Facility, built and designed specifically for dynamic stall flow visualization studies. Mach number was varied from 0.15 to 0.45 and reduced frequency was varied from 0 to 0.1. A mean angle of attack of 10° was used throughout the study. The dynamic stall vortex was found to be present at all Mach numbers and reduced frequencies tested. The strength and formation angle of the vortex is Mach number dependent. The dynamic stall vortex can be held on the airfoil surface by increasing the reduced frequency. The effects of compressibility do not become significant until Mach 0.3 is reached or exceeded. Despite parameter variations, the vortex always convects at a constant velocity of $0.3U_{\infty}$. The origin of the vortex was undeterminable and no shocks were visible near the leading edge for the tests conducted.

Chandrasekhara used the stroboscopic schlieren flow visualization – used in the previous study – with Brydges (Ref. 34) to analyze the effects of amplitude on the dynamic stall vortex. Mean angle of attack, Mach number range, and reduced frequency range were consistent with the previous study (Ref. 32, 33). A NACA 0012 airfoil was once again used. Reynolds number ranged from 200,000 to 900,000. The airfoil oscillated through three different angle of attack ranges. It was determined that a shock is present over the upper surface of an oscillating airfoil for freestream Mach numbers of 0.45 and above. The dynamic stall vortex will form at all amplitudes, regardless of compressibility effects. By increasing the amplitude of the oscillatory motion, it is possible to delay deep stall to higher angles of attack.

To determine the effects of compressibility, unsteadiness, and airfoil geometry on dynamic stall, Jeffrey Currier and K.-Y. Fung (Ref. 35, 36) examined two existing data sets. The data set generated by McCroskey *et al.* (Ref. 23), of the eight airfoils named above, and Lorber and Carta (Ref. 37), a data set for a Sikorsky SSC-A09. A suction peak analysis was conducted, through which it was determined that the peak suction values were approximately the same for all dynamic stall tests, on a single airfoil, above Mach 0.3. This was not the case for tests with freestream Mach values lower than 0.3, where suction peak varied with frequency, amplitude, and mean angle of oscillation. This suggested that stall onset is shock related for Mach-supercritical flows, even if the shock was not observable during testing. A boundary layer analysis was also conducted near the airfoil leading edge. This analysis was computational due to poor experimental resolution in the first 3% of the chord. This analysis took into account potential leading edge bubble bursting and transition effects. It was determined that the various airfoils in question showed different dependence on frequency. Increased unsteadiness does further delay the onset of stall to a higher angle of attack; however, it also promotes boundary layer separation.

Once again, dynamic stall over an oscillating airfoil was studied in the Compressible Dynamic Stall Facility. In this study Carr *et al.*(Ref. 38) used a real-time, point diffraction, interferometry technique to obtain flow field data, rather than the stroboscopic schlieren system used previously (Ref. 32-34). The principles behind this interferometry technique, as well as the implementation of it, were described in detail. Both qualitative and quantitative analyses were completed of the interferograms

obtained. The interferograms represented constant density contours, which were used to calculate Mach number and pressure distributions about the airfoil leading edge. A comparison between the interferograms obtained in this study and the schlieren images obtained in references 32-34 showed strong agreement. This study demonstrated the successful implementation of the new interferometry technique. The dynamic stall vortex produced by an oscillating airfoil was once again observed; however, it was determined that the symmetric density imprint expected from a classical vortex was not present with the dynamic stall vortex. The interferograms obtained in this study were found to allow detailed pressure distribution analysis in the first 1% of the chord that had not been possible previously.

Chandrasekhara (Ref. 39) conducted another flow visualization study of dynamic stall flow fields, in this case, the analysis technique used was laser Doppler velocimetry (LDV). This experimentation was also conducted in the Compressible Dynamic Stall Facility used in studies above (Ref. 32-34, 38). The LDV technique used allowed for the collection of 10,000 coincident samples of each the *u*- and *v*-velocity components for each channel. Phase locking was ensured via circuitry and the flow was seeded with 1μm polystyrene latex particles. The experimental conditions experienced by the NACA 0012 model follow: $M_\infty = 0.3$, oscillation frequency = 21.6 Hz, $k = 0.05$. This was the first time velocity data had been obtained over an oscillating airfoil. The velocity data showed the formation of a separation bubble near the airfoil leading edge that would burst in the vicinity of where the dynamic stall vortex formed. Velocity profiles were found to change within a pitching cycle. Average velocity values were observed as high

as $1.6U_\infty$ at $M_\infty = 0.3$ and $k = 0.05$, while instantaneous velocities were observed as high as $1.8U_\infty$. Circulation increased until the dynamic stall vortex began to convect rearward along the surface.

J. Panda and K. B. M. Q. Zaman (Ref. 40) examined the flow field about a NACA 0012 airfoil sinusoidally oscillated from 5° to 25° angle of attack at reduced frequencies of 0 to 1.6 and chord Reynolds numbers of 22,000 and 44,000. The purpose of this study was to document the evolution and shedding of the dynamic stall vortex. This was a small-scale experiment carried out in a low speed wind tunnel with very low test section freestream turbulence intensity (< 0.1%). A hot-wire probe and smoke wire visualization were the data collection techniques used. Not only was the typical dynamic stall vortex observed forming near the leading edge of the airfoil, but so was an intense vortex of opposite vorticity that formed at the trailing edge just as the leading edge vortex was shed. These two vortices were observed, via flow visualization, to combine to form a "mushroom" shape as they convected away from the airfoil. The rebound after the drop in lift that accompanies the shedding of the leading edge dynamic stall vortex was determined to be caused by the passage of the trailing edge vortex. The fact that the flow field data was phase averaged allowed for unprecedented detail in dynamic stall flow field documentation. For reduced frequencies of 0.1 and below, the oscillating airfoil exhibits quasi-steady behavior; bluff body shedding is not suppressed by the dynamic stall vortex as it is for larger reduced frequencies. If the reduced frequency was too high, the dynamic stall vortex was shed prematurely or multiple dynamic stall vortices were present on the upper surface of the airfoil simultaneously.

The dynamic stall vortex continued to be the focus of experimentation throughout the 1990s. By the end of the decade, Ferrecchia *et al.* (Ref. 41) narrowed the focus further in an attempt to determine the cause of the dynamic stall vortex inception. Vorticity flux on a finite wing and a two-dimensional NACA 0012 aerofoil was investigated for ramp-up pitching motion for multiple non-dimensional pitch rates. Testing was conducted in a low speed wind tunnel with an octagonal cross section measuring 2.13 m by 1.62 m. Surface mounted pressure transducers were the primary data source, but flow visualization was conducted as well. Four motion types were investigated: static – no motion, ramp-up motion, ramp-down motion, and sinusoidal motion. All motion occurred about the quarter chord axis. Data presented was the average of four cycles of 8000 samples. For testing, U_∞ = 50 m/s, Re = 1.5×10^6, and M_∞ = 0.16. A theoretical explanation of vorticity flux was provided. The dynamic stall process was described on both lifting surfaces. Two concentrated sources of vorticity were observed over the forward portion of the aerofoil surface. These vorticity sources were studied for a large range of reduced pitch rates and it was concluded that the reduced pitch rate influences the quantity of vorticity that enters the flow.

In 2005, Ekaterinaris, Chandrasekhara, and Platzer (Ref. 42) assembled an overview of recent advances that were made in the dynamic stall field. They addressed testing that was conducted at true reduced frequency and Mach number scaled conditions with geometrically scaled models. Because this was a scaled investigation, and reduced frequency and Mach number were successfully scaled, it was not possible to scale Reynolds number. Boundary layer trips were used in attempt to make up for this

issue. This research was made up of two phases: identification of the mechanisms of dynamic stall onset; and attempts to control the dynamic stall phenomenon. Testing was conducted in the Compressible Dynamic Stall Facility that was used for over a decade of previous studies (Ref. 32-34, 38, 39). NACA 0012 airfoil models were pitched at an unsteady pitch rate, α^+ of up to 0.03, while the Mach number and reduced frequency were varied from 0.2 to 0.4 and 0 to 0.1, respectively. PDI was the flow analysis method. PDI allowed, for the first time, for the visualization of intricate flow details, specifically, the separation bubble and local shock details in a subsonic freestream. Resulting pressure maps allowed for quantification of the compressible dynamic stall onset mechanisms and the pressure gradient behavior. Unsteady vorticity fields were derived from these quantities. The PDI images were explained to describe the mechanisms of dynamic stall onset. It was determined that flow control will require vorticity to be managed about the airfoil. A dynamically deforming leading edge modification was made to a NACA 0012 model in an attempt to manage vorticity and gain some measure of control over the dynamic stall vortex. A pulsating jet was also examined as a possible flow control method. Experimental and computational results for flow control were analyzed and compared. Both computationally and experimentally, it was possible to use a pulsating jet to maintain an elevated lift coefficient beyond the angle of attack at which separation typically occurs during dynamic stall. Dynamic stall was discussed on both thrust-producing, flapping airfoils and insect wings due to the increasing attention the topics had received over the previous few years. This investigation concluded with an emphasis on the increasing need for more sophisticated experimentation, data

acquisition, and flow control techniques. Computational models and experimentation methods were successfully developed for controlling the flow during the dynamic stall phenomenon.

Over the course of the last 50 years dynamic stall research has been conducted using a variety of methods. The effects of several characteristics of dynamic stall have been studied at length. It has been determined that scale effects are crucial when studying dynamic stall, particularly the effects of Mach number and Reynolds number, which are difficult to simulate at small-scales. Airfoil shape has important effects on dynamic stall, including determining the maximum gain in lift that the airfoil experiences. Reduced frequency is important and was determined to be an effective quantity for comparison across scales. The leading edge flow structure controls the dynamic stall process, particularly the formation, shedding, and convection of a strong vortex. Excessive data exist for surface pressure, skin friction, lift, drag, pitching moment, and flow visualization for a representative number of airfoils, where the NACA 0012 has received the most attention. The current database of dynamic stall data lacks leading edge velocity data at realistic flight conditions.

3. THE DYNAMIC STALL FACILITY AT TEXAS A&M UNIVERSITY

Texas A&M University (TAMU) possesses an experimental facility, known as the dynamic stall facility (DSF), specifically designed, by Dr. Dipankar Sahoo (Ref. 43, 44), for observing dynamic stall at realistic helicopter flight conditions. The DSF consists of wind tunnel test section area reducing inserts, a hydraulic actuation system to provide controlled periodic motion of the wing, and two wings, a NACA 0012 and a Sikorsky SSC-A09.

3.1 Oran W. Nicks Wind Tunnel Facility

Experimentation was conducted in the OWN Low Speed Wind Tunnel. The OWN LSWT has an octagonal test section of 3.05 m in width, 2.13 m in height, and 3.66 m in length (10 ft × 7 ft × 12 ft) with a 0.30 m (1 ft) fillet in each corner. This test section provides a maximum Mach number of 0.25, or 85 m/s (200 mph). The OWN LSWT is a closed circuit tunnel with a circuit length of 120.70 m (396 ft). Vertical venting slots, 7.62 cm (3 in) in width, cut into the sidewalls at the test section exit to maintain near atmospheric static pressure. A diagram of the OWN LSWT can be seen in Figure 1.

The DSF inserts reduce the cross-sectional area of the test section to 2.13 m by 2.13 m (7 ft × 7 ft). This is accomplished by installing five flat panels, a support panel, an inlet panel, a diffuser panel, vortex generators, and fillets on each side of the wind tunnel. There is also a roof panel specific to the DSF. The inlet panels were installed

first, followed by two flat panels on each side of the wind tunnel. The next panel in the sequence to be inserted was the support panel, which has extra structural support that the wing model mounts to after the test section reduction is complete. The remaining three flat panels were inserted next, with the vertical vents on the fourth panel. During installation, the curved inlet panels bolted directly to the OWN LSWT walls. After each of the panels was in place, it was bolted loosely to the previous panel in the sequence. Once all of the flat panels were in place, they were bolted to the floor and the ceiling was inserted. The ceiling was then bolted to the top of the side panels and the panels were bolted together tightly. The diffuser panels were installed last, bolting directly to the diffuser section of the OWN LSWT as well as the last flat panel. Vortex generators were mounted on the diffuser panels to help lessen diffuser separation. Fillets were installed at the junction of the floor and both sidewalls, thus completing the reduction of the test section. Figure 2 shows the reduced wind tunnel test section; the vortex generators, fillets, diffuser section, and ceiling are not shown.

The DSF inserts are composed of aluminum sheets mounted to steel frames. Looking downstream, two flat panels of the right wall contain glass windows for potential data collection. The fifth flat panel of the right wall contains the door for entering the reduced test section. The support panel on the left wall contains a small glass window for PIV data collection at the leading edge of the wing model. The ceiling also contains a glass window, centered over the leading edge near the mid-span of the wing, through which the PIV laser beams enter the wind tunnel.

The support panels bear and distribute the load of the pitching motion during experimentation. The aluminum sheets on these panels are removable for ease of wing model installation. The support structure in these panels is made up of two steel I-beam structures each made of a horizontal I-beam segment with two smaller I-beam segments welded to the center of the horizontal segment at a 45º angle. Tapered roller bearings housed in 20.32 cm by 20.32 cm by 10.16 cm (8 in × 8 in × 4 in) aluminum blocks bolt to the horizontal I-beam structure. A support panel with installed bearing blocks can be seen in Figure 3.

3.2 Hydraulic Actuation Apparatus

A Parker Fluid Power Systems "V-Pak" Hydraulic Power Unit – model number V828VPCHNX12612 – was used to drive the pitching motion of the wing model (Figure 4). The hydraulic unit had a reservoir tank with an 80-gallon capacity. The pump flow rate was variable from 8 gallons per minute to 36 gallons per minute. The maximum pressure sustainable by the unit was 20.68 MPa (3000 psi). The hydraulic unit motor ran at 1800 rpm. The hydraulic power unit also featured three filters for maintaining oil quality by keeping it free of water and debris. A fill gauge displayed oil quantity, color, and temperature. During experimentation, an accumulator bladder supplied the linear actuator with Chevron Rykon AW ISO 46 hydraulic oil through the servo valve.

The hydraulic power unit was connected to a linearly actuating hydraulic cylinder (see Figure 5). The linear actuator connected to the servo valve at two points, the actuator inlet and outlet. The inlet was located at the bottom of the actuator and the outlet was located at the top. The linear actuator was mounted to a base with a single

degree of freedom, rotation about the nominal center of the fully extended cylinder, to allow for motion through a wide range of angles of attack. The hydraulic servo valve, also manufactured by Parker, controlled the amount of hydraulic fluid in the linear actuator at any given time.

The hydraulic servo valve operated through the use of a PID controller interface. RMCWin software (Ref. 45) was used with a modular RMC100 motion controller to achieve position and velocity control of the hydraulic cylinder. RMCWin allowed the user to define extend/retract limits of the actuator, extend/retract feed forward, and extend/retract acceleration feed. Proportional, integral, and differential gains were defined. Event Steps was used to construct a program to control the timing and speed of opening and closing of the servo valve and therefore the motion of the linear actuator. The Event Steps component of RMCWin was also used to send a 5 V signal to the Quantum Composer to trigger the laser pulses at a specified angle of attack. The Quantum Composer will be discussed in Section 4.

The linear actuator induced a sinusoidal pitching motion in the wing model by coupling the sinusoidal motion of the linear actuator with the wing shaft via a moment arm. The moment arm is discussed further in the following section. The sinusoidal wave form the linear actuator follows can be seen in Figure 6.

3.3 Sikorsky SSC-A09 Model

The ARO requested that the focus of this investigation be the Sikorsky SSC-A09 airfoil. This airfoil had been used previously in dynamic stall research by Lorber and Carta (Ref. 37) in 1987. Aside from those tests, the SSC-A09 remains largely untested in

the dynamic stall regimes. The SSC-A09 is a cambered, high-lift airfoil used as the tip of rotor blades found on versions of both Comanche and Black Hawk helicopters.

Sikorsky provided the non-dimensional upper and lower surface coordinates at 66 locations along the airfoil chord. These locations, which are provided in Table 1, were used to create a scatter plot from which sixth order polynomial trend lines were determined for both surfaces. These polynomial equations were used in SolidWorks (Ref. 46) to create a computer model of the future physical wind tunnel testing model. The computer model can be seen in Figure 7. The SolidWorks model was then divided into six pieces for machining manageability.

The wind tunnel testing model has a chord length of 0.46 m (1.5 ft) and spans 2.13 m (6 ft 11.75 in) and is composed of several individual pieces. This span allows for 3.18 mm (1/8 in) clearance on each side of the model between the wing and the wind tunnel side wall. A steel 7.62 cm by 2.54 cm (3 in × 1 in) rectangular shaft runs along the airfoil quarter chord and serves as the support structure for the wing. The airfoil is made up of six aluminum pieces. The top portion of the airfoil is made up a 152.40 cm (5 ft) section, a 30.48 cm (1 ft) section, and a 29.85 cm (11.75 in) section. The bottom portion of the airfoil is comprised of a 121.92 cm (4 ft) section, a 45.72 cm (1.5 ft) section, and a 45.09 cm (1 ft 5.75 in) section. The six airfoil pieces can be seen in Figure 9. The six airfoil pieces affix to the shaft with six 9.53 mm (3/8 in) dowel pins to ensure moment is transferred from the linear actuator to the airfoil. The ends of the inner top and bottom sections of the airfoil are vertically offset to maintain the strength and integrity of the wing model as a whole. The three top sections bolt to the three bottom

sections of the airfoil at 88 locations; 22 span-wise locations with 4 bolts along the chord. The two remaining pieces of the wing model are the gloves that connect the rectangular shaft to a circular shaft of 3.81 cm (1.5 in) necessary for the use of the DSF. The circular shaft was press fitted into the glove. To prevent slippage, 2 bolts and a perpendicular dowel pin passed through both the glove and the shaft. Figure 10 shows a close up of one of the gloves in the testing model. On each side, the circular shaft passes through the wind tunnel side panel and then through a bearing block. Lock collars on both sides of the bearing blocks prevent translational motion of the wing along its span axis. On the left side circular shaft, outside the wind tunnel test section, a moment arm is used to transfer the translational motion of the linear actuator, and create the sinusoidal pitching motion of the wing. The moment arm attached to the wing shaft through a torque transferring locking collar. A clevis attached the moment arm to the hydraulic cylinder. The moment arm can be seen alone in Figure 11 and in the testing setup in Figure 12. A secondary bearing block is used on the left side (looking upstream) circular shaft to prevent vibrational bending along the shaft. This bearing block is located on the outside of the moment arm connected to the linear actuator.

Counter bored holes in the airfoil surfaces housed the 88 bolts and nuts that attached the top surface to the bottom surface. Due to the camber, the top portion of the airfoil was thicker than the bottom portion. For this reason, the bolts were inserted through the bottom surface, while the nuts were attached through the upper airfoil surface. After all of the airfoil pieces had been bolted together, it was necessary to fill the holes to achieve a smooth airfoil surface. This was accomplished by filling the holes

with wax until the nut and bolt heads were covered. The holes were then filled the remainder of the way with a two-part aluminum putty. After the putty had cured, the entire surface was sanded down, progressing from coarse to fine grain paper, to remove any machining imperfections and to achieve a smooth surface that would not trip the boundary layer. The surface was then cleaned of any aluminum dust that may have been left over from the sanding process and painted flat black to prevent any light reflections in the testing environment. The assembly process was completed when the gloves with the circular shafts were attached to the rectangular shaft within the wing. Figure 13 shows the completed testing model prior to insertion into the LSWT. A downstream view of the model after insertion into the OWN LSWT is shown in Figure 14. Figure 15 and Figure 16 provide leading and trailing edge views of the wing while installed into the LSWT. The completed SSC-A09 large-scale testing model is summarized in Table 2.

3.4 Wing Reference Frame and Angle of Attack Calibration Technique

It was necessary to establish a reference frame in the three-dimensional flow field. The origin was fixed at the quarter chord of the wing because the pitching motion rotates about this point. The x-axis points in the upstream direction, parallel to the flow direction, floor, ceiling, and sidewalls. The y-axis points vertically upward, perpendicular to the ceiling and floor, and parallel to the sidewalls. The z-axis completes the right coordinate system and lies along the quarter chord of wing. The data is two-dimensional, collected at the $z = 0$ location, at the location of the laser sheet. Figure 17 shows a diagram of the SSC-A09 rotor blade airfoil, non-dimensionalized by chord length, and the coordinate axes as described above. Also shown is the region of interest

for experimentation, namely the leading edge of the wing just before and at the onset of dynamic stall. The region of interest is the frame of the PIV data collected, which will be discussed in the following sections.

It is important to note that the reference frame is fixed in space and does not pitch with the wing. The angle of attack is measured from the *x*-axis, which passes through the quarter chord. If the leading edge of the wing is above the *x*-axis, the angle of attack is positive; if the leading edge of the wing is below the *x*-axis, the angle of attack is negative. Additionally, the flow direction is considered to be negative as air moves from leading edge to trailing edge.

Calibration of the testing apparatus was required to relate the angle of attack of the SSC-A09 to the position of the linear actuator. Angle of attack was measured with an inclinometer, accurate to ± 0.1°, at a range of linear actuator positions. The linear actuator was set so the floor and ceiling were at 0°. There is a linear relationship between linear actuator position, measured in counts, and angle of attack of the wing in degrees. This relationship for the current study is shown in Figure 18. Angle of attack resolution is 46 counts per degree. Thus, a count, as measured by the linear actuator, is a step of 0.02 degrees. Angles of attack examined in testing – 16°, 18°, 20°, 22°, and 24° – were calculated using this relationship, then verified with the inclinometer.

4. DATA REDUCTION TECHNIQUES

Data reduction requires that the raw image pairs be processed, via DaVis image processing software (Ref. 47), and then post-processed using in-house developed averaging software known as TAMUPIV. The post processed data is then put into a usable format with Tecplot 360 (Ref. 48). This section will discuss the process of reducing the data into understandable formats and meaningful quantities.

4.1 Particle Image Velocimetry

Flow visualization is the observance of the motion of fluid elements. Flow visualization is the most straightforward experimental method for making flow patterns visible. There are three basic methods of flow visualization: surface flow visualization methods; particle tracer methods; and optical methods. Surface flow methods reveal the streamlines on the surface of a solid body. Particle tracer methods allow qualitative flow patterns to be observed and quantitative velocity measurements to be taken in the fluid around a solid body. Optical methods show changes in flow patterns through changes in the fluid's refractive index.

In this research, flow around a pitching wing is being observed. The objective of this research is to quantify the mean velocities, Reynolds stresses, and vorticities of the flow that occurs during dynamic stall created by a pitching wing. Particle image velocimetry is a particle tracer method of flow visualization that will allow this quantification.

4.1.1 Fundamental Principle of PIV

Particle image velocimetry is a technique used to measure velocity in a plane. PIV allows instantaneous velocity measurements to be taken throughout the plane. For this reason it is among the most commonly used methods of velocimetry today. In most applications of the PIV process, tracer particles are inserted into the flow and then illuminated, imaged, and processed to find the instantaneous velocity fields (Ref. 49). It is assumed that the tracer particles move with the flow of the fluid. PIV is based on the direct method of determining the fundamental scope of the velocity, displacement and time.

A laser is used to illuminate a plane within the flow. This plane is most often perpendicular to the direction of the flow and parallel to the cross-section of the solid object within the flow. A laser is used because it can be pulsed at specific time intervals, allowing particle illumination only when capturing images. The tracer particles, also commonly referred to as seed, are illuminated with two short laser pulses. The laser light is scattered by the particles, and the scattered light is recorded on two frames on a charge-coupled device (CCD) camera. The CCD camera then stores the image pairs on a computer for further analysis at a later time. Because the images are taken in pairs with a known time increment between them, the displacement of the particles is used to calculate the velocity at multiple points within the plane of the flow. A diagram of a typical PIV system setup can be seen in Figure 19.

There are several general features of PIV that make it a favorable process. One of the most important among these aspects is that the velocity measurement is gathered in a

non-intrusive manner. There are no probes required, such as those for gathering pressure or temperature measurements, which are used to calculate velocity fields in other methods. This makes PIV an employable method without disturbing the flow in the vicinity of the test area. Additionally, PIV is a whole field technique. This allows velocity to be determined at various points throughout the flow with a single system.

Velocity measurements can only be obtained through evaluation of the PIV image recordings. Each of the digital recordings is divided into small sub-areas known as interrogation areas. The two images are then compared via a statistical auto-correlation or cross-correlation. The local displacement vector for the seed particles of the first and second illumination images is determined. It is assumed that all of the particles within an interrogation area move homogeneously between the two illuminations. A two-component velocity vector, the local flow velocity in the plane of the light sheet, is calculated. This calculation is completed utilizing the known time delay between illuminations and the magnifications of the images. The interrogation, correlation, and velocity vector calculation process is typically completed multiple times for each image pair. The process begins with relatively large interrogation areas and is repeated for subsequently reduced interrogation areas. The larger the interrogation area is, the larger the sample of seed particles is and therefore, the higher the correlation coefficients are for the interrogation area.

4.1.2 Resolution of PIV Results

The resolution of PIV results is affected by several experimental factors. The prominent experimental factors include the intensity of the light scattered by the tracer

particles, as well as how numerous the particles are throughout the flow. These experimental factors determine what size interrogation areas can be reduced to. The higher the image resolution is, the smaller the interrogation areas can be, and the more accurate the instantaneous velocity vector fields will be. This also allows velocity vectors to be determined increasingly closer to the surface of the body disturbing the flow. There is however, a point where increases in resolution can decrease the accuracy of the PIV results. For example, when interrogation areas get too small, and the correlation mesh becomes too fine, the ability to process the PIV recordings no longer exists. It becomes impossible to determine statistical tracer particle displacements when the interrogation area is only a few pixels square. The minimum interrogation area varies for each experimental scenario.

The intensity of the light scattered by the particles influences the resolution of PIV images by affecting the contrast of the PIV recordings as well as the number of particles detected by the imaging camera. The intensity of the scattered particles is also a function of particle size and shape. Therefore, image resolution is also a function of tracer particle size and shape. For this reason choosing the correct scattering particles is a more effective method of changing the resolution than increasing the laser power. In many of the situations where PIV is used, the scattered light follows Mie's scattering theory. Mie scattering applies to spherical particles that have diameters larger than the wavelength of the incident light. Scattered light intensity tends to increase with increasing particle diameter, increasing the image resolution. However, increasing

particle size decreases the accuracy with which the particles follow the flow, especially in gases, and increases the amount of noise in the recordings.

The number of tracer particles per unit area in the image affects the distinction of the image. Three different particle densities can be qualitatively identified. Images of a low particle density are used to identify the individual particles during different illuminations. The process of tracking these individual particles is called particle tracking velocimetry (PTV). In medium density images individual particles are still distinguishable from one another. However, in the second image of a pair the individual particles cannot be paired. For this reason, statistical correlation methods must be used. This process is PIV. For cases characterized by high particle density, it is no longer possible to detect individual particles due to a large quantity of particle overlap. This case is referred to as laser speckle velocimetry (LSV). It is important to be aware that a higher seed density does not correspond to a higher resolution. When too much speckling, or particle overlap, occurs it is no longer possible to determine displacements of interrogation areas. Figure 20 shows three particle densities and the corresponding optical analysis technique to better understand how much seeding is needed in a PIV flow field.

4.1.3. PIV in the DSF

Illumination is provided by a New Wave Solo 120 XT Dual Head Nd:YAG Laser with frequency doubled to provide two pulses that are 532 nm in wavelength. An overview of the illumination system is provided in Figure 21. The laser has an available repetition rate of 15 Hz. Each of the laser heads has a maximum energy output of 152 mJ

at the 532 nm wavelength. The pulse width is 4 ns with a ±1 ns jitter. The beams emerge with parallel polarization. The beams were then overlapped in space with a high energy polarizing 50/50 beam splitter that provides efficient narrow band polarization. This process provided two coincident beams. One beam had parallel polarization and one beam had perpendicular polarization. The laser and beam overlapping optics are shown in Figure 22.

The laser system and corresponding optics mounted to the roof of the wind tunnel. The laser beams were guided into the wind tunnel test section using a series of mirrors and lenses. A 532 nm mirror was used to bend the beam approximately 90º. Then a plano-convex cylindrical lens with a focal length of 150 mm was used in conjunction with a plano-concave cylindrical lens that has a focal length of 50 mm to create a laser sheet. These two lenses were mounted with their flat surfaces touching. A spherical focusing lens with a focal length of 1500 mm was used to focus the beam so that the waist was located just above the test section model. A detailed view of the sheeting optics described above can be seen in Figure 23. The thickness of the laser sheet was less than 1.0 mm.

Vibrations occur when the wind tunnel runs at high speeds. To stabilize the laser beams, two 10.2 cm x 10.2 cm (4 in x 4 in) I-beams were used. The two I-beams run perpendicular to the direction of freestream and span across the top of the wind tunnel test section. They were supported by the wind tunnel's concrete roof. Rubber pads were used between the I-beams and the concrete to isolate the optics from the vibrations of the wind tunnel. For further prevention of vibration and to ensure the I-beams and optics

would not vibrate out of place C-clamps and sand bags were used to hold the I-beams in place. This setup was proven to be an effective method of obtaining a stable laser beam (Ref. 43).

Data were acquired with a Cooke Corporation pco.1600 Camera. The pco.1600 camera is a high dynamic range (14-bit), thermoelectrically cooled (to -20°C) interline transfer CCD camera with a 1600 x 1200 pixel array resolution. The camera had a Nikon f-mount for lenses. The f-number was set to 8. An exposure time of 5.3 μs and trigger delay time of 10 μs is used. The interline transfer rate is sufficient for delays down to 300 ns. The camera frame grabbing software was pco.CamWare version 2.19 (Ref. 50). A Nikon 70 – 300 mm lens was used to focus the camera onto the illuminated particles.

The camera mounted to an H-shaped stand made of aluminum rails. The camera mounted on an extension bar, which in turn attached to the middle rail using a mounting plate. The camera was supported by a telephoto lens support mounted to two micrometer driven translational mounts, mounted parallel and perpendicular to the extension bar. This entire assembly attached to the extension bar. Mounting the camera on the extension bar allowed movement in the direction perpendicular to the flow, parallel to the *z*-axis. For a wide-angle view the camera was moved away from the test section, while for zoomed in, high resolution data, it was moved inward, closer to the test section wall. The mounting plate could slide on the middle rail to provide movement of the camera parallel to the direction of flow. A rotational degree of freedom was provided in the telephoto lens support, which could be rotated freely and secured at an appropriate

angle of rotation. Thus, the camera had three degrees of freedom for alignment. The camera setup during experimentation is shown in Figure 24 and Figure 25.

The synchronization of the camera trigger, laser Q-switch, and laser flash lamps to the wing motion is controlled by a Quantum Composer Model 9618 pulse generator according to the signal output by the hydraulic actuator control box. The Quantum Composer ensures that the pitching motion of the airfoil, the laser sheet and the camera are phase locked to allow image acquisition at particular, specified angles of attack. The pulse generator has 8 channels with 100 ns resolution (jitter < 5 ns). The Quantum Composer can be seen in Figure 26. A 5 V signal, sent by RMCWin, at a specified angle of attack triggers the phase locked laser pulses and image capturing. Raw PIV image pairs acquired with this system can be seen in Figure 27 and Figure 28. Due to the complexity of the experimentation systems, extensive step-by-step instructions for operating the wing pitching system and PIV system are provided in Appendix B.

The wind tunnel is seeded by a MDG Max 5000 Fog generator using MDG neutral fluid, mineral oil for this investigation. The fog generator has a fog output of 10,000 ft^3/min. Fluid consumption is 2.5 L/hr at 40 psi at full volume. The reservoir capacity is 0.66 US gallons. It produces pure white particles of 0.5 to 0.7 μm in diameter. The particles are inserted into the flow downstream of the wing on the left side of the test section (looking upstream). Following Menon and Lai (Ref. 51), the mineral oil particles used in this investigation have a 3dB frequency response of approximately 85 kHz (0.75 μm particles). The seed density was selected such that the resulting

velocity vector density was nearly 100% via real time processing. However, the density was maintained below extreme levels such that the focus was not blurred.

4.1.4 Challenges of PIV

Bright laser reflections from a solid surface interfere with the Mie scattering signal from the small seed particles. The seed particles in this experimentation vary in size from approximately 0.5 to 0.75 μm. An additional complication caused by the reflection of the laser sheet by the surface is called image blooming. In this situation neighboring pixels are saturated with excess charges producing a white band in the image. A balance in the laser power is required optimize the amount of light scattered by the particles and minimize the amount of blooming occurring in the image.

To address these reflection issues, sections of the leading edge of the airfoil were replaced with optically transmitting materials. In some of past experimentation (Ref. 43, 44), on the NACA 0012 model, a 10.2 cm by 2.54 cm (4.0 in × 1.0 in) section of the airfoil leading edge was machined from Plexiglas. The Plexiglas was polished to a clear transmitting surface with Buehler Brand polishing compound (20 μ-in, followed by 5 μ-in). Because the purpose of this insert was to minimize laser sheet reflections, the portion of the wing underneath the Plexiglas was painted flat black so that laser sheet would not reflect back (Ref. 32). The laser energy that was not transmitted by the Plexiglas still masked the data below approximately 1.5 mm. To further reduce the data masking the Plexiglas was coated with a fluorescent (Rhodamine) paint capable of absorbing up to 99% of the incoming light at 532 nm and emitting the light at approximately 590 nm. A second benefit was that the emitted light was diffuse,

compared to the specular laser reflection. The airfoil was painted black approximately to minimize additional light reflections.

In more recent experiments with the NACA 0012, the Plexiglas insert was no longer used. A glass insert with an anti-reflective coating was used for data collection. This insert proved to reduce reflections in raw data images as compared to the Plexiglas insert. While the glass insert was antireflective on its outer surface, some of the transmitted light would reflect off of internal surfaces of the glass and mask data along the airfoil surface.

A similar light-transmitting insert was made for the Sikorsky SSC-A09 model as well. This insert was made of Lexan. The Lexan insert is nominally 2.54 cm by 7.62 cm (1 in × 3 in) in size. This insert was polished to a transparent surface. It fit snugly into the groove in the airfoil leading edge.

In the data acquired for this study, it was discovered that no light-transmitting insert was necessary. By painting the inserts flat black as well, reflections were reduced even further. Data collection has been achieved as close as 0.1 mm from wing surface.

4.1.5 Data Reduction Process

Each PIV sample consists of two images, labeled image A and image B respective to time. Nominally, 1000-2000 image pairs, or samples, were acquired at each angle of attack to ensure statistical convergence of the mean and second order statistics. These images were processed according to the following description.

Velocity fields were created by calculating the displacements of particle groups from image A to image B in the image pairs. These calculations were done using

LaVision DaVis data analysis software. A four-step adaptive correlation calculation using successive interrogation area sizes of 128×128, 64×64, 32×32, and 16×16 pixels respectively with a 50% overlap was performed. Two passes were done at each interrogation window size. A mask was applied prior to processing to prevent the software from completing calculations within the airfoil profile. High accuracy mode was enabled for final passes.

In order to enhance the intensity of correlation peaks relative to random noise, a signal-to-noise ratio filter was used to delete all vectors with a signal-to-noise ratio of 1.0 or less. A post-processing filter was used to remove groups with less than 5 consistent vectors. An interpolation function was enabled to fill in any empty spaces within the image. A smoothing function was also used.

This PIV data reduction process resulted in vector data for each sample. This data could be viewed as vector fields or could be exported into numerical data files of *u*- and *v*-velocity component magnitudes and directions at *x* and *y* locations.

4.2 Image Post-Processing

PIV image processing is made up of multiple steps. Processing the raw data with DaVis provided instantaneous velocity data for each sample. To gain a comprehensive understanding of the flow field, time-averaged quantities were compared, rather than instantaneous quantities. Time-averaging is the first step in image post-processing.

To obtain time-averaged quantities, a post-processing code called TAMUPIV was used. The mean velocity components and the fluctuating velocity components were calculated by TAMUPIV. Additionally, TAMUPIV was also used to calculate mean

Reynolds stresses and vorticities at each angle of attack. TAMUPIV required the input of the chord length in meters (0.45), the freestream velocity in meters per second (nominally 35), the time separation between images (20 μs), the number of pixels per millimeter in the images (approximately 17), and the number of images to average. The number of images was approximately 350 for the downstroke portion of the pitching motion and 1000 for upstroke portion of the pitching motion. The number of samples was different for the upstroke and the downstroke because all downstroke flow fields were expected to show full leading edge separation; therefore, the upstroke was the focus of this study. After the calculations were completed, the output quantities were written to a data file for further use.

Post-processing also involves normalizing the time-averaged quantities calculated by TAMUPIV. Normalization was completed in Tecplot. The mean velocity components were normalized by simply dividing by the freestream velocity, nominally 35 m/s. The fluctuating velocity components alone were not of particular practical interest. The fluctuating velocity components comprise the Reynolds stresses, σ_u, σ_v, and τ_{xy}, which are more practical quantities for comparison. Mean Reynolds stresses were normalized by U_∞^2. Mean vorticities were used for boundary layer insight and were normalized by the chord length and freestream velocity. Tecplot was then used to create visual representations of the normalized, time-averaged numerical data. Final data exhibits a velocity vector approximately every ½ mm.

5. RESULTS FOR M_∞ = 0.1 AND k = 0.1

The testing matrix for the SSC-A09 wing can be seen in Table 3. Three cases were tested wherein data was acquired. Case III is the focus of this study and will be discussed throughout Sections 5 and 6 because, of the three cases studied, it provides the most comprehensive understanding of dynamic stall on the SSC-A09. Case I is static data taken during a mechanical test of the SSC-A09 model in the wind tunnel for the first time. This data provided a basis for comparison. Case II is dynamic data where the angle of attack range for oscillations was 0° to 20°. The data acquired in Case II were used to determine what the angles of attack of interest would be for Case III. Through Case II it was determined that the angle of attack oscillation range needed to be changed to effectively observe dynamic stall.

This chapter first discusses an extensive PIV processing parameter study that was done in DaVis to determine the best settings for consistent PIV processing results. The discussion of the dynamic stall flow field is broken up into two parts, the upstroke and the downstroke. For both motions, mean velocity fields and Reynolds stresses are discussed for all angles of attack of interest. For the upstroke, vorticity is also discussed for 16°, 18°, and 20°. For 18° a boundary layer analysis was performed for the upstroke phase of oscillation.

5.1 PIV Processing Parameter Study

LaVision's DaVis software offered many options for PIV data processing that had not been available in our previously used PIV processing software. For this reason, it was necessary to determine how changing various parameters in DaVis affected the instantaneous and mean flow fields. DaVis also offered significantly faster processing, which allowed for numerous parameters and their effects to be investigated. Parameters studied include interrogation window shapes, sizes, and percentage overlap, as well as the number of passes completed at that window size. DaVis offered velocity vector post-processing options such as smoothing, vector deletion depending on signal to noise ratio, and interpolation, that were also investigated. The processing study was conducted at an angle of attack of 16°. When further investigation was required, data acquired at 18° angle of attack was used. All parameter studies were conducted on upstroke data where the flow was attached.

The shape of the interrogation window was found to largely affect the resulting instantaneous and mean velocity fields. The available interrogation area shapes are square, circle, 2:1 ellipse, 4:1 ellipse, and adaptive window shape. Multiple orientations of the ellipse were available for both elliptical window options – the semi-major axis could run north-south, east-west, northwest-southeast, or northeast-southwest. It was determined that the square shaped window could not get close enough to the surface of the wing, particularly at the leading edge, and nearly 50 pixels of data were not resolvable. The circular window allowed for resolution of data closer to the wing surface near the quarter chord, but had poorer resolution at and upstream of the leading edge.

The elliptical windows of both sizes provided holes in the data due to the curvature of the wing surface. Ellipses of different orientations were required to resolve the leading edge and downstream of the leading edge. Adaptive windows uses different window shapes at various locations in the image. The window shape that provides the most vectors with the best signal to noise ratio is the shape chosen at that location by the adaptive PIV process. For this reason, it was determined that adaptive window shapes would be used for the reduction of data.

Interrogation window size also largely affects the mean flow fields. Window size is dependent on the time separation between image A and image B. As the flow accelerates around the wing's leading edge, it can reach great enough speeds that correlation cannot be successfully achieved because the particles move out of the interrogation window. For the data acquired in Case III, it was determined that a window size of 128×128 pixels was an appropriate initial pass size and 16×16 pixels was an appropriate final pass size.

Percentage of window overlap can provide additional consistency among vectors because more vectors are generated when the overlap percentage is larger. The 350 image pairs for 16° upstroke were processed with overlap percentages of 25%, 50%, and 75%. While only 25% overlap is not commonly used in PIV data processing, it was included in this study to better see the effects of changing overlap percentage. When adjusting the overlap percentage from 25% to 50%, there were several noticeable differences in the mean flow fields, particularly the considerably smaller number of vectors obtained. When comparing 50% overlap to 75% overlap, it was determined that

contour plots of the mean velocities were nearly identical. There was no noticeable gain in precision as was seen when adjusting from 25% to 50%. An overlap percentage of 50% was chosen as a final processing parameter.

The final multi-pass parameter to adjust was the number of passes completed for each interrogation window size. The data was processed for 1 pass, 2 passes, and 3 passes at each interrogation window size. Similarly to the overlap percentage, adjusting the number of passes at each of the four interrogation window sizes from 1 to 2 caused increased consistency in vectors. This aided in the resolution of the flow at the leading edge. When increasing the number of passes from 2 to 3, there was no discernable difference between the mean flow fields; however, the processing took nearly twice as long. It was determined that 2 passes at each interrogation window size provided slightly better resolution without adding a considerable amount of processing time.

The vector post-processing parameter study began with studying the effects of smoothing. Smoothing was turned on and off for 350 image pairs at both 16° and 18° angle of attack. It was determined that smoothing helped slightly to resolve the flow at the leading edge. Additionally, the freestream flow vectors were more consistent with the smoothing parameter turned on. For these reasons smoothing was used when during the final processing of the PIV data.

Vector deletion and the resulting effects were investigated next. Vectors could be deleted for two reasons in DaVis. First, a vector could be deleted if it did not have an appropriate signal to noise ratio – DaVis calls this the quality factor, Q. The threshold of acceptable values for Q was set by the analyst. To determine appropriate values of Q to

test, histograms were generated for all angles of attack that showed the vector intensity at the mean velocities. Through these, it was possible to determine that Q is a highly sensitive parameter, and changing it even slightly can eliminate hundreds or thousands of vectors. Appropriate Q values for this case were determined to be 0.9 and 1.0; therefore, data was processed at both values and compared. Increasing the threshold to 1.0 from 0.9 was found to eliminate vectors that were inconsistent. This allowed for greater resolution near the leading edge and increased the resolution near the wing surface. The second method of vector deletion was also intended to reduce inconsistencies in the flow by deleting vectors based on the group of vectors it was located in. By removing groups with fewer than 5 vectors it was possible to even further resolve the vector field near the leading edge. For these reasons, vectors were deleted if they possessed a $Q < 1.0$ or were in a group of less than 5 vectors.

After studying the effects of vector deletion, the effects of the interpolation option on the mean flow field were assessed. The interpolation option can drastically affect PIV data analysis. While interpolation increases the vector density for an image, it also obtains the extra vectors mathematically based on the surrounding vectors. The surrounding vectors may not produce an accurate representation of what is happening in the flow at that point. If it is the instantaneous flow field that is of interest, interpolation should not be used, but within the mean flow field interpolation provides data with higher levels of precision. Interpolation, when coupled with the vector deletion parameters described above, provided greater resolution of the mean flow field about the

leading edge. These two parameters helped to clarify what was physically occurring at the leading edge.

Through studying the effects of these processing parameters, it was possible to resolve data to within 1.0 mm of the wing surface. Additionally, physical phenomena were identifiable within the flow. The previously difficult to resolve leading edge region and upstream of the leading edge region were resolvable. A summary of the results of the processing parameter study is given in Table 4. Some representative data contours for U and τ_{xy} are provided in Appendix C.

5.2 Upstroke – Airfoil Pitching Up Motion

The SSC-A09 wing was pitching about its quarter chord, sinusoildally oscillating from 5° to 25° angle of attack. Throughout oscillations, the flow field is the most interesting during the pitching up motion. It is during the upstroke that the significant delays in stall characteristics are observed. For this reason, the upstroke will be discussed first. Also, this is the reason excess data was acquired for an angle of attack of 18°. The mean velocity components and the Reynolds stresses throughout the flow field will be discussed in detail for 16°, 18°, 20°, 22°, and 24°.

It is important to note that while the overall average data for 18° showed that the flow was attached in the field of view, there were several instantaneous images that showed partial separation in the field of view. The instantaneous images that showed full attachment were averaged independently from the instantaneous images that showed partial separation. If the non-dimensional u-velocity was less than 0.9 at $x/c \geq 0.12$ and $y/c \geq 0.09$ – on the reference frame shown in Figure 17 – the flow was considered

separated for that sample. Separate mean velocity fields, Reynolds stresses, vorticity fields, and vector fields were obtained for 18° overall, 18° fully attached flow, and 18° partially separated flow. For an angle of attack of 18°, the flow was found to be partially separated in this field of view for 10.1% of the images acquired.

Similar circumstances were observable for an angle of attack of 20°. For 20°, however, the average of all the images acquired showed total separation from the wing leading edge. The instantaneous samples were once again sorted for independent post-processing. The samples were either categorized as fully separated or partially attached. Separation was again determined based on the non-dimensional u-velocity component. The sample was considered partially attached if the normalized u-velocity component was greater than 1.2 at $x/c \leq 0.22$ and $y/c = 0.09$. At 20° angle of attack, the flow was determined to be partially attached for 7.3% of the samples acquired.

5.2.1 Mean Velocity Flow Field

Contours of the mean velocity components about the leading edge region of the SSC-A09 wing during the upstroke are shown in Figure 29 to Figure 46 for 16° to 24° angle of attack. Insight into the flow field about the wing that can be drawn from these velocity contours are discussed in this section.

At 16° angle of attack there is delay of stall condition onset due to dynamic stall. The static stall angle of attack for a Sikorsky SSC-A09 is approximately 16.5° at our flow conditions (Ref. 52); in the U-velocity contour shown in Figure 29, it is apparent that the flow remains attached at the leading edge at 16°. This figure shows the magnitude of the U in the first 13% of the chord length. The change in magnitude of U

can be seen as the flow accelerates around the leading edge of the wing. The maximum velocity reached is nearly $3.0U_\infty$ at 1% to 2% of the chord. The magnitude of U then begins to slow down as it follows the curvature of the wing surface. U is slightly negative below the leading edge of the airfoil due to the flow above the location of the stagnation point turning to follow the curvature of the airfoil. As expected, moving outward, away from the wing surface, U decreases as it approaches the freestream velocity. The mean velocity in the y-direction for 16° angle of attack is shown in Figure 30. V is greatest in magnitude at the leading edge where the flow must turn to follow the wing surface. When V is nearly zero, the flow is parallel to the freestream velocity, which is observable at 6% of the chord.

At 18° angle of attack, three pairs of velocity contours were generated. Figure 31, Figure 33, and Figure 35 show the mean velocity component in the x-direction for all samples acquired, samples acquired showing full attachment in the field of view observed, and samples acquired showing partial separation in the field of view observed, respectively. Figure 32, Figure 34, and Figure 36 show the mean velocity in the y-direction for these three conditions. Overall, in the majority of samples acquired at 18°, the flow was shown to be attached. It is important to point out that this is past the static stall angle of approximately 16° mentioned previously. U increases about the leading edge of the wing, following the surface curvature, until it reaches its maximum along the surface at between 2% and 3% of the chord. The maximum velocity observed is again approximately $3.0U_\infty$. Downstream of this chord location, the velocity slowly decreases until separation occurs at a location outside the investigated field of view. At locations

increasingly farther outward, away from the wing surface, U decreases in magnitude. The maximum magnitude of mean velocity in the y-direction is observable at the leading edge, as the vectors follow the curvature of the wing surface. There are no significant differences between the overall mean velocity contours and the velocity contours of the fully attached samples, mean velocity magnitudes showed changes on the order of $0.1U_\infty$ or less. There are significant differences between contours in these two cases as compared to the partially separated flow. For the partially separated flow, U shows a small wedge of $0.75U_\infty$ or less is visible from 10% of the chord and rearward. This wedge appears to be approaching from the trailing edge and has velocities of nearly zero near the wing surface. Downstream of 8% of the chord the flow does not follow the curvature of the wing surface, it follows the edge of the separation wedge. The velocity contour in the y-direction does not show a considerable change magnitude of V at the locations of the separation wedge observed in the U contours. This is due to the small magnitudes of V at these locations regardless of separation.

Three pairs of velocity contours were also generated for an angle of attack of 20°. Because the overall flow was fully separated for 20°, the additional two pairs of velocity contours are for the mean of the instantaneous velocity samples showing full separation from the leading edge and instantaneous velocity samples showing partial attachment in the field of view investigated. U and V contours for all the samples acquired at 20° upstroke are shown in Figure 37and Figure 38. Figure 39 and Figure 40 show the average velocities of the samples acquired that showed full separation from the leading edge. Figure 41 and Figure 42 show the average velocities of the instantaneous velocity

samples that showed only partial separation. The overall mean velocities clearly show the separation from the leading edge of the airfoil. Along the entire surface of the airfoil, U is less than $0.75U_\infty$. U increases along the edge of the separation wedge until the freestream velocity is matched at a location outside this field of view. Within this field of view the maximum U, $2.5U_\infty$, occurs at 10% of the chord and at a y/c location of 0.17. In the separation wedge, there is a clear reverse flow region where U near the wing surface is positive (opposite the freestream flow). The separation wedge is also clearly visible in the overall V contour. The maximum magnitude of V, $2.0U_\infty$, occurs just upstream of the leading edge, where the flow is changing direction to get to the upper surface of the wing. Along the edge of the separation wedge the magnitude of V decreases moving farther outward. Within the separation wedge, a region is observable where V points inward toward the wing surface. There are no significant differences between the overall average velocity contours and the fully separated average velocity contours. This is expected because 92.7% of the samples acquired were fully separated. There are two significant differences observable between the overall average velocity contours and the partially attached average velocity contours. First, the separation wedge has moved downstream by 3% of the chord to x/c = 0.22. Second, the contours themselves are much more jagged in appearance. The magnitudes of both U and V are consistent across all three contour pairs.

The flow field is fully separated at angles of attack of 22° and 24°. For this reason, the mean velocity contours for these two angles are very similar. In all four contours (Figure 43-Figure 46) the separation wedge is clearly visible. The U contours

for both angles of attack feature the reverse flow region. The maximum magnitude U occurs at 7% of the chord for both angles of attack; however, the maximum U is greater for 22° than it is for 24° by $0.5U_\infty$. For both angles of attack the maximum magnitude of V occurs at the leading edge, where the flow is turning to follow the shape of the separation wedge.

5.2.2 Reynolds Stresses

This section describes the contours of the three Reynolds stresses, σ_u, σ_v, and τ_{xy}, during the pitching up motion of the wing at 16°, 18°, 20°, 22°, and 24°. For all angles of attack investigated the normal and shear Reynolds stresses are only found within the separated area or shear layer. Reynolds stresses for each angle of attack, during the upstroke, can be seen in Figure 47-Figure 73.

For an angle of attack of 16°, the flow remains attached throughout the field of view used in this study, during the upstroke. As expected, the Reynolds stresses in this case are only found along the surface of the wing in the shear layer. The averaged stream-wise normal Reynolds stress appears primarily at the leading edge, but can also be seen along the airfoil surface, downstream from 8% of the chord on (Figure 47). The maximum σ_u is 0.6 along the surface of the wing within the first 1% of the chord. The vertical normal Reynolds stress also appears primarily at the leading edge, but can also be observed downstream of 9% of the chord. For 16° upstroke, the maximum σ_v is 0.75 at the leading edge (Figure 48). The Reynolds shear stress, τ_{xy}, is found only at the wing leading edge and has a maximum value of 0.45 (Figure 49).

As discussed previously, 3 sets of contours were generated for 18° angle of attack. Differences are more noticeable between the contours sets in the average Reynolds stress contours than in the velocity contours discussed above. In the overall contours, the Reynolds stresses are observable primarily at the wing leading edge (Figure 50, Figure 51 and Figure 52). The stream-wise normal Reynolds stress is also observable downstream of 8% of the chord (Figure 50). Slight thickening of the shear layer is visible at the edge of the field of view. For the average of the attached samples, the thickening of the shear layer toward the edge of the field of view, in the stream-wise normal stress contour, is no longer evident (Figure 53). The vertical normal stress and shear stress are only observable at the leading edge of the wing (Figure 54 and Figure 55). There is shear stress data at the rear of the field of view that is being masked by the high stresses at the leading edge in the contours shown. For the average of the 10.1% of partially separated images there are indicators of the thickening of the shear layer and separation onset in all three Reynolds stress contours. According to the σ_u contour, the shear layer begins to thicken at 6% of the chord (Figure 56). The σ_v contour shows thickening of the shear layer starting at 10% of the chord (Figure 57). Figure 58 shows the Reynolds shear stress contour, τ_{xy}, which shows shear layer thickening beginning at 9% of the chord.

Three sets of Reynolds stress contours were also generated for 20° angle of attack. Because 92.7% of the instantaneous samples were attached, the overall averages (Figure 59, Figure 60, and Figure 61) and the fully separated averages (Figure 62, Figure 63, and Figure 64) are very similar and will be discussed as a single set of contours. The

stream-wise normal stress contour shows the separated region and emphasizes the shear layer. The shear layer clearly begins at the leading edge and follows a nearly constant slope up and to the left (downstream). A peak in σ_u can be seen in the first 4% of the chord, within the shear layer. The vertical normal stress contour shows the shear layer curving around the leading edge of the SSC-A09 wing. The maximum value of σ_v is found at the leading edge. The shear stress is observable curving around the upper portion of the leading edge and throughout the shear layer and separated region. The maximum shear stress occurs at 3% of the chord. The average stress contours generated from the partially attached instantaneous samples at 20° angle of attack are particularly interesting. These contours show the point of separation. The stream-wise normal stress shows the shear layer at the leading edge becomes unattached at 4% of the chord (Figure 65). σ_u peaks at 7% of the chord. Figure 66 shows the vertical normal stress and the onset of separation at 4% of the chord. The Reynolds shear stress is shown in Figure 67. Once again at 4% of the airfoil chord, the transition of the shear layer from attached to separated is evident.

At 22° and 24° the flow is fully separated and the Reynolds stresses are confined to the separated region and shear layer. The Reynolds stress contours for these angles can be seen in Figure 68-Figure 73. In all contours, the maximum stress is located in the first 5% of the chord. Both the vertical normal stresses and the shear stresses wrap around the front of the leading edge.

5.2.3 Vorticity Analysis for α = 16°, 18°, and 20°

A vorticity analysis was conducted for 16°, 18°, and 20° angle of attack during the upstroke motion of the wing. The generated contours for non-dimensional mean vorticity at these angles of attack can be seen in Figure 74 through Figure 80.

At the angles of attack that show significant attachment, 16° and 18°, there is a large positive vorticity that wraps around the airfoil leading edge. Once again, 18° and 20° data were analyzed in three sets, as described previously. From 16° to 18° there is a noticeable thickening of the vorticity along the wing surface in the field of view. At 18° when comparing all three set averages, the positive vorticity region is smallest for the fully attached samples and largest for the partially separated samples. A drastic increase in vorticity is observable in the separation onset region.

At 20°, positive vorticity is largest along the outer edge of the separated region near the leading edge in all three analysis sets. The overall data and the fully separated data agree well due to the 92.7% of samples the two sets have in common. For these two sets, the vorticity is greatest near the leading edge and decreases in magnitude as you move outward – away from the wing suface – and further downstream. Several vortices are visible throughout the separated region of the 7.3% of samples that showed partial attachment. This contour also shows indications of a small vortex near the separation point. This vortical structure is highlighted in Figure 80.

5.2.4 Boundary Layer Analysis for α = 18°

Streamline and vector field data were generated for 16°, 18°, and 20° angle of attack to provide further insight into the boundary layer. These data can be seen in

Figure 81-Figure 97. It was only possible to resolve the upper edge of the boundary layer for 18° angle of attack during the upstroke phase of the pitching motion. The velocity vectors and streamlines for 18° angle of attack, upstroke are shown in Figure 83-Figure 91. Zoomed in views of velocity vectors along the rear portion of the leading edge region – from 6.5% to 15% of the airfoil chord – provide a better understanding of what happens to the velocity as the airfoil surface is approached.

Figure 85 shows the boundary layer vectors for the overall mean data acquired at 18°. As expected, the velocity vectors decrease in magnitude as they approach the airfoil surface within the boundary layer. Figure 88 exhibits a similar decrease in velocity vector magnitude approaching the airfoil surface within the boundary layer. This figure shows the boundary layer mean velocity vectors for the samples taken at 18° that showed full attachment within the field of view. The decrease in boundary layer velocity vector magnitude is smaller in this case than in the mean of all the acquired data. Figure 91 shows a zoomed-in view of the boundary layer and first indications of separation onset for the 10.1% of samples with observable separation. Here, the decrease in velocity vector magnitude is much more significant as the separated region is approached. The mean velocity in the separated region is between 0 and 0.1 times the freestream velocity. For this subset of samples, the direction of the velocity vectors has also changed, because of the separation region. It is also observable in this data subset that as you move downstream from the leading edge toward the edge of the field of view, the velocity vectors decrease in magnitude until a minimum is reached in the

separated region. The state of the boundary layer remains unknown as the flow accelerates around the leading edge.

5.3 Downstroke – Airfoil Pitching Down Motion

During the sinusoidal pitching down about the quarter chord, the flow field was observed for 16°, 20°, 22°, and 24° angle of attack. At all angles of attack, the flow field was fully separated during the downstroke. For this reason, the downstroke can be discussed as a whole, rather than for each angle of attack. Significantly less data was acquired during this portion of oscillation; only approximately 350 images per angle of attack, rather than the approximately 1025 that were acquired per angle during the upstroke. Additionally, no data was recorded for 18° angle of attack during the downstroke due to time restrictions in the LSWT testing environment.

5.3.1 Mean Velocity Flow Field

Once again the mean velocity flow field was broken up into components, U and V, for each angle of attack. The contours of the mean velocity components can be seen from Figure 98 to Figure 105. All angles of attack clearly showed separated regions beginning at the leading edge. The reverse flow region near the surface of the wing was also apparent at all angles of attack in the stream-wise velocity component contours. The vertical velocity component contours identify the area of peak V as the leading edge. The magnitude of the peak velocity component in the y-direction is approximately $1.2U_\infty$ for all four angles of attack investigated.

5.3.2 Reynolds Stresses

The Reynolds stresses are also fairly consistent for 16°, 20°, 22°, and 24° during the downstroke phase of the pitching motion. The shear layer and separated region is clearly identifiable for each angle of attack in σ_u, σ_v, and τ_{xy}. Reynolds stress contours for the downstroke motion are provided in Figure 106-Figure 117. The stream-wise normal stress contours for all four angles are very similar and are shown in Figure 106, Figure 109, Figure 112, and Figure 115. They all show the shear layer beginning on the upper surface of the leading edge region. The location of maximum stream-wise normal stress changes with angle of attack. As angle of attack increases, the location of maximum stream-wise normal stress moves upstream along the wing surface. The location of peak σ_u is in the first 4% of the airfoil chord at all angles of attack observed. The magnitude of the peak σ_u is between 0.1 and 0.2 for these four angles of attack. The average vertical normal Reynolds stress contours are very similar to one another and are shown in Figure 107, Figure 110, Figure 113, and Figure 116. For all four angles of attack the shear layer begins on the upper surface of the leading edge region. The location of the maximum vertical normal stress also changes with angle of attack. As angle of attack increases, the location of peak σ_v moves upstream. Once again, the maximum σ_v is located upstream of 4% of the airfoil chord for all angles of attack investigated. The maximum value of the vertical normal stress is between 0.075 and 0.085 for these angles of attack. The trends that were observed in σ_u and σ_v can also be observed in τ_{xy}, as shown in Figure 108, Figure 111, Figure 114, and Figure 117. The location of the maximum Reynolds shear

stress is upstream of 4% chord for these for angles of attack. The peak value of τ_{xy} ranges between 0.5 and 0.7 for these cases.

5.4 Uncertainty Analysis

Uncertainty estimates were made for angle of attack, position, mean velocity, Reynolds stresses, and vorticity for 18° and 20° angle of attack at three locations – near the leading edge, near the edge of the field of view downstream of the leading edge, and in the freestream. Uncertainties can be found in Table 5 and Table 6. The angle of attack uncertainty was determined based on the uncertainty of the inclinometer used to measure angle of attack. Uncertainty in position was determined based on the location of the airfoil edge. Statistical uncertainty was determined using methods described by Benedict and Gould (Ref. 53). Uncertainty estimates were generated for both 18° and 20° angle of attack during the upstroke, because the number of PIV samples acquired at 18° was nominally double the number acquired at 20°. This uncertainty analysis accounts only for random statistical error.

6. CONCLUSIONS AND FUTURE WORK

An investigation has been conducted of the leading edge flow during dynamic stall on a pitching Sikorsky SSC-A09 wing. The testing model was constructed specifically for use in the TAMU DSF. The wing was oscillated sinusoidally from 5° to 25° angle of attack at a frequency of 2.5 Hz using a hydraulic actuation apparatus. The Mach and Reynolds numbers of testing were 0.1 and 1.0×10^6, respectively. PIV data were taken at 16°, 18°, 20°, 22°, and 24° during the upstroke and downstroke phases of oscillation. The image pairs acquired during testing were processed and post-processed to determine mean flow field characteristics. A PIV processing parameter study was carried out to determine the best settings in DaVis PIV analysis software for resolving data on a pitching airfoil. Velocity components and Reynolds stresses were analyzed. Usable data were acquired to within 1.0 mm of the wing surface.

6.1 Conclusions

Several conclusions can be drawn from the velocity component contours taken during the upstroke and downstroke phases of pitching motion. For a SSC-A09 airfoil, the flow remains fully attached in the first 14% of the chord at 16° angle of attack. A maximum velocity of approximately $3.0U_\infty$ is reached parallel to the freestream as the flow accelerates around the leading edge of the airfoil. The location of this maximum with respect to chord moves downstream as angle of attack increases from 16° to 18°. The first indications of separation during the upstroke are seen at 18° angle of attack.

This shows a delay in stall onset compared to the static stall angle of 16.5° (Ref. 52). At 18°, the flow shows at least partial separation before 14% of the chord 10.1% of the time. By 20° angle of attack the flow is fully separated 92.7% of the time. It is at 20° that reverse flow is first observable on the surface of the SSC-A09 airfoil in the separated region. Once the flow field has fully separated over the airfoil, the flow field remains largely the same, and there is no significant difference between 22° and 24° angle of attack.

The analysis of Reynolds stresses during the upstroke also allowed for several conclusions to be drawn. If the flow is attached then the shear layer runs along the airfoil surface, and both normal and shear Reynolds stresses appear only in the shear layer. This was seen at 16° angle of attack. Peak Reynolds stresses occur at the leading edge of the airfoil. It is currently uncertain if this is a physical flow phenomenon or the result of challenges in PIV data processing. If the flow is separated, the shear layer forms the boundary between the inviscid flow outside the separated region and the separated region. This was observed for 22° and 24° angle of attack. The Reynolds stresses provided the most insight into the location of the separation point, which was observable at 20° angle of attack in the 7.3% of data at that angle that showed only partial separation.

Vorticity data was analyzed for the three angles of attack that showed attachment during the upstroke phase of the airfoil pitching motion. A vorticity analysis was conducted to provide insight into the boundary layer characterization. Increased vorticity precedes separation and stall onset. This was observable for 16° and 18° angle of attack.

The vorticity region expanded and the vorticity magnitude increased as stall was approached. While the flow is attached, the vorticity is present along the wing surface. At 20° angle of attack, the vorticity was no longer attached to the surface, but followed the boundary of the separated region. For the samples that showed partial attachment at 20°, several vortices were observable, including a vortex downstream of the leading edge near the point of separation.

The edge of the boundary layer was resolvable only for 18° angle of attack due to the field of view of the data acquired. The magnitude of the mean flow velocity vectors was found to decrease as the airfoil surface was approached, after the edge of the boundary layer had been crossed. The velocity vector profile was observed just before separation onset. The magnitude of the velocity vectors decreases as you move from leading edge downstream to the edge of the field of view along the airfoil surface. More data points in the boundary layer are required to do a detailed boundary layer analysis at other angles of attack. Currently, we only have approximately 5 data points in the boundary layer.

The most important conclusion that can be drawn from this study of upstroke data for dynamic stall is the 18° data. Because such a small percentage of samples acquired at 18° showed separation onset, it can be said that separation is incipient in leading edge region at 18° angle of attack. Data were not previously available when separation was imminent, but had not yet occurred. Providing boundary layer velocity data to the CFD community will allow model verification and validation.

It was observed that the downstroke data were pointedly similar across the range of angles of attack. Dynamic stall flow reattachment does not occur until an angle of attack below those studied in this investigation. The average velocity fields showed separation and reversed flow. The Reynolds stresses appeared only in the shear layer and separated region. The shear layer again formed the boundary between the separated flow region and the inviscid outside flow.

6.2 Future Work

There is a great deal of future research that can be conducted with the SSC-A09 model constructed for this study. Among the most important research that should be conducted is a detailed study of the flow field from 17° through 21° angle of attack. The angle of attack resolution could be finer, in increments of ½ degrees instead of the 2 degree increments used in this study. Additionally, the data acquired was of too large a field of view to conduct a detailed study of the boundary layer. It is important to acquire new data of the first 5-7% of the airfoil chord in order to do this. These additions to the research would provide a better understanding of the angle at which dynamic stall becomes the dominant flow phenomenon. A larger field of view would also be useful to gain a better understanding of the flow over the entirety of the airfoil chord. This would be useful because separation occurs at lower angles of attack outside of our current field of view.

This study was only conducted at Mach 0.1 and a reduced frequency of 0.1. It would be of future interest to study dynamic stall on the SSC-A09 at other Mach numbers within the appropriate range for helicopters, Mach 0.2-0.4, where at higher

Mach numbers, the stall process changes fundamentally. Additionally, helicopters often experience reduced frequencies ranging as low as 0.05. Adding an additional reduced frequency to the study would be of great value.

REFERENCES

[1]Gessow, A., and Myers, G. C., Jr., *Aerodynamics of the Helicopter*, Frederick Ungar Publishing Co., New York, NY, 1967, Chapters 1-4, 7-10.

[2]Leishman, J. G, *Principles of Helicopter Aerodynamics*, 2nd Ed., Cambridge University Press, New York, NY, 2006, Chapters 2, 4, 6, 8-9.

[3]Seddon, J., and Newman, S., *Basic Helicopter Aerodynamics*, 2nd Ed., American Institute of Aeronautics and Astronautics, Inc., Reston, VA, 2001, Chapters 1, 4-6.

[4]Ekaterinaris, J. A., and Platzer, M. F., "Computational Prediction of Airfoil Dynamic Stall," *Progress in Aerospace Sciences*, Vol. 33, (11-12), 1998, pp. 759-846.

[5]Madden, P. A., "Angle-of-Attack Distribution of a High Speed Helicopter Rotor," *Journal of the American Helicopter Society*, Vol. 12, (2), April 1967, pp. 41-49.

[6]Carta, F. O., "An Analysis of the Stall Flutter Instability of Helicopter Rotor Blades," *Journal of the American Helicopter Society*, Vol. 12, (4), October 1967, pp. 1-18.

[7]Ham, N. D., "Stall Flutter of Helicopter Rotor Blades: A Special Case of the Dynamic Stall Phenomenon," *Journal of the American Helicopter Society*, Vol. 12, (4), October 1967, pp. 19-21.

[8]Ham, N. D., and Garelick, M. S., "Dynamic Stall Considerations in Helicopter Rotors," *Journal of the American Helicopter Society*, Vol. 13, (2), April 1968, pp. 49-55.

[9]Harris, F.D., and Pruyn, R. R., "Blade Stall – Half Fact, Half Fiction," *Journal of the American Helicopter Society*, Vol. 13, (2), April 1968, pp. 27-48.

[10]Liiva, J., and Davenport, F. J., "Dynamic Stall of Airfoil Sections for High-Speed Rotors," *Journal of the American Helicopter Society*, Vol. 14, (2), April 1969, pp. 26-33.

[11]Johnson, W., "The Effect of Dynamic Stall on the Response and Airloading of Helicopter Rotor Blades," *Journal of the American Helicopter Society*, Vol. 14, (2), April 1969, pp. 68-79.

[12]Ericsson, L. E., and Reding, J. P., "Dynamic Stall of Helicopter Blades," *Journal of the American Helicopter Society*, Vol. 17, (1), January 1972, pp. 11-19.

[13]McCroskey, W. J., and Fisher, R. K., Jr., "Detailed Aerodynamic Measurements on a Model Rotor in the Blade Stall Regime," *Journal of the American Helicopter Society*, Vol. 17, (1), January 1972, pp. 20-30.

[14]Johnson, W., and Ham, N. D., "On the Mechanism of Dynamic Stall," *Journal of the American Helicopter Society*, Vol. 17, (4), October 1972, pp. 36-45.

[15]Carta, F. O., Commerford, G. L., and Carlson, R. G., "Determination of Airfoil and Rotor Blade Dynamic Stall Response," *Journal of the American Helicopter Society*, Vol. 18, (2), April 1973, pp. 31-39.

[16]Martin, J. M., Emrey, R. W., McCroskey, W. J., and Caradouma, F. X., "An Experimental Analysis of Dynamic Stall on an Oscillatory Airfoil," *Journal of the American Helicopter Society*, Vol. 19, (1), January 1974, pp. 26-32.

[17]McCroskey, W. J., Carr, L. W., and McAlister, K. W., "Dynamic Stall Experiments on Oscillating Airfoils," AIAA Paper No. 75-125, AIAA 13th Aerospace Sciences Meeting, Pasadena, CA, January 20-22, 1975.

[18]McCroskey, W. J., Carr, L. W., and McAlister, K. W., "Dynamic Stall Experiments on Oscillating Airfoils," *AIAA Journal*, Vol.14, (1), January 1976, pp. 57-63.

[19]Prouty, R. W., "A State-of-the-Art Survey of Two-Dimensional Airfoil Data," *Journal of the American Helicopter Society*, Vol. 20, (4), October 1975, pp. 14-25.

[20]Ericsson, L. E., and Reding, J. P., "Dynamic Stall Analysis in Light of Recent Numerical and Experimental Results," *Journal of Aircraft*, Vol. 13, (4), April 1976, pp. 248-255.

[21]Pierce, G. A., Kunz, D. L., and Malone, J. E., "The Effect of Varying Freestream Velocity on Airfoil Dynamic Stall Characteristics," *Journal of the American Helicopter Society*, Vol. 23, (2), April 1978, pp. 27-33.

[22]McCroskey, W. J., "The Phenomenon of Dynamic Stall," NASA TM-81264, Presentation to von Kármán Institute Lecture Series on Unsteady Airloads and Aeroelastic Problems in Separated and Transonic Flows, Rhode Saint Genèse, Belgium, March 9-13, 1981.

[23]McCroskey, W. J., McAlister, K. W., Carr, L. W., Pucci, S. L., Lambert, O., and Indergrand, Lt. R. F., USAF, "Dynamic Stall on Advanced Airfoil Sections," *Journal of the American Helicopter Society*, Vol. 26, (3), July 1981, pp. 40-50.

[24]McCroskey, W. J., McAlister, K. W., Carr, L. W., and Pucci, S. L., "An Experimental Study of Dynamic Stall on Advanced Airfoil Sections Volume 1. Summary of the Experiment," NASA TM-84245, July 1982.

[25]McAlister, K. W., Pucci, S. L., McCroskey, W. J., and Carr, L. W., "An Experimental Study of Dynamic Stall on Advanced Airfoil Sections Volume 2. Pressure and Force Data," NASA TM-84245, September 1982.

[26]Carr, L. W., McCroskey, W. J., McAlister, and K. W., Pucci, S. L., "An Experimental Study of Dynamic Stall on Advanced Airfoil Sections Volume 3. Hot-Wire and Hot-Film Measurements," NASA TM-84245, December 1982.

[27]Ericsson, L. E., and Reding, J. P., "Unsteady Flow Concepts for Dynamic Stall Analyis," *Journal of Aircraft*, Vol. 21, (8), August 1984, pp. 601-606.

[28]Carr, L. W., "Dynamic Stall Progress in Analysis and Prediction," AIAA TP 82-1769, Atmospheric Flight Mechanics Conference, Snowmass, CO, August 19-21, 1985.

[29]Carr, L. W., "Progress in Analysis and Prediction of Dynamic Stall," *Journal of Aircraft*, Vol. 25, (1), January 1988, pp. 6-17.

[30]Ericsson, L. E., and Reding, J. P., "Dynamic Stall Overshoot of Static Airfoil Characteristics," AIAA Paper No. 85-1773, 1985, pp. 61-77.

[31]Walker, J. M., and Chou, D. C., " Forced Unsteady Vortex Flows Driven by Pitching Airfoils," AIAA Paper No. 87-1331, AIAA 19th Fluid Dynamics, Plasma Dynamics and Lasers Conference, Honolulu, HI, June 8-10, 1987.

[32]Chandrasekhara, M., and Carr, L., "Flow Visualization Studies of the Mach Number Effects on the Dynamic Stall of an Oscillating Airfoil," AIAA Paper No. 82-0023, 27th Aerospace Sciences Meeting, Reno, NV, January 9-12, 1989.

[33]Chandrasekhara, M. S., and Carr, L. W., "Flow Visualization Studies of the Mach Number Effects on the Dynamic Stall of an Oscillating Airfoil," *Journal of Aircraft*, Vol. 27, (6), June 1990, pp. 516-522.

[34]Chandrasekhara, M. S., and Brydges, B. E., "Amplitude Effects on Dynamic Stall of an Oscillating Airfoil," AIAA Paper No. 90-0575, 28th Aerospace Sciences Meeting, Reno, NV, January 8-11, 1990.

[35]Currier, J., and Fung, K.-Y., "An Analysis of the Onset of Dynamic Stall," AIAA Paper No. 91-0003, 29th Aerospace Sciences Meeting, Reno, NV, January 7-10, 1991.

[36]Currier, J. M., and Fung, K.-Y., "Analysis of the Onset of Dynamic Stall," *AIAA Journal*, Vol. 30, (10), October 1992, pp. 2469-2477.

[37]Lorber, P. F., and Carta, F. O., "Unsteady Stall Penetration Experiments at High Reynolds Number," AFOSR TR-87-1202, April 14, 1987.

[38]Carr, L. W., Chandrasekhara, M. S., Ahmed, S., and Brock, N. J., "A Study of Dynamic Stall Using Real Time Interferometry," AIAA Paper No. 91-0007, 29th Aerospace Sciences Meeting, Reno, NV, January 7-10, 1991.

[39]Chandresekhara, M. S., Ahmed, S., "Laser Velocimetry Measurement of Oscillating Airfoil Dynamic Stall Flow Field," AIAA Paper No. 91-1799, AIAA 22nd Fluid Dynamics, Plasma Dynamics, and Lasers Conference, Honolulu, HI, June 24-26, 1991.

[40]Panda, J., and Zaman, K. B. M. Q., " Experimental Investigation of the Flowfield of and Oscillating Airfoil," AIAA Paper No. 92-2622, 1992.

[41]Ferrecchia, A., Coton, F. N., and Galbraith, R. A. McD., "An Examination of Dynamic Stall Vortex Inception on a Finite Wing and on a NACA 0015 Aerofoil," AIAA Paper No. 99-3112, 1999.

[42]Ekaterinaris, J. A., Chandrasekhara, M. S., and Platzer, M. F., "Recent Developments in Dynamic Stall Measurements, Computations and Control," AIAA Paper No. 2005-1296, 43rd AIAA Aerospace Sciences Meeting and Exhibit, Reno, NV, January 10-13, 2005.

[43]Sahoo, D., "Experimental Analysis of the Vorticity and Turbulent Flow Dynamics of a Pitching Airfoil at Realistic Flight (Helicopter) Conditions," PhD Dissertation, Aerospace Engineering Department, Texas A&M University, College Station, TX, May 2008.

[44]Sahoo, D., Bowersox, R. D. W., and Goss, L., "Experimental Investigation of the Leading-Edge Flow of a Dynamically Pitching Airfoil," AIAA Paper No. 2008-651, 46th AIAA Aerospace Sciences Meeting and Exhibit, Reno, NV, January 7-10, 2008.

[45]RMCWin, Motion Control, Software Package, Ver. 2.29.0, Delta Computer Systems, Inc., Battle Ground, WA, 2007.

[46]SolidWorks, 3-D Computer Aided Design, Software Package, 2010-2011 Student Edition, Dassault Systemes SolidWorks Corp., Concord, MA, 2009.

[47]DaVis, PIV Analysis, Software Package, Ver. 8.0.7, LaVision GmbH, Goettingen, Germany, 2011.

[48]Tecplot 360 2011, Numerical and CFD Visualization, Software Package, Release 1 Build 13.1.1.16309, Tecplot, Inc., Bellevue, WA, 2011.

[49]Raffel, M., Willert, E. C., and Kompenhans, J., *Particle Image Velocimetry - A Practical Guide*, Springer Publications, Berlin, Germany, 1998, Chapters 1-6, 8.

[50]pco.CamWare, Camera Image Grab, Software Package, Ver. 2.19, PCO AG, Kelheim, Germany.

[51]Menon, R., and Lai, W. T., "Key Considerations in the Selection of Seed Particles for LDV Measurements," *Laser Anemometry*, *Advances and Applications*, Vol. 2, Fourth International Conference on Laser Anemometry, Advances and Applications, August, 1991, pp. 719-730.

[52]Lorber, P. F., Carta, F. O., and Covino, A. F., Jr., "An Oscillating Three-Dimensional Wing Experiment: Compressibility, Sweep, Rate, Waveform, and Geometry Effects on Unsteady Separation and Dynamic Stall," United Technologies Research Center Report No. R92-958325-6, ARO Report No. ARO 26631.8-EG, November 30, 1992.

[53]Benedict, L. H., and Gould, R. D., "Towards Better Uncertainty Estimates for Turbulence Statistics," *Experiments in Fluids*, Vol. 22, 1996, pp. 129-136.

Supplemental References Consulted

Ahmed, S., and Chandrasekhara, M.S., "Reattachment Studies of an Oscillating Airfoil Dynamic Stall Flowfield," *AIAA Journal*, Vol. 32, (5), May 1994, pp. 1006-1012.

Ahn, T., Kim, C., and Rho, O.-H., "Dynamic-Stall Control Based on an Optimal Approach," *Journal of Aircraft*, Vol. 41, (5), September-October 2004, pp. 1106-1116.

Barwey, D., and Gaonkar, G.H., "Dynamic-Stall and Structural-Modeling Effects on Helicopter Blade Stability with Experimental Correlation," *AIAA Journal*, Vol. 32, (4), April 1994, pp. 811-819.

Bellinger, E. D., "Analytical Investigation of the Effects of Blade Flexibility, Unsteady Aerodynamics, and Variable Inflow on Helicopter Rotor Stall Characteristics," *Journal of the American Helicopter Society*, Vol. 17, (3), July 1972, pp. 35-44.

Bousman, W. G., "A Qualitative Examination of Dynamic Stall from Flight Test Data," *Journal of the American Helicopter Society*, Vol. 43, (4), October 1998, pp. 279-295.

Bousman, W. G., "Evaluation of Airfoil Dynamic Stall Characteristics for Maneuverability," *Journal of the American Helicopter Society*, Vol. 46, (4), October 2001, pp. 239-250.

Bowles, P.O., and Corke, T.C., "Stall Detection on a Leading-edge Plasma Actuated Pitching Airfoil Utilizing Onboard Measurement," AIAA Paper No. 2009-0093, 47th AIAA Aerospace Sciences Meeting Including The New Horizons Forum and Aerospace Exposition, Orlando, FL, January 6-8, 2009.

Carr, L., and Chandrasekhara, M., "Design & Development of a Compressible Dynamic Stall Facility," AIAA Paper No. 89-0647, 27th Aerospace Sciences Meeting, Reno, NV, January 9-12, 1989.

Carr, L.W., and Chandrasekhara, M.S., "Design and Development of a Compressible Dynamic Stall Facility," *Journal of Aircraft*, Vol. 29, (3), May-June 1992, pp. 314-318.

Carr, L.W., and Brock, N.J., "Quantitative Study of Unsteady Compressible flow on an Oscillating Airfoil," *Journal of Aircraft*, Vol. 31, (4), July-August 1994, pp. 892-898.

Chandar, D.D.J, and Damodaran, M., "Computation of Unsteady Low Reynolds Number Free-flight Aerodynamics of Flapping Wings," *Journal of Aircraft*, Vol. 47, (1), January-February 2010, pp. 141-150.

Chandrasekhara, M.S., Carr, L.W., and Wilder, M.C., "Interferometric Investigations of Compressible Dynamic Stall over a Transiently Pitching Airfoil," *AIAA Journal*, Vol. 32, (3), March 1994, pp. 586-593.

Chandrasekhara, M.S., Wilder, M.C., and Carr, L.W., "Boundary Layer Tripping Studies of Compressible Dynamic Stall Flow," AIAA Paper No. 94-2340, 25th AIAA Fluid Dynamics Conference, Colorado Springs, CO, June 20-23, 1994.

Chandrasekhara, M.S., Wilder, M.C., and Carr, L.W., "Boundary-layer-tripping Studies of Compressible Dynamic Stall Flow," *AIAA Journal*, Vol. 34, (1), January 1996, pp. 96-103.

Chandrasekhara, M.S., Wilder, M.C., and Carr, L.W., "Reynolds Number Influence on 2-D Compressible Dynamic Stall," AIAA Paper No. 96-0073, AIAA 34th Aerospace Sciences Meeting and Exhibit, Reno, NV, January 15-18, 1996.

Chandrasekhara, M.S., Wilder, M.C., and Carr, L.W., "On the Competing Mechanisms of Compressible Dynamic Stall," AIAA Paper No. 96-1953, AIAA 27th Fluid Dynamics Conference, New Orleans, LA, June 17-20, 1996.

Chandrasekhara, M. S., Martin, P. B., and Tung, C., " Compressible Dynamic Stall Performance of a Variable Droop Leading Edge Airfoil with a Gurney Flap," *Journal of the American Helicopter Society*, Vol. 53, (1), January 2008, pp. 18-25.

Choudhuri, P.G., and Knight, D.D., "Effects of Compressibility, Pitch Rate, and Reynolds Number on Unsteady Incipient Leading-edge Boundary Layer Separation Over a Pitching Airfoil," *Journal of Fluid Mechanics*, Vol. 308, 1996, pp. 195-217.

Clark, B.M., Bain, J.J., Sankar, L.N., and Prasad, J.V.R., "Modeling Dynamic Stall of the SC-1095 Airfoil at High Mach Number," AIAA Paper No. 2010-877, 48th AIAA Aerospace Sciences Meeting Including The New Horizons Forum and Aerospace Exposition, Orlando, FL, January 4-7, 2010.

Collicott, S.H., "Transition from Particle Image Velocimetry to Laser Speckle Velocimetry with Increasing Density," *Laser Techniques and Applications in Fluid Mechanics*, edited by R.J. Adrian, D.F.G. Durão, F. Durst, M.V. Heitor, M. Maeda, and J.H. Whitelaw, Springer-Verlag, Berlin, 1993, pp. 181-194.

Cukurel, B., "Intentionally Triggered Dynamic Stall for Cascade Lift Enhancement," AIAA Paper No. 2007-163, 45th AIAA Aerospace Sciences Meeting and Exhibit, Reno, NV, January 8-11, 2007.

Depailler, G., and Friedmann, P.P., "Reduction of Vibrations Due to Dynamic Stall in Helicopters Using an Actively Controlled Flap," AIAA Paper No. 2002-1431, 43rd AIAA/ASME/ASCE/AHS/ASC Structures, Structural Dynamics, and Materials Con, Denver, CO, April 22-25, 2002.

Dindar, M., and Kaynak, Ü., "Effect of Turbulence Modeling on Dynamic Stall of a NACA 0012 Airfoil," AIAA Paper No. 92-0027, 30th Aerospace Sciences Meeting & Exhibit, Reno, NV, January 6-9, 1992.

Dindar, M., Kaynak, Ü., and Fujii, K., "Nonequilibrium Turbulence Modeling Study on Light Dynamic Stall of a NACA0012 Airfoil," *Journal of Aircraft*, Vol. 30, (3), May-June 1993, pp. 304-308.

dPIV, 32-bit PIV Analysis Code, Software Package, Ver. 2.1, Innovative Scientific Solutions Inc., Dayton, OH, 2005.

Ekoto, I.W., Bowersox, R.D.W., Beutner, T., and Goss, L., "Response of Supersonic Turbulent Boundary Layers to Local and Global Mechanical Distortions," *Journal of Fluid Mechanics*, Vol. 630, 2009, pp. 225-265.

Erickson, G.E., "High Angle-of-Attack Aerodynamics," *Annual Review of Fluid Mechanics*, Vol. 27, 1995, pp. 45-88.

Ericsson, L.E., "Problem of Dynamic Stall Simulation Revisited," *Journal of Aircraft*, Vol. 31, (4), July-August 1994, pp. 782-786.

Francis, M. S., and Keesee, J. E., "Airfoil Dynamic Stall Performance with Large-amplitude Motions," *AIAA Journal*, Vol. 23, (11), November 1985, pp. 1653-1659.

Fung, K.-Y., and Carr, L.W., "The Effects of Compressibility on Dynamic Stall," AIAA Paper No., 88-3541-CP, 1988.

Gangwani, S. T., "Prediction of Dynamic Stall and Unsteady Airloads for Rotor Blades," *Journal of the American Helicopter Society*, Vol. 27, (4), October 1982, pp. 57-64.

Geissler, W., and Sobieczky, H., "Unsteady Flow Control on Rotor Airfoils," AIAA Paper No. 95-1890-CP, 1995.

Ghia, K.N., Yang, J., Osswald, G.A., and Ghia, U., "Study of the Dynamic Stall Mechanism Using Simulation of Two-Dimensional Navier-Stokes Equations," AIAA Paper No. 91-0546, 29th Aerospace Sciences Meeting, Reno, NV, January 7-10, 1991.

Ghia, K.N., Yang, J., Osswald, G.A., and Ghia, U., "Study of the Role of Unsteady Separation in the Formation of Dynamic Stall Vortex," AIAA Paper No. 92-0196, 30th Aerospace Sciences Meeting & Exhibit, Reno, NV, January 6-9, 1992.

Grohsmeyer, S.P., Ekaterinaris, J.A., and Platzer, M.F., "Numerical Investigation of the Effect of Leading Edge Geometry on Dynamic Stall of Airfoils," AIAA Paper No. 91-1798, AIAA 22nd Fluid Dynamics, Plasma Dynamics & Lasers Conference, Honolulu, HI, June 24-26, 1991.

Helin, H.E., and Walker, J.M., "Interrelated Effects of Pitch Rate and Pivot Point on Airfoil Dynamic Stall," AIAA Paper No. 85-0130, AIAA 23rd Aerospace Sciences Meeting, Reno, NV, January 14-17, 1985.

Johnson, W., "Recent Developments in Rotary-Wing Aerodynamic Theory," *AIAA Journal*, Vol. 24, (8), August 1986, pp. 1219-1244.

Juliano, T.J., Peng, D., Jensen, C., Gregory, J.W., Liu, T., Montefort, J., Palluconi, S., Crafton, J., and Fonov, S., "PSP Measurements on an Oscillating NACA

0012 Airfoil in Compressible Flow," AIAA Paper No. 2011-3728, 41st AIAA Fluid Dynamics Conference and Exhibit, Honolulu, HI, June 27-30, 2011.

Kerho, M., "Adaptive Airfoil Dynamic Stall Control," AIAA Paper No. 2005-1365, 43rd Aerospace Sciences Meeting, 2005.

Ko, S., and McCroskey, W.J., "Computations of Unsteady Separating Flows Over an Oscillating Airfoil," AIAA Paper No. 95-0312, 33rd Aerospace Sciences Meeting and Exhibit, Reno, NV, January 9-12, 1995.

Lee, T., and Gerontakos, P., "Investigation of flow over an oscillating airfoil," *Journal of Fluid Mechanics*, Vol. 512, 2004, pp. 313-341.

Leishman, J. G., "Modeling Sweep Effects on Dynamic Stall," *Journal of the American Helicopter Society*, Vol. 34, (3), July 1989, pp. 18-29.

Leishman, J. G., and Beddoes, T. S., "A Semi-Empirical Model for Dynamic Stall," *Journal of the American Helicopter Society*, Vol. 34, (3), July 1989, pp. 3-17.

Li, X., and Fleeter, S., "Dynamic Stall Generated Airfoil Oscillations Including Chaotic Responses," AIAA Paper No. 97-1022, 1997.

Liu, L., Friedmann, P. P., Kim, I., and Bernstein, D. S., "Rotor Performance Enhancement and Vibration Reduction in Presence of Dynamic Stall Using Actively Controlled Flaps," *Journal of the American Helicopter Society*, Vol. 53, (4), October 2008, pp. 338-350.

Mai, H., Dietz, G., Geißler, W., Richter, K., Bosbach, J., Richard, H., and deGroot, K., "Dynamic Stall Control by Leading Edge Vortex Generators," *Journal of the American Helicopter Society*, Vol. 53, (1), January 2008, pp. 26-36.

Mai, H., Dietz, G., Geißler, W., Richter, K., Bosbach, J., Richard, H., and deGroot, K., "Errata: Dynamic Stall Control by Leading Edge Vortex Generators," *Journal of the American Helicopter Society*, Vol. 53, (3), July 2008, p. 301.

Maresca, C. A., Favier, D. J., and Rebont, J. M., "Unsteady Aerodynamics of an Aerofoil at High Angle of Incidence Performing Various Linear Oscillations in a Uniform Stream," *Journal of the American Helicopter Society*, Vol. 26, (2), April 1981, pp. 40-45.

Marongiu, C., and Tognaccini, R., "Simulation of the Dynamic Stall at Low Reynolds Number," AIAA Paper No. 2010-513, 48th AIAA Aerospace Sciences Meeting Including The New Horizons Forum and Aerospace Exposition, Orlando, FL, January 4-7, 2010.

Martin, P.B., Wilson, J.S., Berry, J.D., Wong, T.-C., Moulton, M., and McVeigh, M.A., "Passive Control of Compressible Dynamic Stall," AIAA Paper No. 2008-7506, 26th AIAA Applied Aerodynamics Conference, Honolulu, HI, August 18-21, 2008.

McCroskey, W.J., "Unsteady Airfoils," *Annual Review of Fluid Mechanics*, Vol. 14, 1982, pp. 285-311.

McCroskey, W.J., and Pucci, S.L., "Viscous-inviscid Interaction on Oscillating Airfoils," AIAA Paper No. 81-0051, AIAA 19th Aerospace Sciences Meeting, St. Louis, MO, January 12-15, 1981.

Mulleners, K., Henning, A., Mai, H., Raffel, M., Le Pape, A., and Costes, M., "Investigation of the Unsteady Flow Development over a Pitching Airfoil by Means of

TR-PIV," AIAA Paper No. 2009-3504, 27th AIAA Applied Aerodynamics Conference, San Antonio, TX, June 22-25, 2009.

Paganotto, C., Favier, D., Maresca, C., Berton, E., and Agnès, A., "Airfoil Dynamic Stall Investigation in 3D Unsteady Flow," AIAA Paper No. 96-2513, 14th AIAA Applied Aerodynamics Conference, New Orleans, LA, June 18-20, 1996.

Petot, D., Arnaud, G., Harrison, R., Stevens, J., Dieterich, O., van der Wall, B. G., Young, C., and Széchényi, E., "Stall Effects and Blade Torsion – An Evaluation of Predictive Tools," *Journal of the American Helicopter Society*, Vol. 44, (4), October 1999, pp. 320-331.

Reisenthel, P.H., "Towards a Semi-Analytic Tool For The Prediction Of Dynamic Stall," AIAA Paper No. 94-0537, 32nd Aerospace Sciences Meeting & Exhibit, Reno, NV, January 10-13, 1994.

Reu, T., Ying, S.X., "Hybrid Grid Approach to Study Dynamic Stall," *AIAA Journal*, Vol. 30, (11), November 1992, pp.2670-2676.

Reuster, J.G., and Baeder, J.D., "Leading Edge Deformation for Dynamic Stall Control," AIAA Paper No. 2001-0120, 39th AIAA Aerospace Sciences Meeting & Exhibit, Reno, NV, January 8-11, 2001.

Reuster, J.G., and Baeder, J.D., "Dynamic Stall from Pitching and Plunging Airfoil Motions," AIAA Paper No. 2002-3272, 1st Flow Control Conference, St. Louis, MO, June 24-26, 2002.

Rival, D., and Tropea, C., "Characteristics of Pitching and Plunging Airfoils Under Dynamic-Stall Conditions," *Journal of Aircraft*, Vol. 47, (1), January-February 2010, pp. 80-86.

Sankar, N.L., and Tassa, Y., "Reynolds Number and Compressibiltiy Effects on Dynamic Stall of a NACA 0012 Airfoil," AIAA Paper No. 80-0010, AIAA 18th Aerospace Sciences Meeting, Pasadena, CA, January 14-16, 1980.

Sheng, W., Galbraith, R.A.McD., and Coton, F.N., "A Modified Dynamic Stall Model for Low Mach Numbers, AIAA Paper No. 2007-626, 45th AIAA Aerospace Sciences Meeting and Exhibit, Reno, NV, January 8-11, 2007.

Shih, C., Lourenco, L.M., and Krothapalli, A., "Investigation of Flow at Leading and Trailing Edges of Pitching-Up Airfoil," *AIAA Journal*, Vol. 33, (8), August 1995, pp. 1369-1376.

Simpson, R.L., "Turbulent Boundary-layer Separation," *Annual Review of Fluid Mechanics*, Vol. 21, 1989, pp. 205-234.

Sinha, S.K., "Improving the Accuracy and Resolution of Particle Image or Laser Speckle Velocimetry," *Experiments in Fluids*, Vol. 6, 1988, pp. 67-68.

Spentzos, A., Barakos, G., Badcock, K., and Richards, B., "CFD Study of 3-D Dynamic Stall," AIAA Paper No. 2005-1107, 43rd AIAA Aerospace Sciences Meeting and Exhibit, Reno, NV, January 10-13, 2005.

Tuncer, I.H., Walz, R., and Platzer, M.F., "A Computational Study on the Dynamic Stall of a Flapping Airfoil," AIAA Paper No. 98-2519, 1998.

Tyler, J. C., and Leishman, J. G., "Analysis of Pitch and Plunge Effects on Unsteady Airfoil Behavior," *Journal of the American Helicopter Society*, Vol. 37, (3), July 1992, pp. 69-82.

Visbal, M.R., "Effect of Compressibility on Dynamic Stall of a Pitching Airfoil," AIAA Paper No. 88-0132, AIAA 26th Aerospace Sciences Meeting, Reno, NV, January 11-14, 1988.

Visbal, M.R., "Dynamic Stall of a Constant-rate Pitching Airfoil," *Journal of Aircraft*, Vol. 27, (5), May 1990, pp. 400-407.

Visbal, M.R., "On the Formation and Control of the Dynamic Stall Vortex on a Pitching Airfoil," AIAA Paper No. 91-0006, 29th Aerospace Sciences Meeting, Reno, NV, January 7-10, 1991.

Visbal, M.R., "Numerical Investigation of Deep Dynamic Stall of a Plunging Airfoil," AIAA Paper No. 2010-4458, 40th Fluid Dynamics Conference and Exhibit, Chicago, IL, June 28-July 1, 2010.

Wernert, P., Geissler, W., Raffel, M., and Kompenhans, J., "Experimental and Numerical Investigations of Dynamic Stall on a Pitching Airfoil," *AIAA Journal*, Vol. 34, (5), May 1996, pp. 982-989.

Wilby, P. G., "The Development of Rotor Airfoil Testing in the UK," *Journal of the American Helicopter Society*, Vol. 46, (3), July 2001, pp. 210-220.

Wu, J.C., Wang, C.M., and Tuncer, I.H., "Unsteady Aerodynamics of Rapidly Pitched Airfoils," AIAA Paper No. 86-1105, AIAA/ASME 4th Fluid Mechanics, Plasma Dynamics and Lasers Conference, Atlanta, GA, May 12-14, 1986.

Yang, H.Q., "Comparison of Numerical and Experimental Optical Images of Compressible Dynamic Stall," AIAA Paper No. 94-1947-CP, 1994.

Yang, H.Q., and Przekwas, A.J., "Dynamic Stall on a Three-Dimensional Rectangular Wing," AIAA Paper No. 93-0637, 31st Aerosapce Sciences Meeting & Exhibit, Reno, NV, January 11-14, 1993.

APPENDIX A

FIGURES AND TABLES

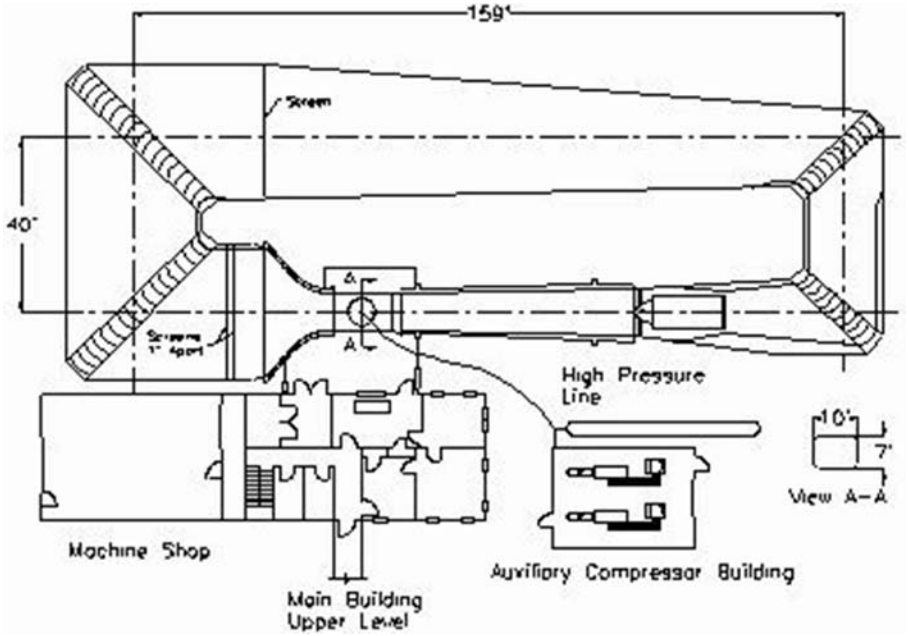

Figure 1. OWN LSWT schematic

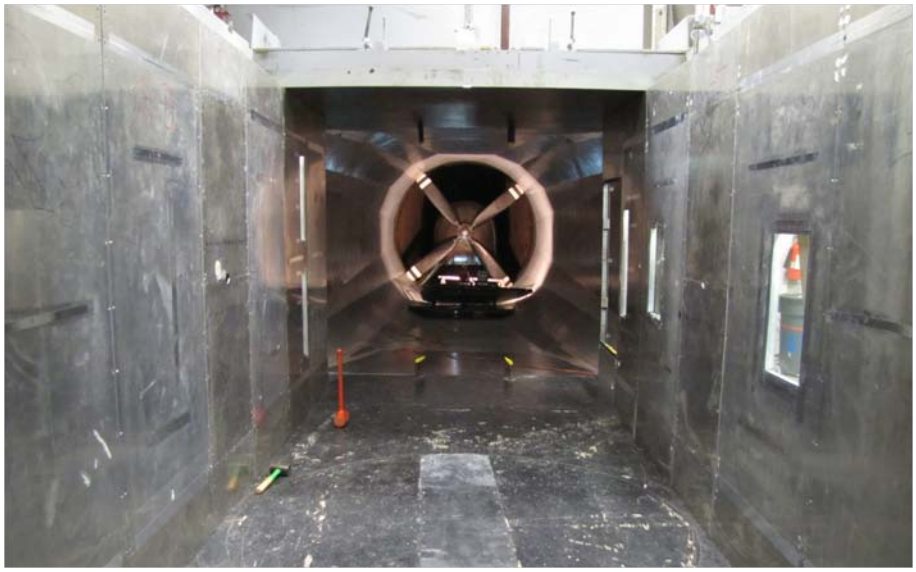

Figure 2. Reduced LSWT test section (7 ft × 7 ft) – looking downstream

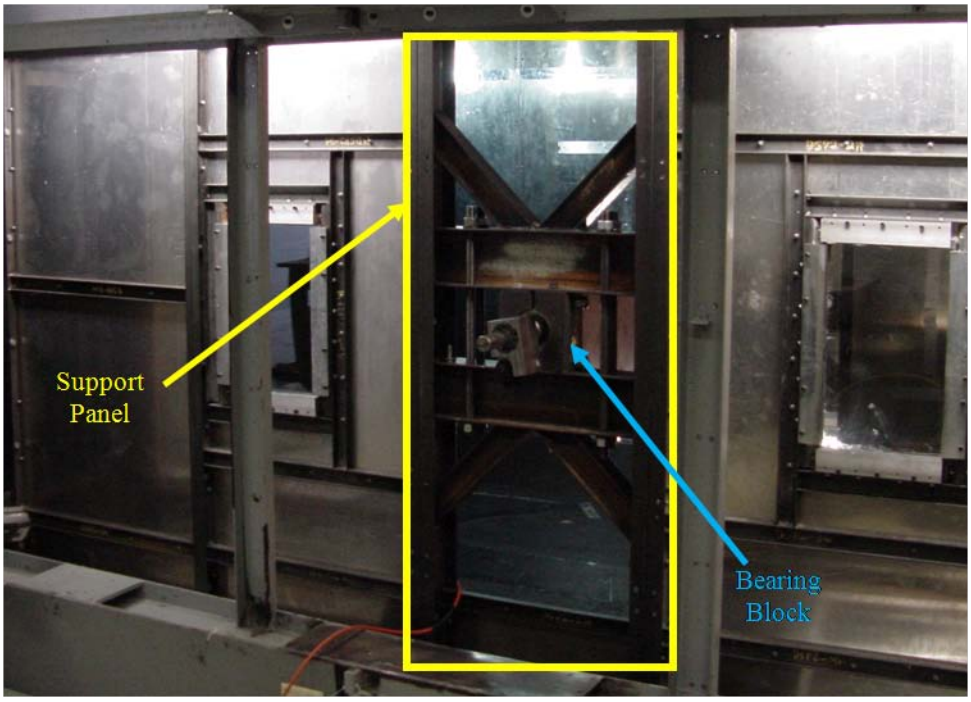

Figure 3. Wing support panel

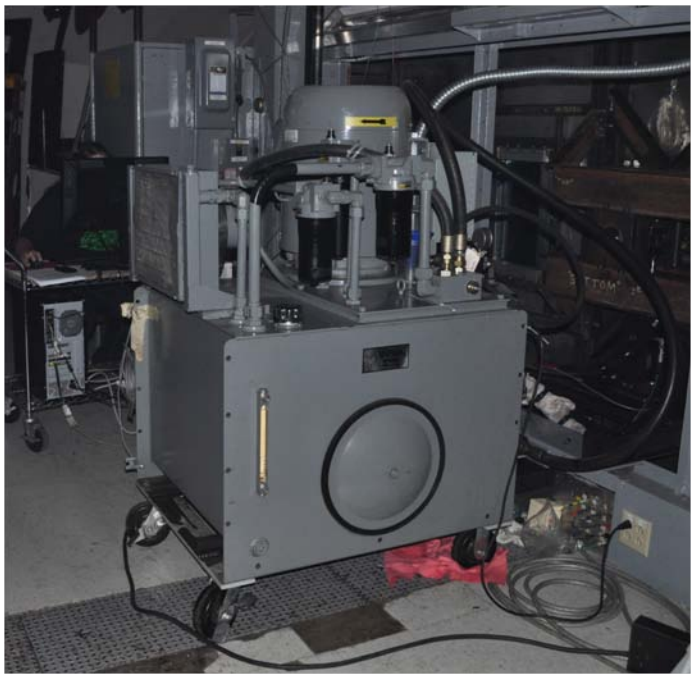

Figure 4. Hydraulic power unit

Figure 5. Linearly actuating hydraulic cylinder

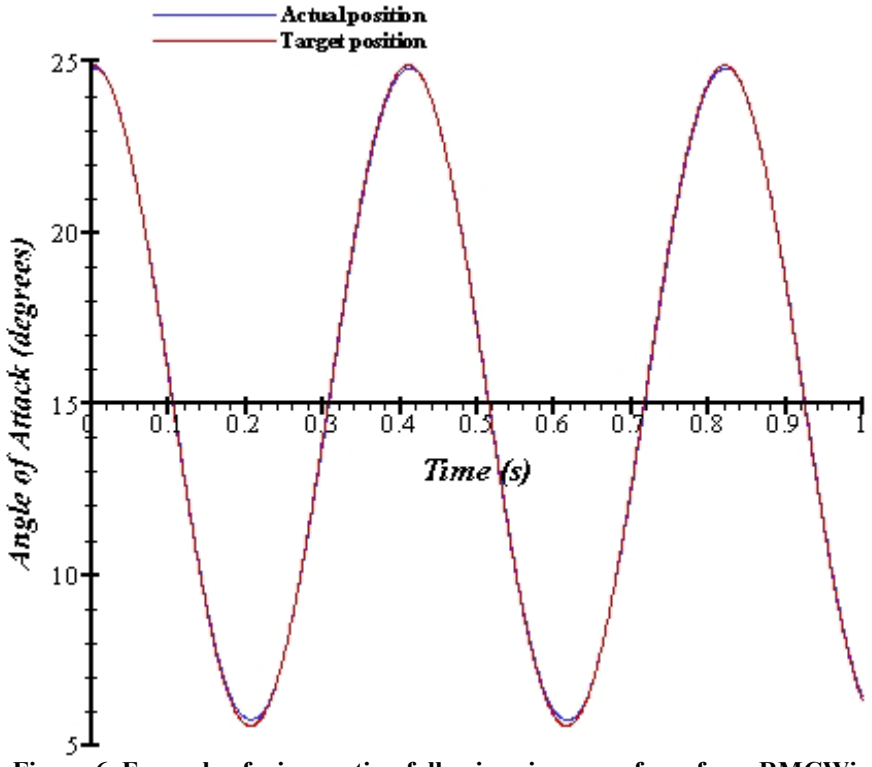

Figure 6. Example of wing motion following sine wave form from RMCWin

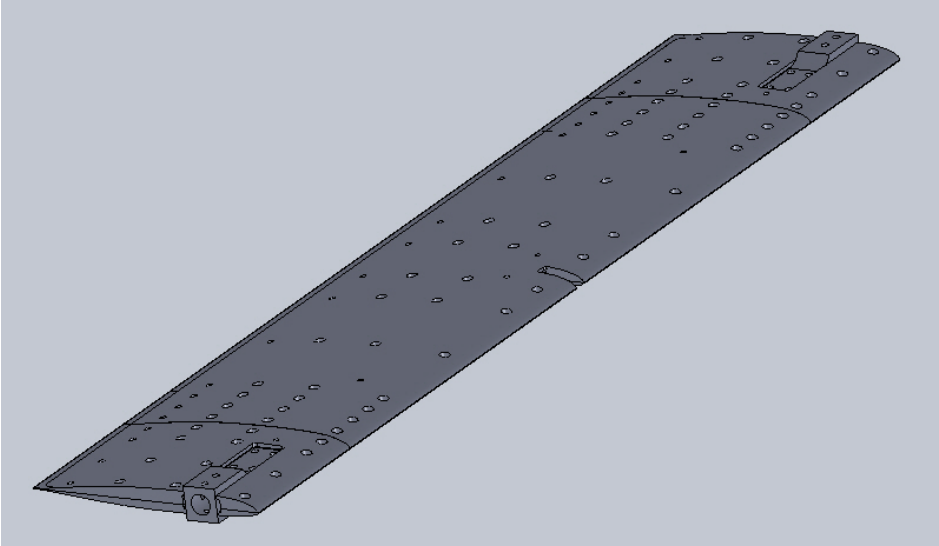

Figure 7. SolidWorks model of SSC-A09 assembly

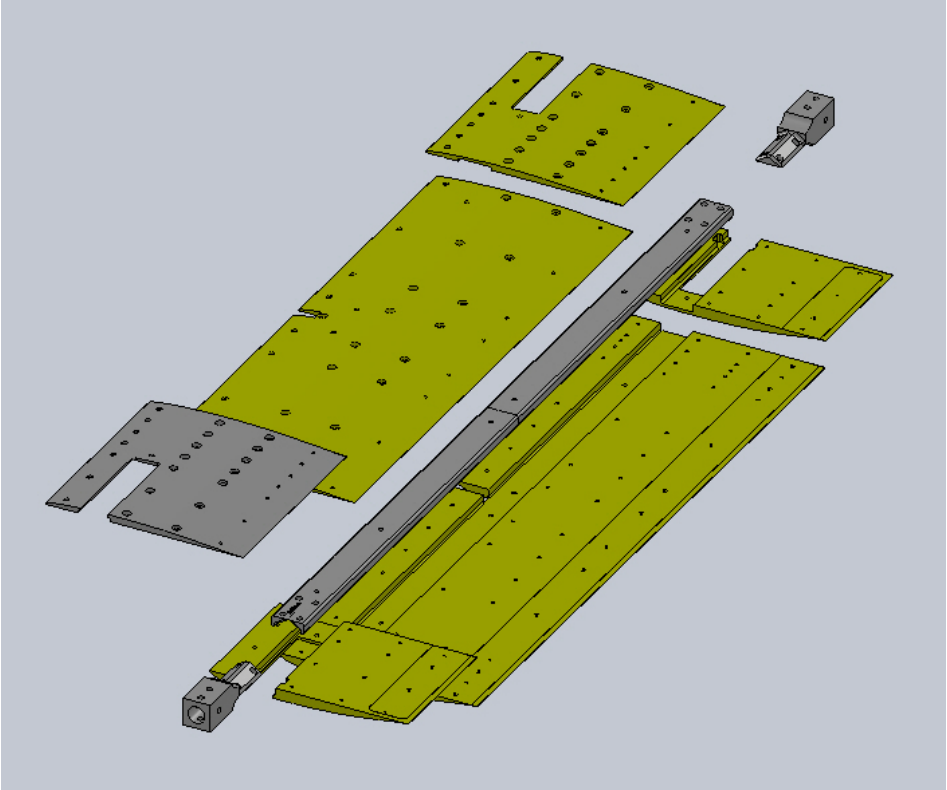

Figure 8. Exploded view of SSC-A09 SolidWorks model (bottom up)

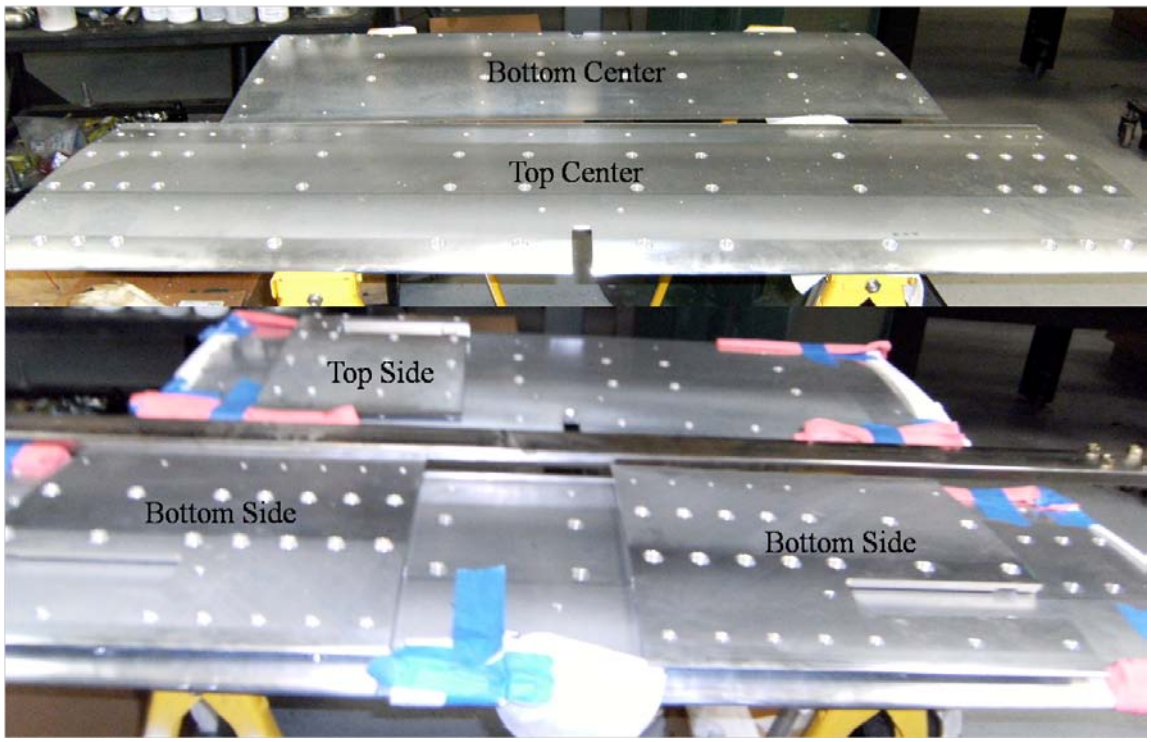

Figure 9. SSC-A09 wing model sections

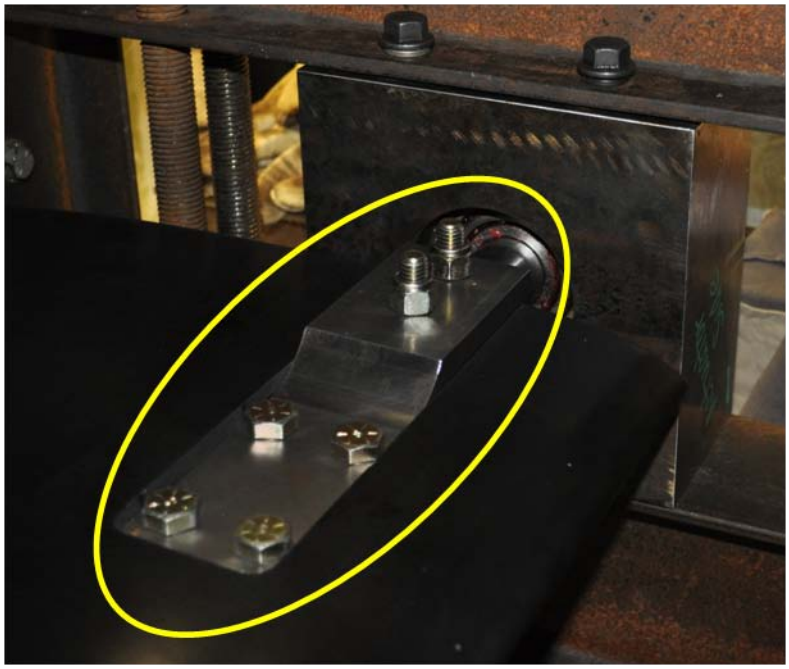

Figure 10. Glove connecting rectangular shaft to circular shaft

Figure 11. Moment arm

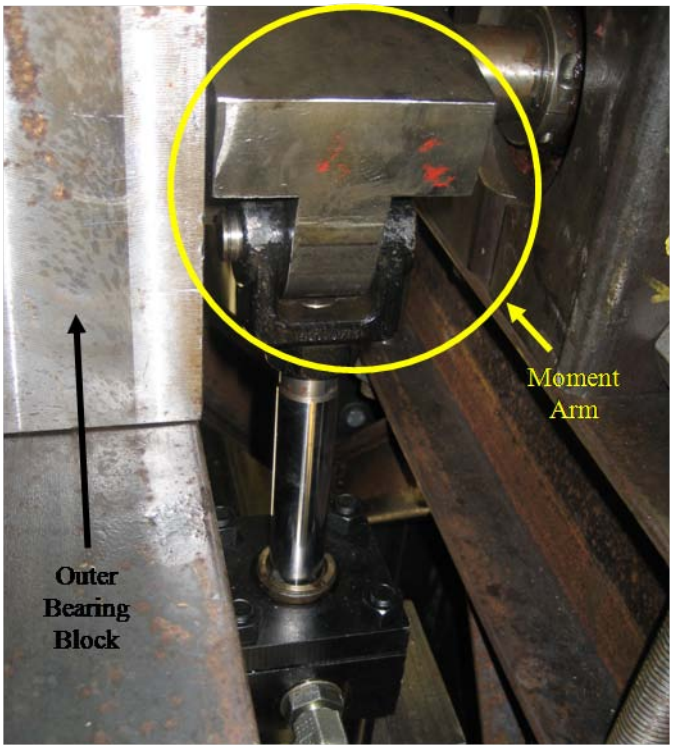

Figure 12. Moment arm attached to linear actuator and cylindrical shaft

Figure 13. SSC-A09 wind tunnel testing model

Figure 14. SSC-A09 model installed in OWN LSWT

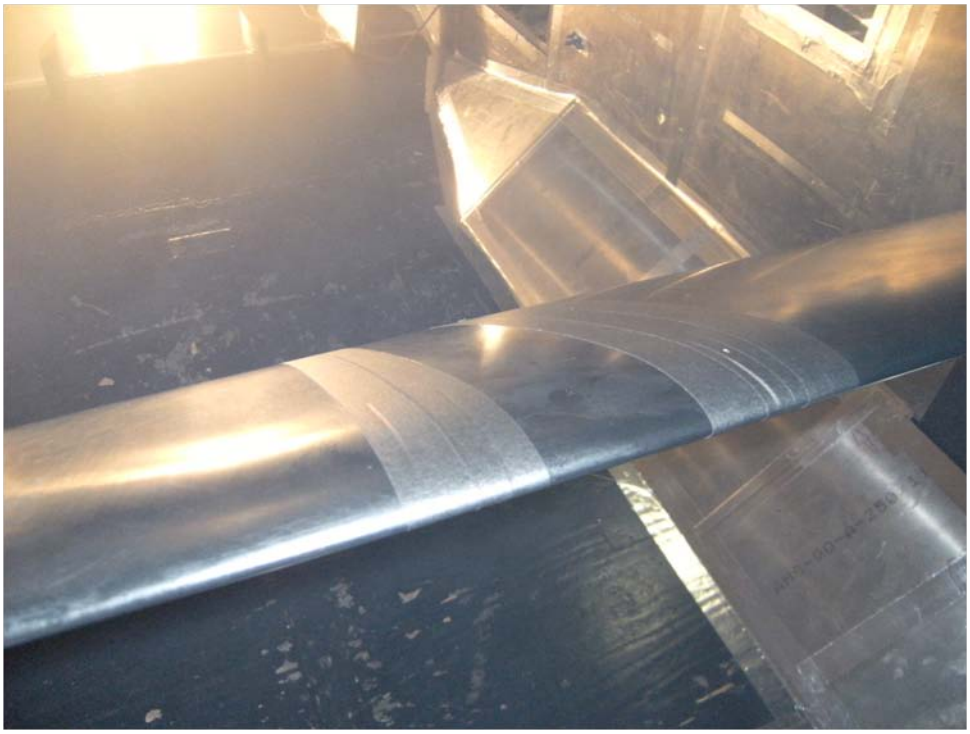

Figure 15. Leading edge view of SSC-A09 wing installed in OWN LSWT

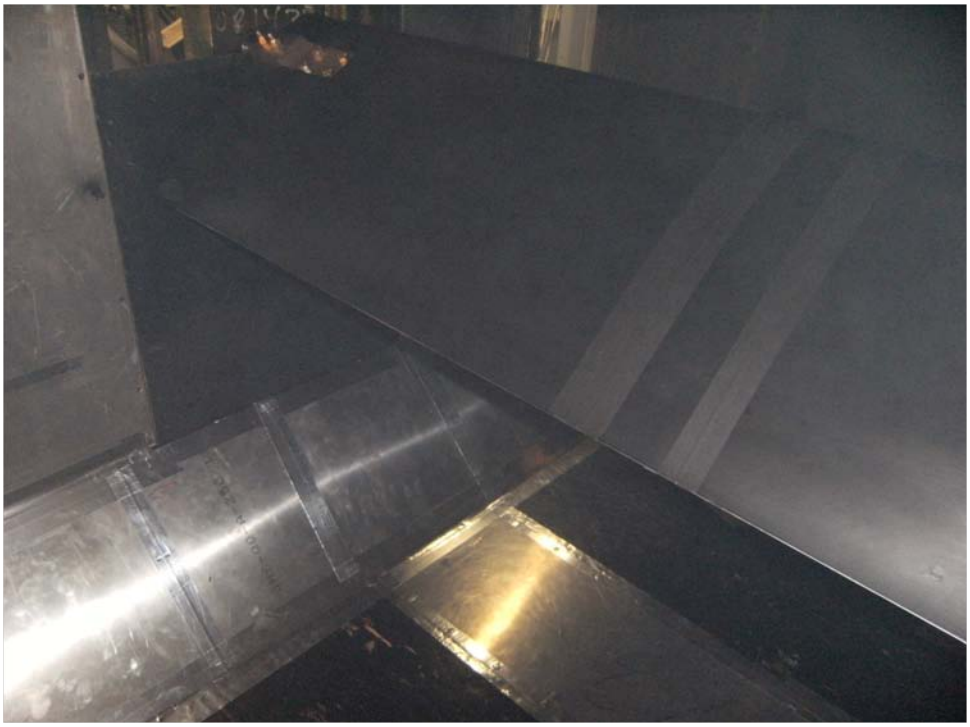

Figure 16. Trailing edge view of SSC-A09 wing installed in OWN LSWT

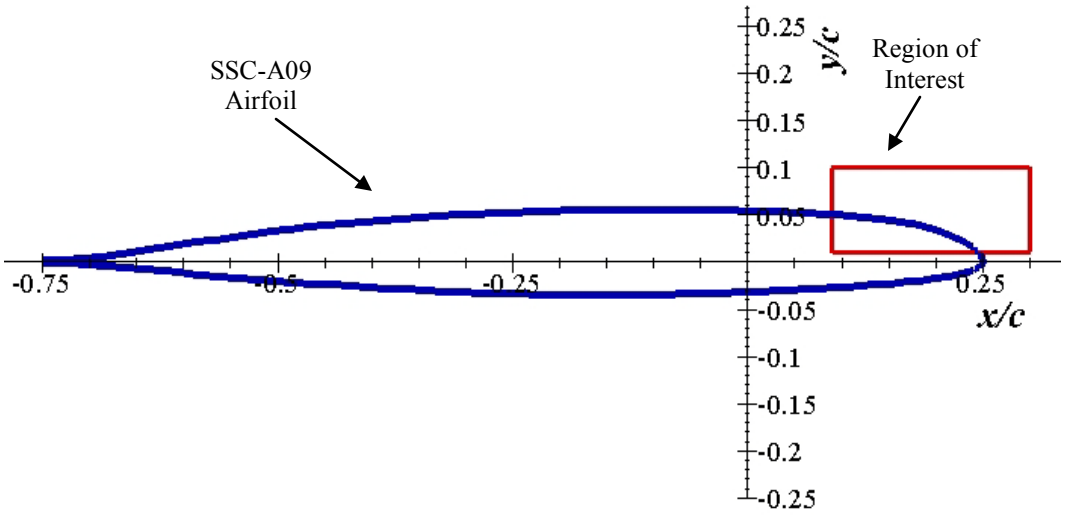

Figure 17. Coordinate frame for non-dimensional SSC-A09 profile and experimental region of interest

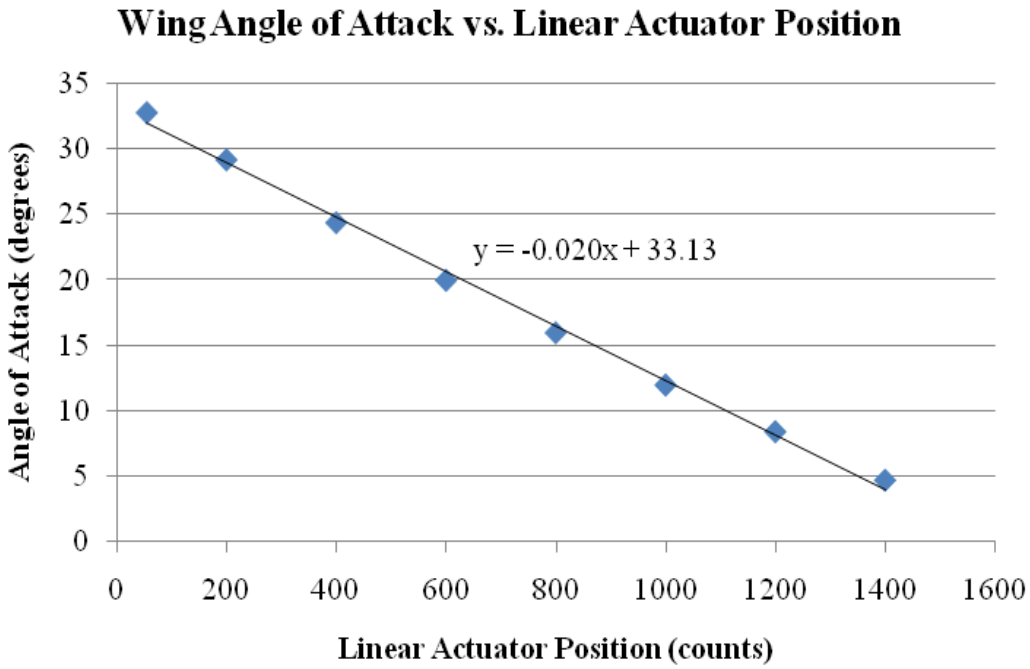

Figure 18. Calibration of wing angle of attack

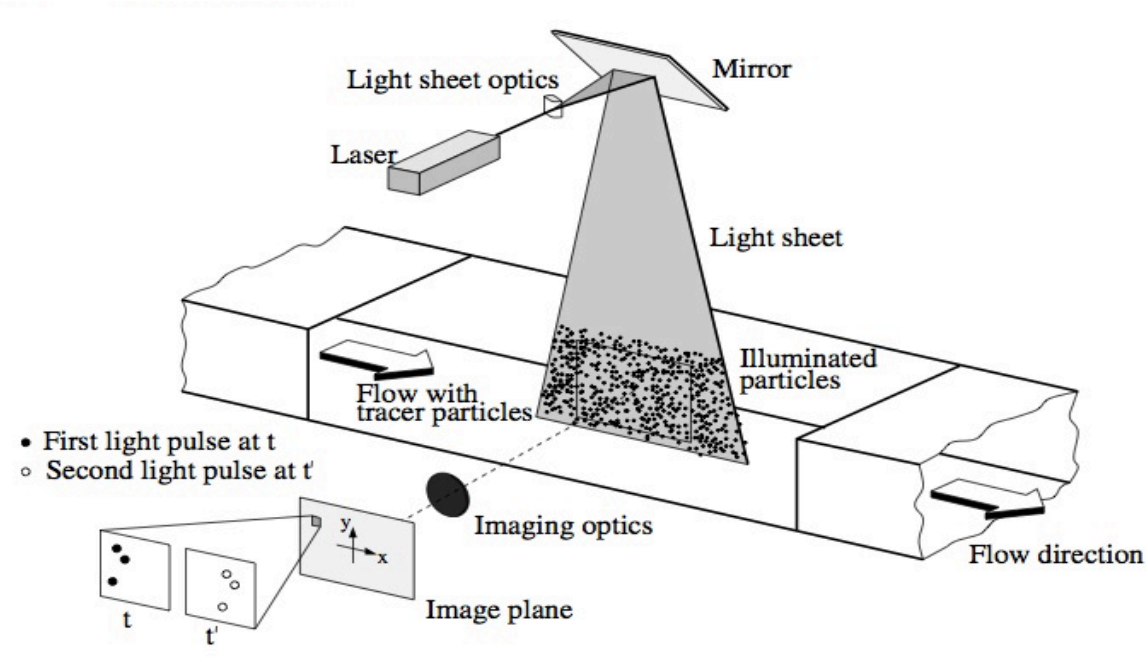

Figure 19. Fundamental experimental setup for PIV in a wind tunnel (Ref. 49)

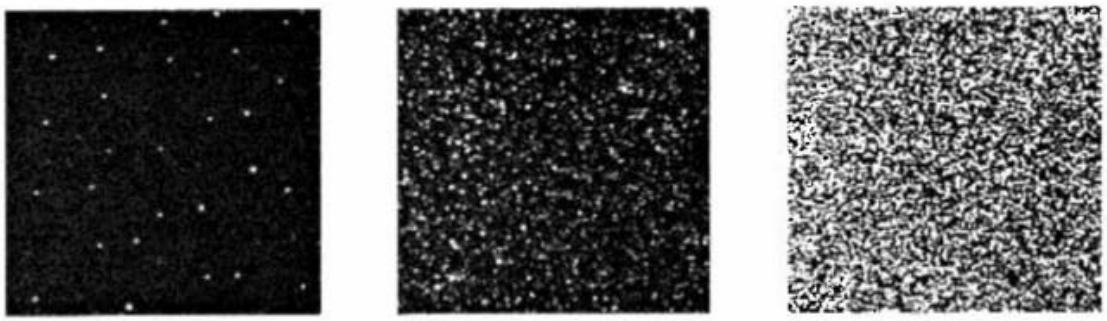

(a) Low density (PTV) **(b) Medium density** **(c) High density (LSV)**

Figure 20. Particle densities for various optical flow analysis methods (Ref. 49)

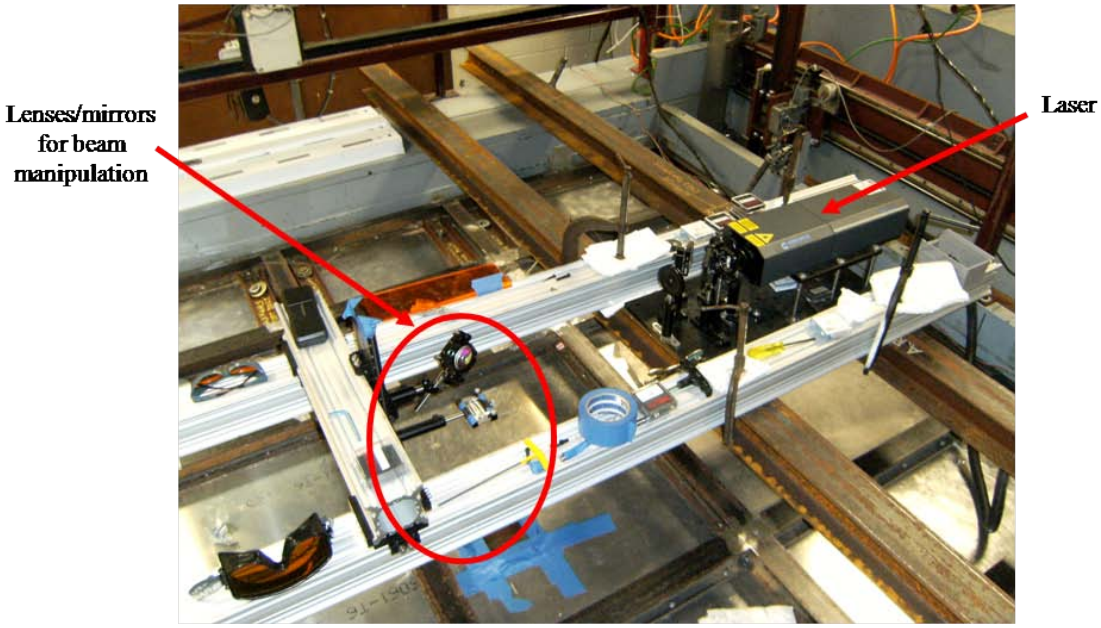

Figure 21. Optical system for PIV testing in the DSF

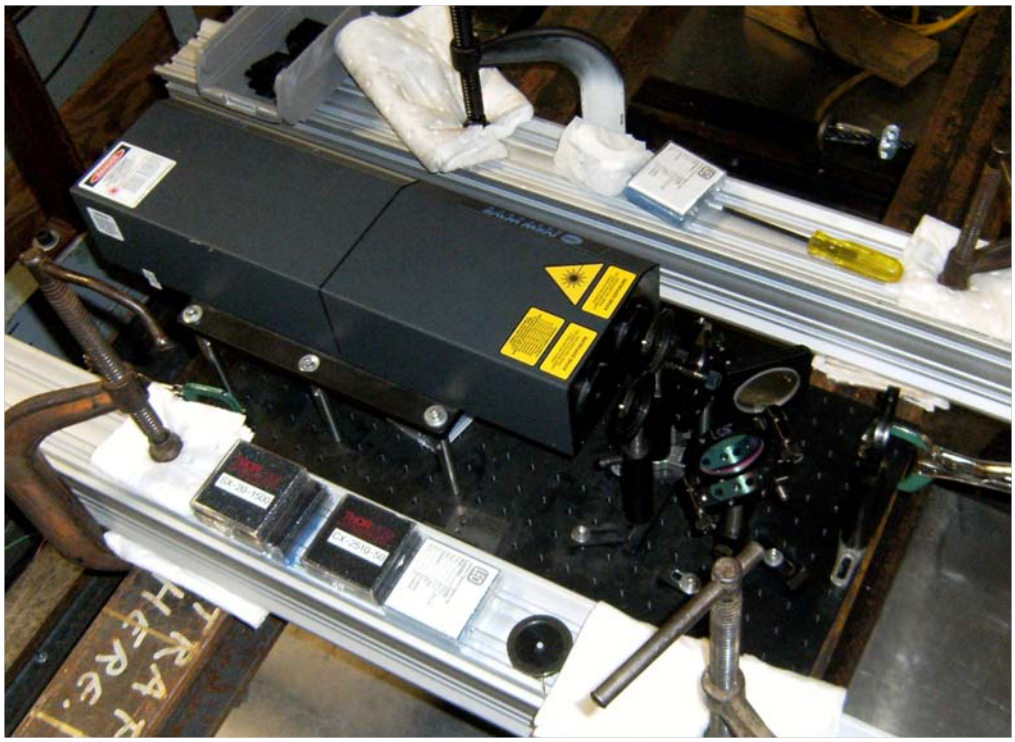

Figure 22. Close-up view of laser and beam overlapping optics

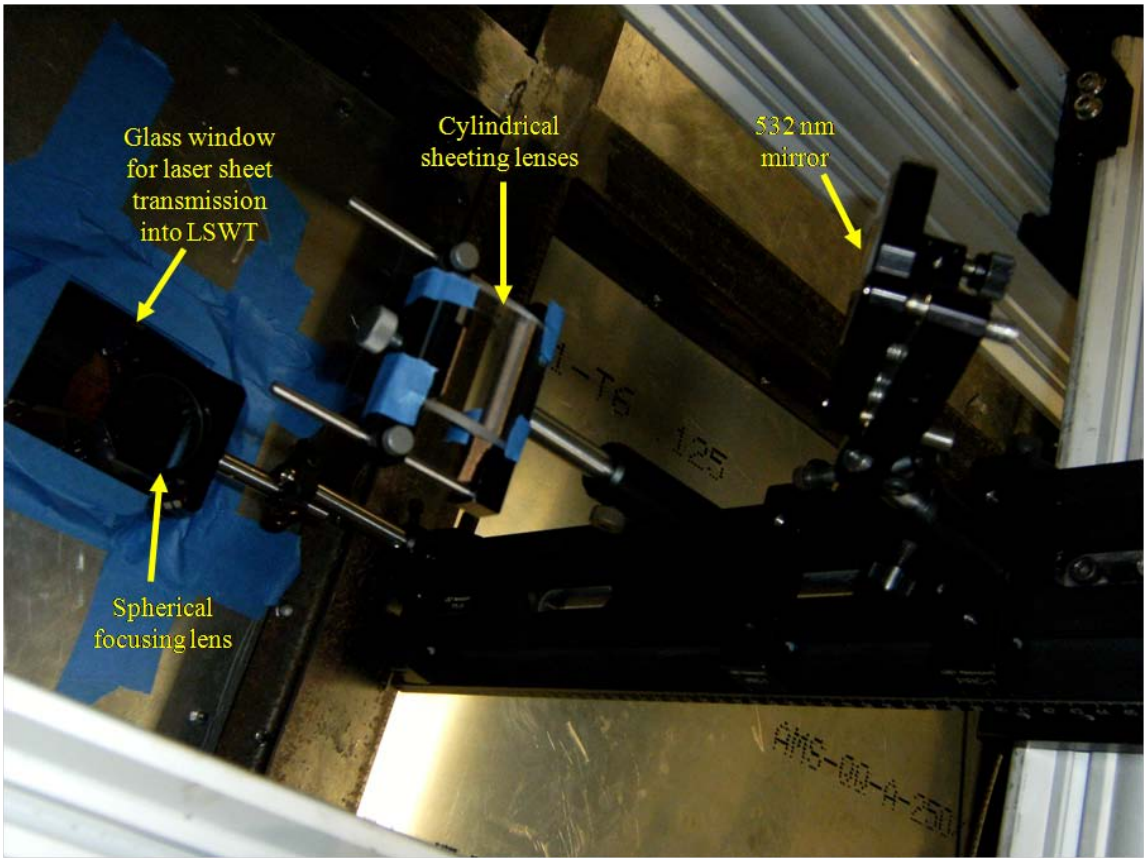

Figure 23. Close-up view of beam bending and sheeting optics

Figure 24. Experimental camera setup

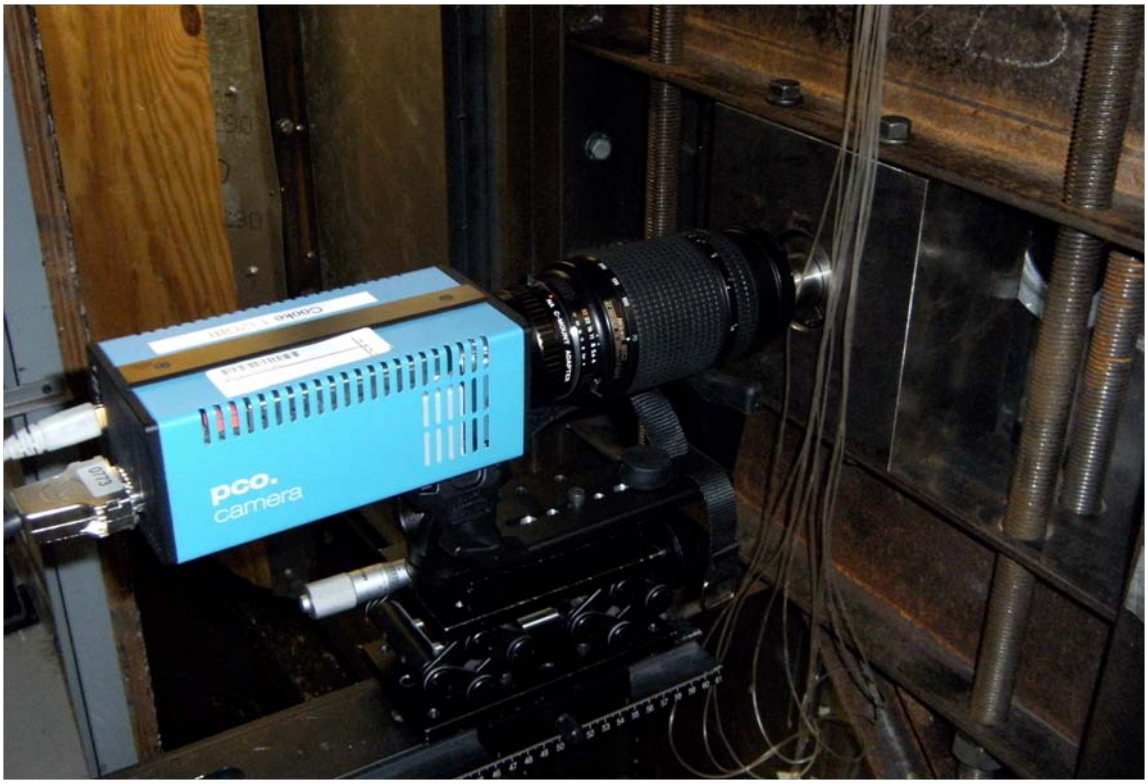

Figure 25. Close-up view of experimental setup for PIV camera

Figure 26. Quantum Composer connected to laser, camera, and motion controller

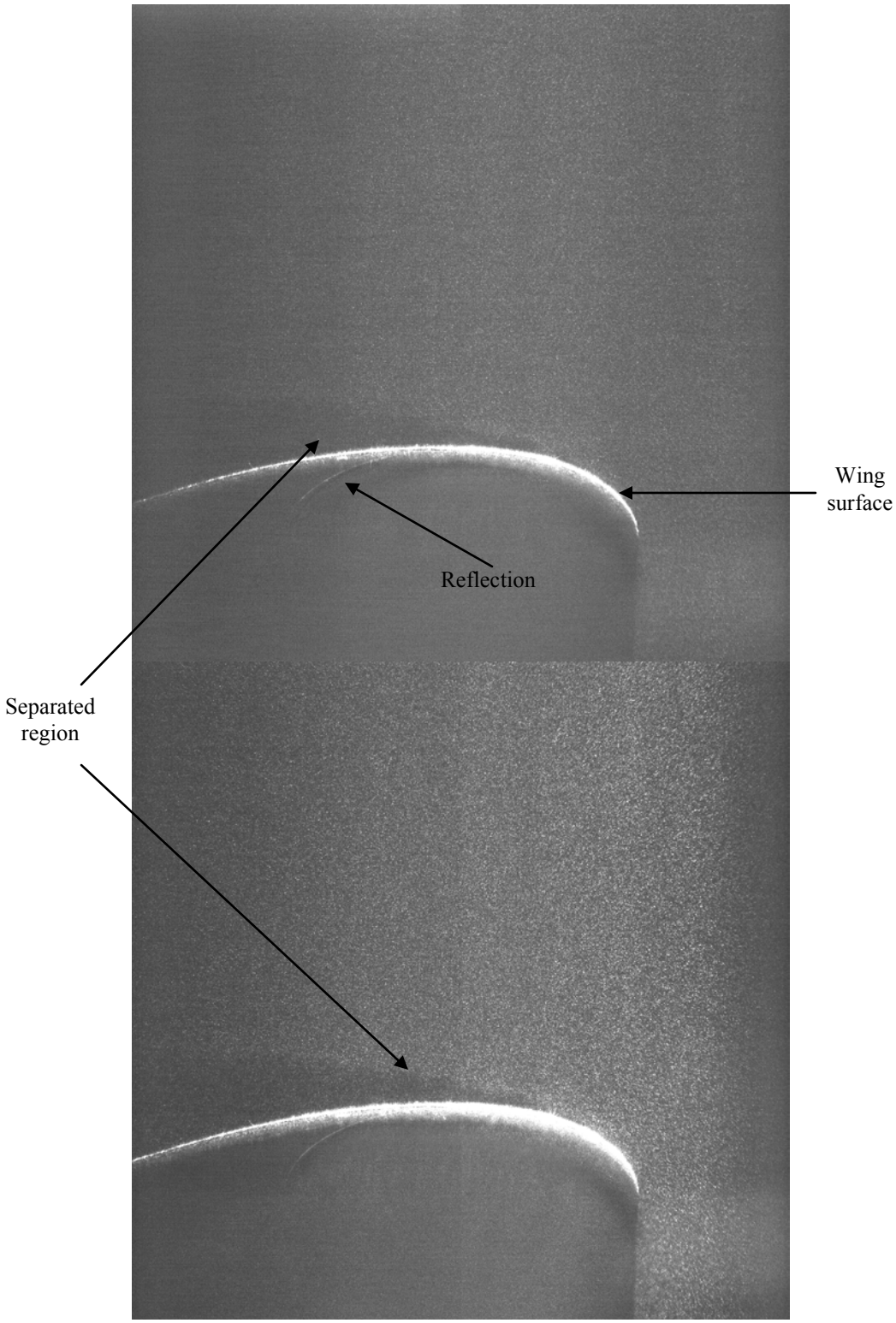

Figure 27. Sample raw PIV image pair for α = 18° upstroke: Image A (top) and Image B (bottom) taken 20 μs apart

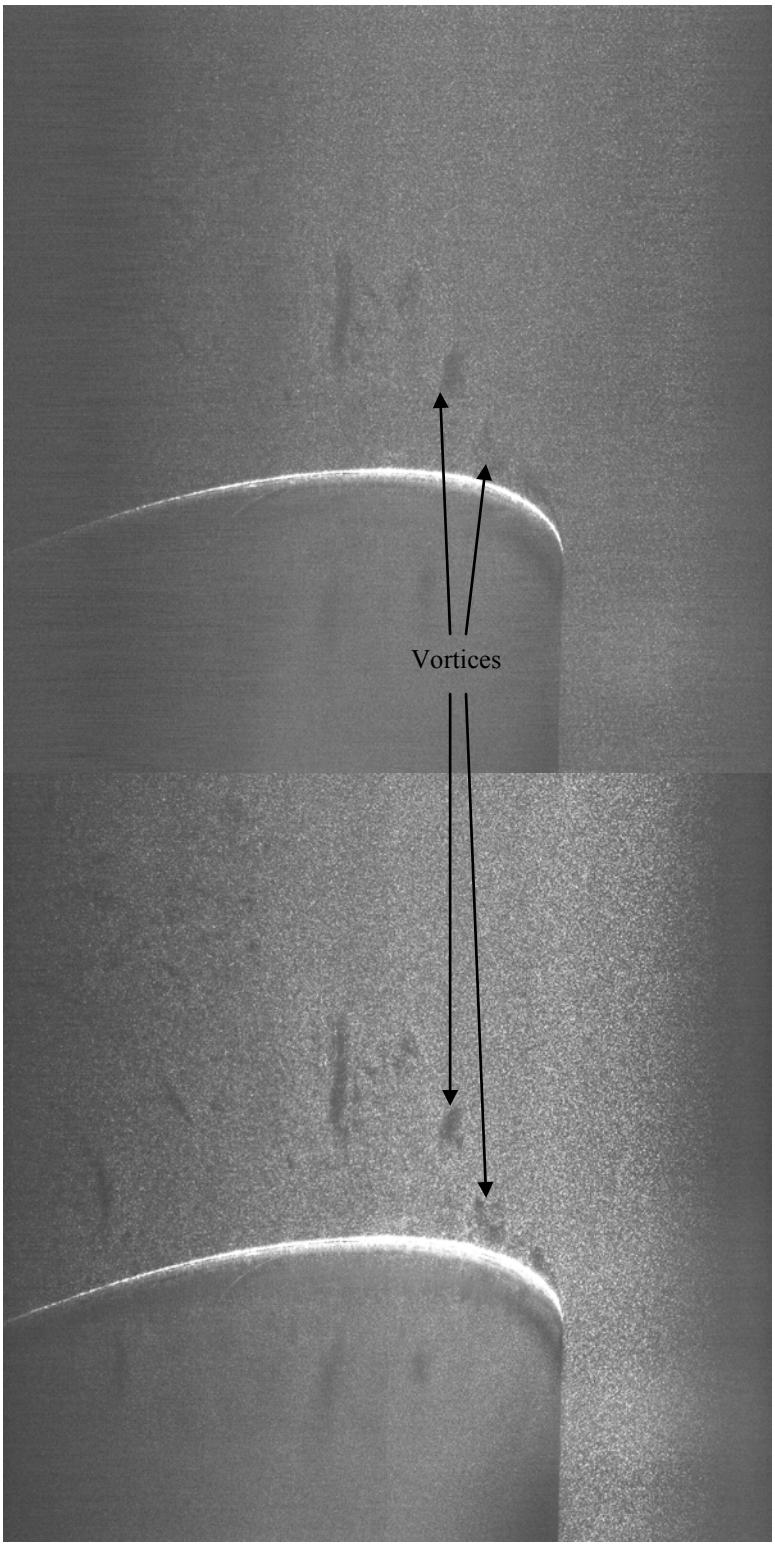

Figure 28. Sample raw PIV image pair for α = 20° upstroke: Image A (top) and Image B (bottom) taken 20 μs apart

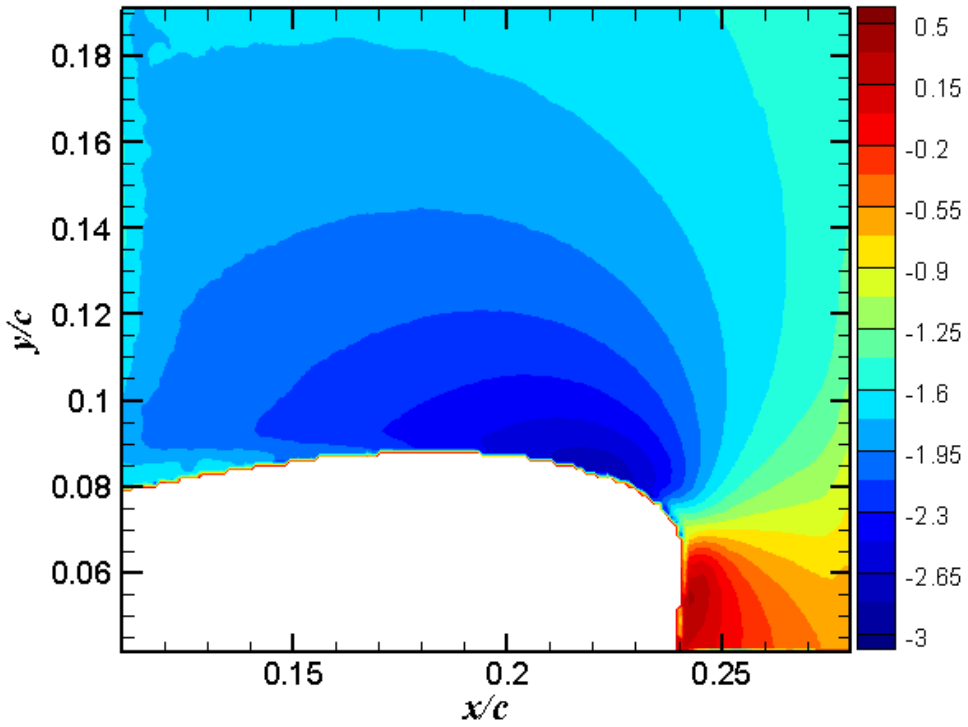

Figure 29. Normalized mean velocity component in the *x*-direction for $\alpha = 16°$, upstroke

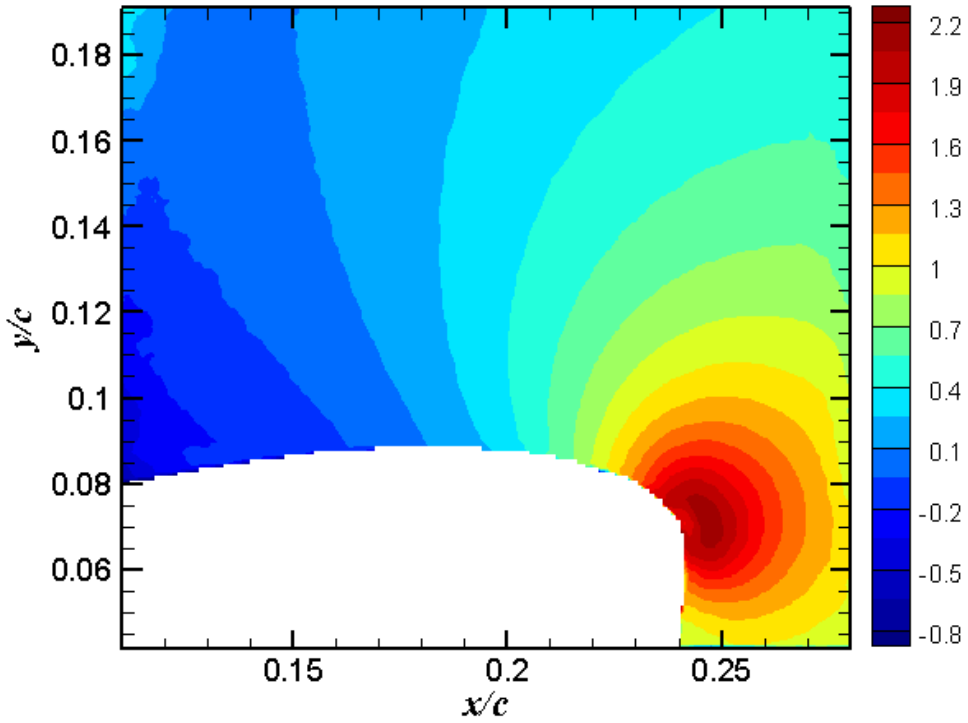

Figure 30. Normalized mean velocity component in the *y*-direction for $\alpha = 16°$, upstroke

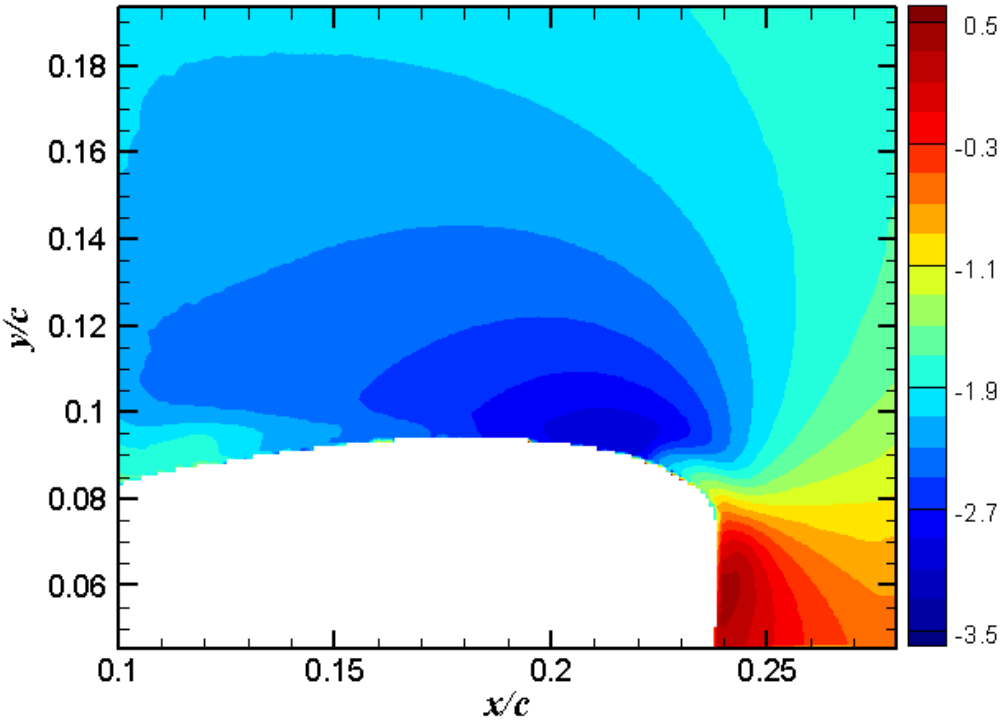

Figure 31. Normalized mean velocity component in the *x*-direction for $\alpha = 18°$, upstroke

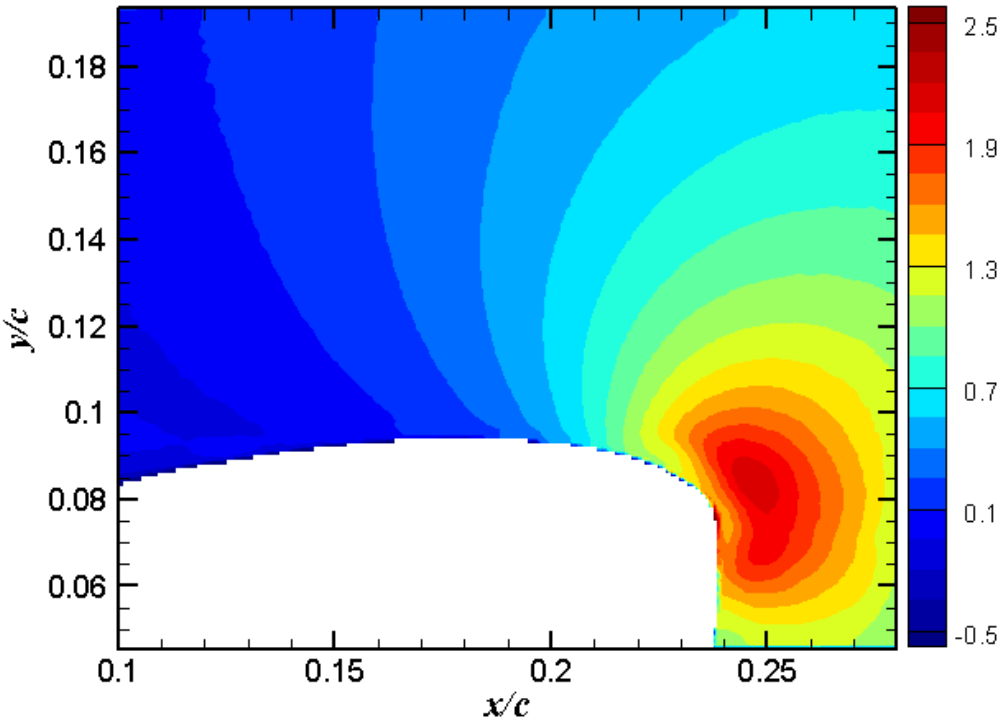

Figure 32. Normalized mean velocity component in the *y*-direction for $\alpha = 18°$, upstroke

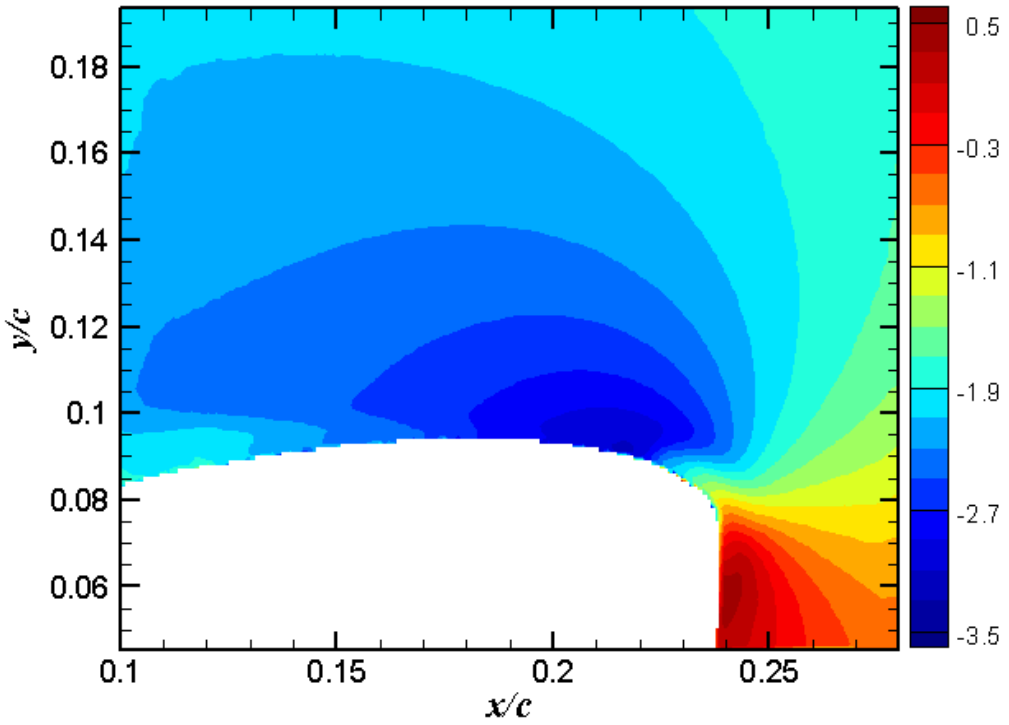

Figure 33. Normalized mean velocity component in the *x*-direction for $\alpha = 18°$, upstroke, fully attached flow

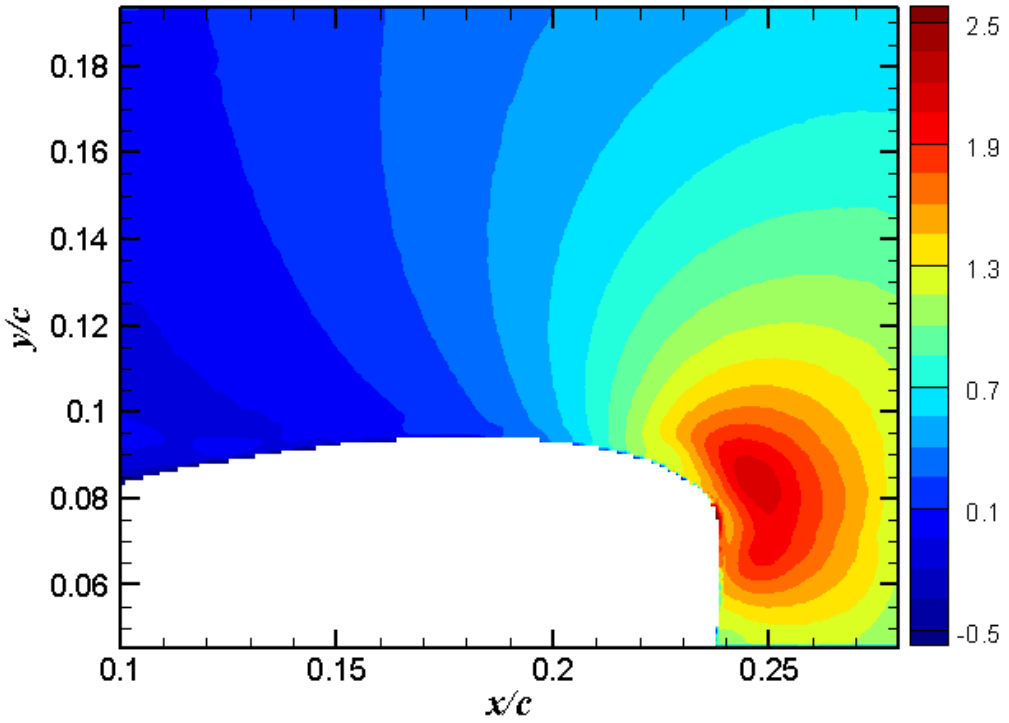

Figure 34. Normalized mean velocity component in the *y*-direction for $\alpha = 18°$, upstroke, fully attached flow

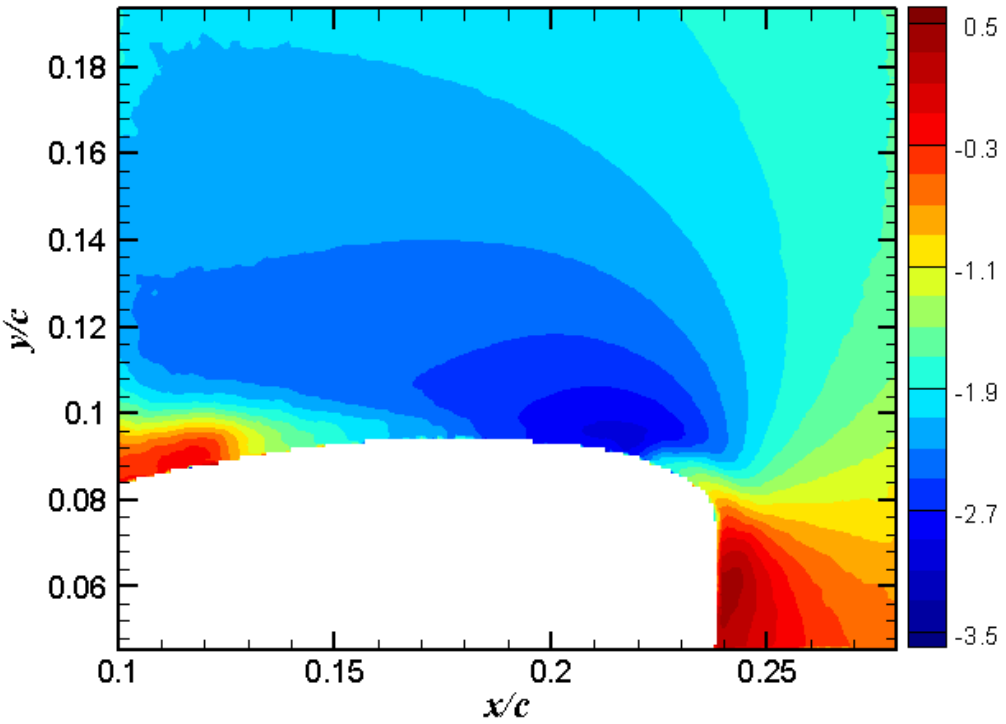

Figure 35. Normalized mean velocity component in the *x*-direction for $\alpha = 18°$, upstroke, partially separated flow

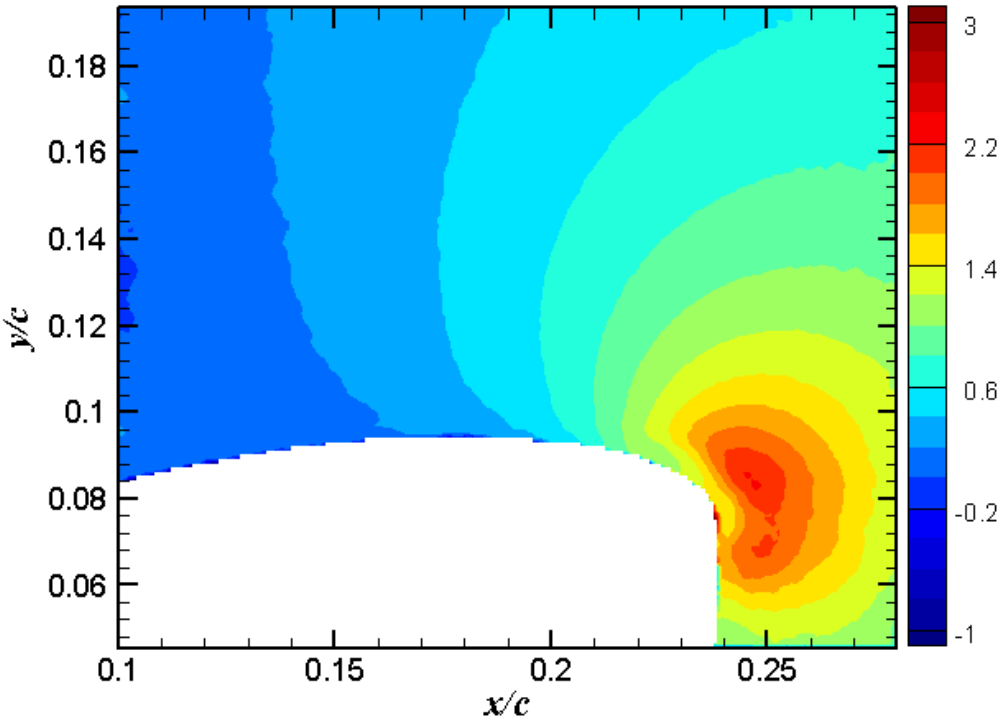

Figure 36. Normalized mean velocity component in the *y*-direction for $\alpha = 18°$, upstroke, partially separated flow

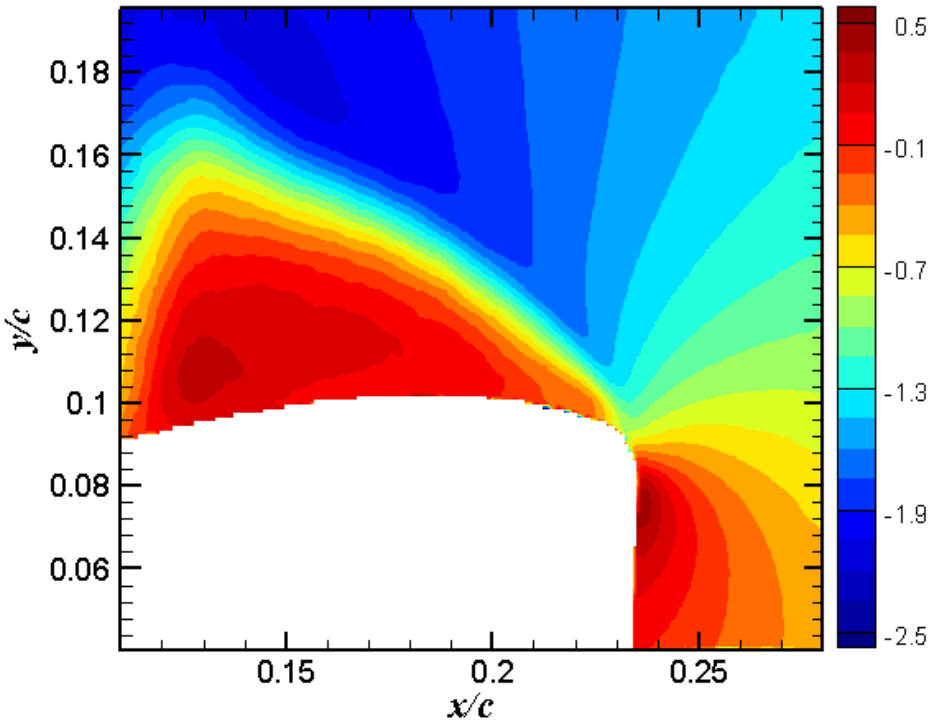

Figure 37. Normalized mean velocity component in the *x*-direction for $\alpha = 20°$, upstroke

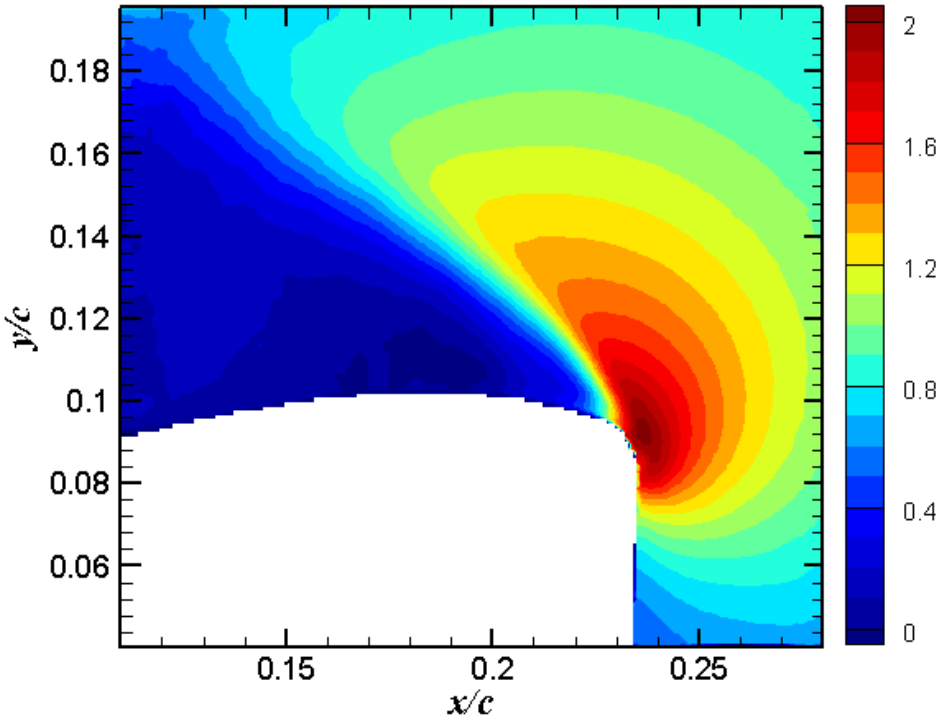

Figure 38. Normalized mean velocity component in the *y*-direction for $\alpha = 20°$, upstroke

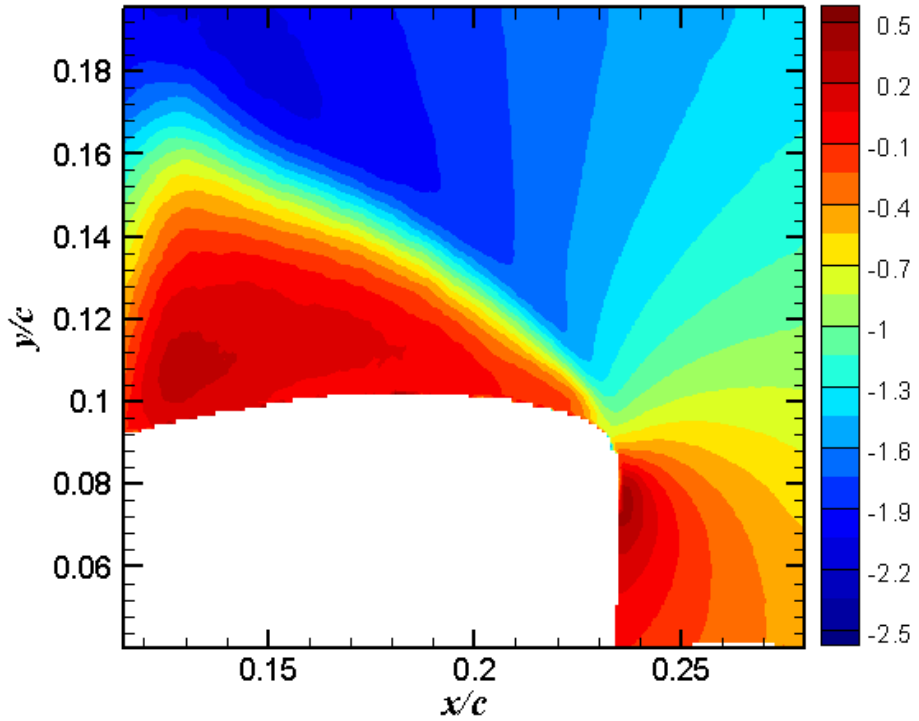

Figure 39. Normalized mean velocity component in the *x*-direction for $\alpha = 20°$, upstroke, fully separated flow

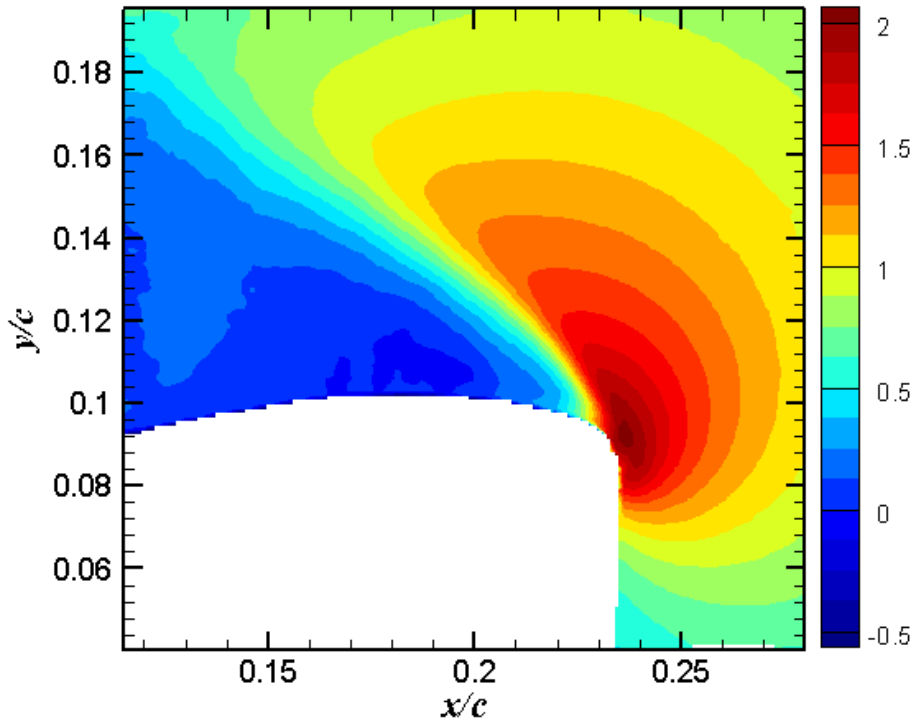

Figure 40. Normalized mean velocity component in the *y*-direction for $\alpha = 20°$, upstroke, fully separated flow

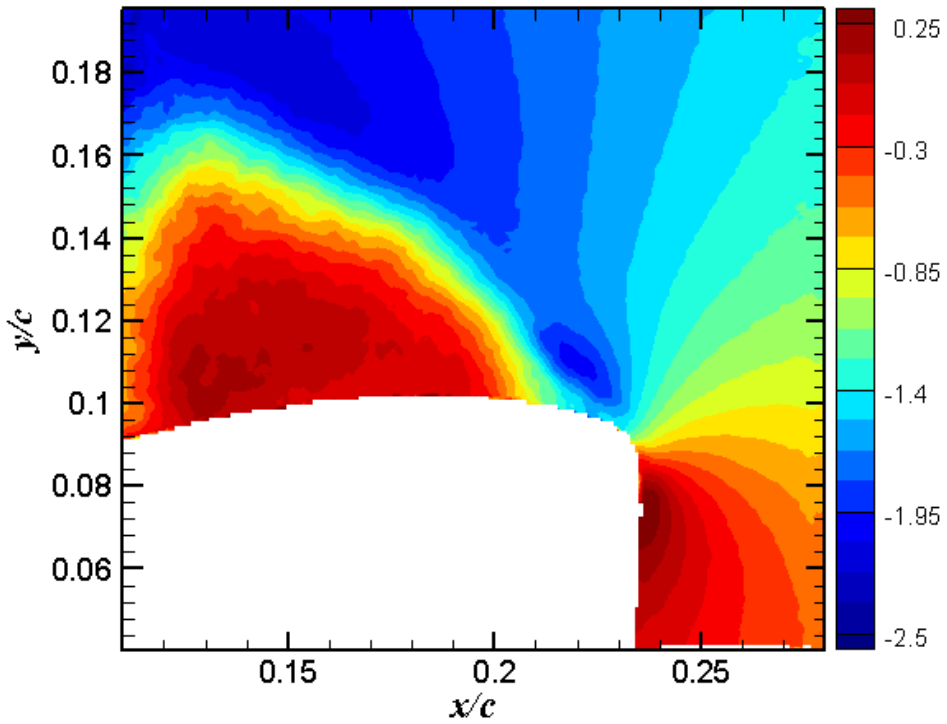

Figure 41. Normalized mean velocity component in the *x*-direction for $\alpha = 20°$, upstroke, partially attached flow

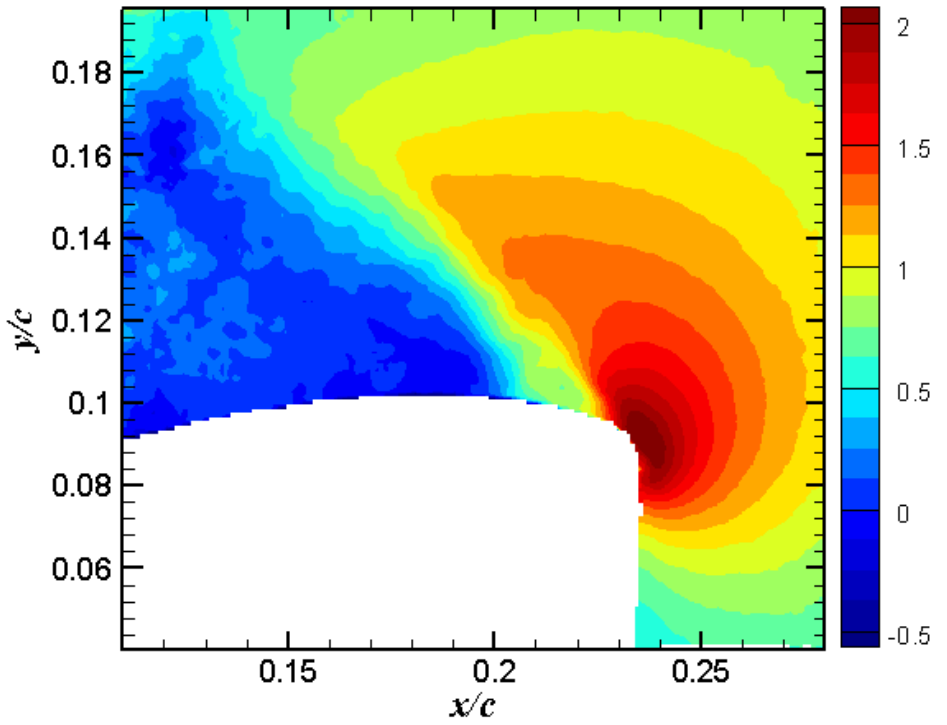

Figure 42. Normalized mean velocity component in the *y*-direction for $\alpha = 20°$, upstroke, partially attached flow

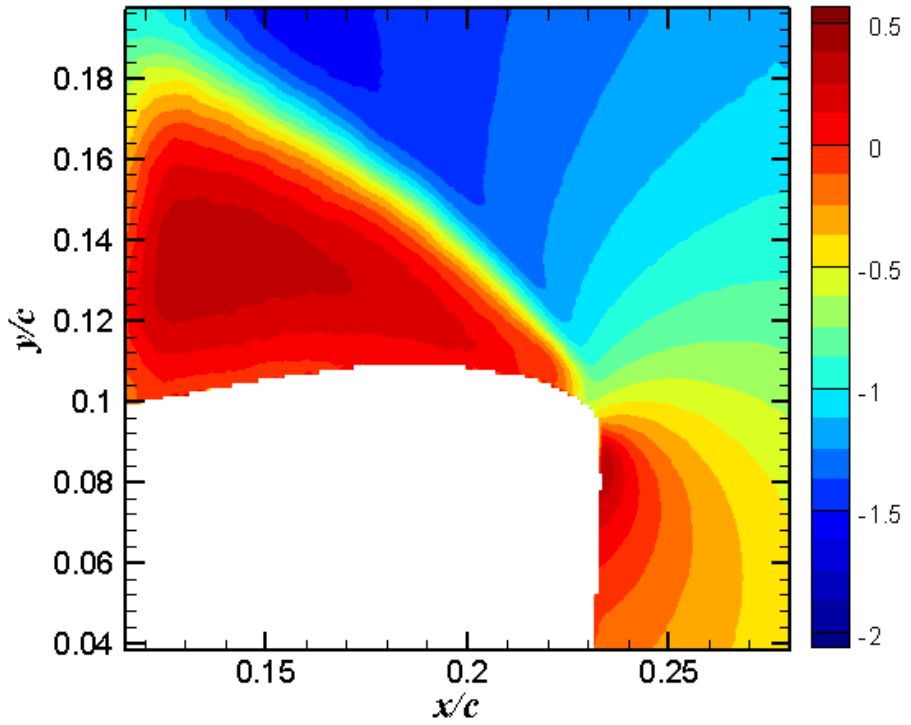

Figure 43. Normalized mean velocity component in the *x*-direction for $\alpha = 22°$, upstroke

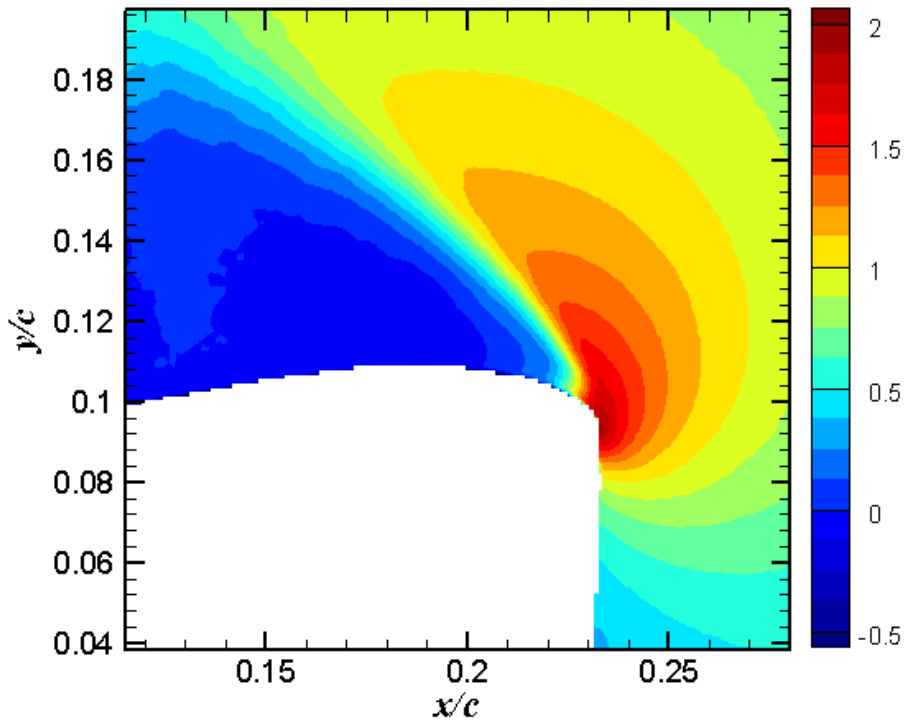

Figure 44. Normalized mean velocity component in the *y*-direction for $\alpha = 22°$, upstroke

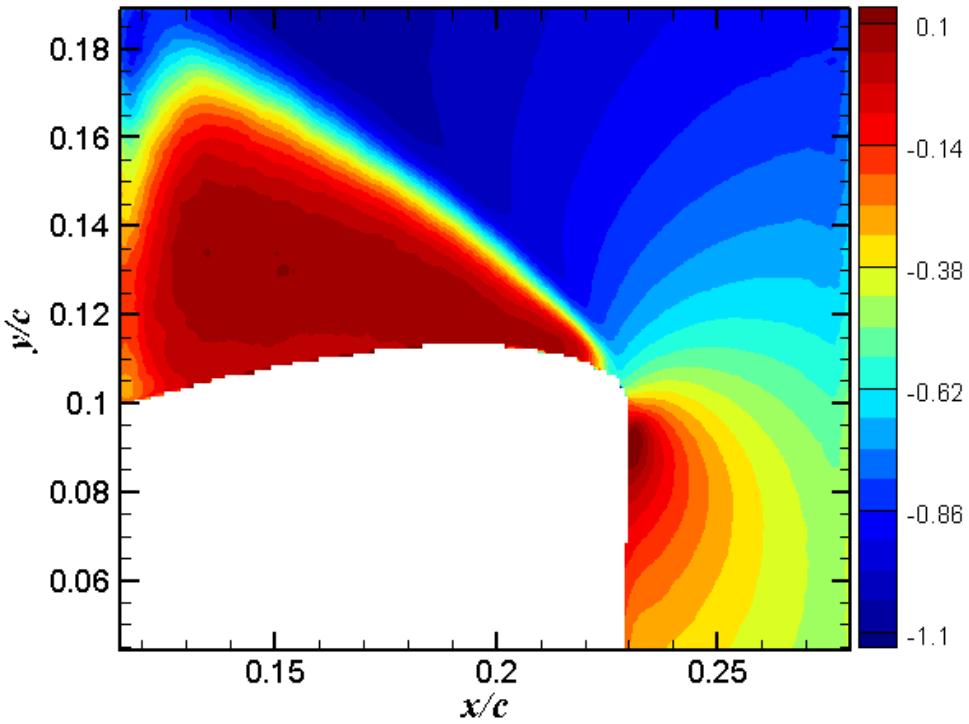

Figure 45. Normalized mean velocity component in the *x*-direction for $\alpha = 24°$, upstroke

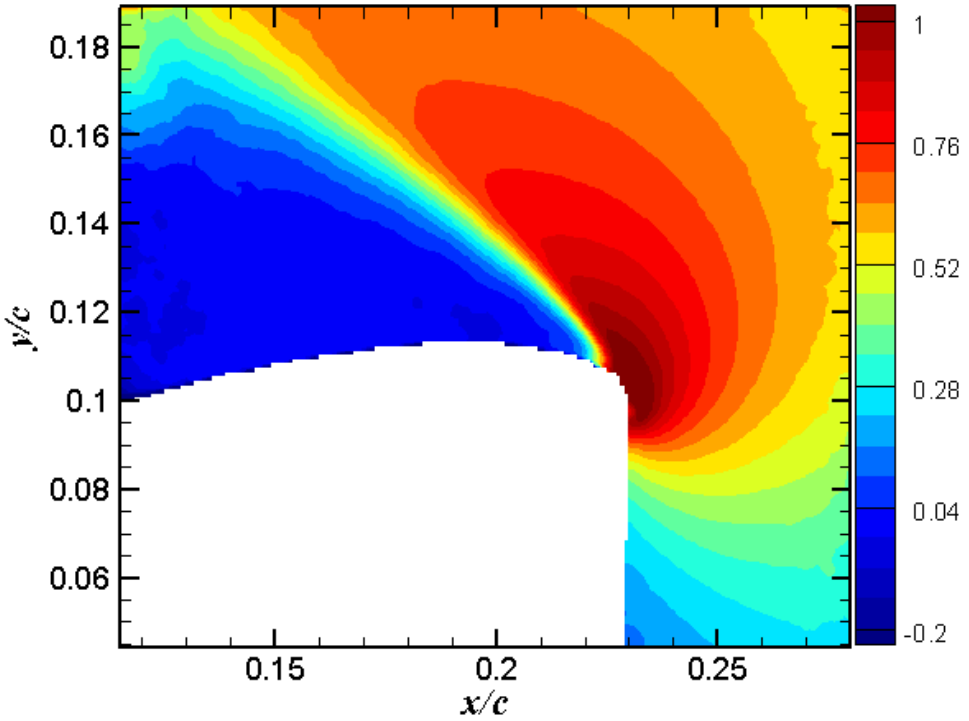

Figure 46. Normalized mean velocity component in the *y*-direction for $\alpha = 24°$, upstroke

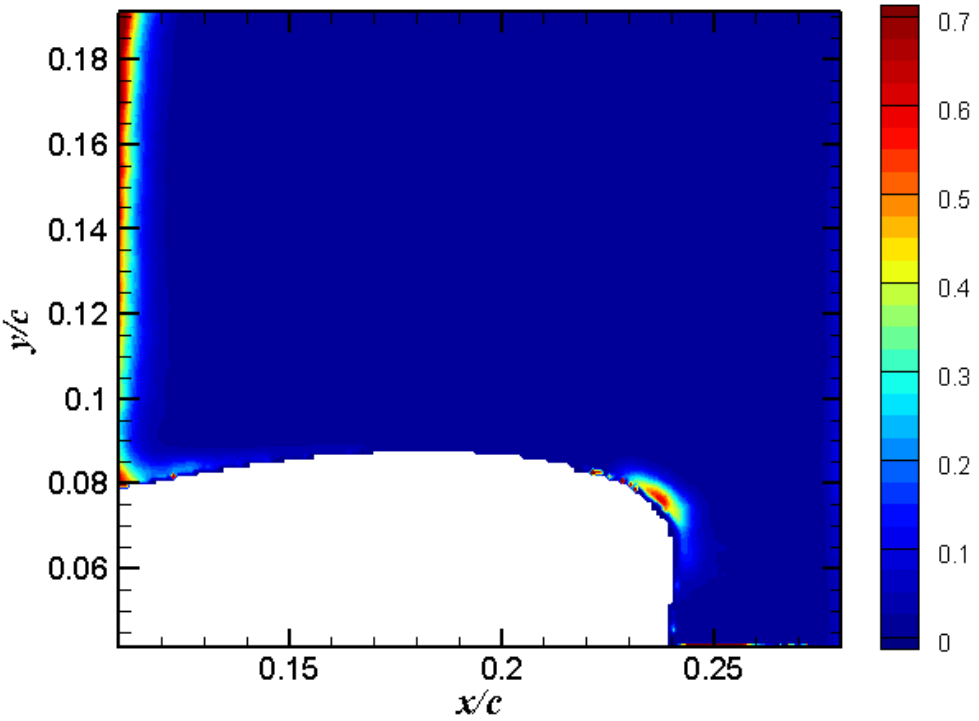

Figure 47. σ_u for $\alpha = 16°$, upstroke

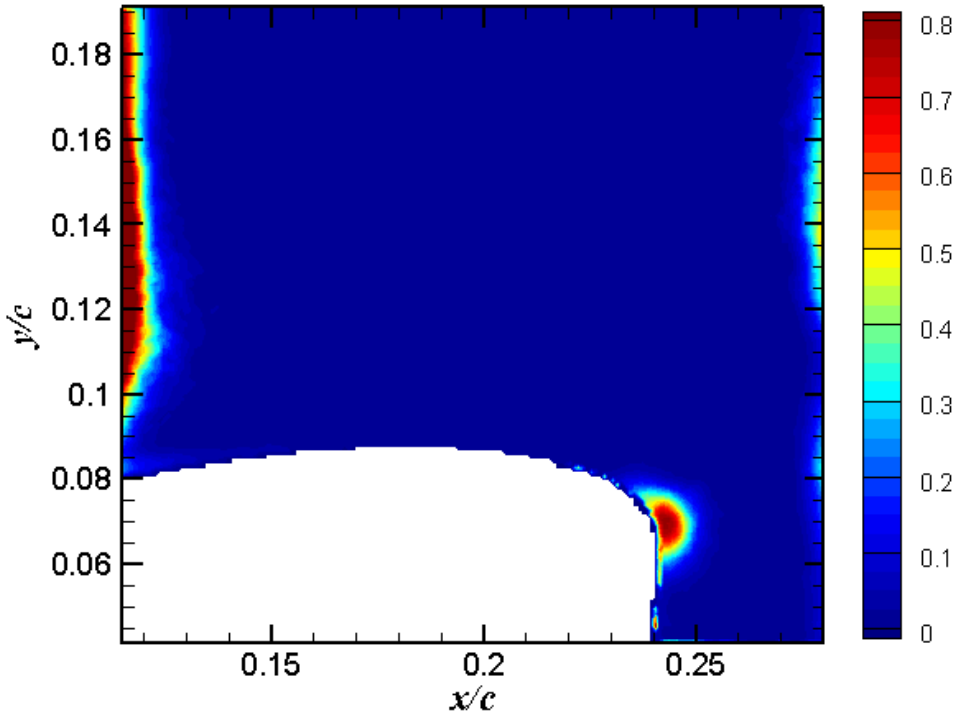

Figure 48. σ_v for $\alpha = 16°$, upstroke

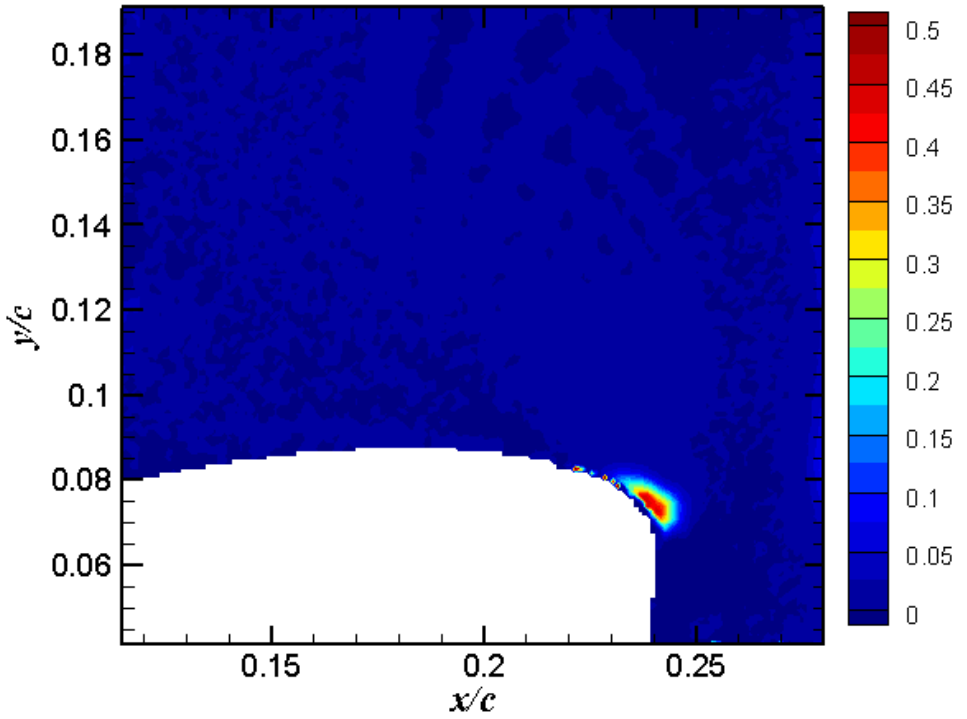

Figure 49. τ_{xy} for α = 16°, upstroke

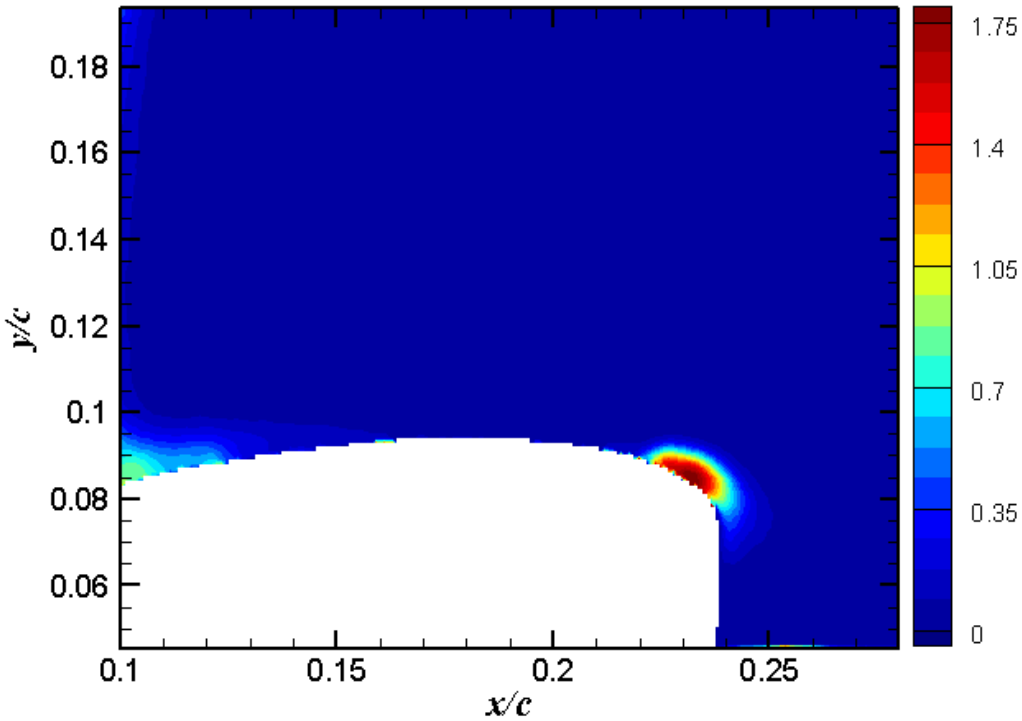

Figure 50. σ_u for α = 18°, upstroke

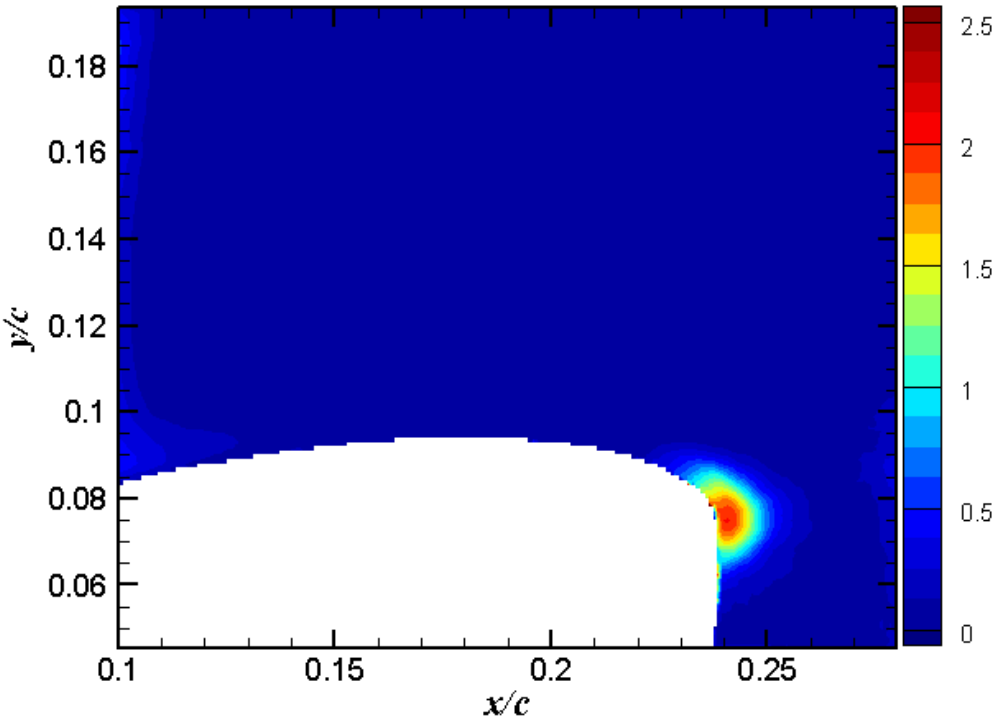

Figure 51. σ_y for $\alpha = 18°$, upstroke

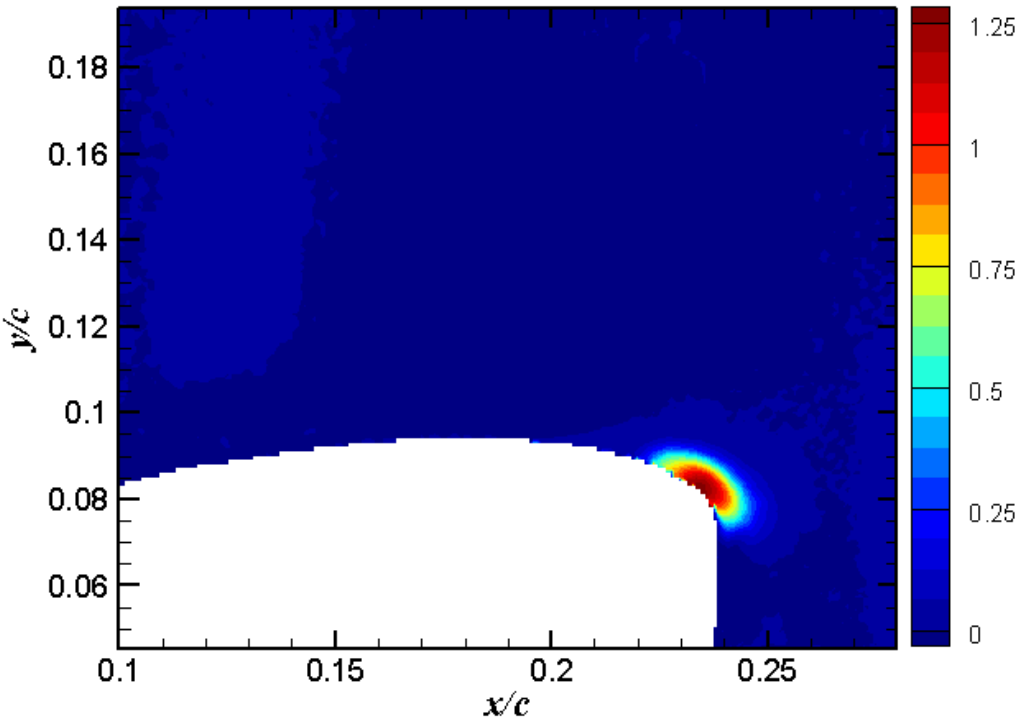

Figure 52. τ_{xy} for $\alpha = 18°$, upstroke

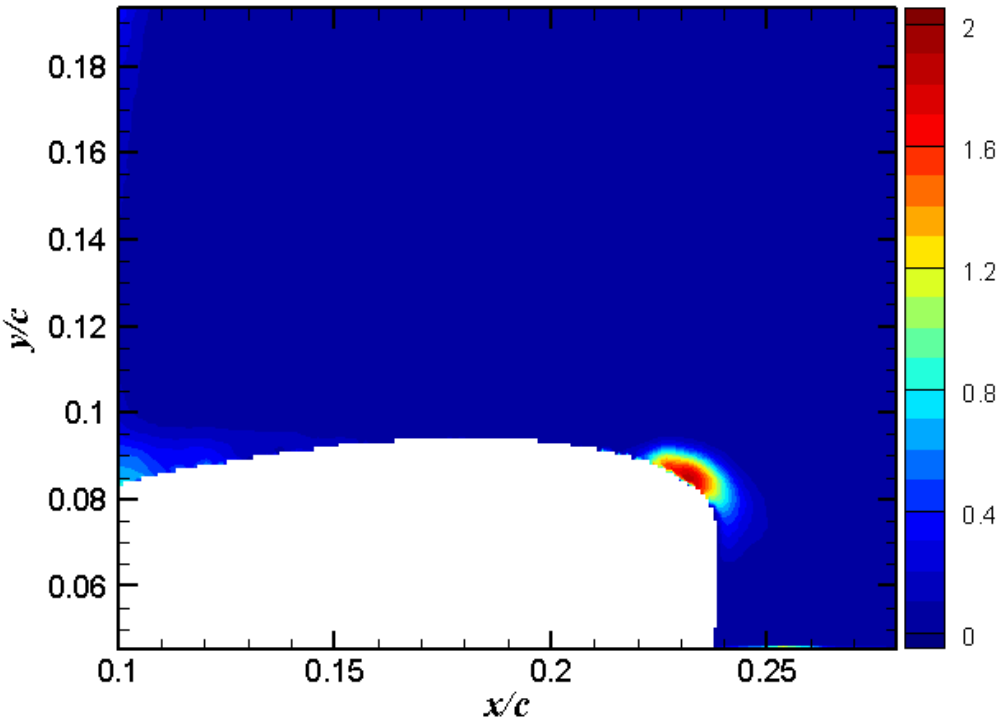

Figure 53. σ_u for $\alpha = 18°$, upstroke, fully attached flow

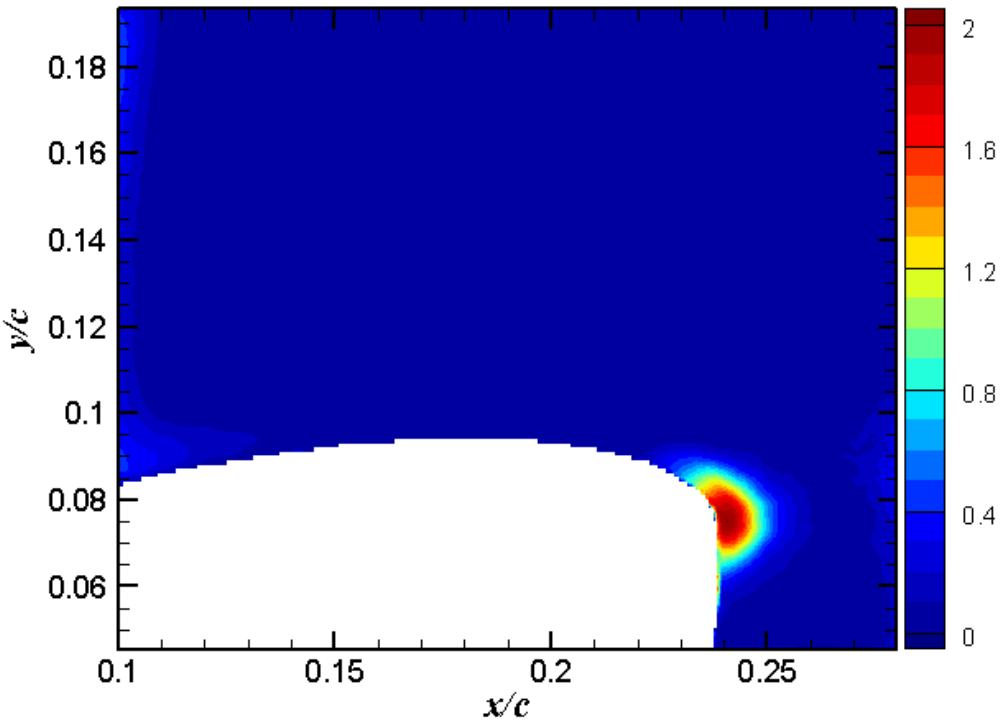

Figure 54. σ_v for $\alpha = 18°$, upstroke, fully attached flow

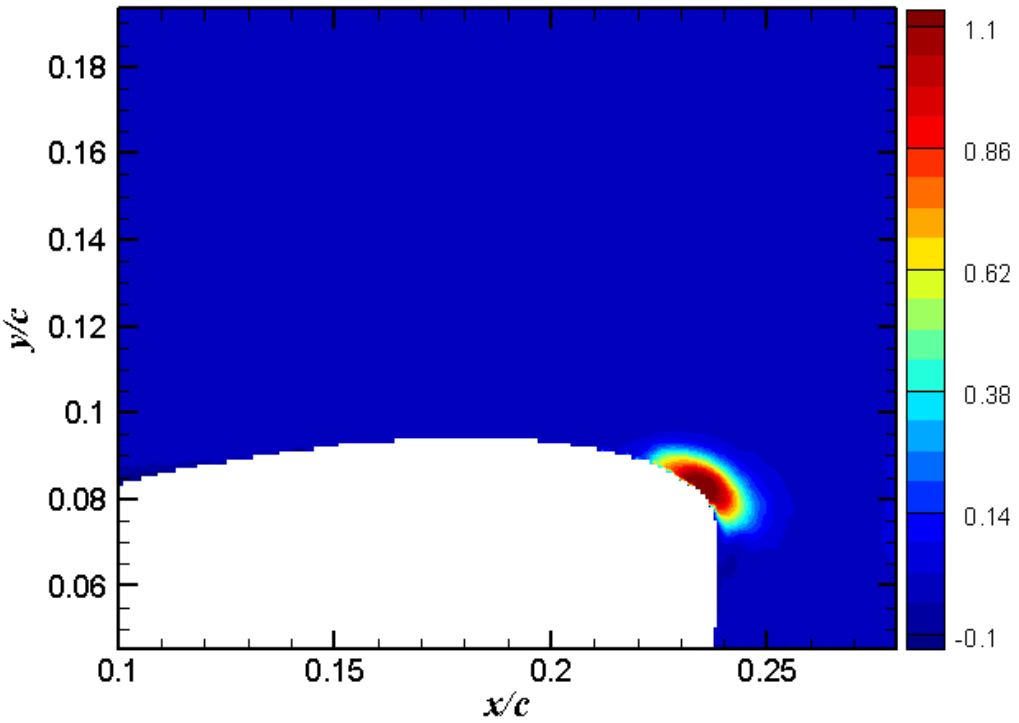

Figure 55. τ_{xy} for α = 18°, upstroke, fully attached flow

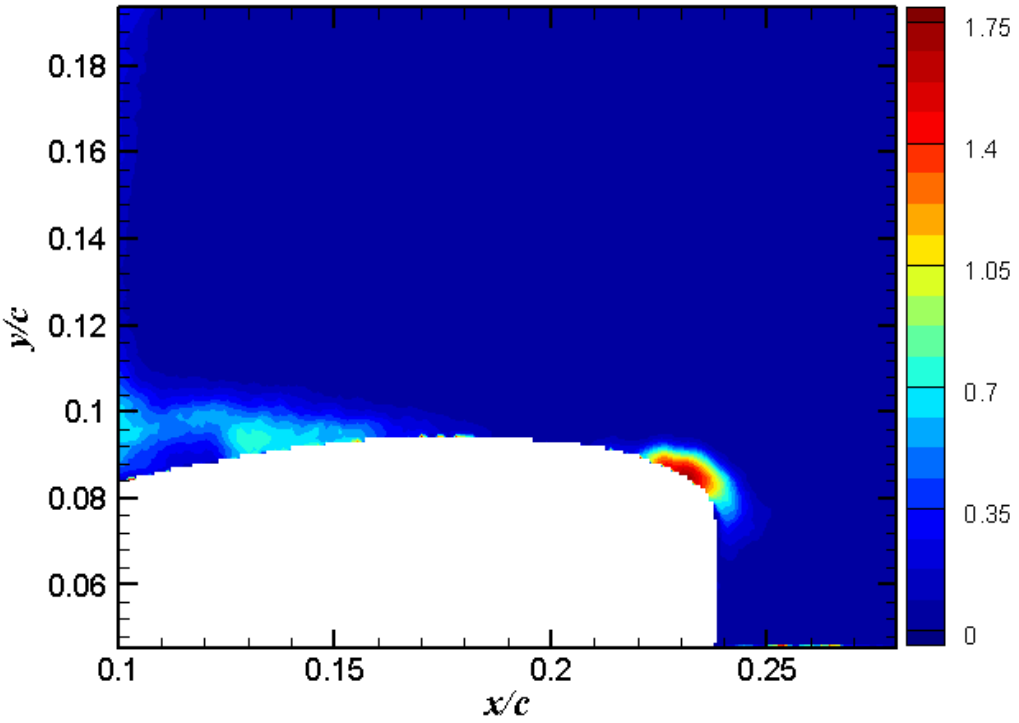

Figure 56. σ_u for α = 18°, upstroke, partially separated flow

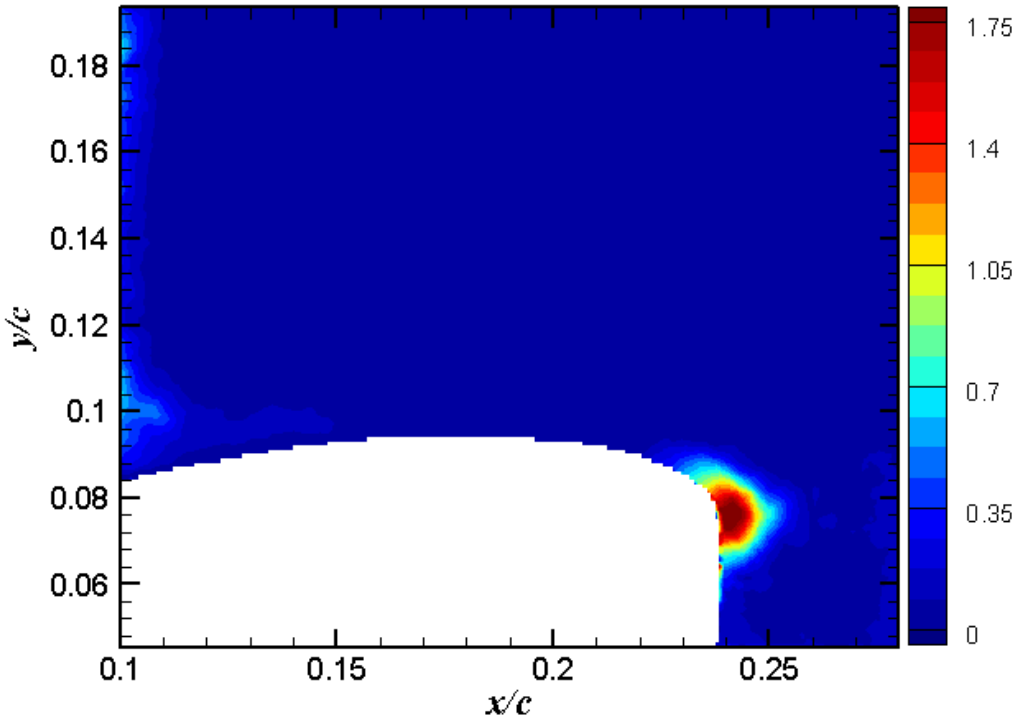

Figure 57. σ_y for α = 18°, upstroke, partially separated flow

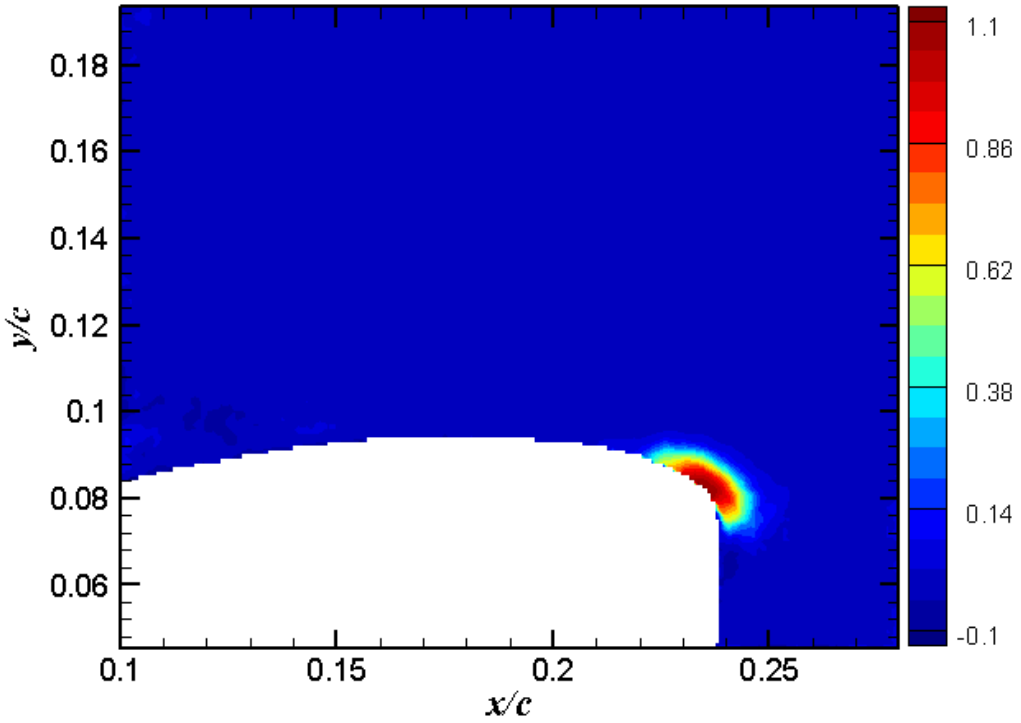

Figure 58. τ_{xy} for α = 18°, upstroke, partially separated flow

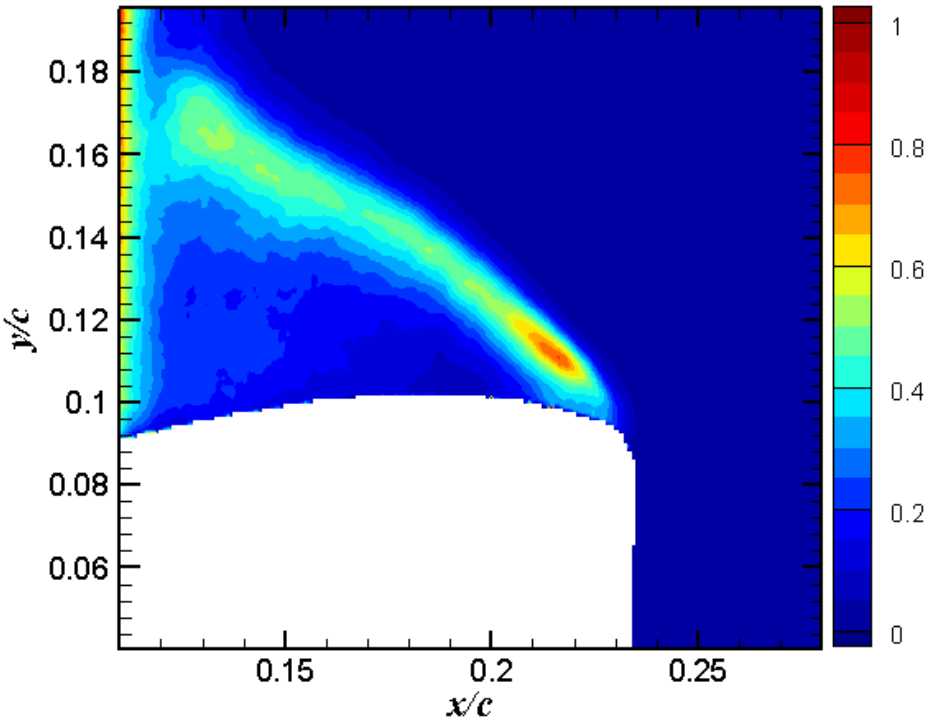

Figure 59. σ_u for $\alpha = 20°$, upstroke

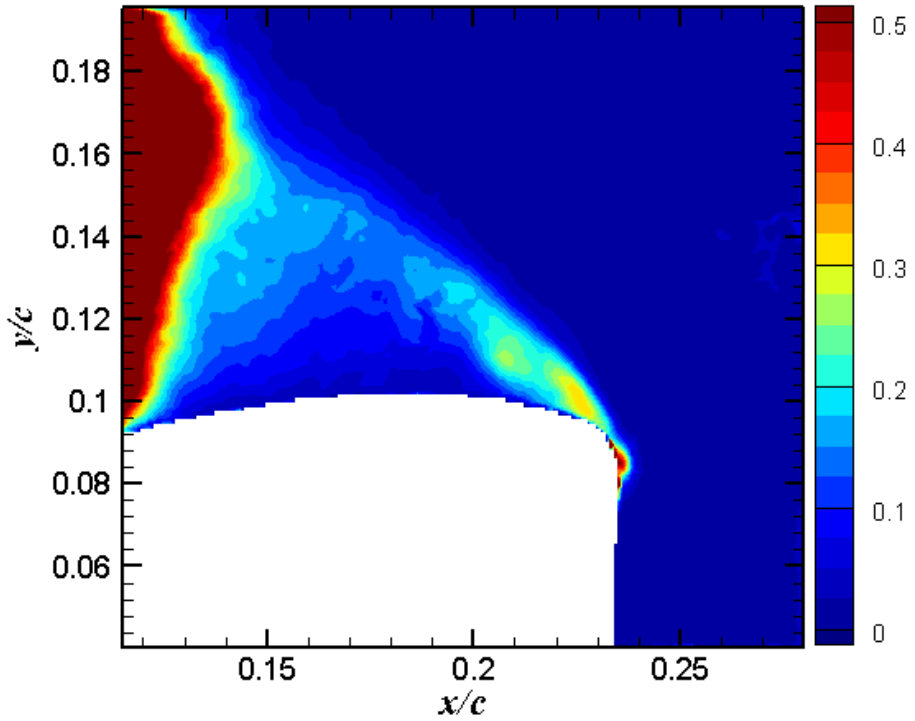

Figure 60. σ_v for $\alpha = 20°$, upstroke

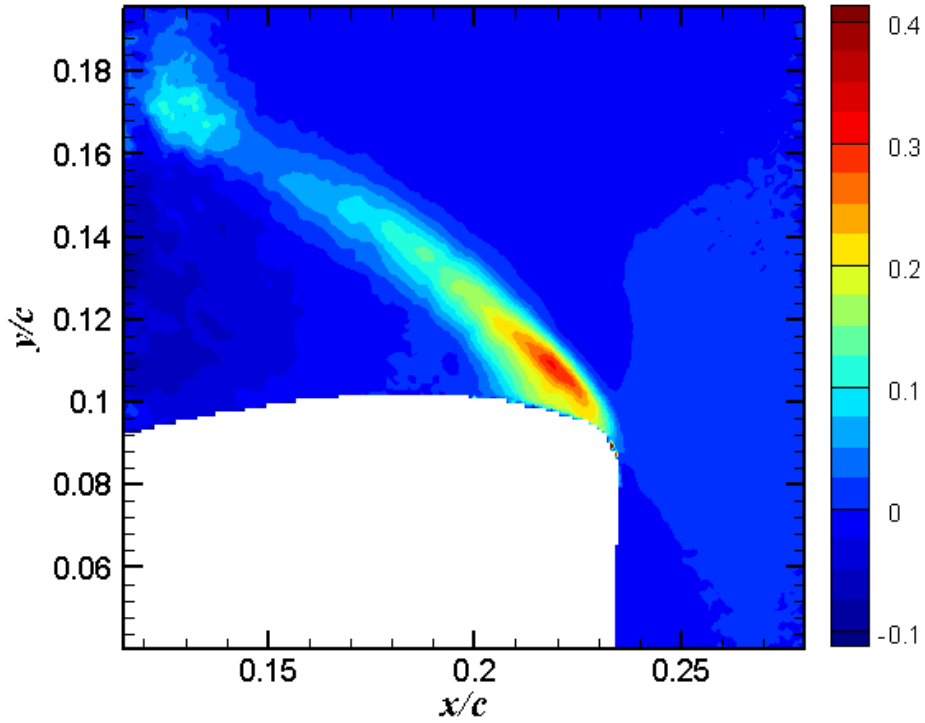

Figure 61. τ_{xy} for $\alpha = 20°$, upstroke

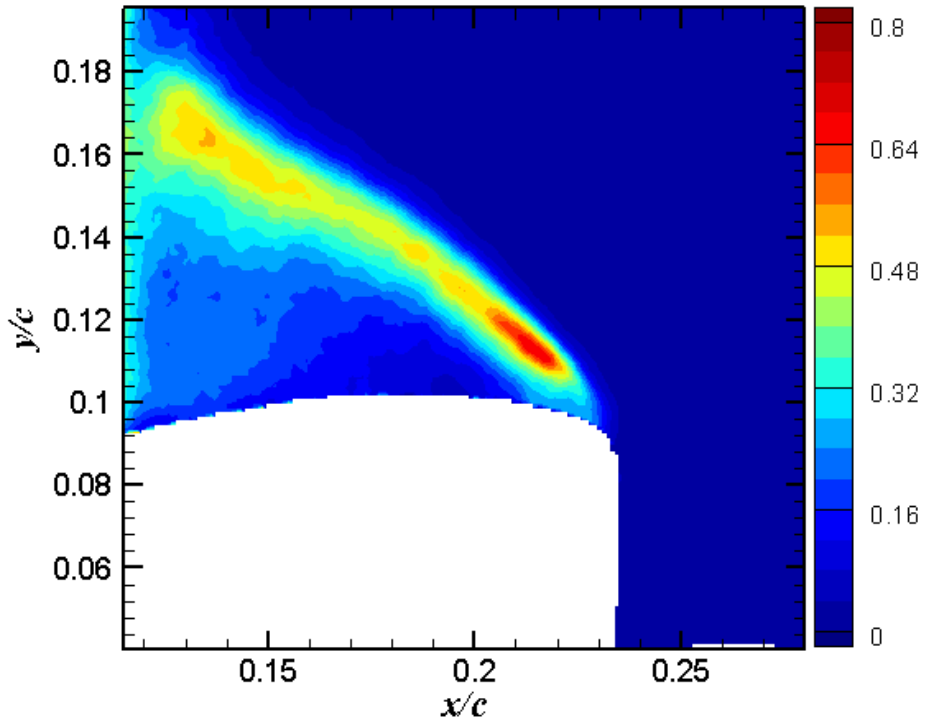

Figure 62. σ_u for $\alpha = 20°$, upstroke, fully separated flow

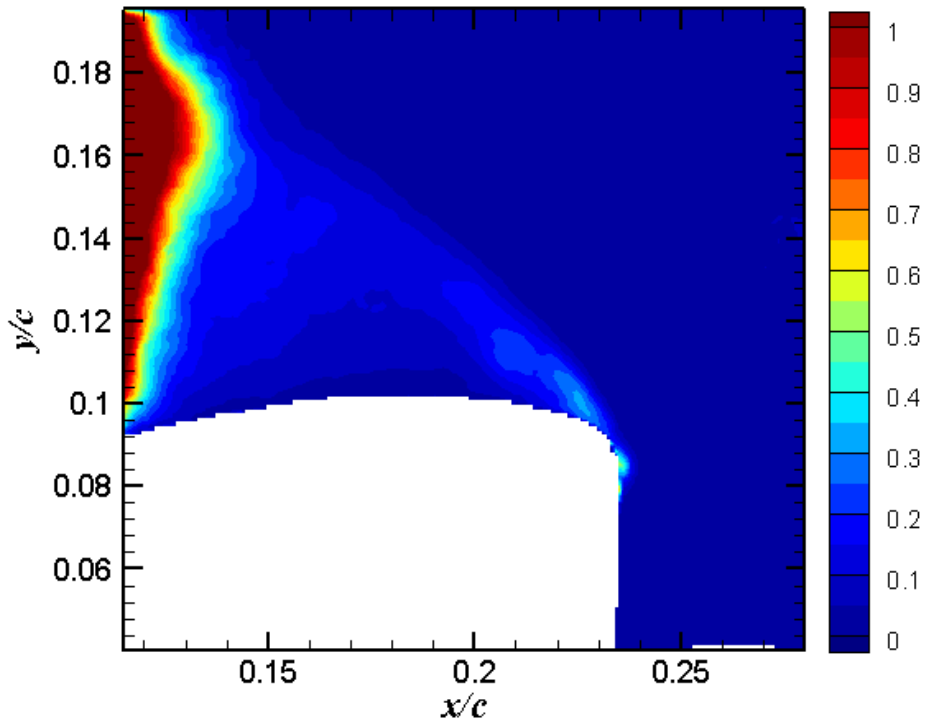

Figure 63. σ_v for $\alpha = 20°$, upstroke, fully separated flow

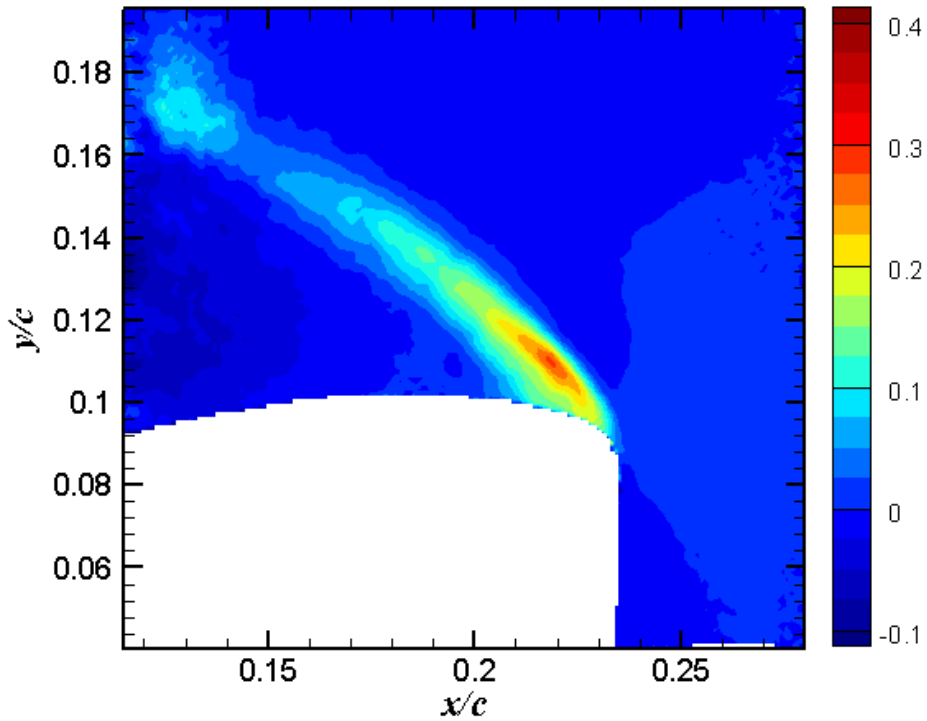

Figure 64. τ_{xy} for $\alpha = 20°$, upstroke, fully separated flow

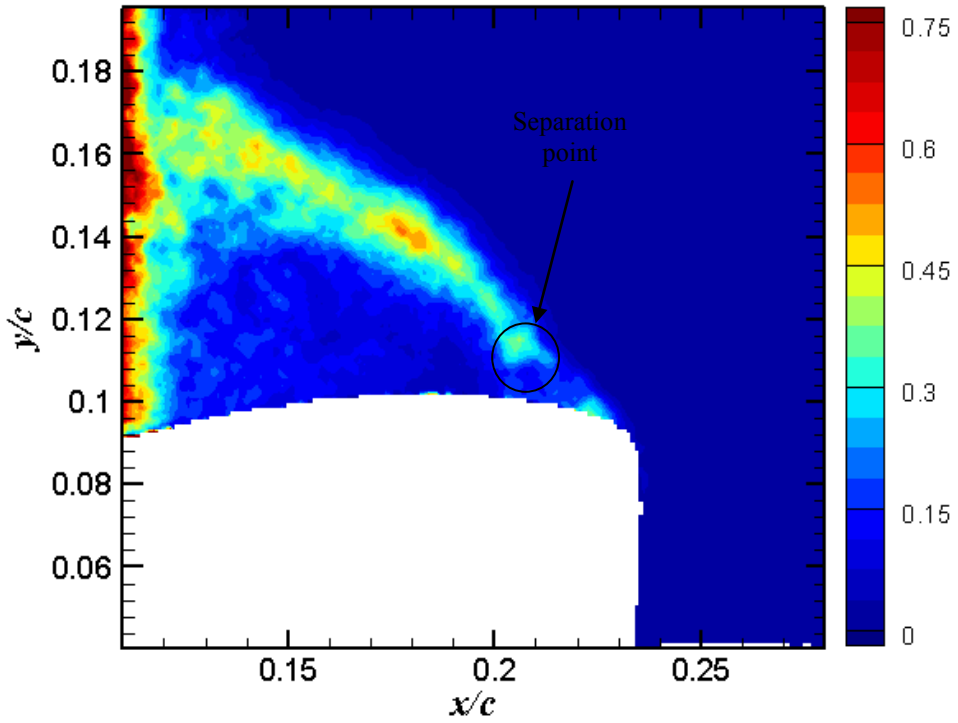

Figure 65. σ_u for $\alpha = 20°$, upstroke, partially attached flow

Figure 66. σ_v for $\alpha = 20°$, upstroke, partially attached flow

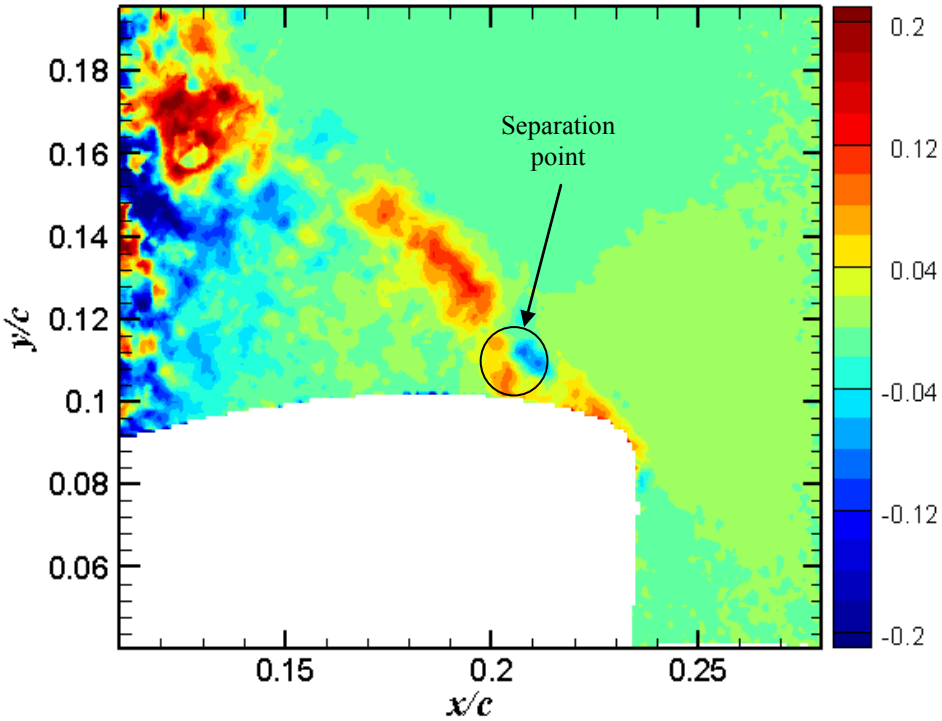

Figure 67. τ_{xy} for $\alpha = 20°$, upstroke, partially attached flow

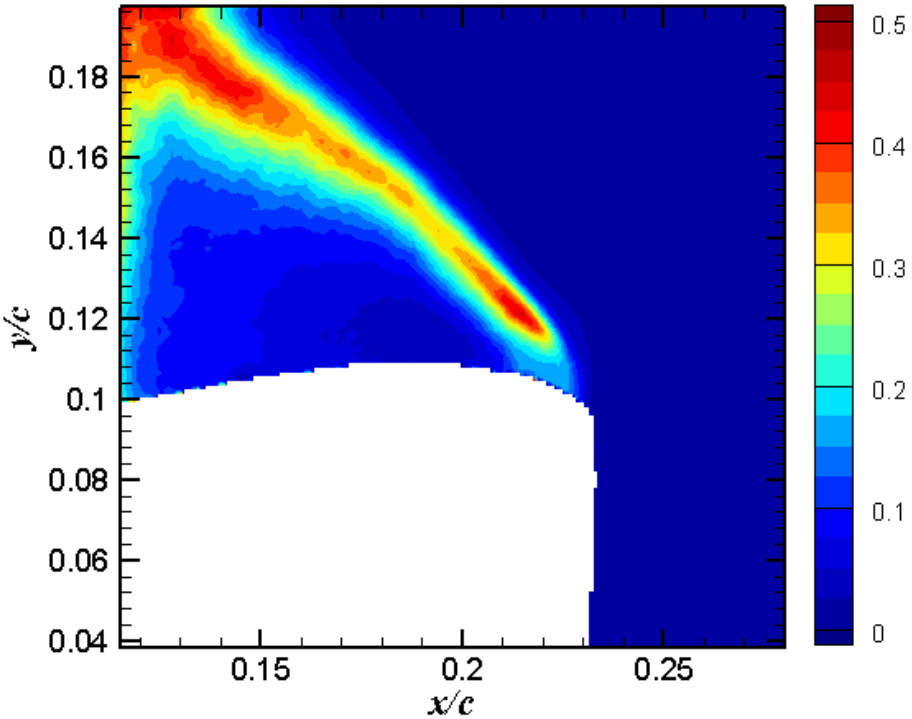

Figure 68. σ_u for $\alpha = 22°$, upstroke

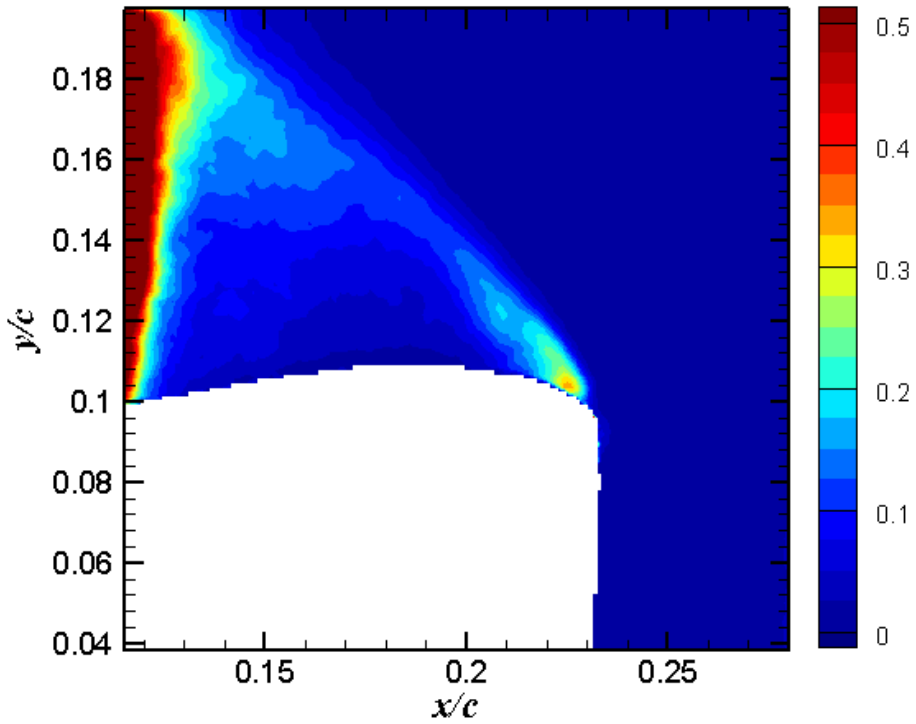

Figure 69. σ_y for $\alpha = 22°$, upstroke

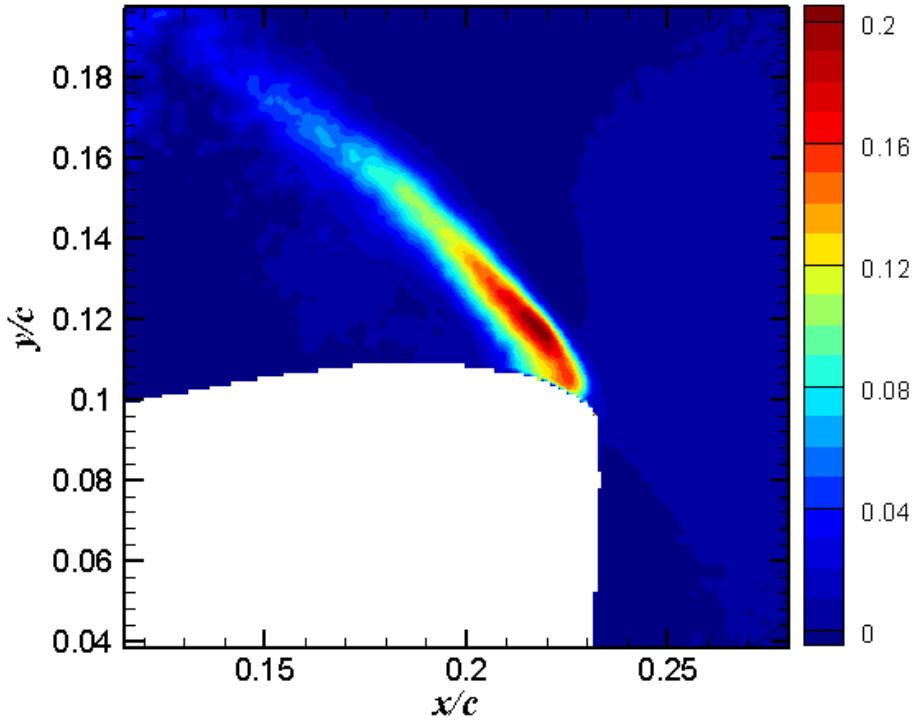

Figure 70. τ_{xy} for $\alpha = 22°$, upstroke

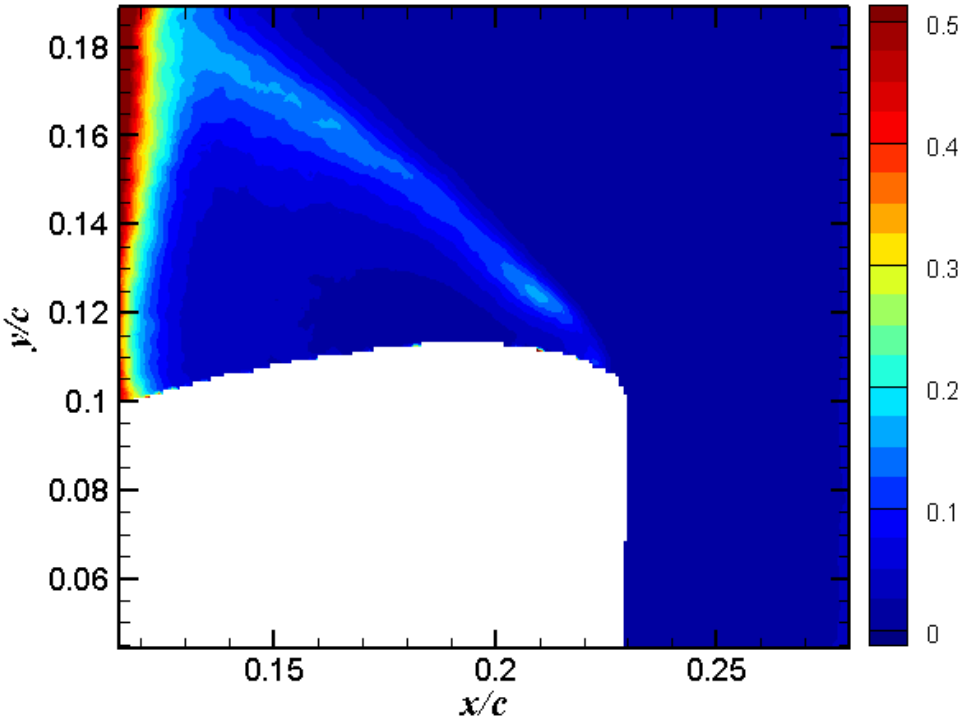

Figure 71. σ_u for $\alpha = 24°$, upstroke

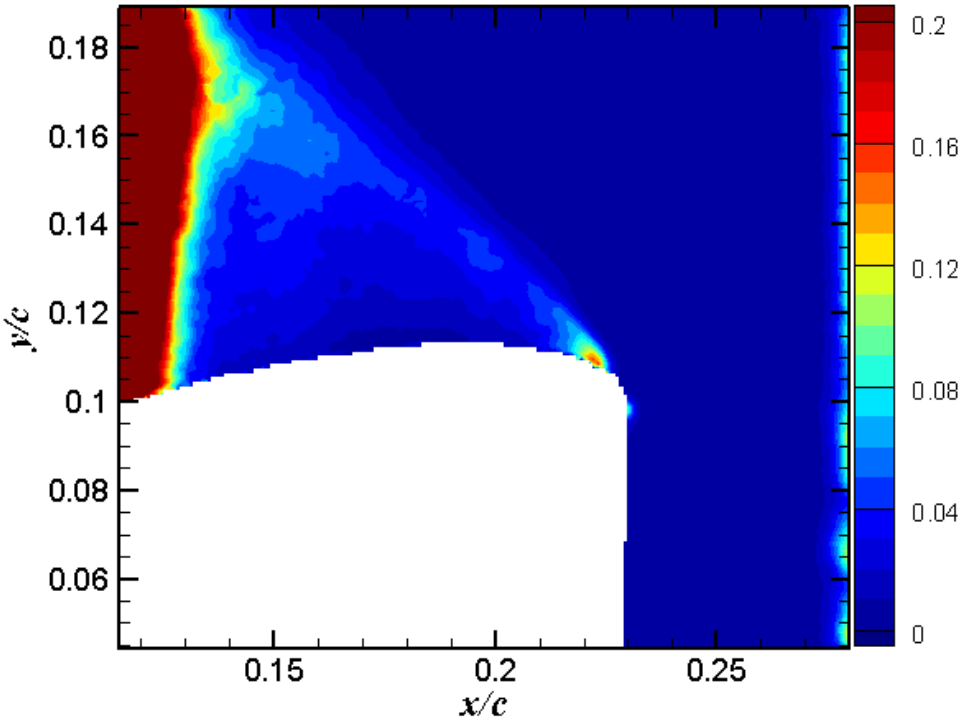

Figure 72. σ_v for $\alpha = 24°$, upstroke

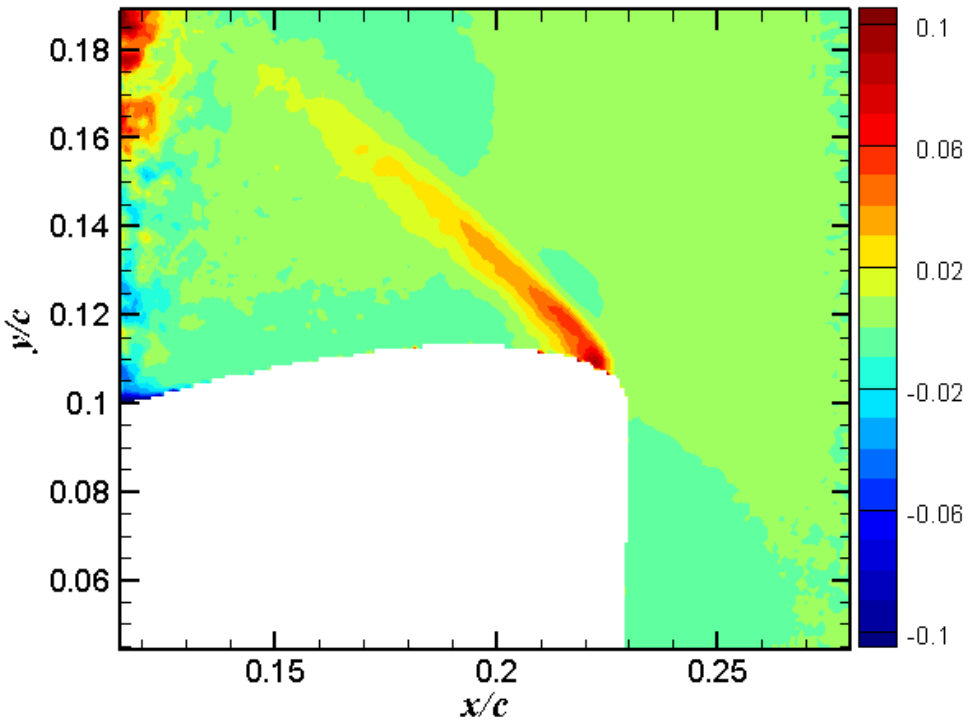

Figure 73. τ_{xy} for α = 24°, upstroke

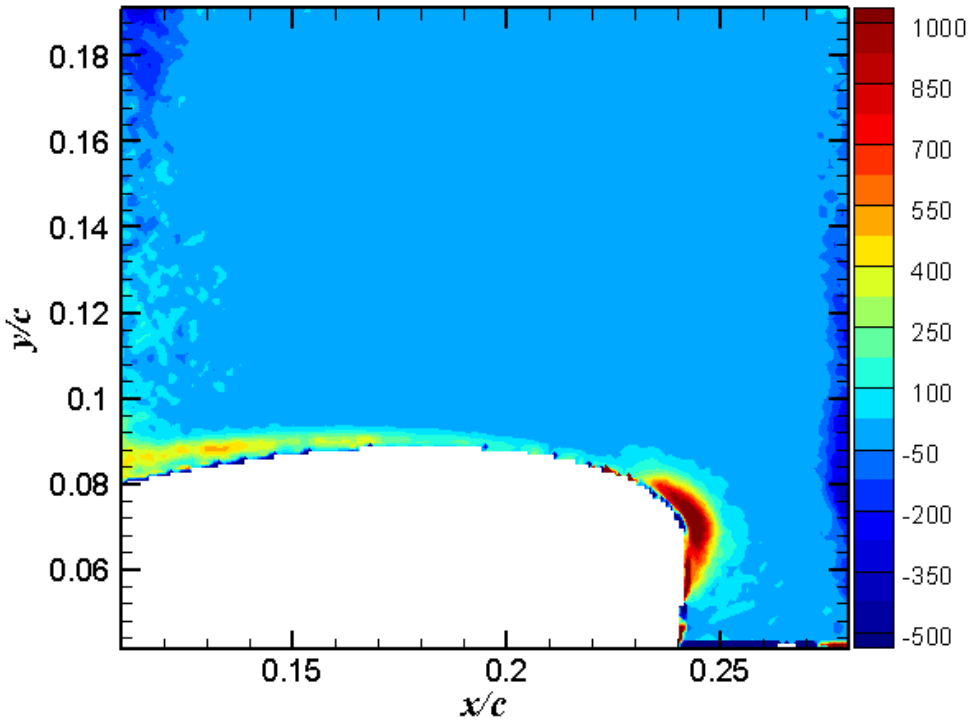

Figure 74. Vorticity (ω_z) at α = 16°, upstroke

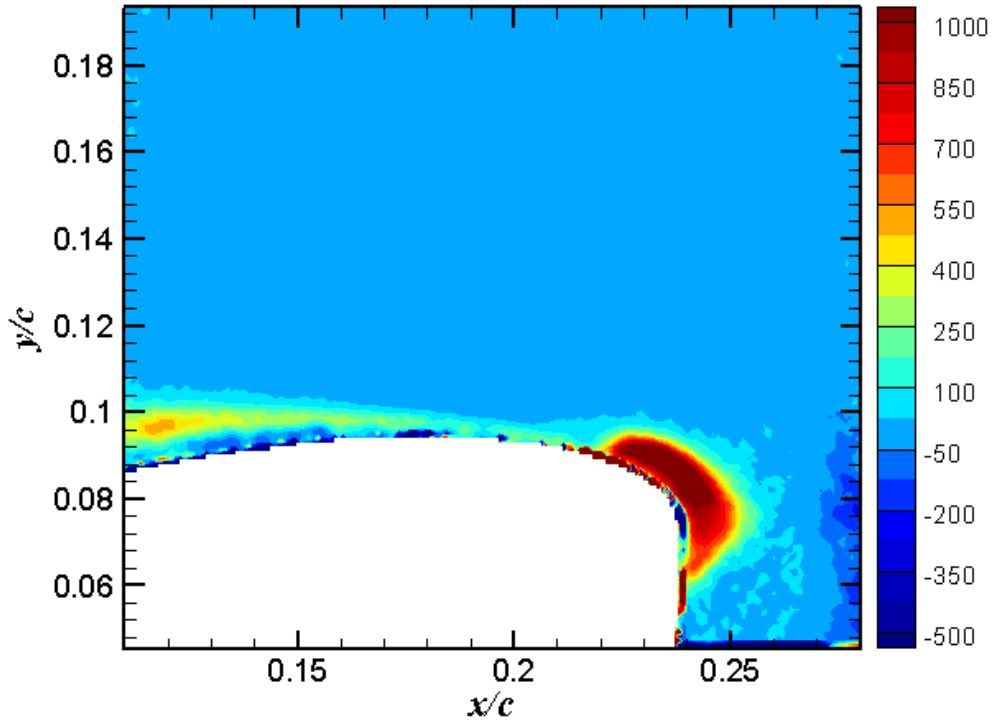

Figure 75. Vorticity (ω_z) at α = 18°, upstroke, overall

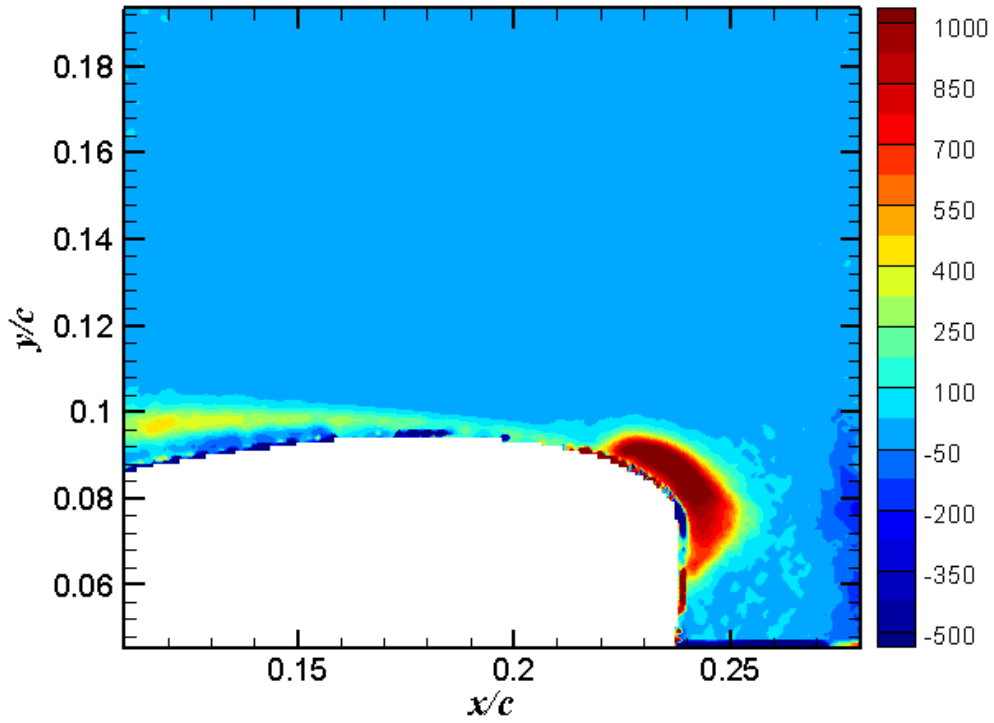

Figure 76. Vorticity (ω_z) at α = 18°, upstroke, fully attached

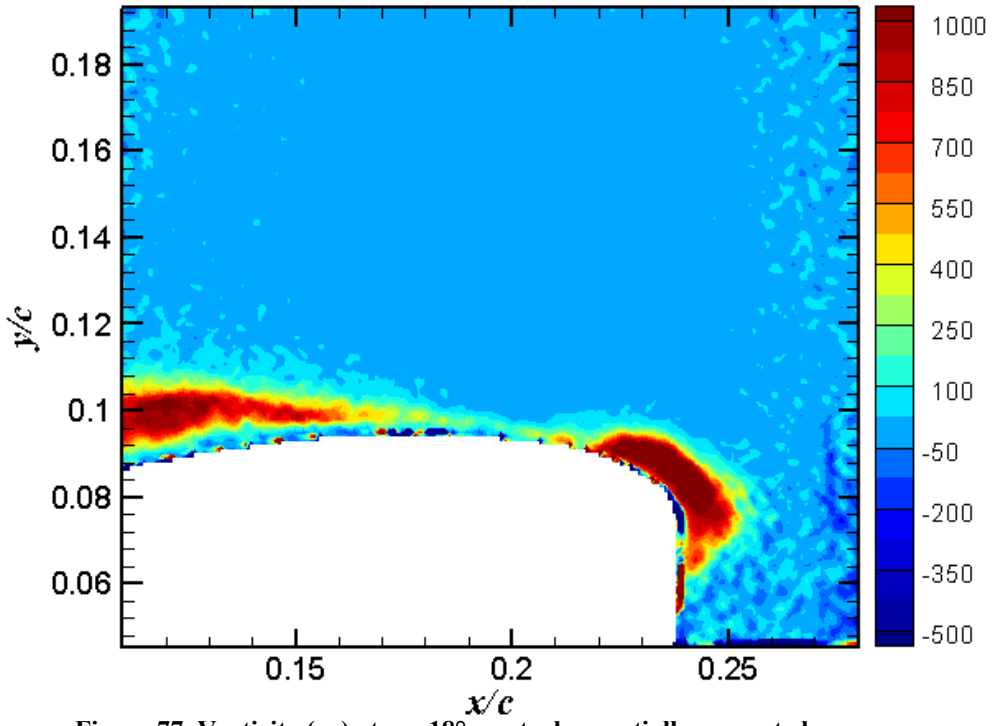

Figure 77. Vorticity (ω_z) at α = 18°, upstroke, partially separated

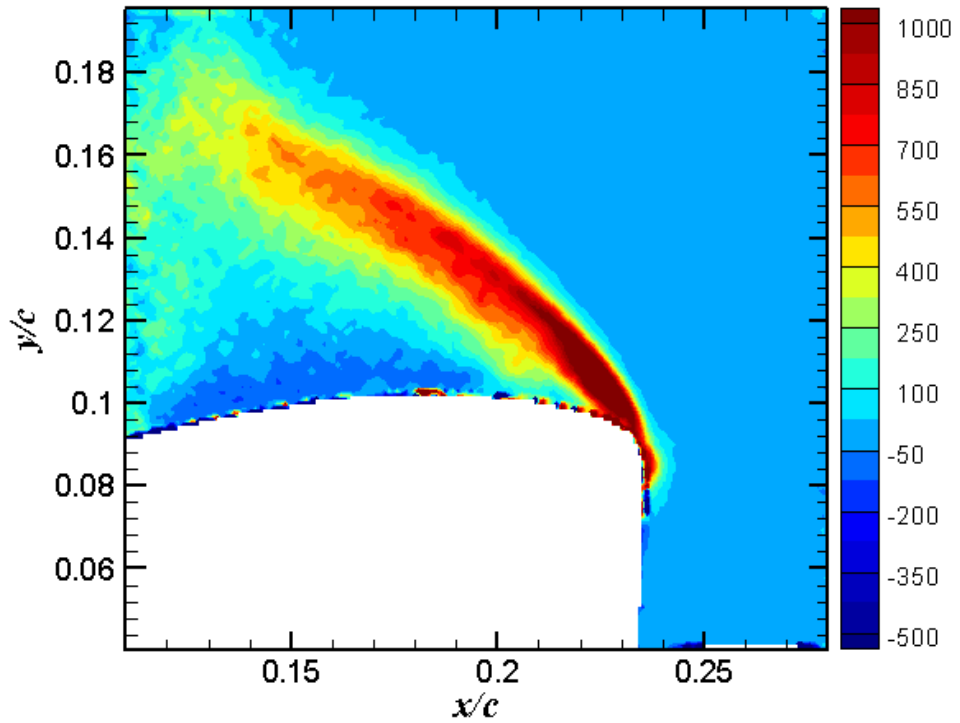

Figure 78. Vorticity (ω_z) at α = 20°, upstroke, overall

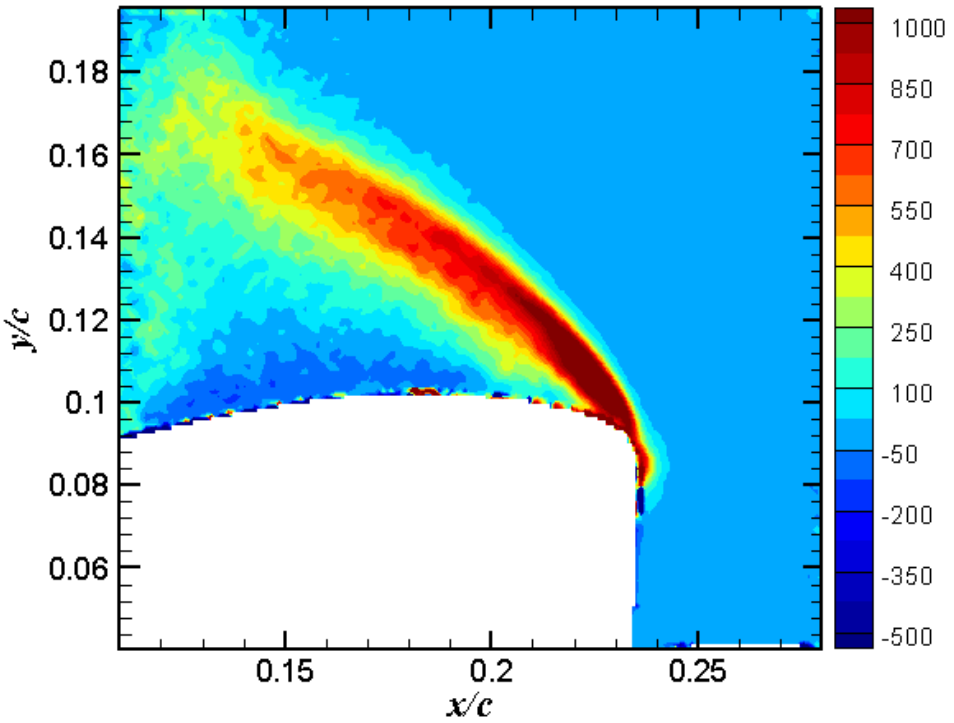

Figure 79. Vorticity (ω_z) at α = 20°, upstroke, fully separated

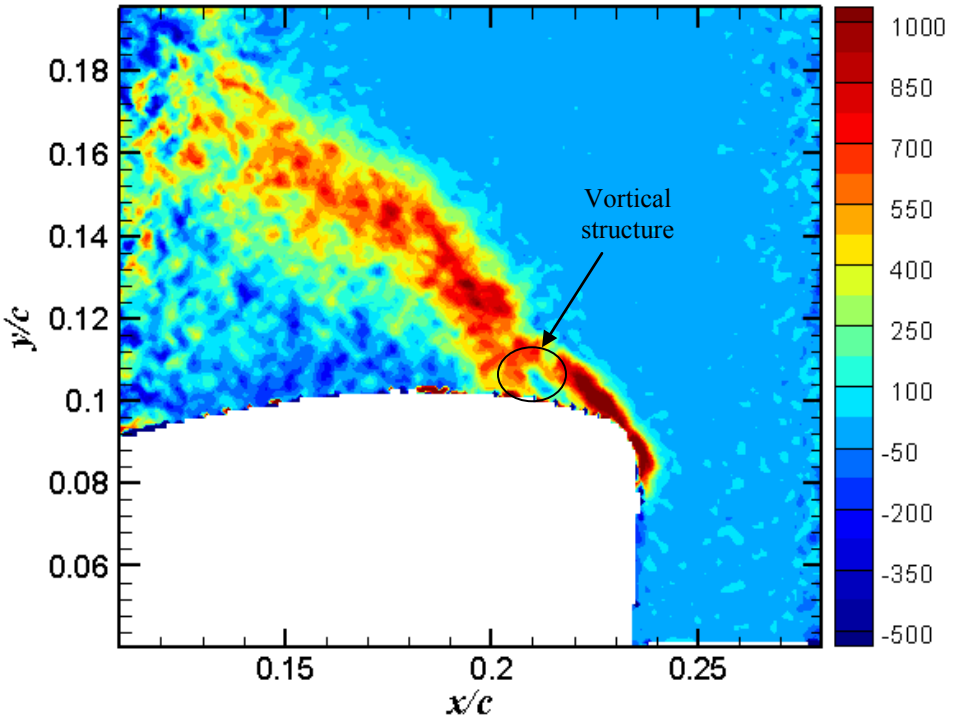

Figure 80. Vorticity (ω_z) at α = 20°, upstroke, partially attached

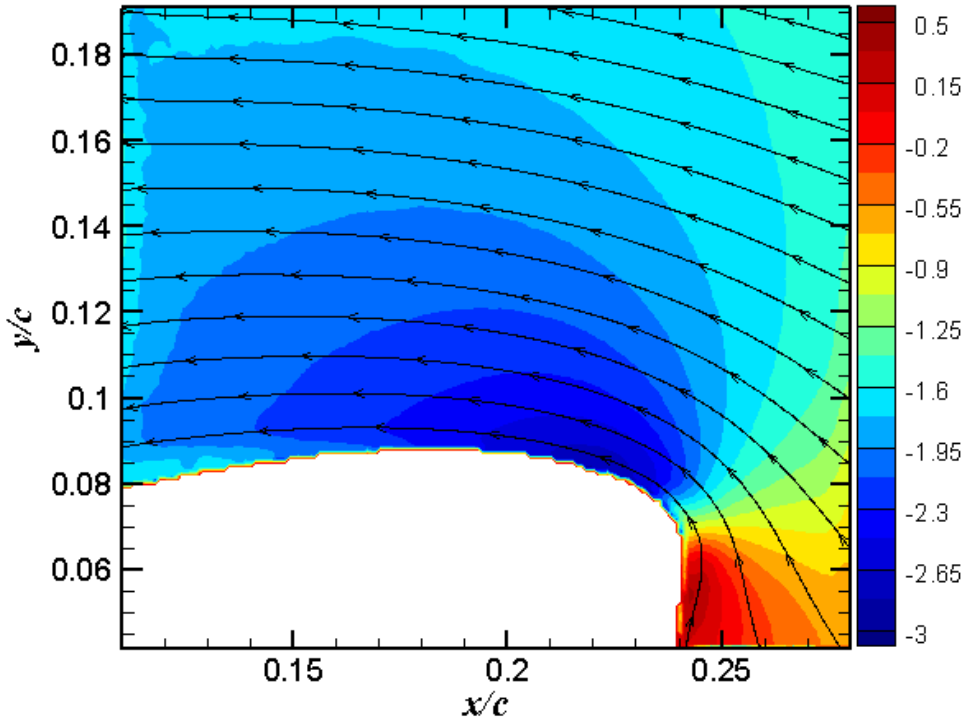

Figure 81. Streamlines for α = 16°, upstroke, over *U*-velocity contour

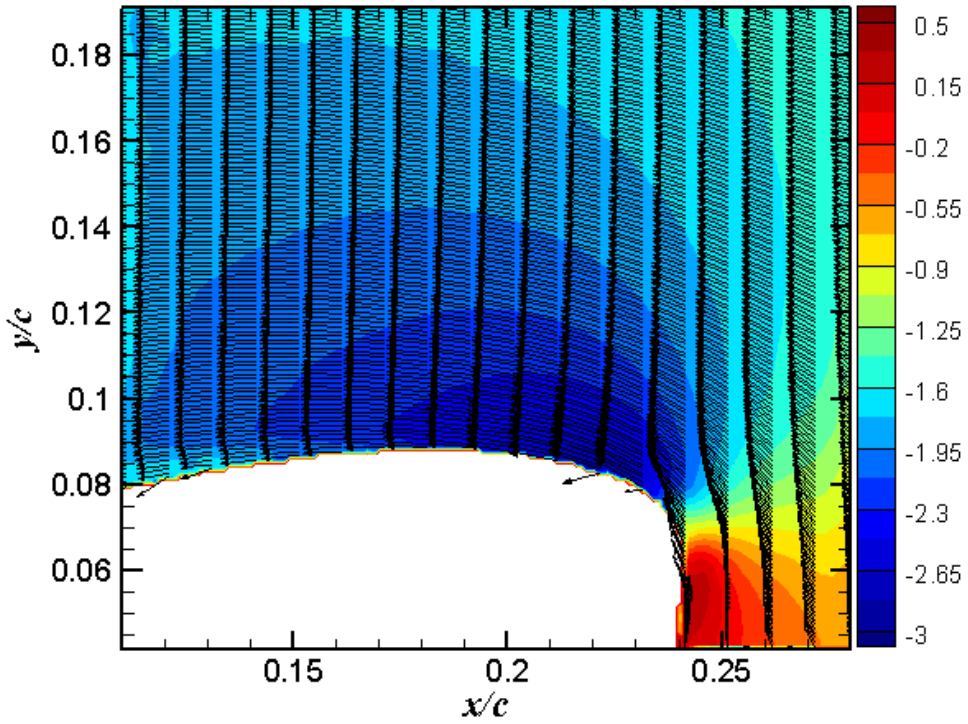

Figure 82. Velocity vectors for α = 16°, upstroke, over *U*-velocity contour

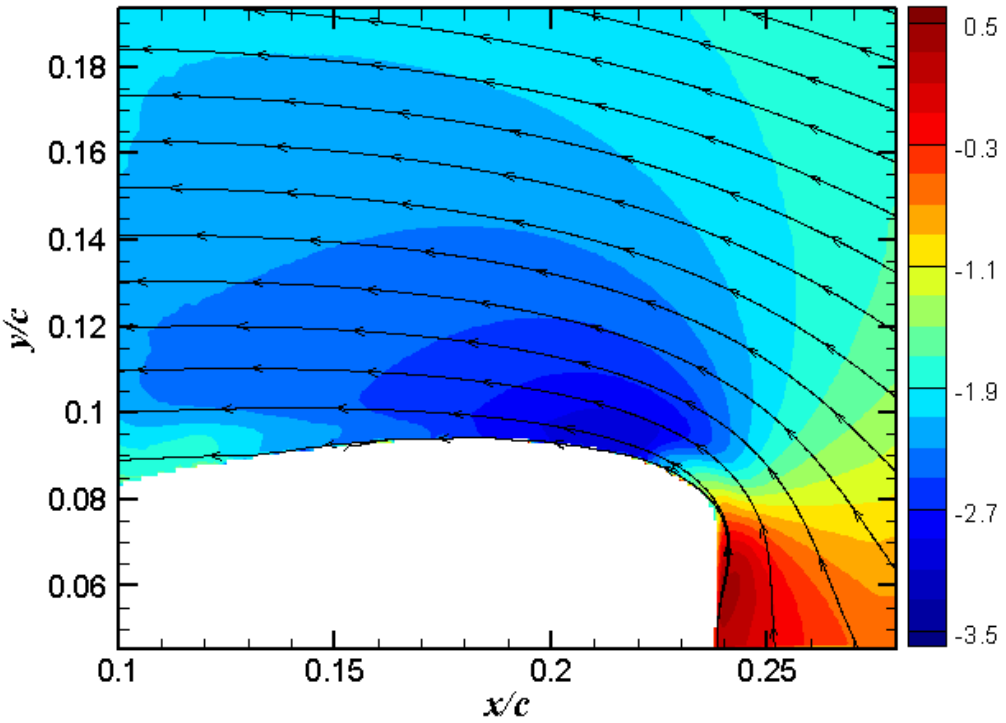

Figure 83. Streamlines for α = 18°, upstroke, over *U*-velocity contour

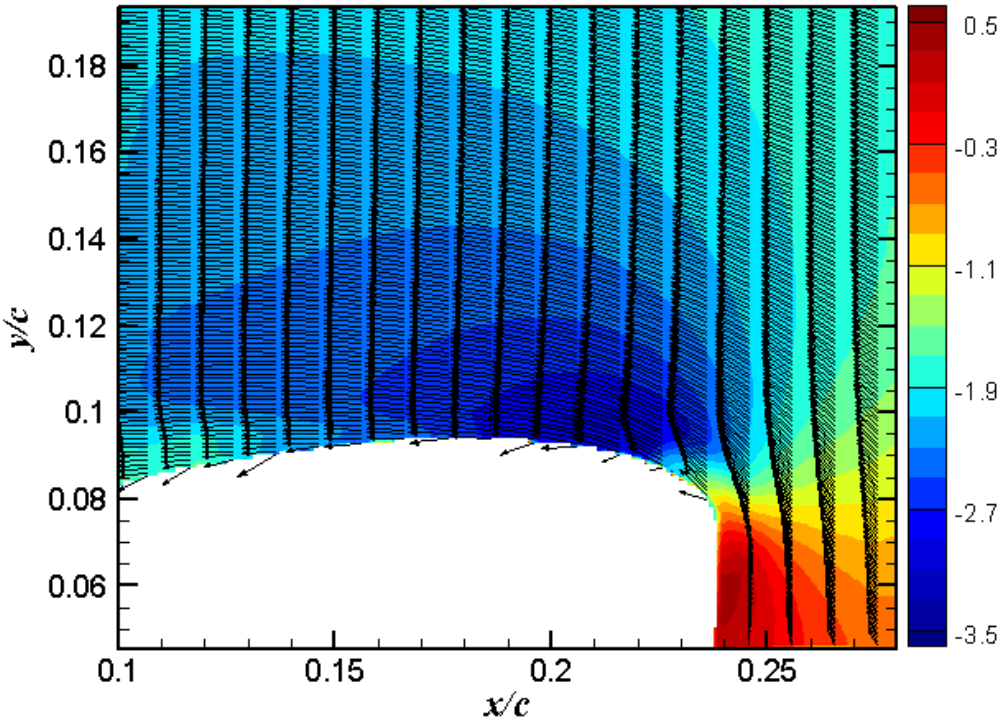

Figure 84. Vectors for α = 18°, upstroke, over *U*-velocity contour

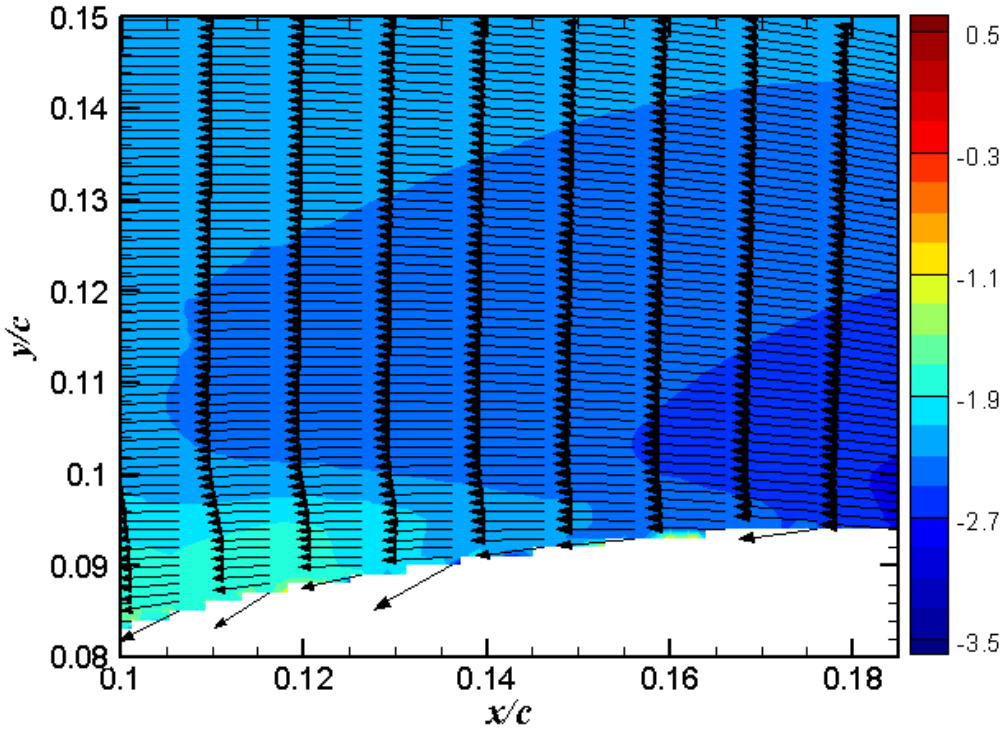

Figure 85. Zoom of boundary layer vectors for α = 18°, upstroke, over *U*-velocity contour

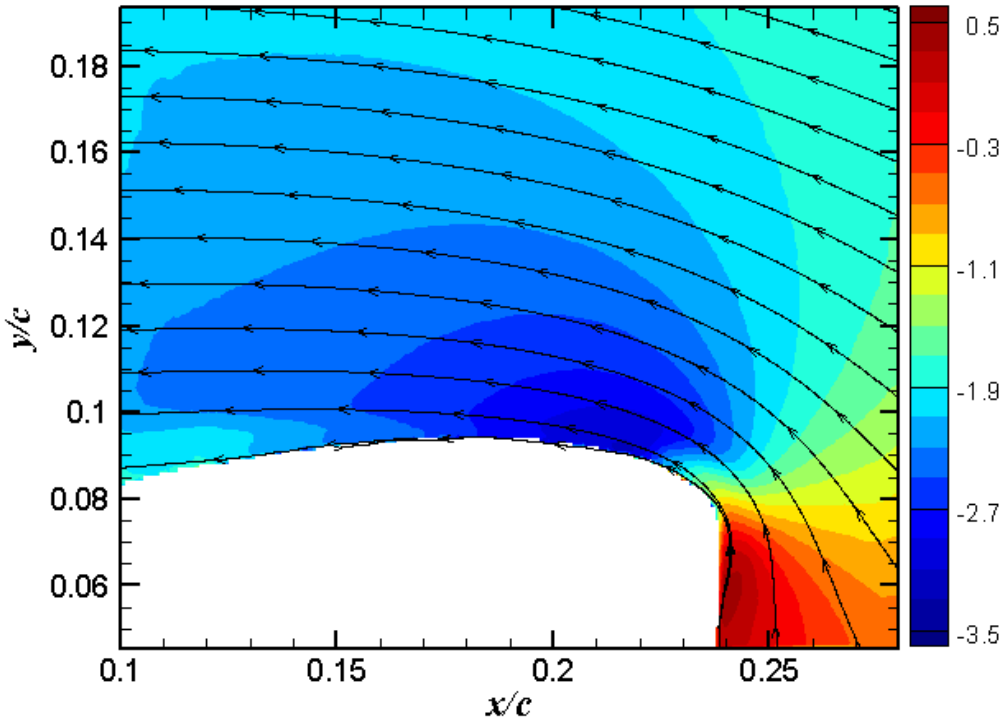

Figure 86. Streamlines for α = 18°, upstroke, fully attached, over *U*-velocity contour

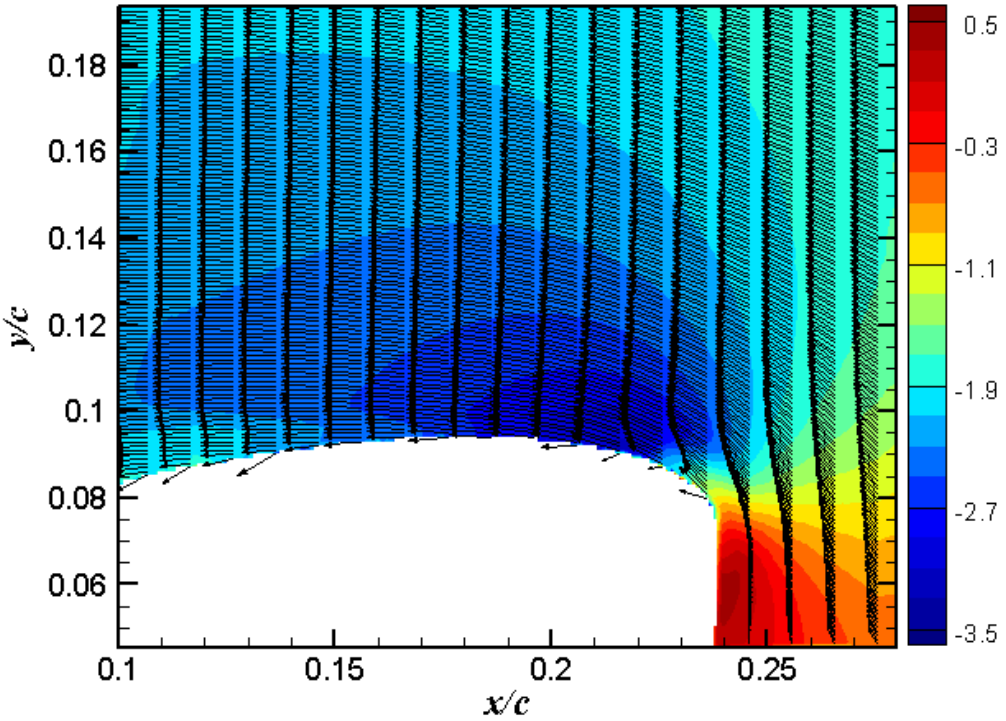

Figure 87. Vectors for α = 18°, upstroke, fully attached, over *U*-velocity contour

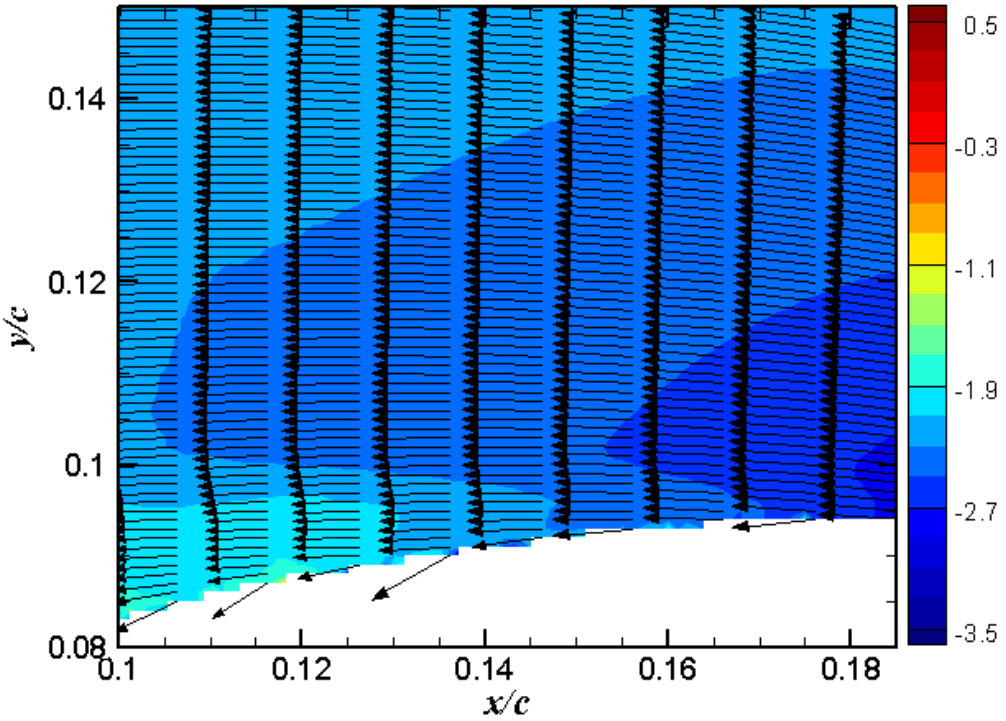

Figure 88. Zoom of boundary layer vectors for α = 18°, upstroke, fully attached, over *U*-velocity contour

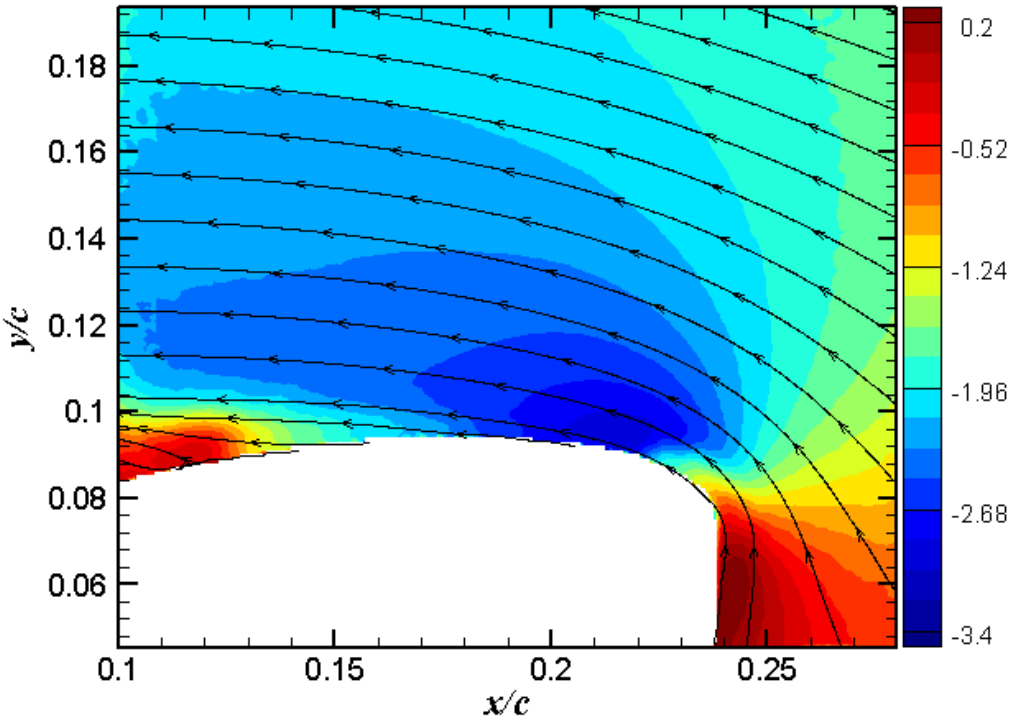

Figure 89. Streamlines for α = 18°, upstroke, partially separated, over *U*-velocity contour

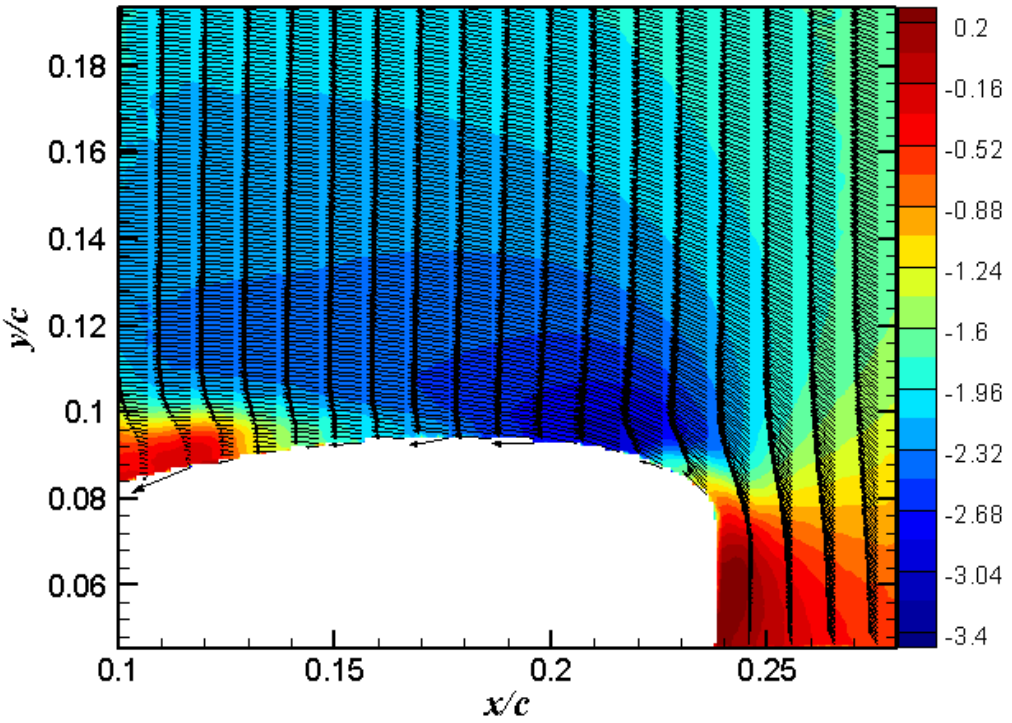

Figure 90. Vectors for α = 18°, upstroke, partially separated, over *U*-velocity contour

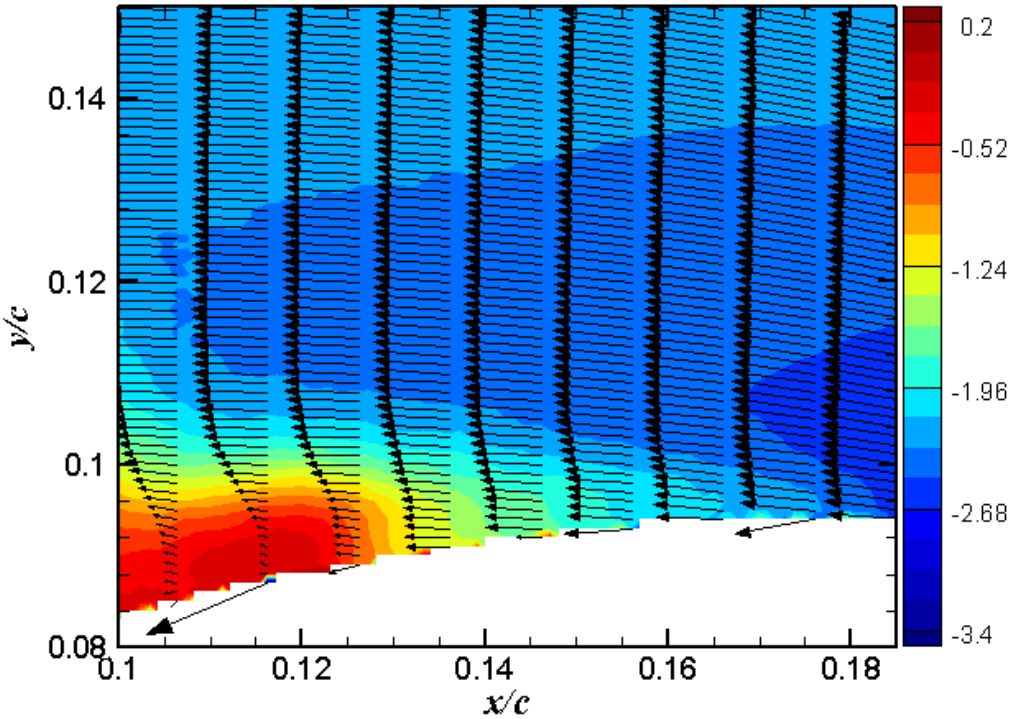

Figure 91. Zoom of boundary layer vectors for α = 18°, upstroke, partially separated, over *U*-velocity contour

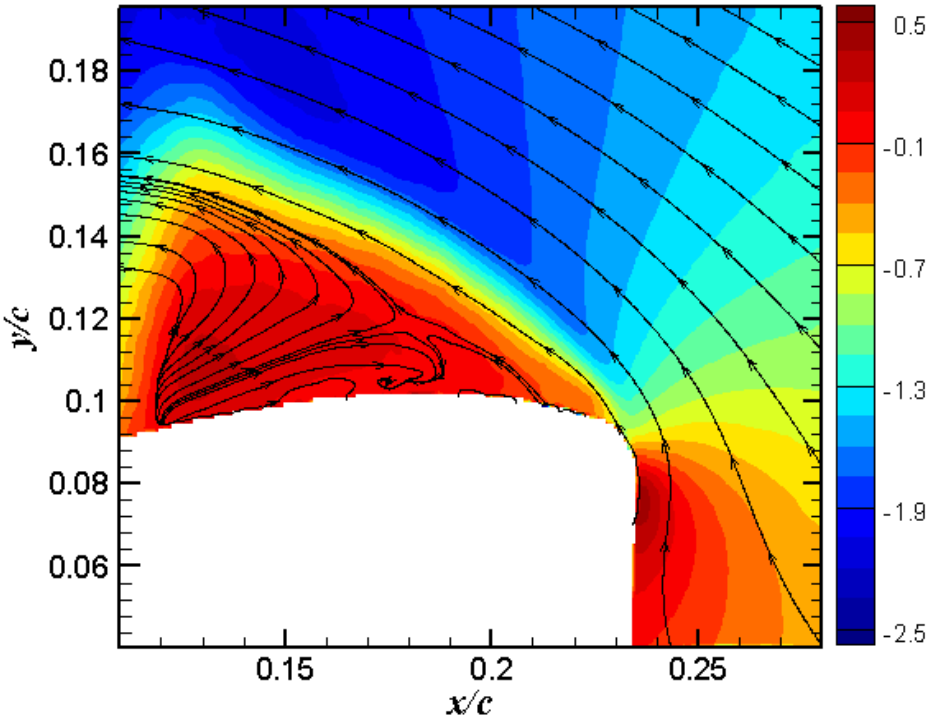

Figure 92. Streamlines for α = 20°, upstroke, over *U*-velocity contour

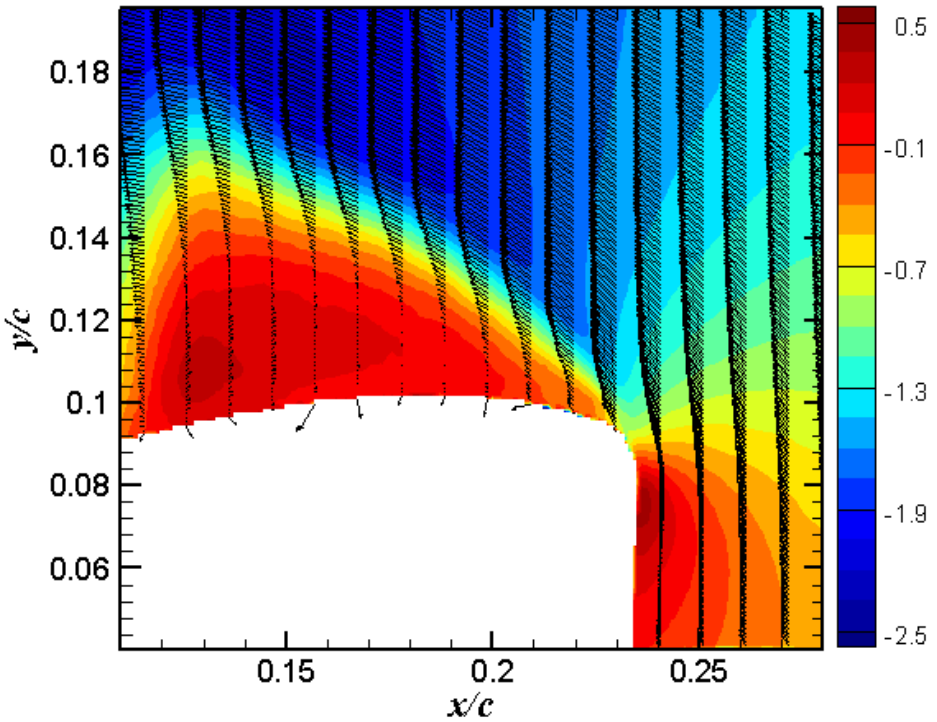

Figure 93. Vectors for α = 20°, upstroke, over *U*-velocity contour

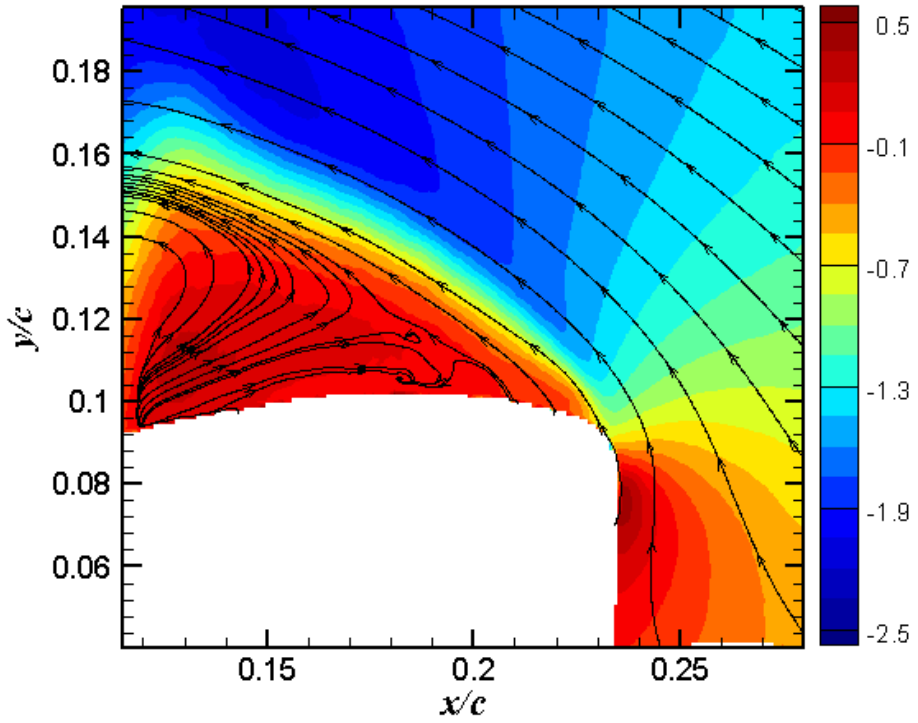

Figure 94. Streamlines for α = 20°, upstroke, fully separated, over *U*-velocity contour

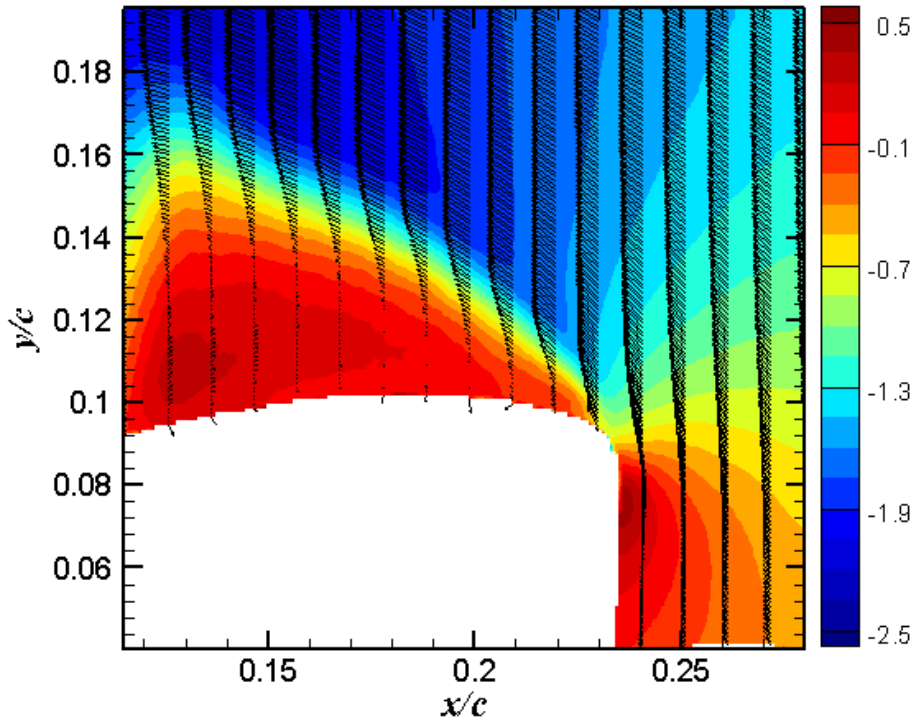

Figure 95. Vectors for α = 20°, upstroke, fully separated, over *U*-velocity contour

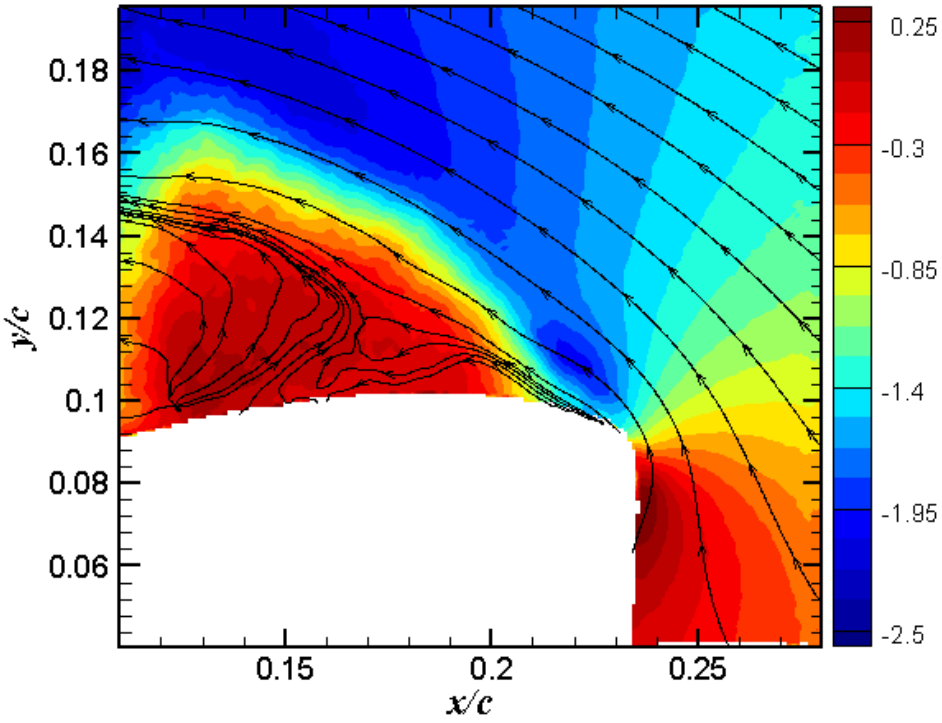

Figure 96. Streamlines for α = 20°, upstroke, partially attached, over *U*-velocity contour

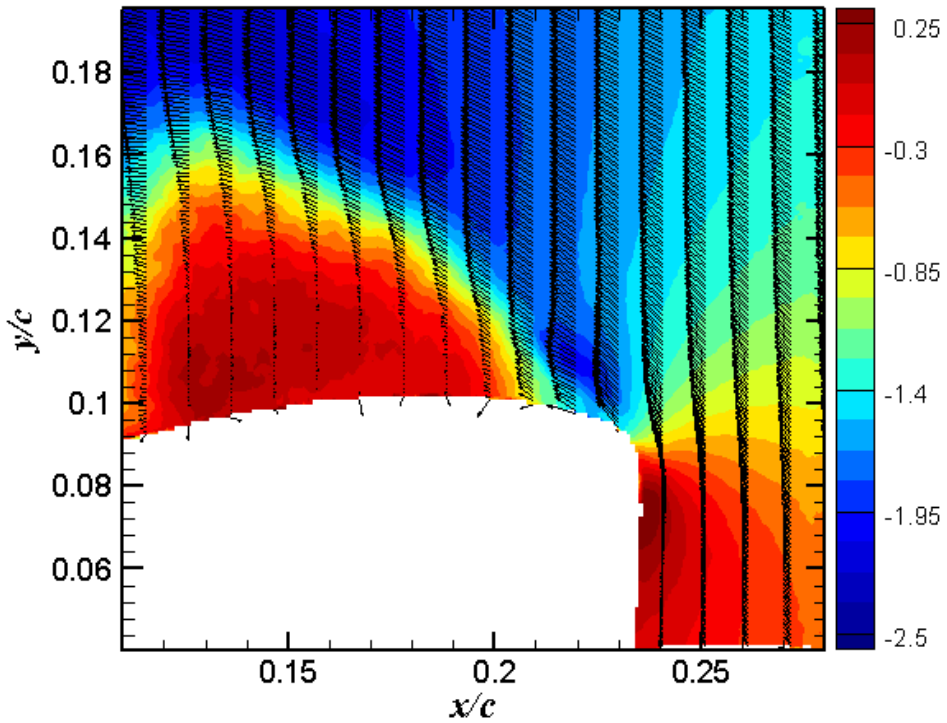

Figure 97. Vectors for α = 20°, upstroke, partially attached, over *U*-velocity contour

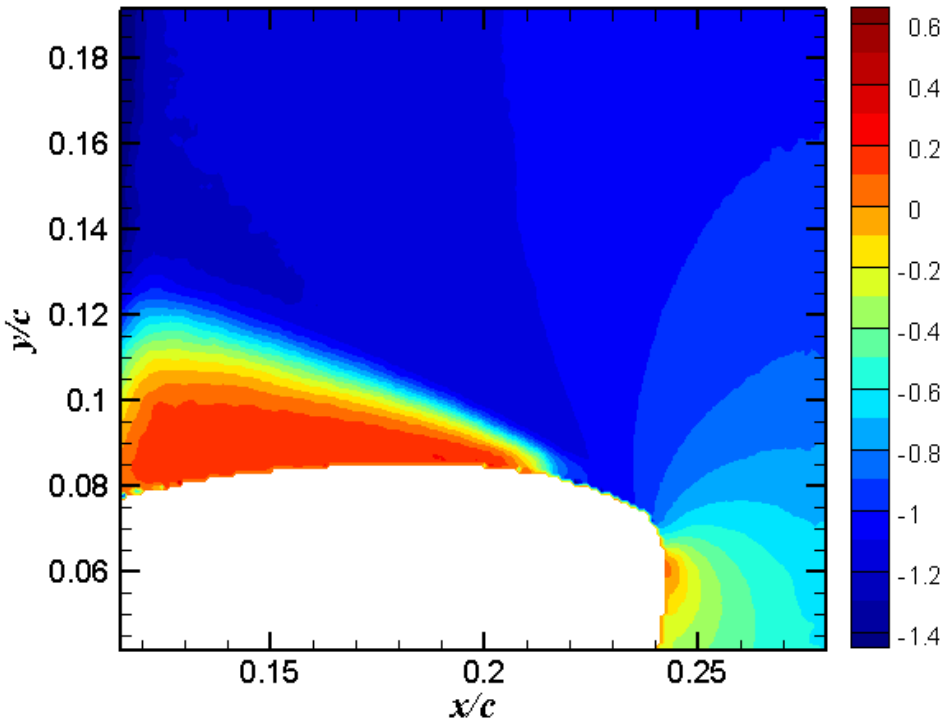

Figure 98. Normalized mean velocity component in the *x*-direction for α = 16°, downstroke

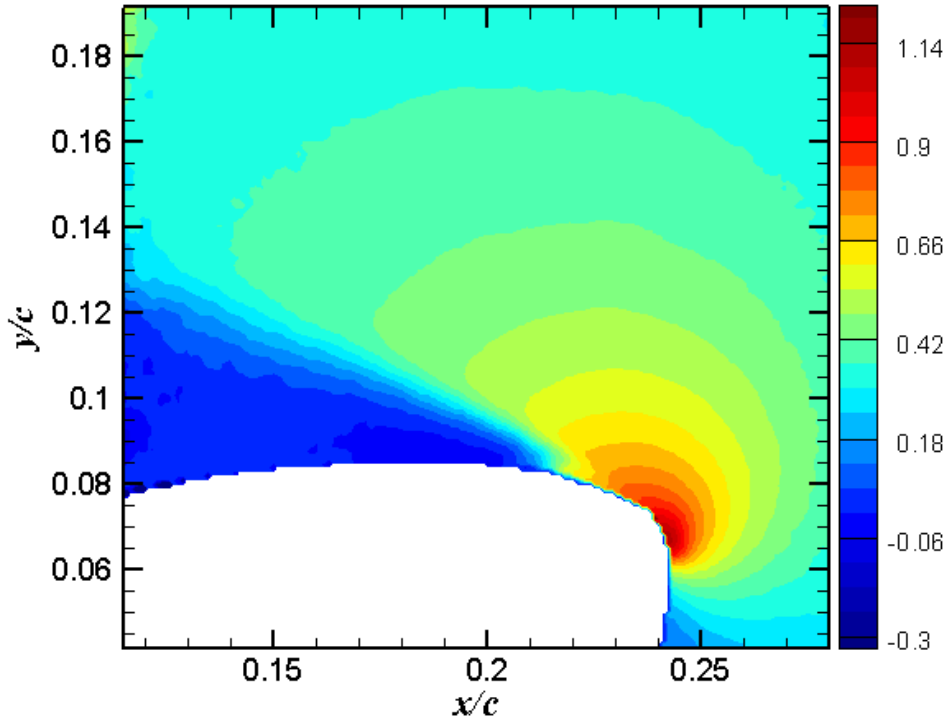

Figure 99. Normalized mean velocity component in the *y*-direction for $\alpha = 16°$, downstroke

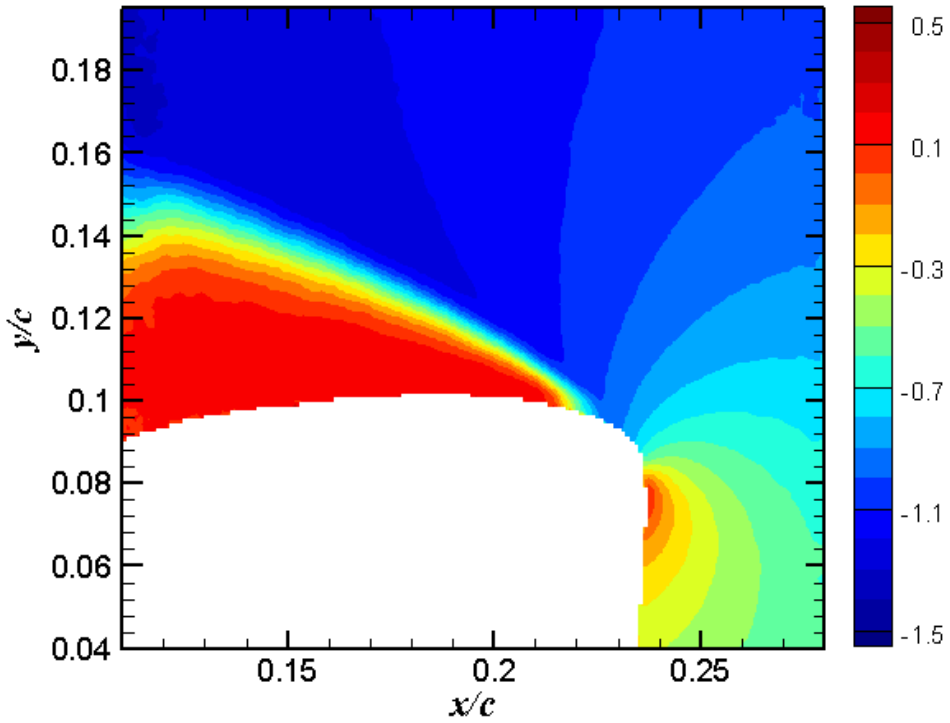

Figure 100. Normalized mean velocity component in the *x*-direction for $\alpha = 20°$, downstroke

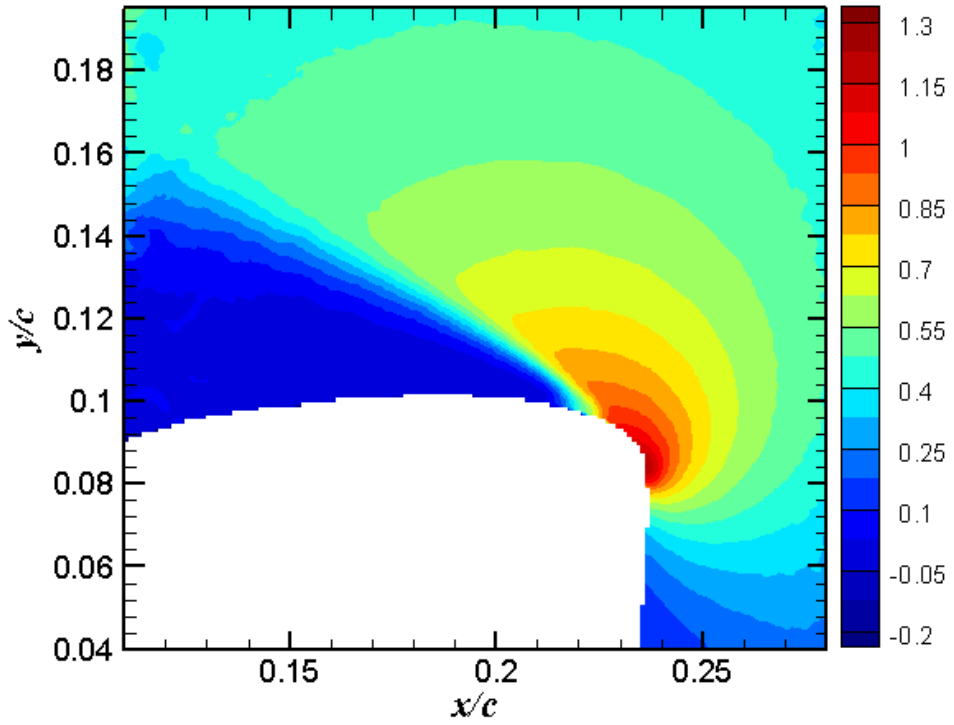

Figure 101. Normalized mean velocity component in the *y*-direction for $\alpha = 20°$, downstroke

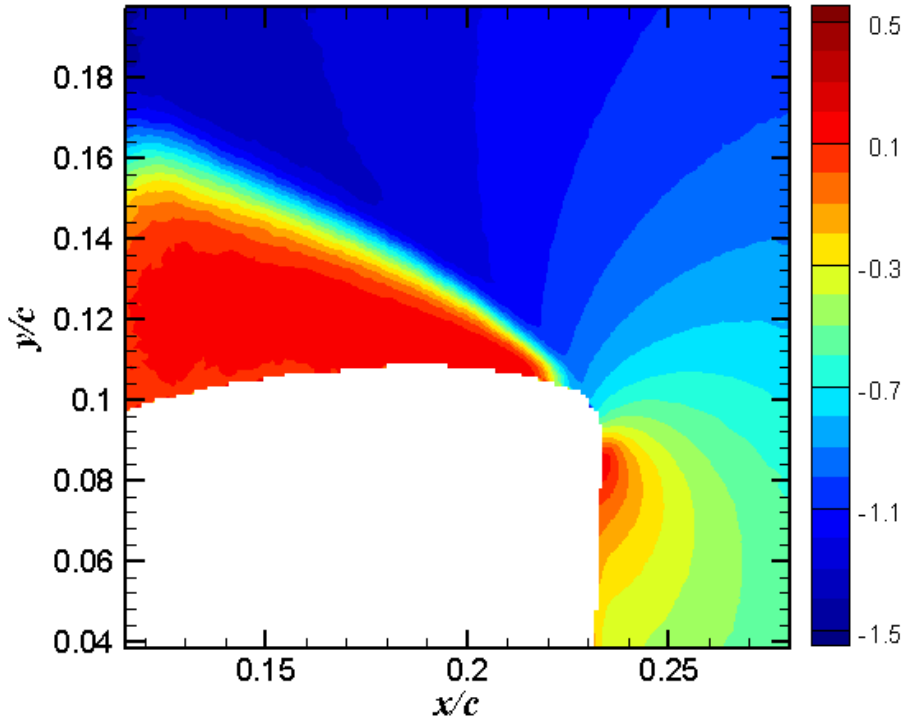

Figure 102. Normalized mean velocity component in the *x*-direction for $\alpha = 22°$, downstroke

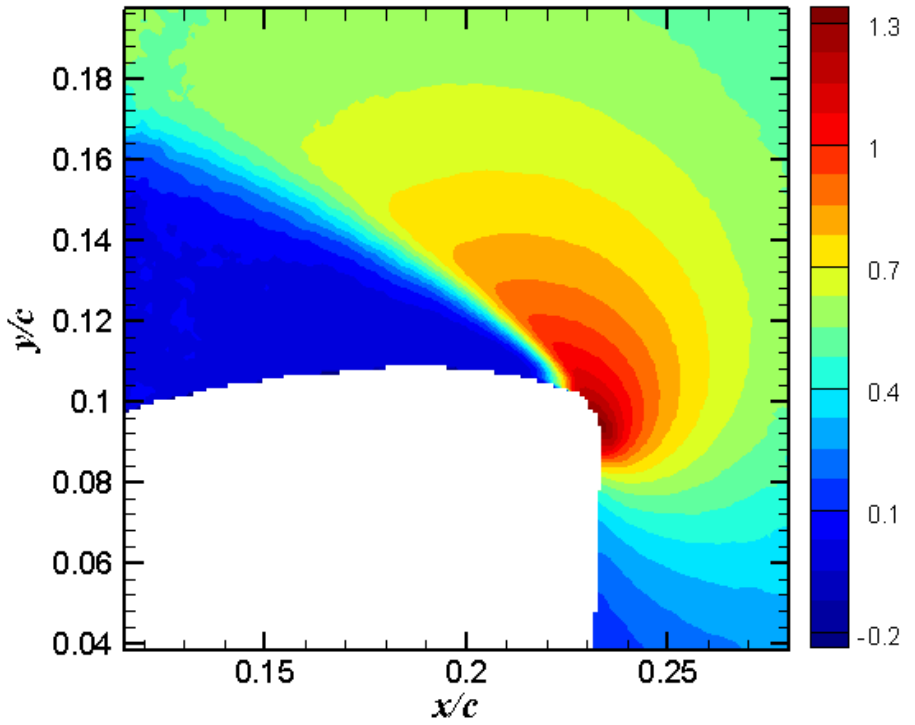

Figure 103. Normalized mean velocity component in the *y*-direction for $\alpha = 22°$, downstroke

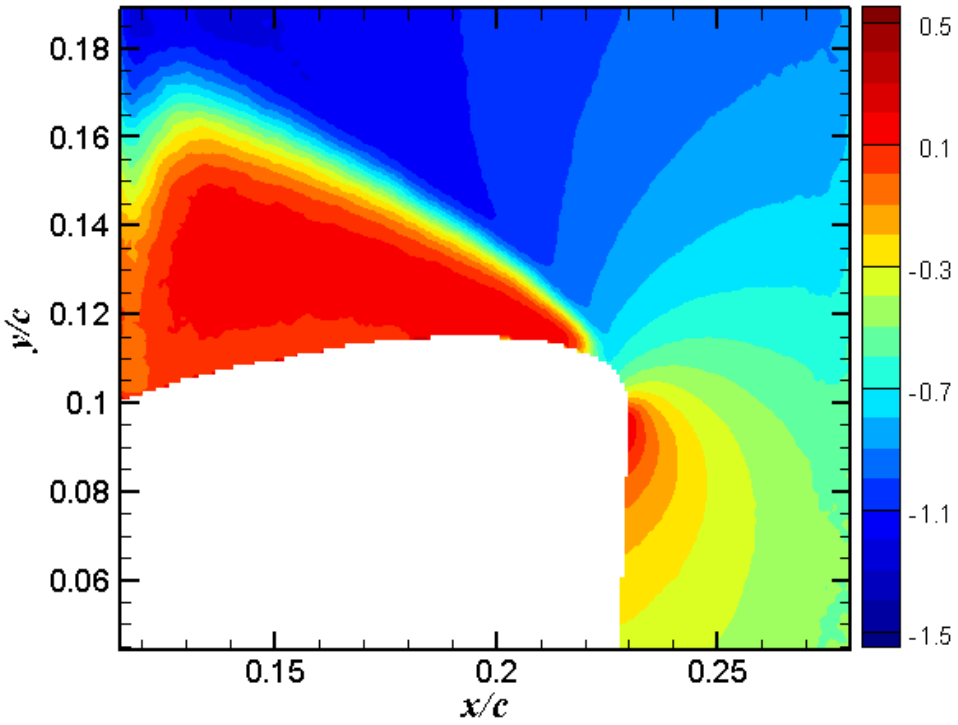

Figure 104. Normalized mean velocity component in the *x*-direction for $\alpha = 24°$, downstroke

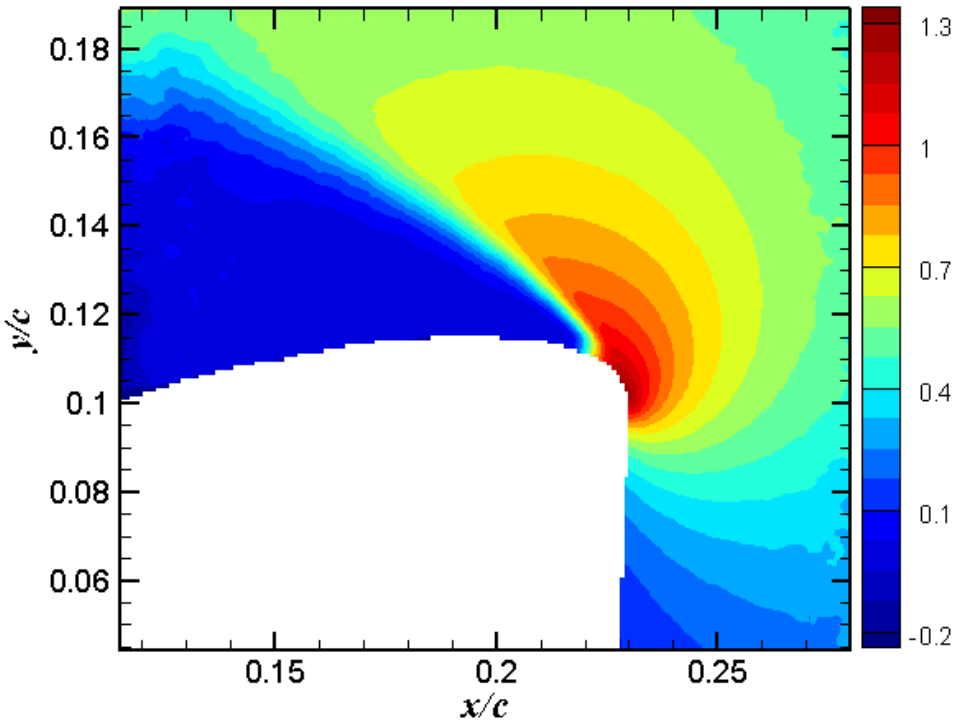

Figure 105. Normalized mean velocity component in the *y*-direction for $\alpha = 24°$, downstroke

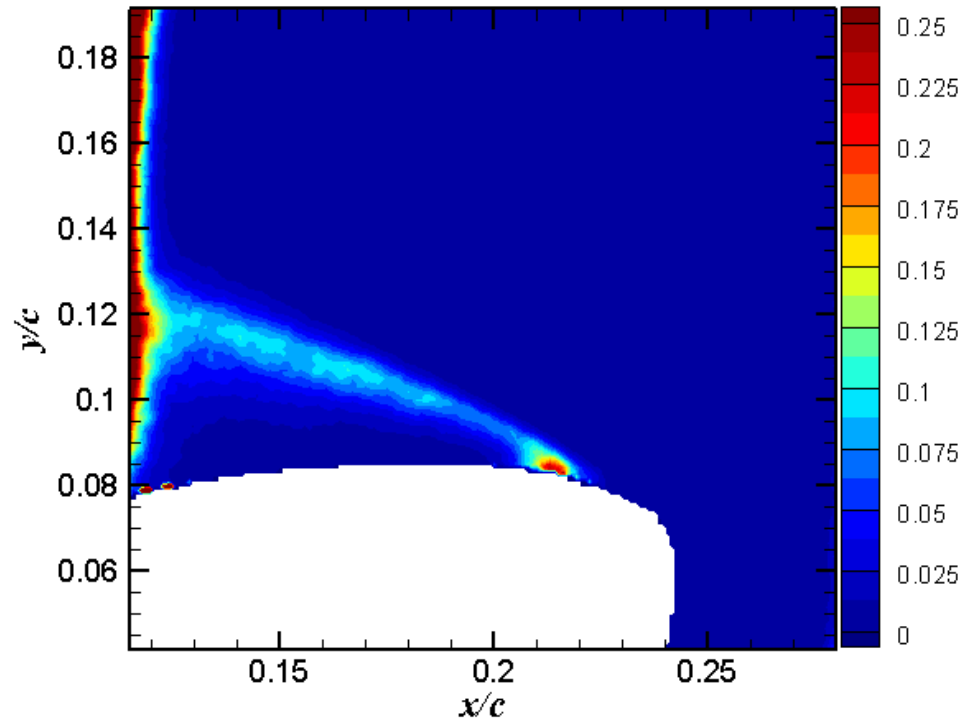

Figure 106. σ_u for $\alpha = 16°$, downstroke

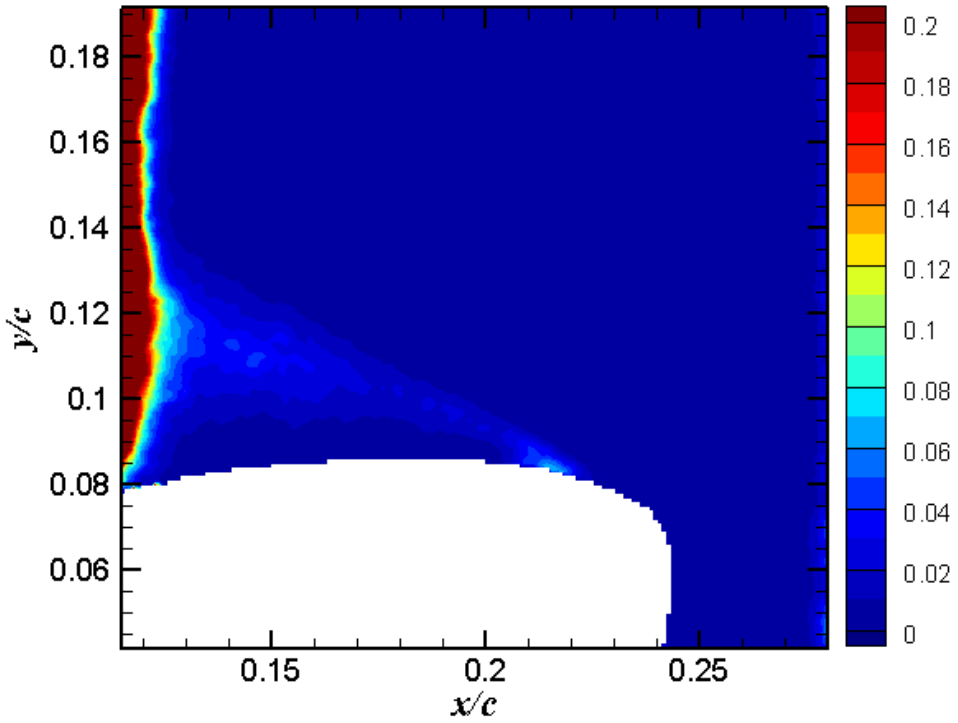

Figure 107. σ_y for $\alpha = 16°$, downstroke

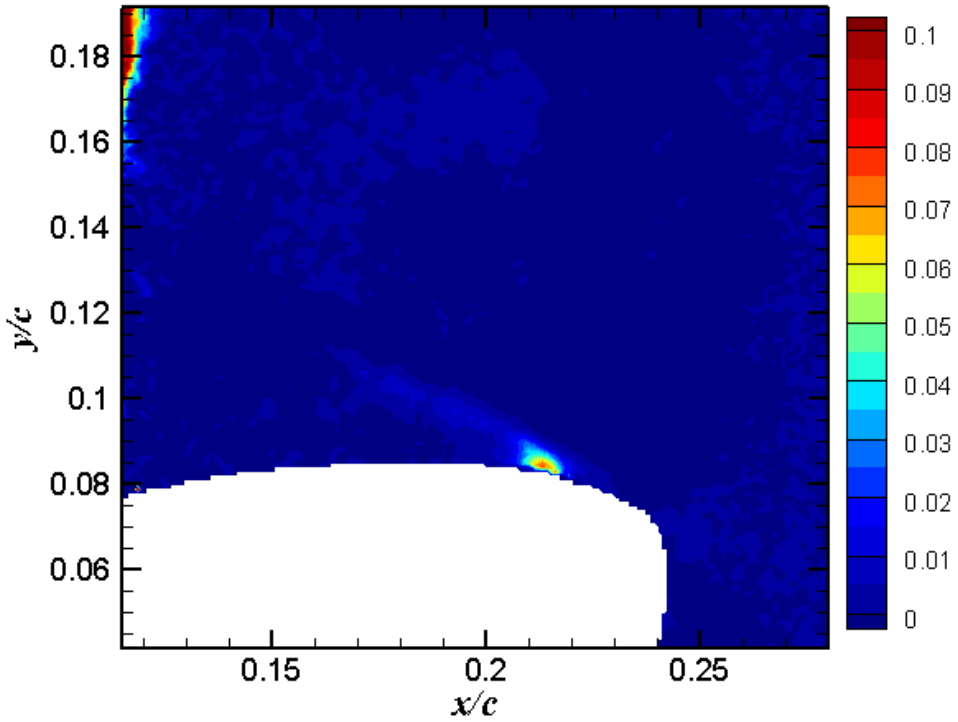

Figure 108. τ_{xy} for $\alpha = 16°$, downstroke

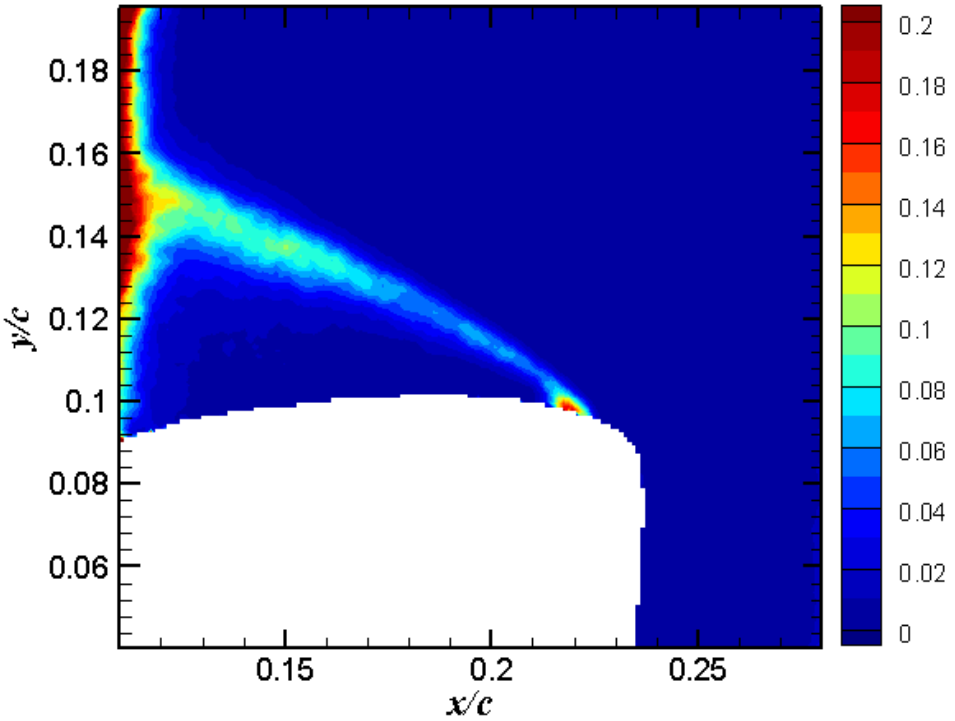

Figure 109. σ_u for $\alpha = 20°$, downstroke

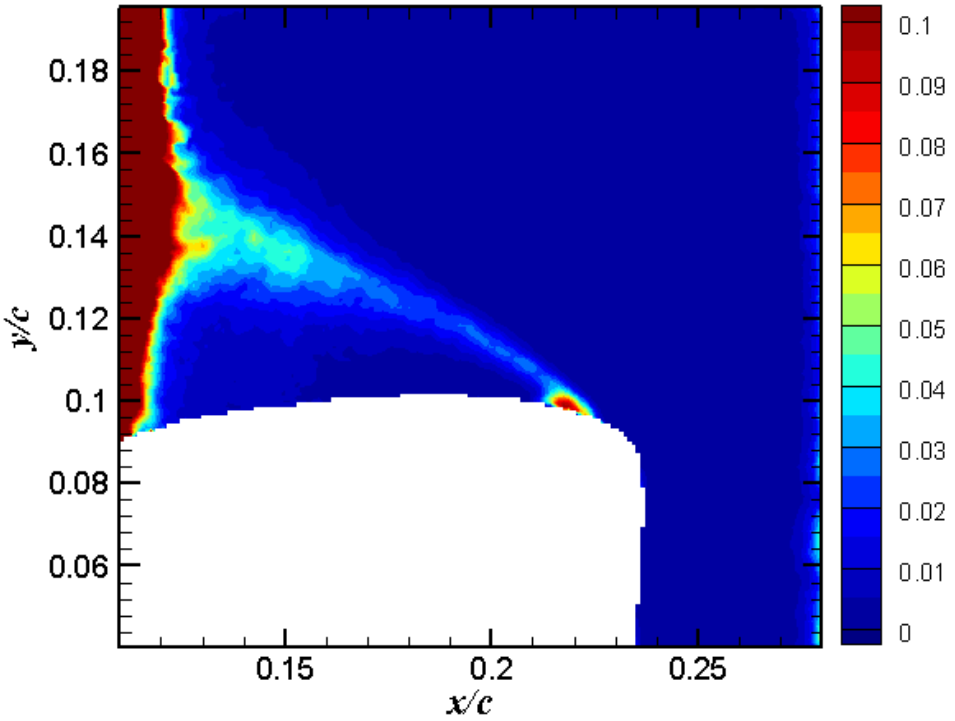

Figure 110. σ_v for $\alpha = 20°$, downstroke

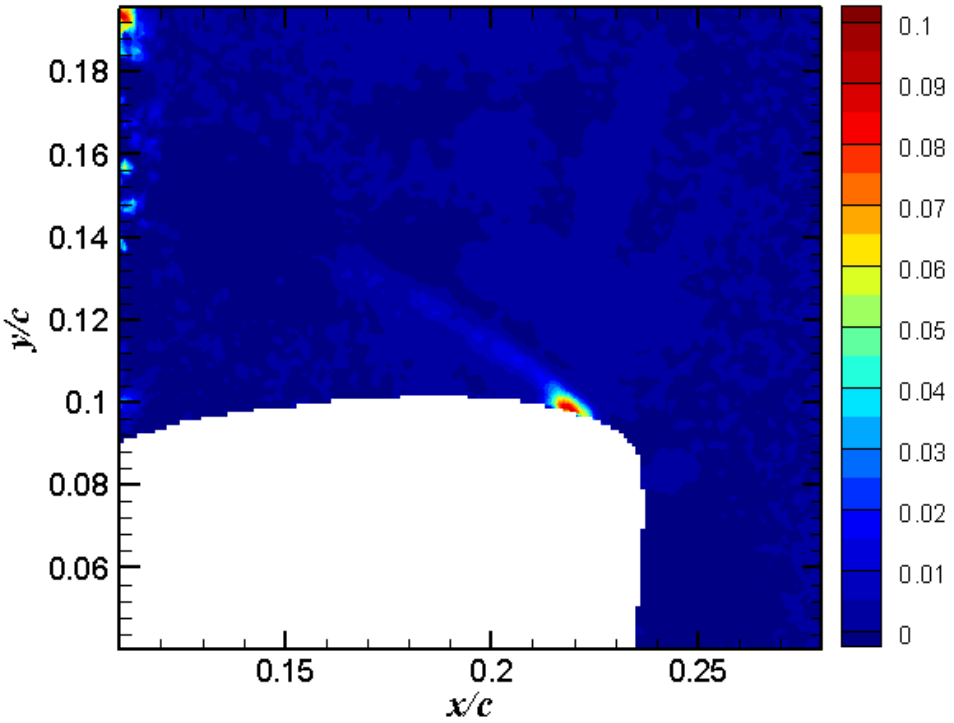

Figure 111. τ_{xy} for $\alpha = 20°$, downstroke

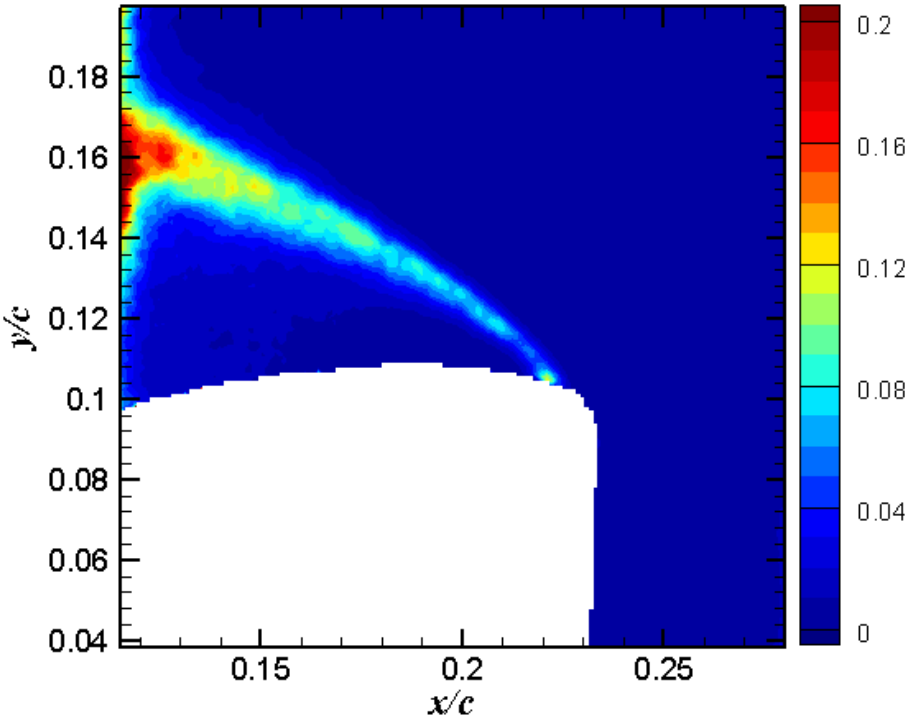

Figure 112. σ_u for $\alpha = 22°$, downstroke

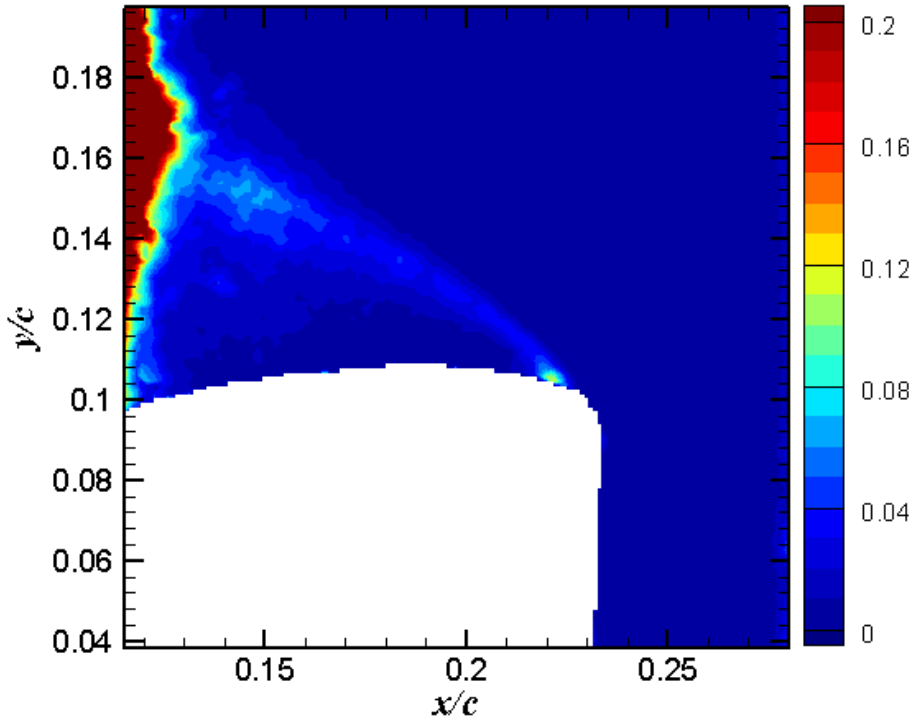

Figure 113. σ_v for $\alpha = 22°$, downstroke

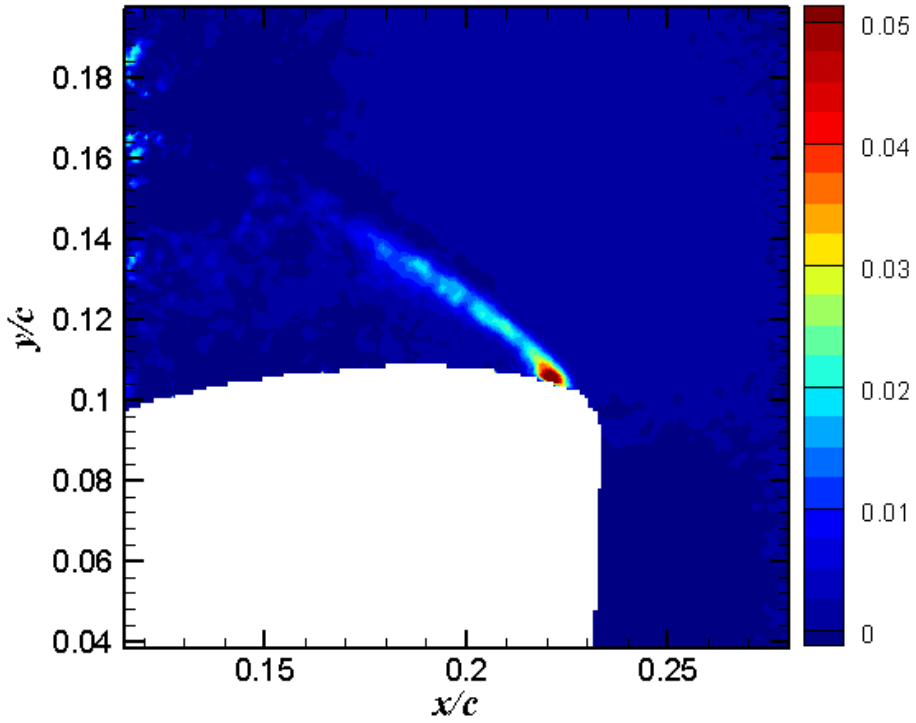

Figure 114. τ_{xy} for $\alpha = 22°$, downstroke

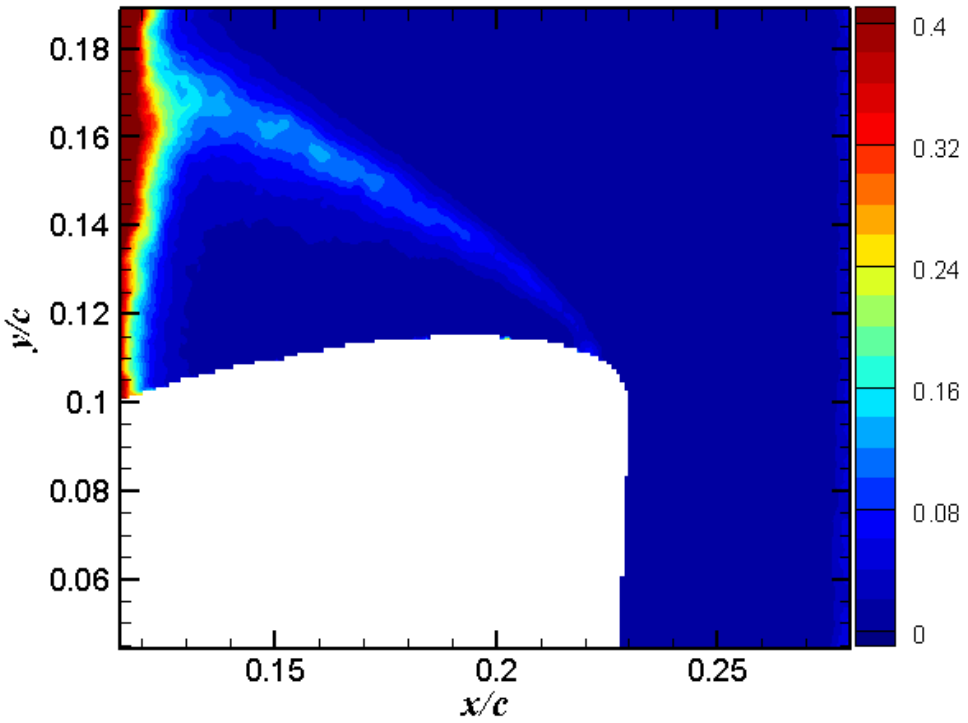

Figure 115. σ_u for $\alpha = 24°$, downstroke

Figure 116. σ_v for $\alpha = 24°$, downstroke

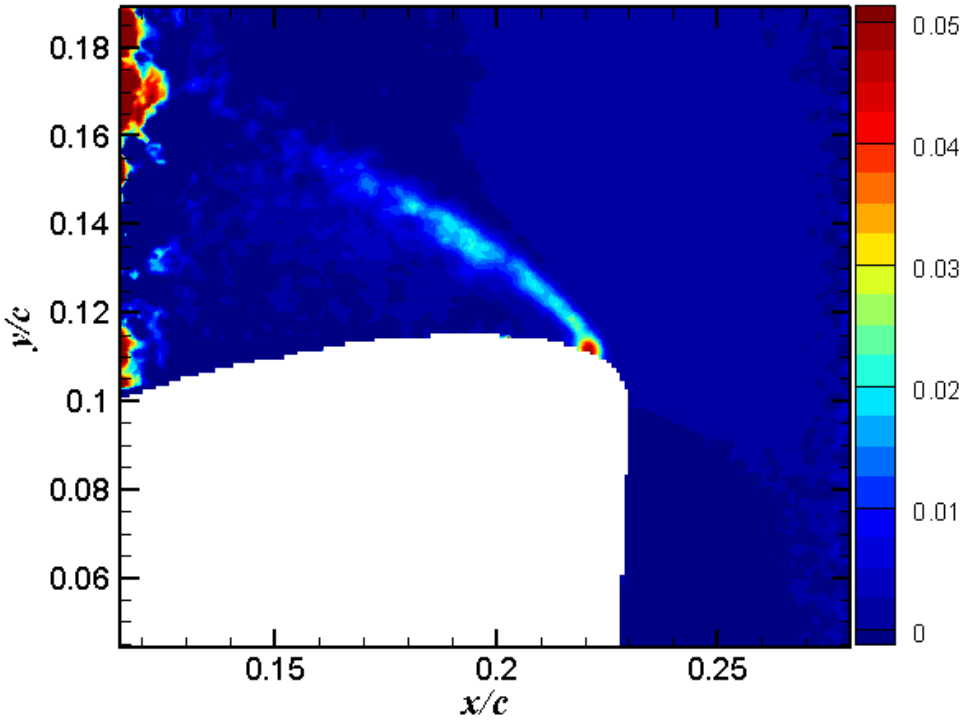

Figure 117. τ_{xy} for α = 24°, downstroke

Table 1. Upper and Lower Surface Coordinates of Sikorsky SSC-A09 Airfoil, Normalized by Chord

x/c Coordinate	*y/c upper* Coordinate	*y/c lower* Coordinate
0.000000	0.000000	0.000000
0.000199	0.002000	-0.001454
0.000798	0.003946	-0.002869
0.001994	0.006482	-0.004573
0.002991	0.008029	-0.005446
0.004487	0.009868	-0.006445
0.006979	0.012392	-0.007703
0.009970	0.014921	-0.008877
0.015952	0.019076	-0.010704
0.021934	0.022500	-0.012175
0.027916	0.025445	-0.013447
0.033898	0.028039	-0.014588
0.039881	0.030369	-0.015631
0.045863	0.032494	-0.016594
0.051845	0.034449	-0.017487
0.057827	0.036249	-0.018314
0.067797	0.038903	-0.019568

Table 1. Continued

x/c Coordinate	*y/c upper* Coordinate	*y/c lower* Coordinate
0.077767	0.041143	-0.020691
0.087737	0.043016	-0.021706
0.097707	0.044583	-0.022638
0.112663	0.046504	-0.023910
0.127618	0.048054	-0.025064
0.142573	0.049345	-0.026124
0.157529	0.050444	-0.027104
0.172485	0.051385	-0.028013
0.187440	0.052184	-0.028853
0.202395	0.052860	-0.029628
0.217350	0.053427	-0.030339
0.232305	0.053911	-0.030988
0.247261	0.054322	-0.031579
0.277171	0.054958	-0.032594
0.307082	0.055369	-0.033402
0.336992	0.055564	-0.034007
0.376873	0.055494	-0.034506
0.416754	0.055039	-0.034637
0.436694	0.054663	-0.034558
0.456635	0.054182	-0.034376
0.476575	0.053595	-0.034087
0.496515	0.052899	-0.033683
0.516456	0.052093	-0.033165
0.536396	0.051176	-0.032532
0.556336	0.050149	-0.031790
0.576277	0.049009	-0.030949
0.596217	0.047755	-0.030018
0.616157	0.046381	-0.029002
0.636097	0.044875	-0.027904
0.656039	0.043220	-0.026720
0.675979	0.041391	-0.025448
0.695919	0.039368	-0.024088
0.715860	0.037140	-0.022642
0.735800	0.034719	-0.021121
0.755740	0.032138	-0.019540
0.775680	0.029445	-0.017918
0.795621	0.026681	-0.016272
0.815561	0.023871	-0.014617
0.835501	0.021012	-0.012957
0.855442	0.018089	-0.011289
0.875382	0.015093	-0.009598

Table 1. Continued

x/c Coordinate	*y/c upper* Coordinate	*y/c lower* Coordinate
0.895323	0.012051	-0.007863
0.915264	0.009046	-0.006081
0.935204	0.006229	-0.004290
0.955144	0.003849	-0.002610
0.975084	0.002288	-0.001325
0.985055	0.001987	-0.000992
0.995025	0.002135	-0.000863
1.000000	0.002408	-0.000803
0.000000	0.000000	0.000000

Table 2. SSC-A09 Testing Model Specifications

Parameter	SI Units	Imperial Units
Chord Length	0.46 m	18 in
Span	2.13 m	6 ft 11 ¾ in
Mass/Weight	81.6 kg	180 lbf
Mass Moment of Inertia, about *c*/4	521.1 N-m	4612 in-lb

Table 3. Testing Matrix

Case	M_∞	Re_c ($\times 10^6$)	α (°)	k	f (Hz)	Data Acquired at α[a]
I	0.1	1.0	Static	0	N/A	0-20
II	0.1	1.0	$\alpha = 10 \pm 10 sin(2\pi ft)$	0.1	2.5	12-18
III	0.1	1.0	$\alpha = 15 \pm 10 sin(2\pi ft)$	0.1	2.5	16-24[b]

[a]2.0° increments

[b]No downstroke data acquired for $\alpha = 18°$

Table 4. Results of PIV Processing Parameter Study

Parameter	Most Effective Setting
Window size (in pixels)	128×128 → 64×64 → 32×32 → 16×16
Window shape	Adaptive
Overlap	50%
Number of passes at each window size	2
Smoothing	On
Delete vectors	$Q < 1.0$
Remove groups with	< 5 vectors
Interpolate	On (Fill-up empty spaces)

Table 5. Uncertainty Estimates for $\alpha = 18°$

Parameter	Uncertainty		
	@ $x/c = 0.21$, $y/c = 0.095$	@ $x/c = 0.14$, $y/c = 0.095$	@ $x/c = 0.24$, $y/c = 0.17$
α (°)	0.1	0.1	0.1
x, y	0.5%	0.5%	0.5%
U, V	0.5%	1.0%	0.5%
$\overline{u'u'}, \overline{v'v'}$	2.5%	2.5%	2.5%
$\overline{u'v'}$	5%	5%	5%

Table 6. Uncertainty Estimates for $\alpha = 20°$

Parameter	Uncertainty		
	@ $x/c = 0.23$, $y/c = 0.1$	@ $x/c = 0.14$, $y/c = 0.1$	@ $x/c = 0.21$, $y/c = 0.175$
α (°)	0.1	0.1	0.1
x, y	0.5%	0.5%	0.5%
U, V	1.5%	1.5%	0.5%
$\overline{u'u'}, \overline{v'v'}$	3%	3%	2.5%
$\overline{u'v'}$	8%	8%	5%

APPENDIX B

DSF OPERATING INSTRUCTIONS

B.1 Google Chat

Google Chat is used for communication between the two computer users operating the computers for pitching the wing and data collection, as these two computers are located on opposite sides of the low speed wind tunnel.

B.1.1 Google Chat Usernames and Passwords

For wing driving computer (near side of wind tunnel):

DSF.TAMU@gmail.com

Password: WeAreSahoo3.0

For data collecting computer (far side of wind tunnel):

NAL.TAMU@gmail.com

Password: AirSoxOne

B.1.2 Communication Procedure

DSF – choose appropriate event step settings (file)

Give angle and upstroke/downstroke to NAL

NAL – Create folder

Tell DSF how much seeding (in seconds) to put into flow

DSF – Add seeding

Give OK to take images

NAL – take desired number of batches of images (typically 3-4)

Notify DSF when all images have been captured

Repeat for each angle for upstroke and downstroke.

B.2 General Checklist

- Photograph installation process.
- Empty hydraulic oil (Chevron Rykon ISO 46) from unit.
- Move blue bolt box to wind tunnel ready room.
- Install 7×7 foot wind tunnel test section. For instructions see Sahoo's Dissertation (Ref. 43).
- Move hydraulic unit to ready room.
    - Leave linear actuator attached to hydraulic unit (disconnect from wing) and move upstairs together.
    - Once upstairs, refill with hydraulic oil.
- Move wing driving computer station to ready room (on near side of tunnel by hydraulic unit).
- Move PIV data collection computer to ready room (on far side of tunnel).
- Insert wing prior to inserting side panels.

- Move optics system to tunnel.
- Connect hydraulic unit to power (480 V).
- Make connections according to following sections.
- Make sure cracks/gaps in wind tunnel test section are sealed with aluminum tape.

B. 3 Hydraulic System

- Hydraulic Servo Valve connected to Control Box
- Computer connected to Control Box (DB15 wire)
- Servo Valve on tank to Power Supply
- Control Box to Power Supply
- Accumulator Valve is perpendicular to flow direction
- Check all fittings are tight
- Power on
- Run motor (warm-up) for 30 minutes at low pressure
- Set the pressure to 2000 psi (black knob)
- *After testing is complete for the day turn pressure back down to minimum and turn off hydraulic unit*

B.4 RMC100 Instrumentation Circuit

- "+ out 0" on bottom of RMC100 (red connector) goes to positive terminal of the 5 Volt power supply.

- "– out 0" on bottom of RMC100 (black connector) goes to positive (red) alligator clip attached to BNC cable.
- Negative terminal of the 5 Volt power supply goes to negative (black) alligator attached to BNC cable.
- The above BNC goes to EXT/GATE of quantum composer.
- Set the power supply voltage to 5.000 V.

B.5 Quantum Composer (settings for SSC-A09 testing conducted in R. Vannelli's M.S. Thesis)

- Connections
  - T1 → FL1 (Flash Lamp 1)
  - T2 → FL2 (Flash Lamp 2)
  - T4 → QS2 (Q-switch 2)
  - T8 → QS1 (Q-switch 1)
  - T6 → Camera (pco.1600)

B.5.1 For Static Data

- Global mode – CONTINUOUS
- External triggering – OFF
- Change delay time as necessary
  - Delay time changes based on flow field time separation of particles in desired field of view.

B.5.2 For Dynamic Data

- **Global settings**
  - Mode – BURST
    - #/pulse = 1
  - Ext in – TRIGGERED
  - Trig – RISING EDGE
- **T1**
  - Gate – DISABLED
  - Channel – ENABLED
  - Sync – T_0
  - Delay – 0 µs
  - Width – 20 µs
  - Mode – NORMAL
  - Wait – 0 PULSES
  - Polarity – ACTIVE HIGH
  - Amplitude – 5.0 Volts
  - Mux – 1
- **T2**
  - Gate – DISABLED
  - Channel – ENABLED
  - Sync – T1
  - Delay – 20 µs

- Width – 20 µs
- Mode – NORMAL
- Wait – 0 PULSES
- Polarity – ACTIVE HIGH
- Amplitude – 5.0 Volts
- Mux – 10

- **T4**
  - Gate – DISABLED
  - Channel – ENABLED
  - Sync – T1
  - Delay – 220 µs
  - Width – 20 µs
  - Mode – NORMAL
  - Wait – 0 PULSES
  - Polarity – ACTIVE HIGH
  - Amplitude – 5.0 Volts
  - Mux – 1000

- **T8**
  - Gate – DISABLED
  - Channel – ENABLED
  - Sync – T1
  - Delay – 200 µs

- Width – 20 µs
- Mode – NORMAL
- Wait – 0 PULSES
- Polarity – ACTIVE HIGH
- Amplitude – 5.0 Volts
- Mux – 1000 0000

- **T6**
  - Gate – DISABLED
  - Channel – ENABLED
  - Sync – T1
  - Delay – 180 µs
  - Width – 20 µs
  - Mode – NORMAL
  - Wait – 0 PULSES
  - Polarity – ACTIVE HIGH
  - Amplitude – 5.0 V
  - Mux – 10 0000

B.6 CamWare 2.19 (settings for SSC-A09 testing conducted in R. Vannelli's M.S. Thesis)

- Camera Control
  - External Exp. Start
    - Exposure – 5.3 µs

        - Delay – 10 μs
    - Sensor (Misc.)
        - ADC Converter – 2
    - Recording
        - Mode – SEQUENCE
        - Acquire – AUTO
        - NO TIMESTAMP
- To SAVE – EXPORT RECORDER, SPLIT double shutter images

B.7 Testing Environment and RMCWin

B.7.1 General RMCWin Commands

- G – Step to command value position
- E – Execute
- K – Kill
- O – Override/Open command (takes linear actuator to highest position)

B.7.2 Calibration Instructions

Need to calibrate for each wing at each tunnel entry.

1. Open the MS Excel file "Calibration 06-2010."
2. Measure the height of the wind tunnel test section.
    a. Divide this number by 2 and input into cell B12.

b. When trailing edge of wing is at this height, the angle of attack is zero degrees.

c. Attempt to achieve this height using the "G" command and note the number of counts of the linear actuator in the Excel file in cell B13.

3. Using the "G" command in RMCWin, go to linear actuator counts of approximately 100, and 200 to 1400 in steps of 200. (100, 200, 400, 600, …, 1400).

   a. At each step note the Y position of the trailing edge in the Excel file provided.

4. Excel will calculate the value of DY and the angle.

5. Plot counts vs. angle of attack and line fit the data points in Excel.

   a. This line fit gives you the equation: $counts = slope \times \alpha + zero\_count$.

6. Input this slope into the Excel worksheet in cell B14.

7. Plot angle of attack vs. counts and line fit the data points.

   a. This line fit gives you the equation: $\alpha_{fit} = slope \times counts + zero\_\alpha$.

8. Put this new slope in cell B15 and zero_alpha in B16 to compute the fitted angle of attack and the error.

OR

1. Zero out the inclinometer on the wind tunnel floor, just below the wing leading edge.
2. Using the "G" command in RMCWin, go to linear actuator counts of approximately 100, and 200 to 1400 in steps of 200. (100, 200, 400, 600, …, 1400).
    a. At each step measure the angle of attack of the wing with the inclinometer.
        i. For the NACA 0012 – remove the Plexiglas insert and measure the angle along the flat surface that runs along the wing chord.
        ii. For the SSC-A09 – measure on one of the gloves at either end of the wing.
3. Plot counts vs. angle of attack and line fit the data points in Excel.
    a. This line fit gives you the equation: $counts = slope \times \alpha + zero\_count$.
4. Input this slope into the Excel worksheet in cell B14.
5. Plot angle of attack vs. counts and line fit the data points.
    a. This line fit gives you the equation: $\alpha_{fit} = slope \times counts + zero\_\alpha$.
6. Put this new slope in cell B15 and zero_alpha in B16 to compute the fitted angle of attack and the error.
7. Verify the angles of attack for the testing angles using the same inclinometer.

B.7.3 Recording Testing Conditions

1. Open the file labeled “Test Condition 06-2010” in MS Excel.
    a. Type over the old conditions listed in this file.
2. Record the wind tunnel run.
3. Record the date and time.
4. Record the temperature in °F.
5. Record the measured freestream velocity, lowest count position and amplitude, in counts, of the sine wave the wing travels through.
6. Acquire data file from the wind tunnel staff. – *Make sure they are aware you are going to want the data file BEFORE testing begins.*

B.7.4 Wing Operating Instructions

1. Open RMCWin from Start menu.
2. Open “4 JUNE 2010.bd1” (found in “ARO Wing Testing 2010_June 11-June16” folder).
    a. Click “P” button at top of RMCWin window to set parameters.
3. Calibrate the linear actuator.
    a. Run the open loop command (“O”). Go to the lowest position of the cylinder (0). Note the count.
    b. Go to the maximum position (1500). Run in open loop with “O” COMMAND. Note the count.

c. Input those values in the calibration window (Tools→Position/Scale Offset Calibration-Axis0). Click "Apply" and the software is calibrated.

4. Open Event Steps Editor (in Tools menu).
   a. Open appropriate file for angle of attack and up/downstroke (find: "ARO Wing Testing 2010_June 11-June16/RMCWin Files").
      i. Number following AOA is the flapping angle of attack.
      ii. Number following TRIG is at what degree the camera and laser are triggered.
   b. Edit the Event Steps files in RMCWin to appropriate counts.
      i. Change minimum number of counts (Column 4, Row 5). Should be the number of counts that equals the highest angle in the pitching range.
      ii. Change amplitude of motion (Column 5, Row 5). Number of counts at lowest angle in pitching range minus number of counts at highest angle in pitching range divided by 2.
      iii. Change angle triggering values (Row 9, Columns: 200, 201, 203, 205). Input number of counts equal to the angle of attack for the angle at which the laser should trigger.
   c. Load the module (click button 2nd from the right).
5. In RMCWin in COMMAND box (bottom left of RMCWin window).

a. COMMAND VALUE 4 200

COMMAND E E

↑ ↑

(AXIS0) (AXIS1)

i. AXIS0 operates the linear actuator.

ii. AXIS1 triggers the laser and camera.

6. "E" must be entered for both axes.
7. Save a plot and data file of the wing motion (target vs. actual position). -- Only have to save the plot file, the raw data file is embedded in it.
    a. Save these files in the folder titled "RMCWin Data."
    b. Organize by date and label with angle of attack, trigger angle, and up or down stroke. Sample: AOA10TRIG15UP .
8. Repeat steps 4-7 for each angle of attack.
    a. RMCWin will update in real time when you load the module, causing the wing to alter its behavior without the need to retype "E" in the COMMAND line.
9. Type "K" in the COMMAND line to "kill" all action.

NOTES:

- For each trigger angle of attack there is a separate event steps file (for both upstrokes and downstrokes).
- Double check the frequency before loading the module. The hydraulic actuator will follow your command even if the frequency you input is much

to high (should be 2.5 Hz, 250 in column 5 cell 4 for Mach 0.1 testing regime).

- Approximate Mach/Frequency correlations for reduced frequency, k = 0.1:
  - $M_\infty = 0.1, f = 2.5$ Hz
  - $M_\infty = 0.2, f = 5.0$ Hz
  - $M_\infty = 0.3, f = 7.5$ Hz
  - $M_\infty = 0.4, f = 10.0$ Hz

- If laser/camera are not triggering check the count in columns 200-205.
  - At high angles of attack and frequencies the wing may not reach the count.
    - This should not be a problem when operating at Mach 0.1.

APPENDIX C

PROCESSING PARAMETER AND FILTER STUDY CONTOURS

The following figures show some of the results of the processing parameter study discussed in Section 5.1. These figures are meant only to provide insight into why the parameters listed in Table 4 were chosen. The following images represent a four step correlation process down to a final interrogation area size of 16×16 pixels with a 50% overlap. Only *U*-velocity and Reynolds shear stress data for attached cases are provided. The *U*-velocity contours are all shown on a single color scale; the τ_{xy} contours are all shown on a single, different color scale.

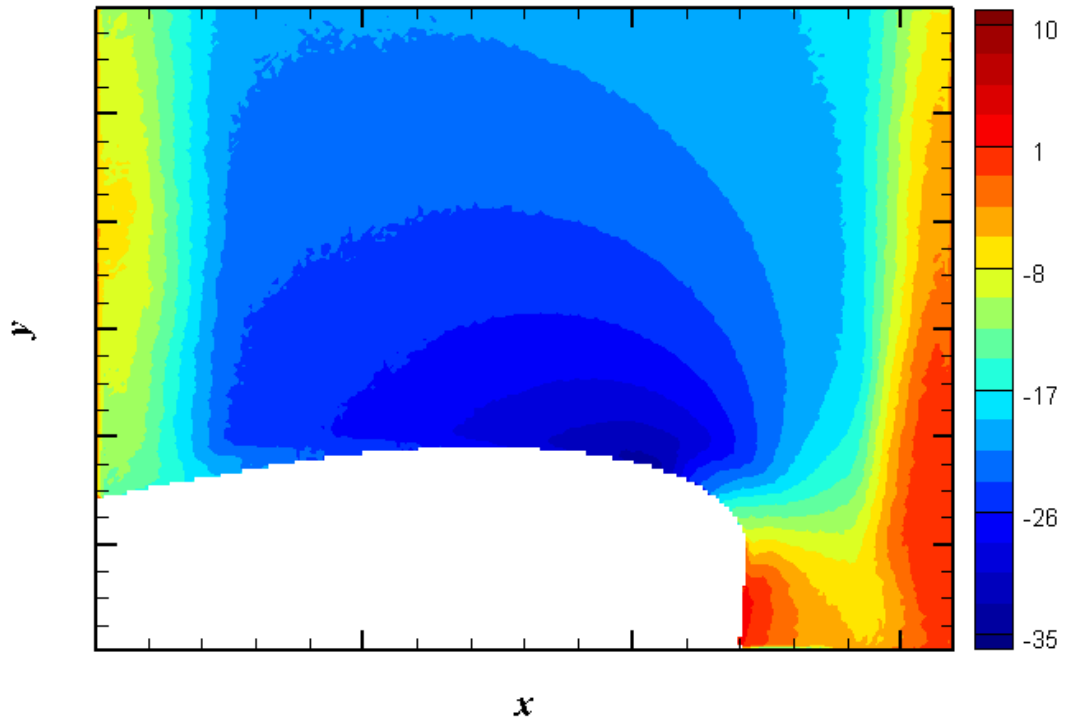

Figure C-1. *U* for α = 16° upstroke, square interrogation window, no post-processing

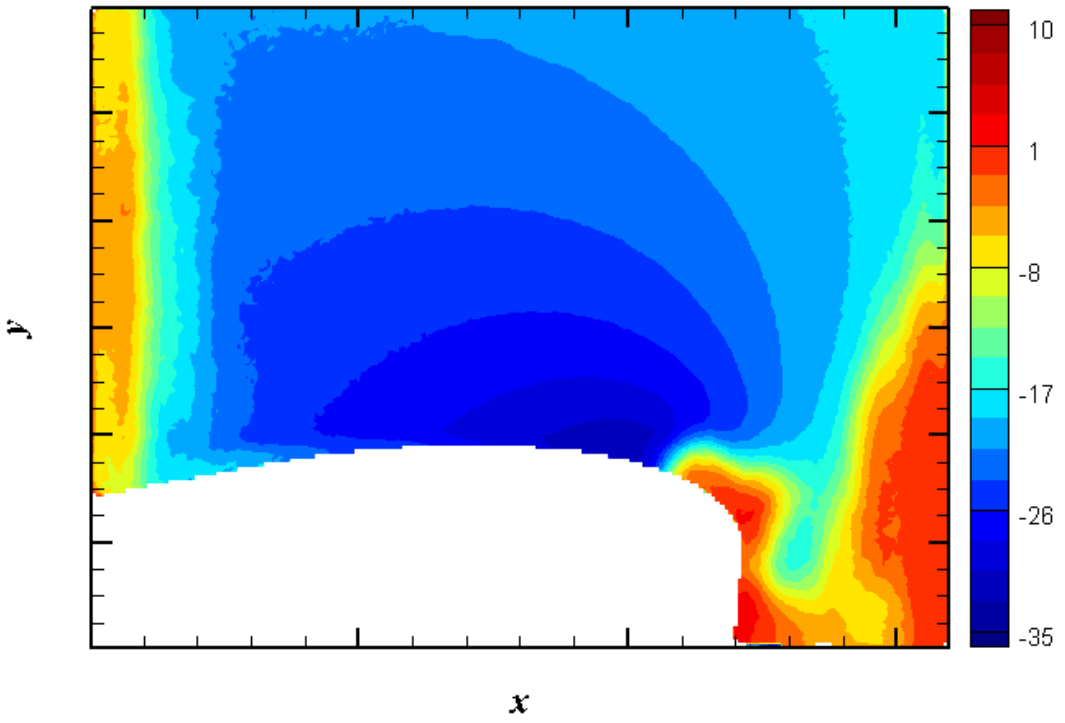

Figure C-2. *U* for α = 16° upstroke, circular interrogation window, no post-processing

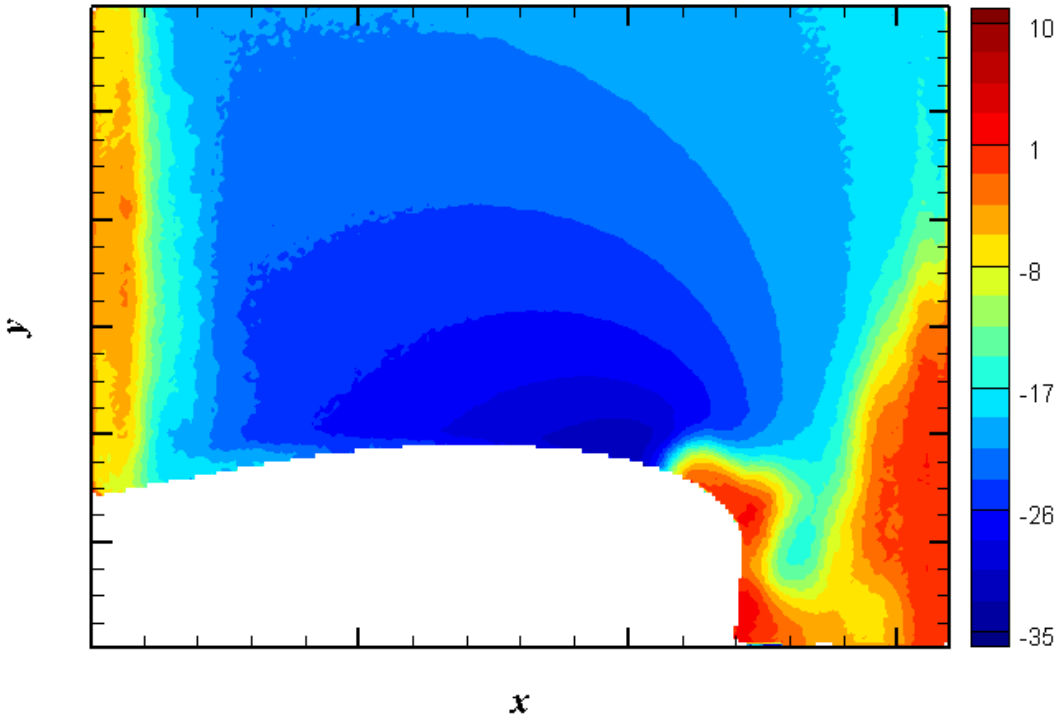

Figure C-3. *U* for α = 16° upstroke, 2:1 elliptical interrogation window, no post-processing

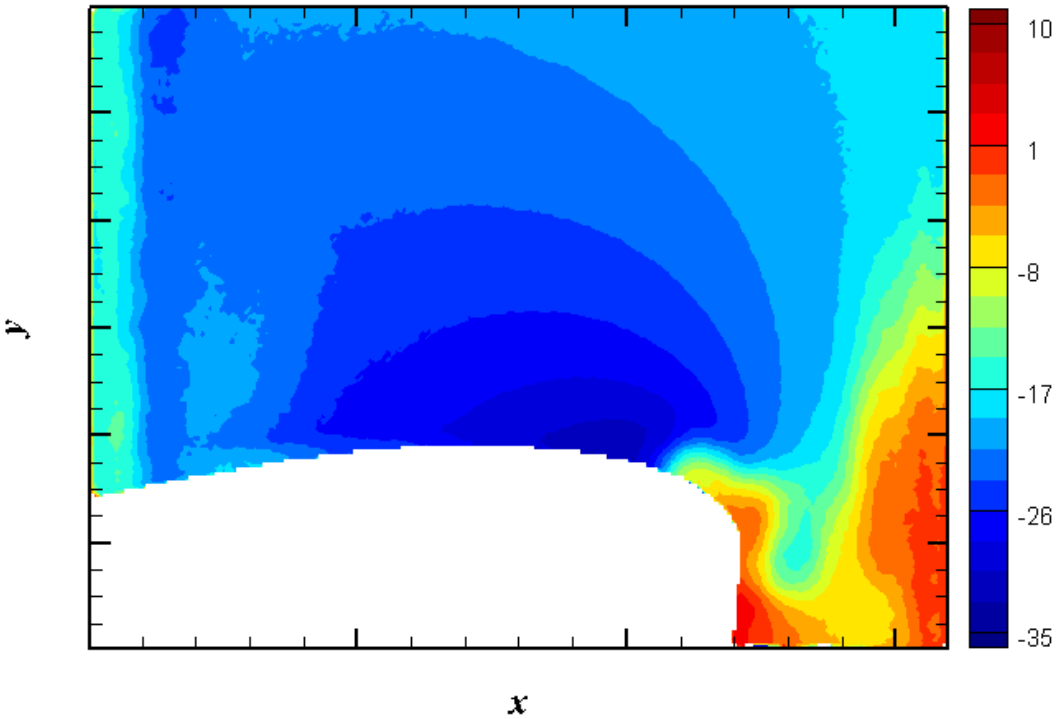

Figure C-4. *U* for α = 16° upstroke, adaptive interrogation window, no post-processing

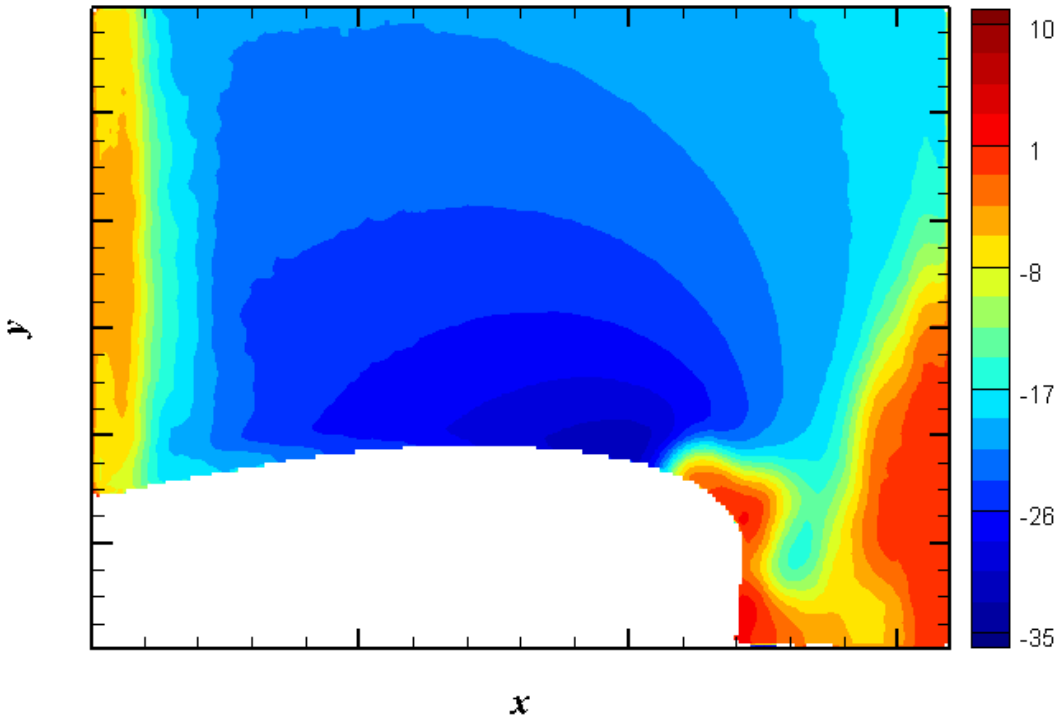

Figure C-5. *U* for α = 16° upstroke, adaptive interrogation window, smoothing on

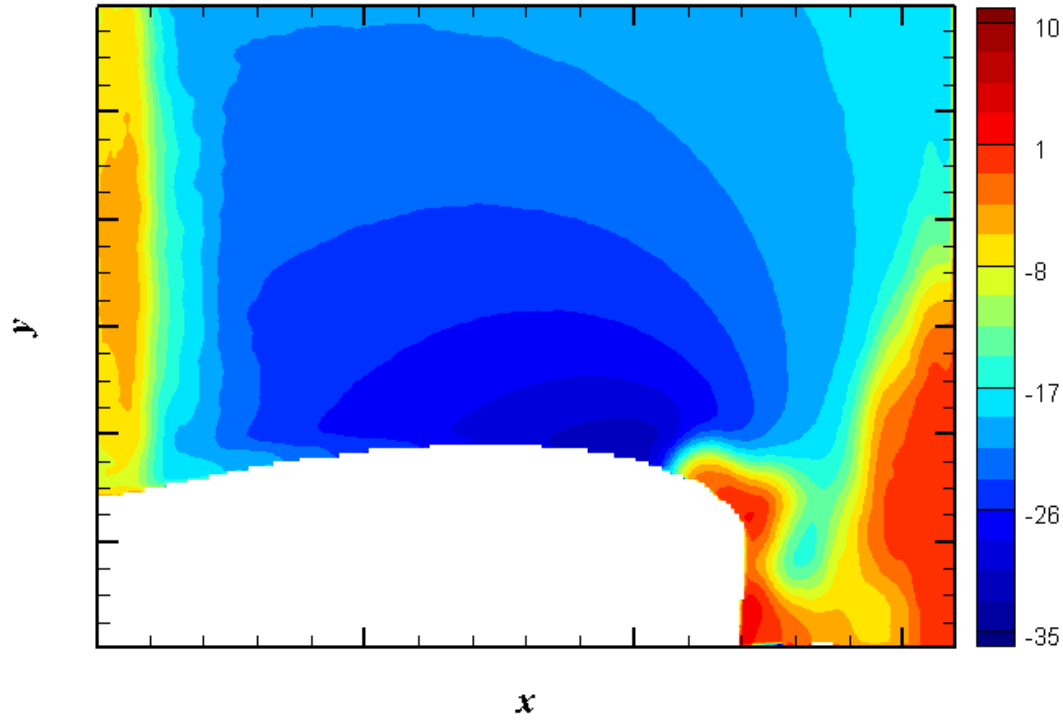

Figure C-6. *U* for α = 16° upstroke, adaptive interrogation window, smoothing and interpolation on

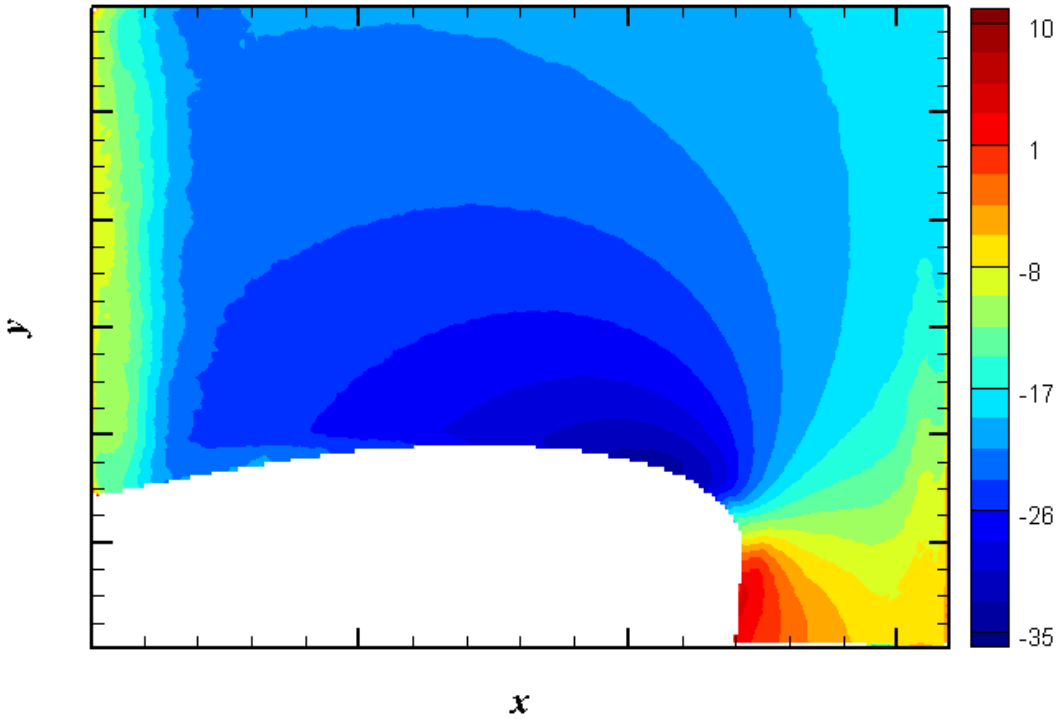

Figure C-7. *U* for α = 16° upstroke, adaptive interrogation window, 2 passes at each window size, smoothing and interpolation on

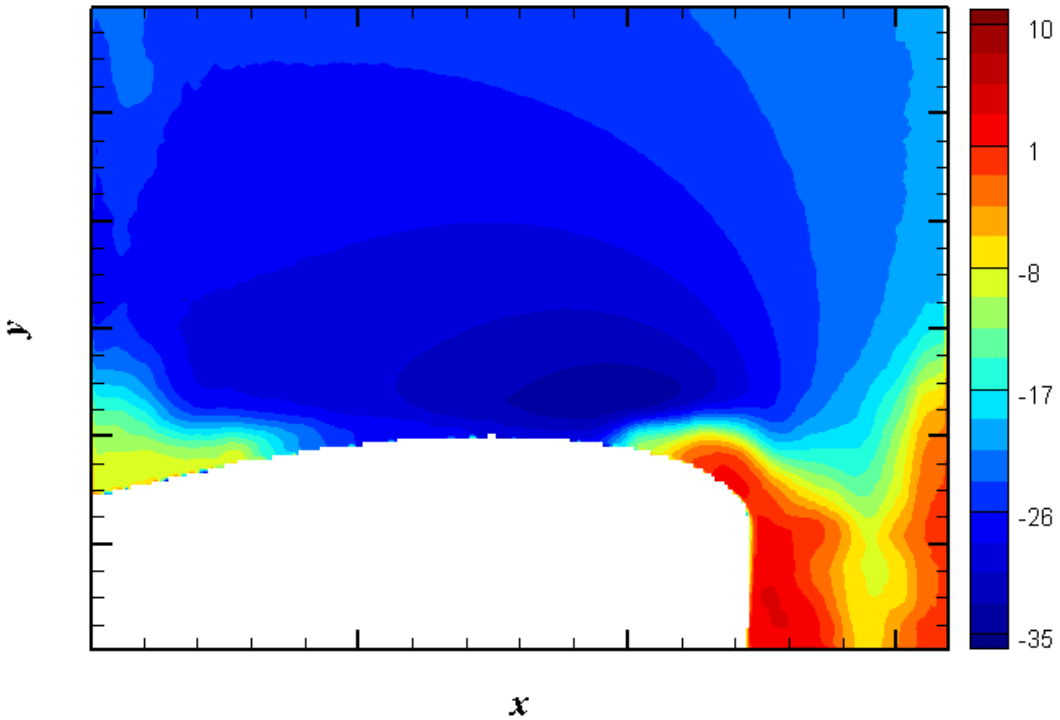

Figure C-8. *U* for α = 18° upstroke, adaptive interrogation window, smoothing and interpolation on

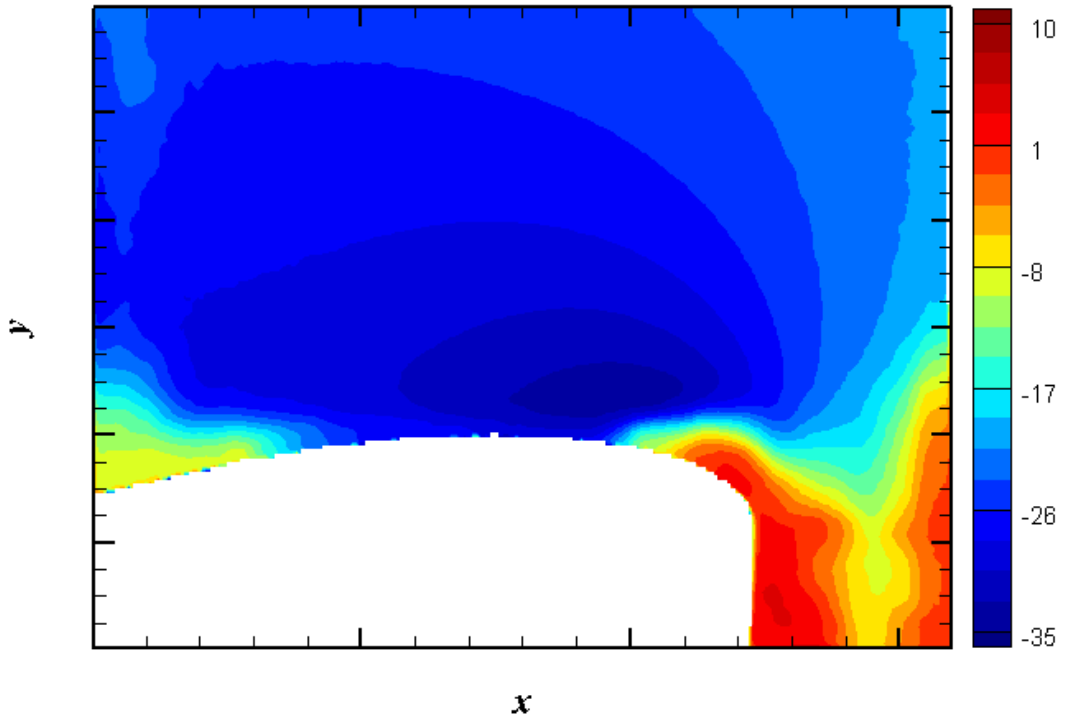

Figure C-9. *U* for $\alpha = 18°$ upstroke, adaptive interrogation window, smoothing and interpolation on, delete if $Q < 0.9$, remove groups with < 3 vectors

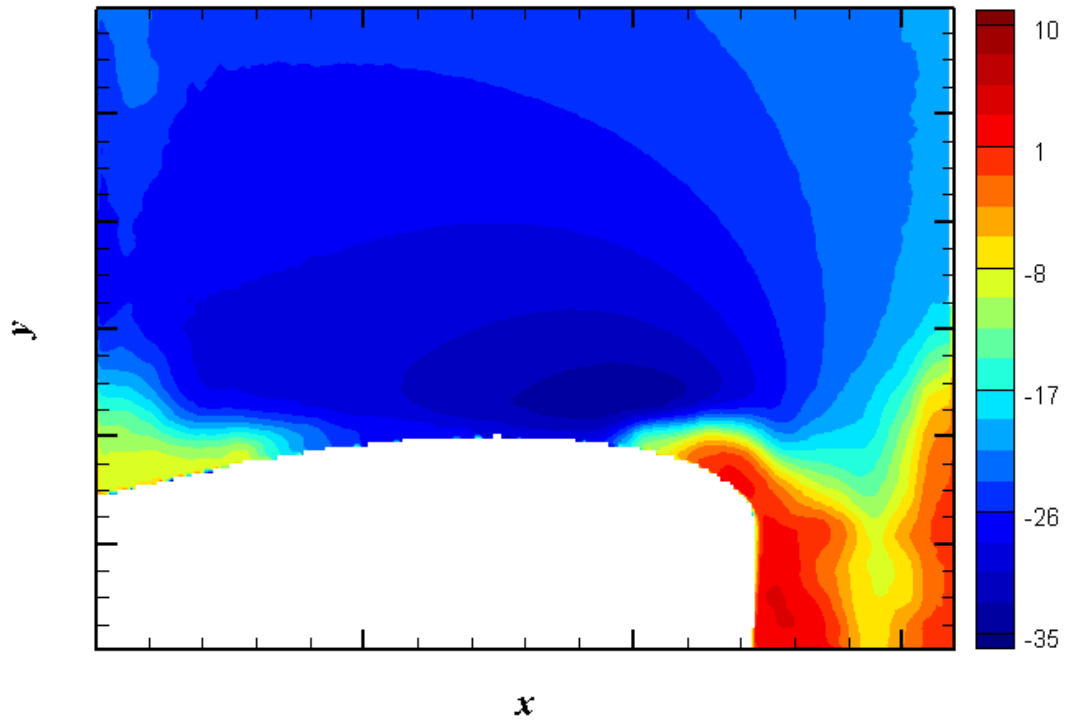

Figure C-10. *U* for $\alpha = 18°$ upstroke, adaptive interrogation window, smoothing and interpolation on, delete if $Q < 1.0$, remove groups with < 5 vectors

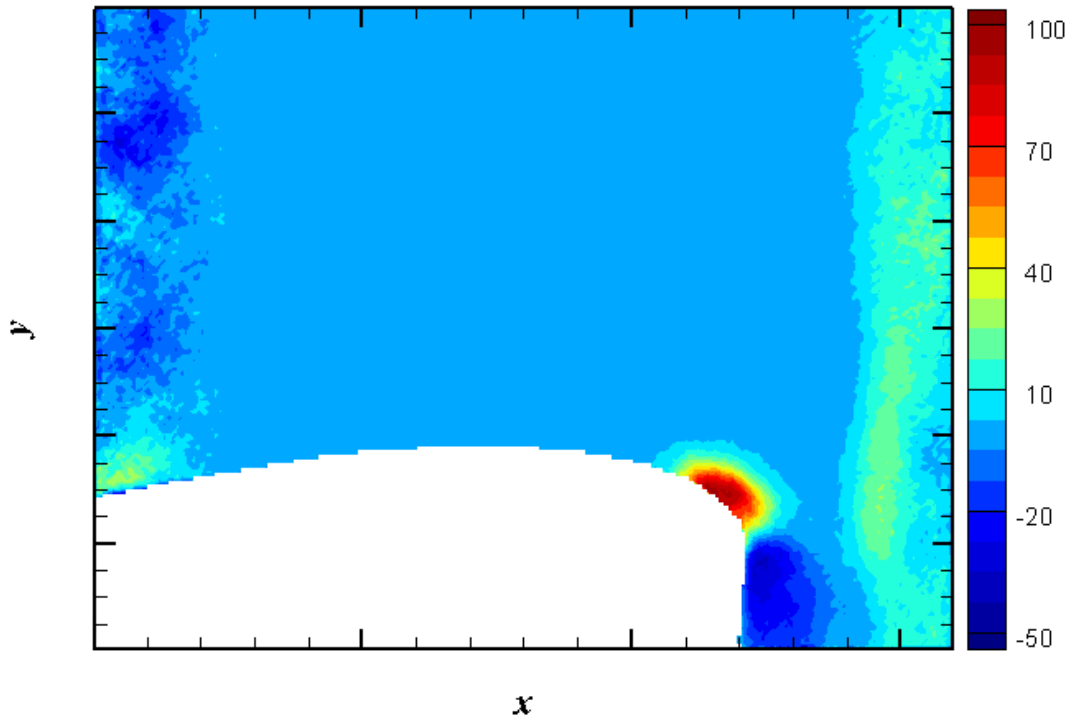

Figure C-11. τ_{xy} for α = 16° upstroke, square interrogation window, no post-processing

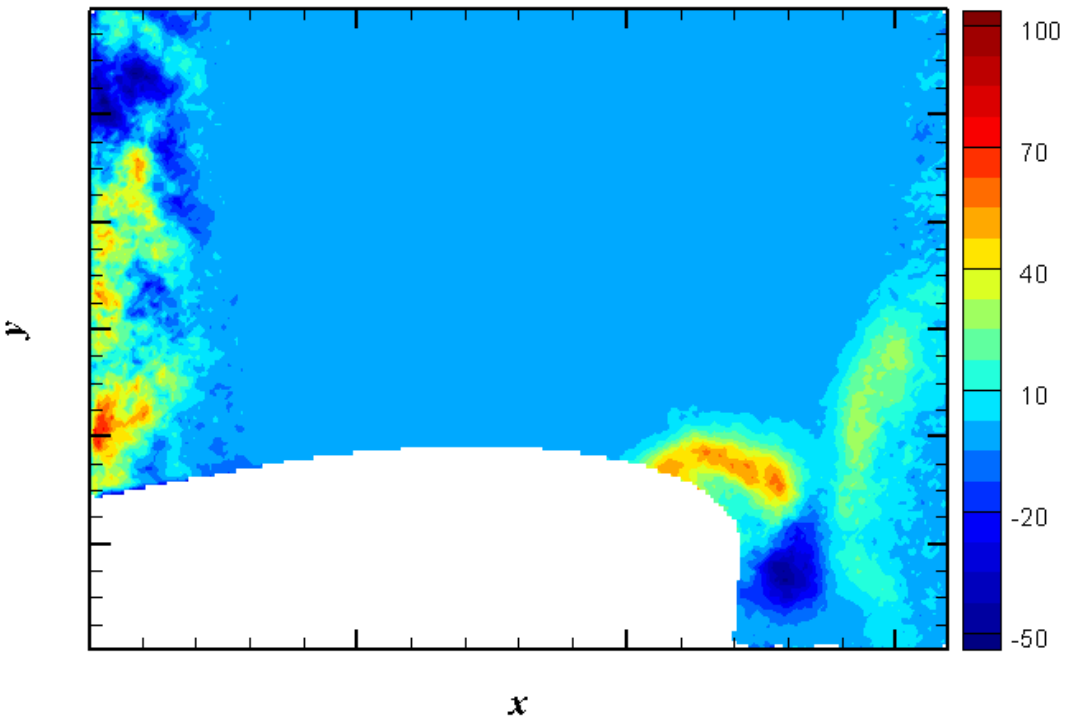

Figure C-12. τ_{xy} for α = 16° upstroke, circular interrogation window, no post-processing

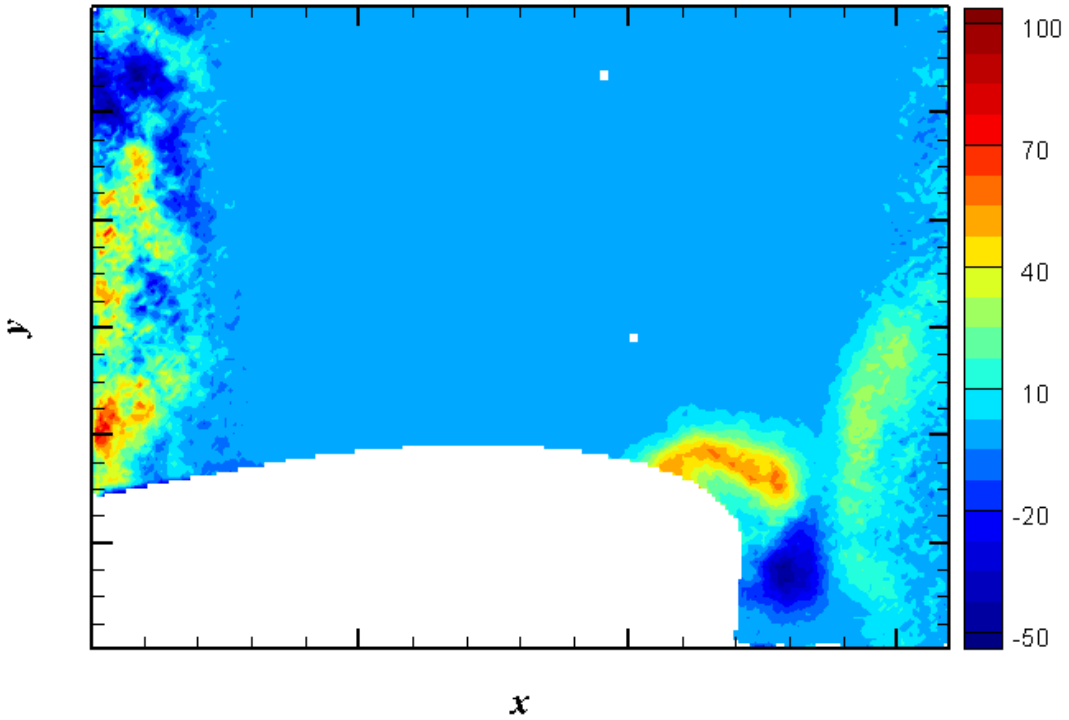

Figure C-13. τ_{xy} for α = 16° upstroke, 2:1 elliptical interrogation window, no post-processing

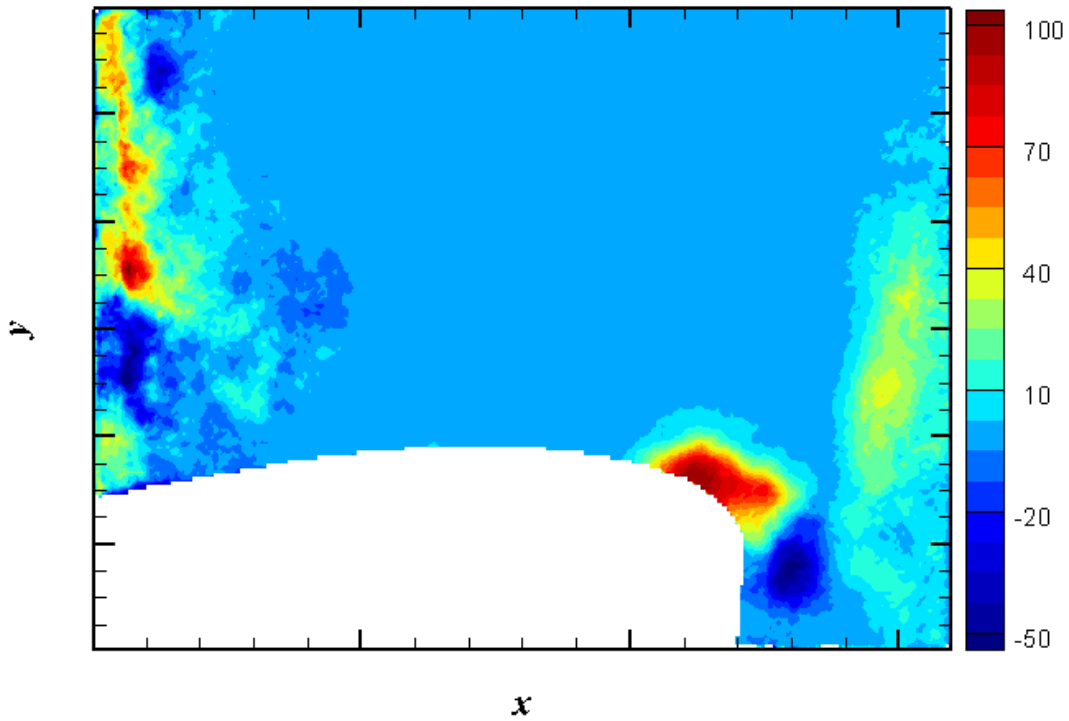

Figure C-14. τ_{xy} for α = 16° upstroke, adaptive interrogation window, no post-processing

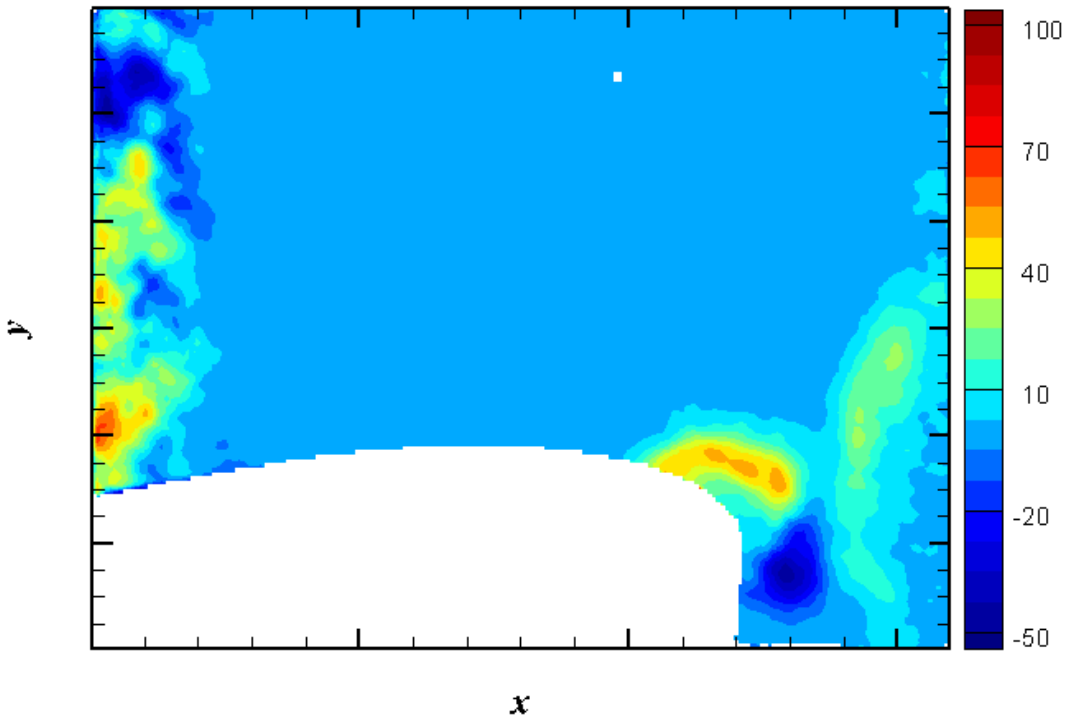

Figure C-15. τ_{xy} for $\alpha = 16°$ upstroke, adaptive interrogation window, smoothing on

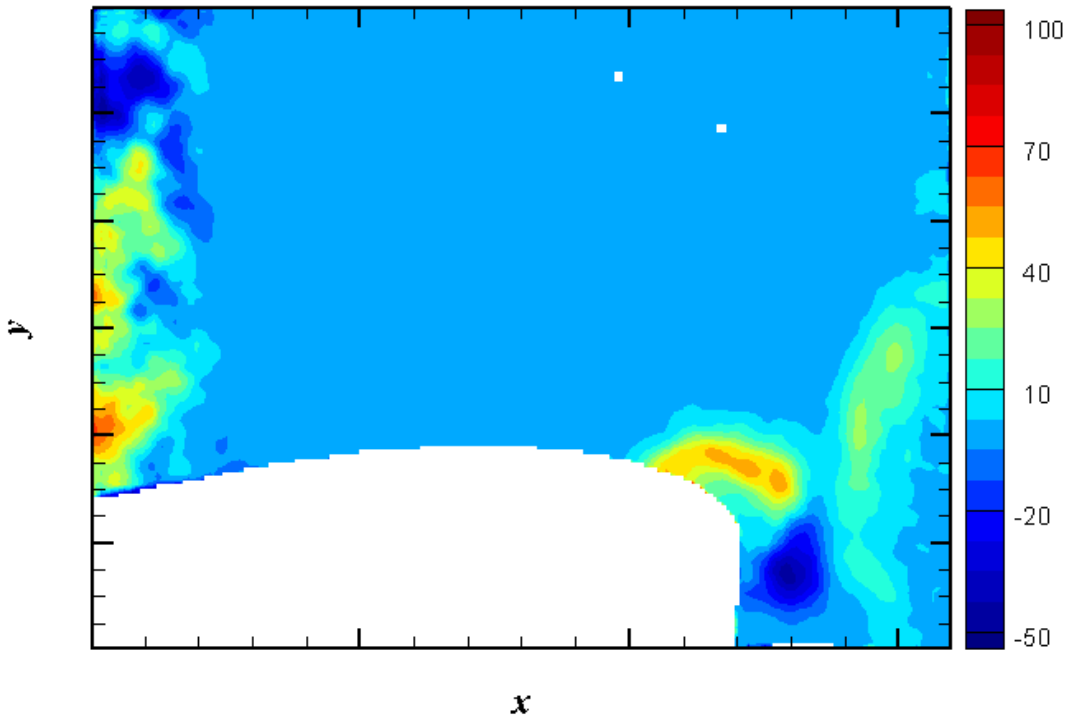

Figure C-16. τ_{xy} for $\alpha = 16°$ upstroke, adaptive interrogation window, smoothing and interpolation on

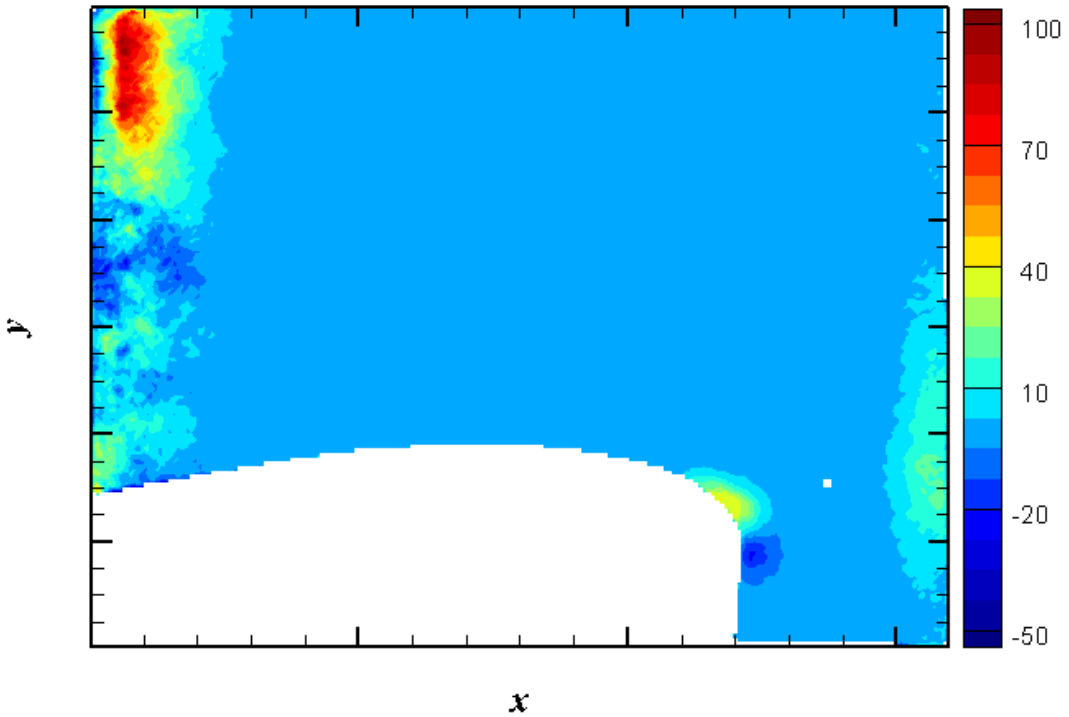

Figure C-17. τ_{xy} for α = 16° upstroke, adaptive interrogation window, 2 passes at each window size, smoothing and interpolation on

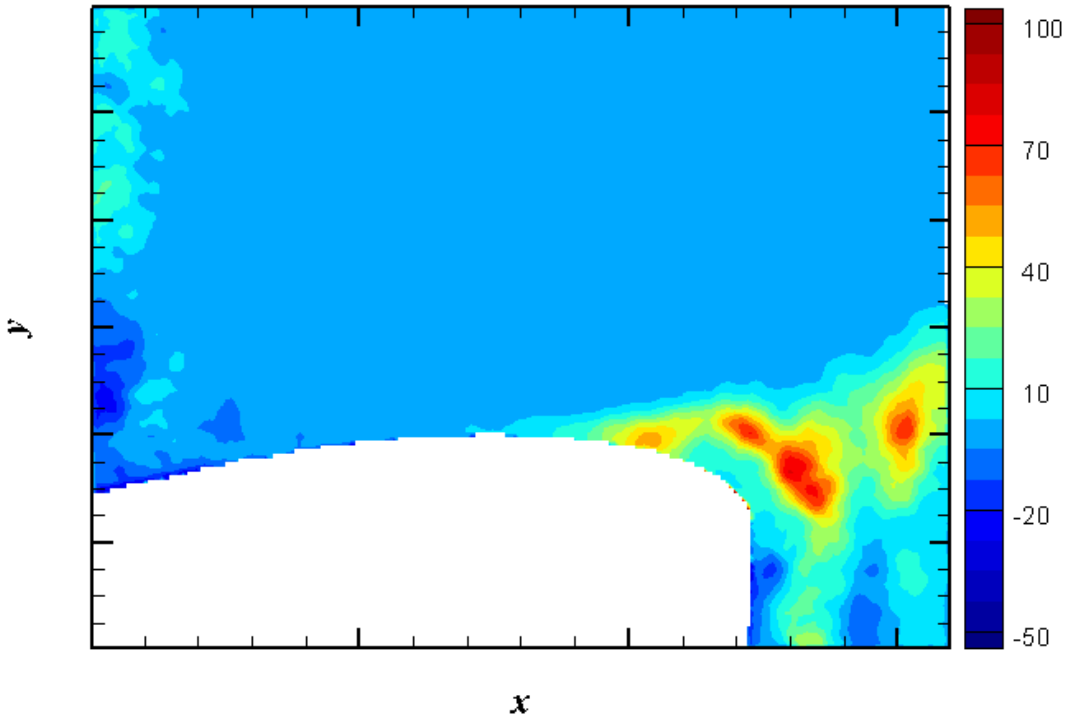

Figure C-18. τ_{xy} for α = 18° upstroke, adaptive interrogation window, smoothing and interpolation on

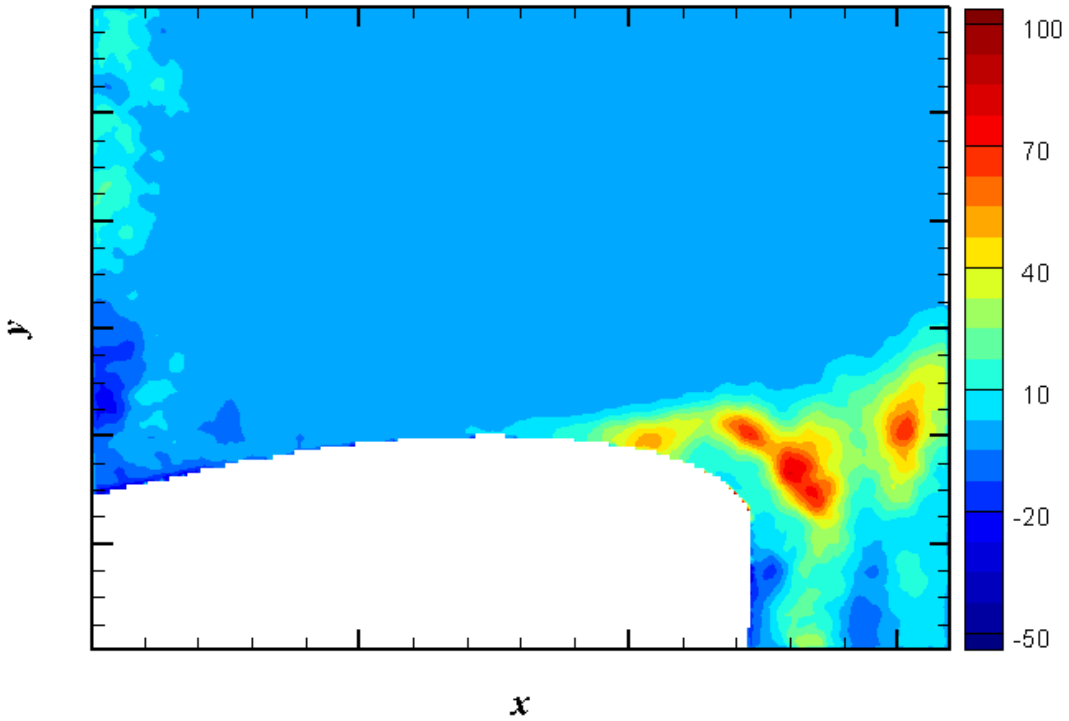

Figure C-19. τ_{xy} for $\alpha = 18°$ upstroke, adaptive interrogation window, smoothing and interpolation on, delete if $Q < 0.9$, remove groups with < 3 vectors

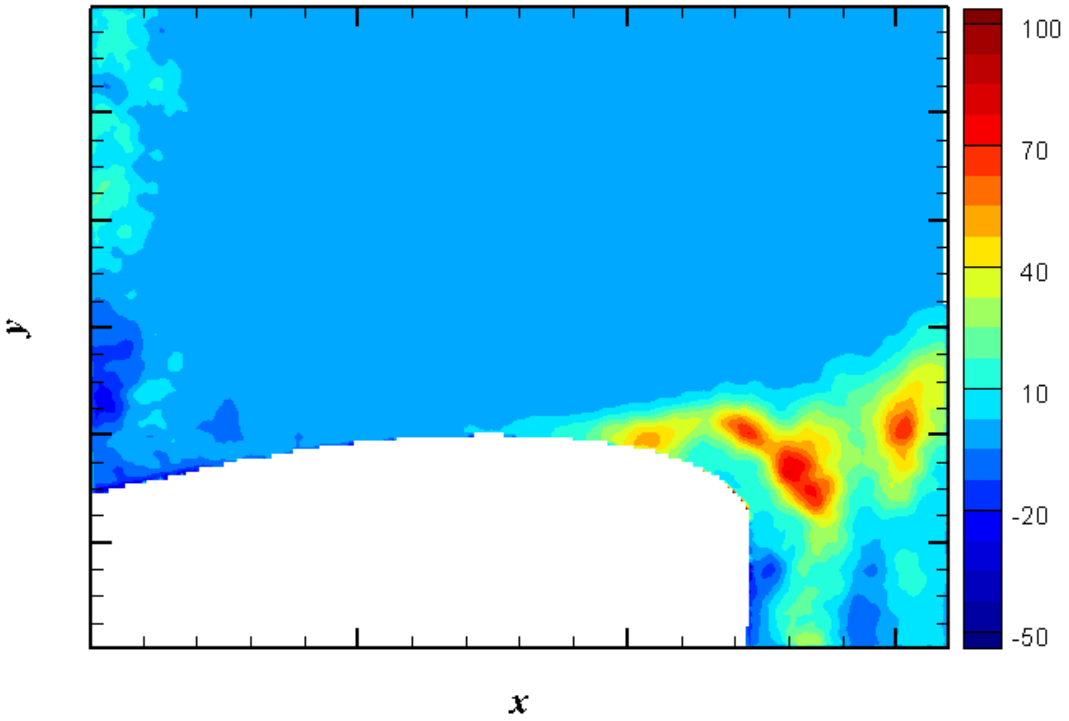

Figure C-20. τ_{xy} for $\alpha = 18°$ upstroke, adaptive interrogation window, smoothing and interpolation on, delete if $Q < 1.0$, remove groups with < 5 vectors

The following figures show the *U*-velocities and Reynolds shear stresses generated with TAMUPIV during a post-processing filter study. All of these figures are data for $\alpha = 16°$ during the upstroke phase of the pitching motion, shown with one color scale for velocity and another for Reynolds shear stress. A filtering factor of 2.0σ was used for the final data processing. All results shown in Appendix A use this filtering factor.

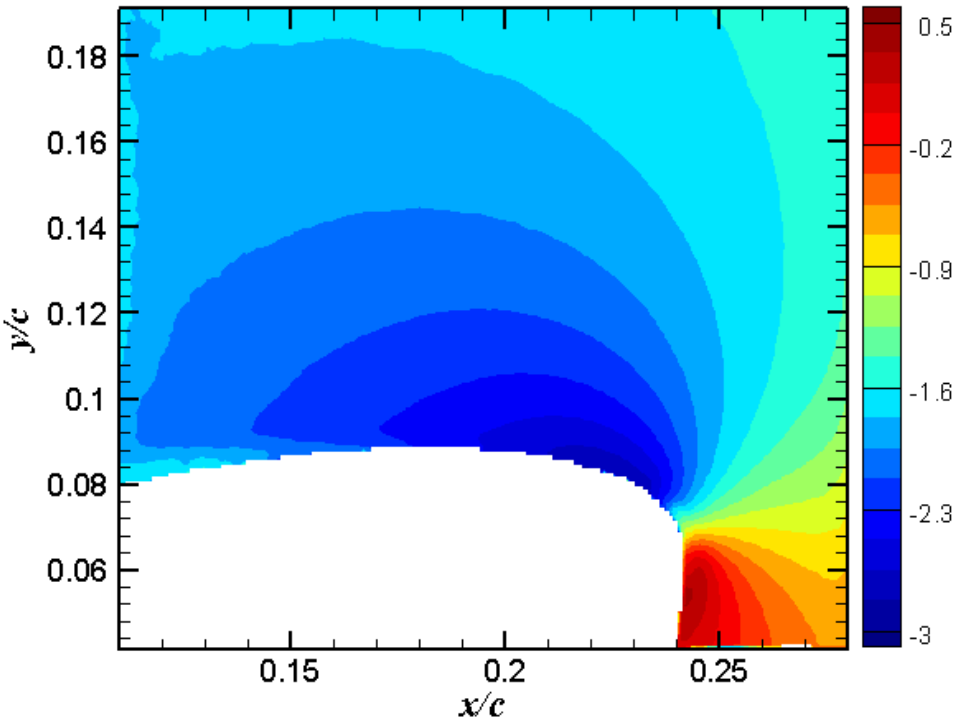

Figure C-21. *U* contour for $\alpha = 16°$, upstroke, with a filtering factor of 1.0σ

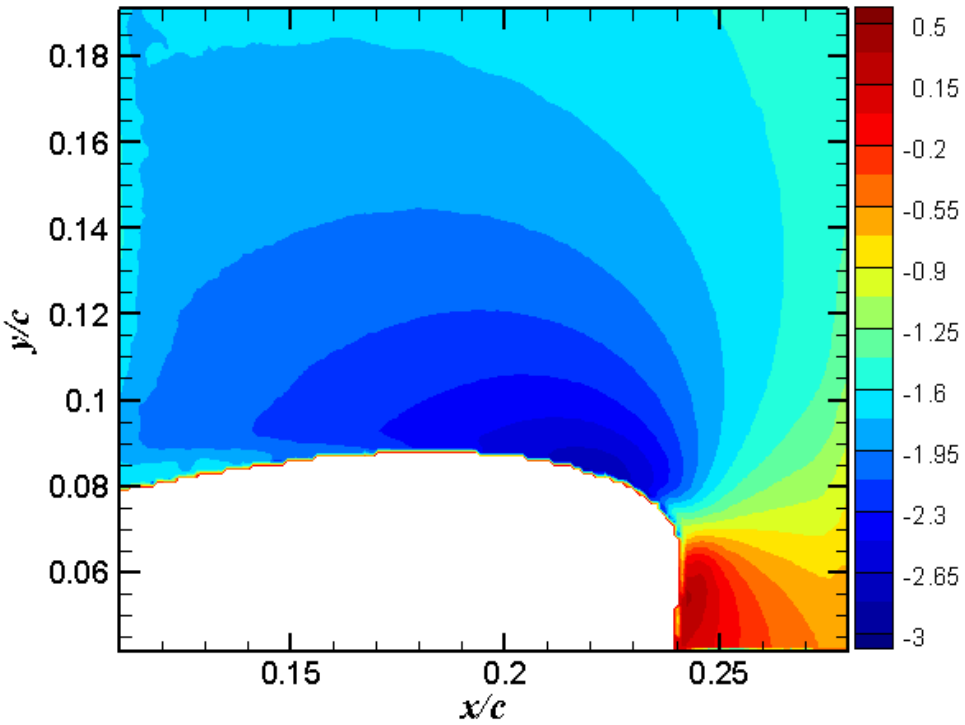

Figure C-22. *U* contour for α = 16°, upstroke, with a filtering factor of 2.0σ

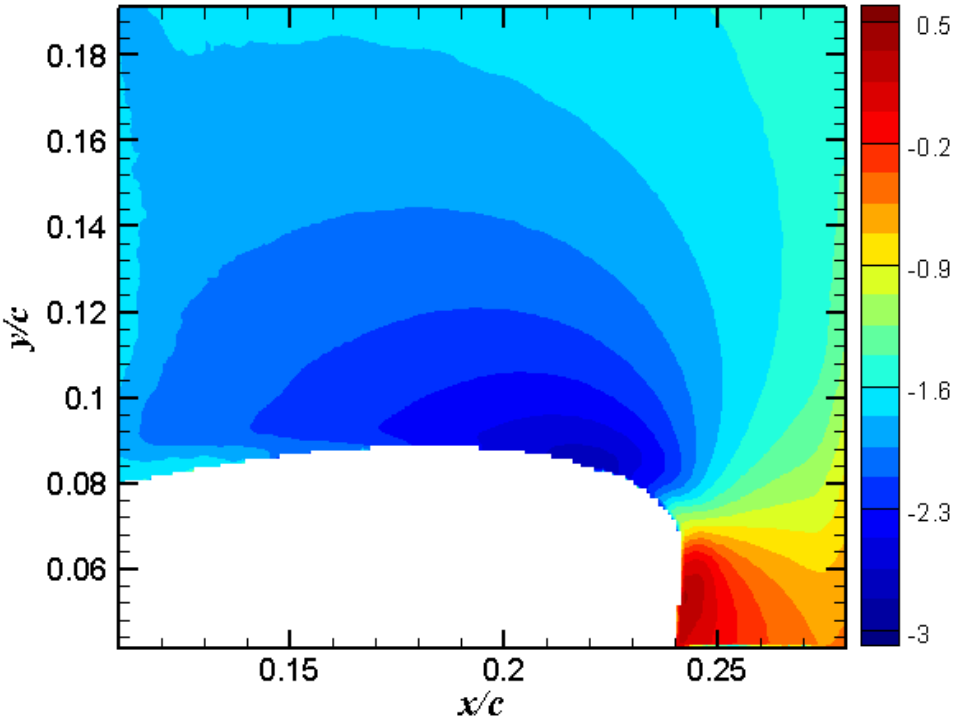

Figure C-23. *U* contour for α = 16°, upstroke, with a filtering factor of 3.0σ

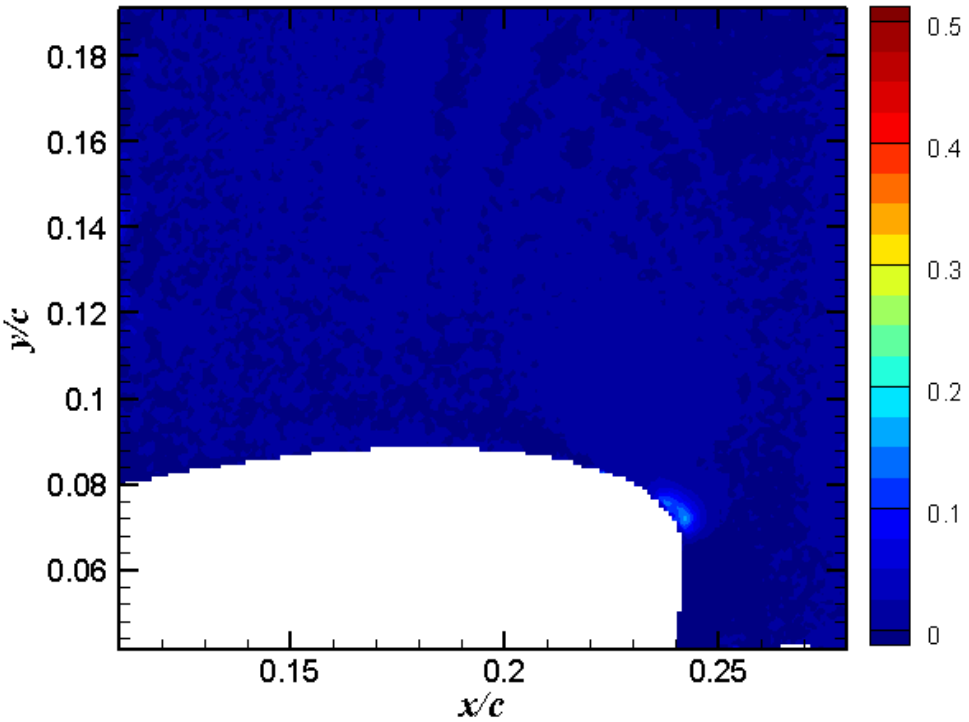

Figure C-24. τ_{xy} contour for α = 16°, upstroke, with a filtering factor of 1.0σ

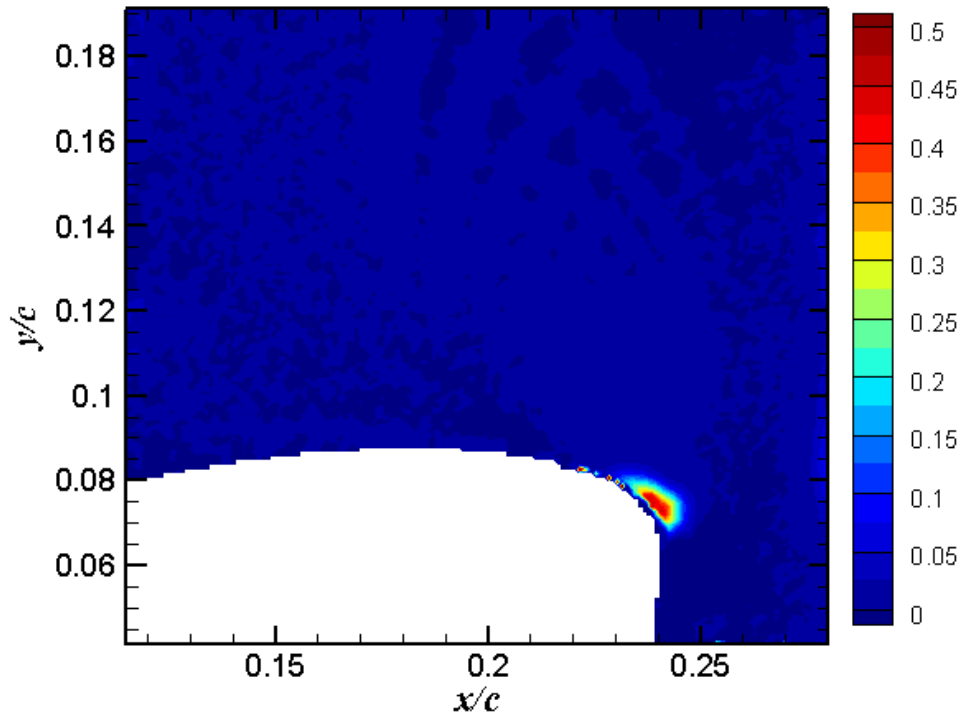

Figure C-25. τ_{xy} contour for α = 16°, upstroke, with a filtering factor of 2.0σ

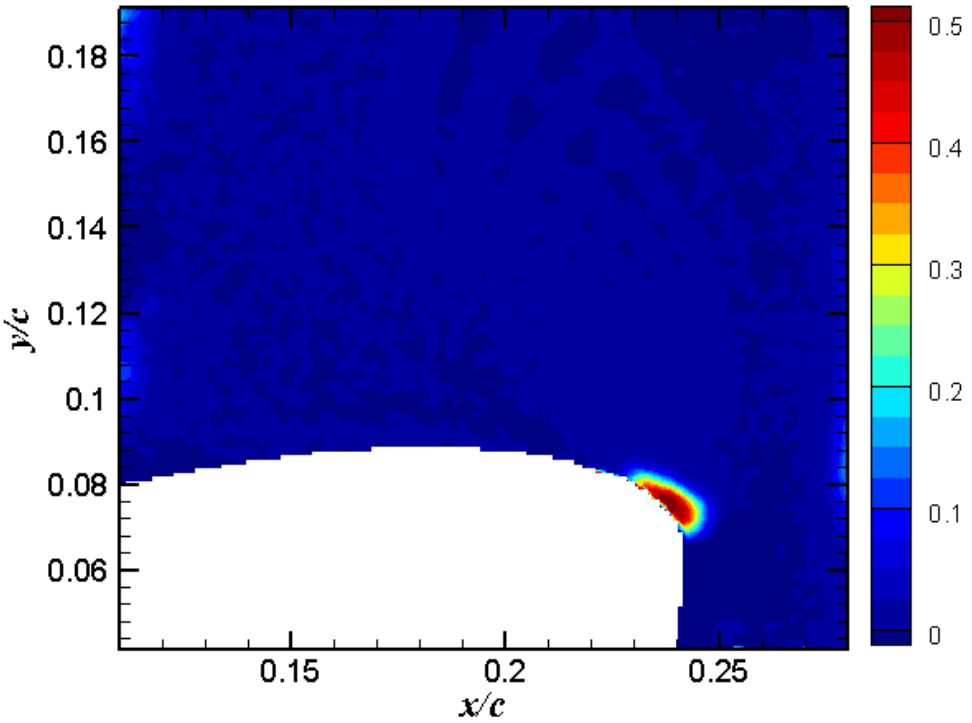

Figure C-26. τ_{xy} contour for α = 16°, upstroke, with a filtering factor of 3.0σ

VITA

Name:	Rachel Renee Vannelli
Address:	H. R. Bright Building, Room 701 c/o Dr. Rodney Bowersox 3141 TAMU College Station, TX 77843-3141
Email Address:	rachel.vannelli@gmail.com
Education:	B.S., Aerospace Engineering, Texas A&M University, 2008 M.S., Aerospace Engineering, Texas A&M University, 2011